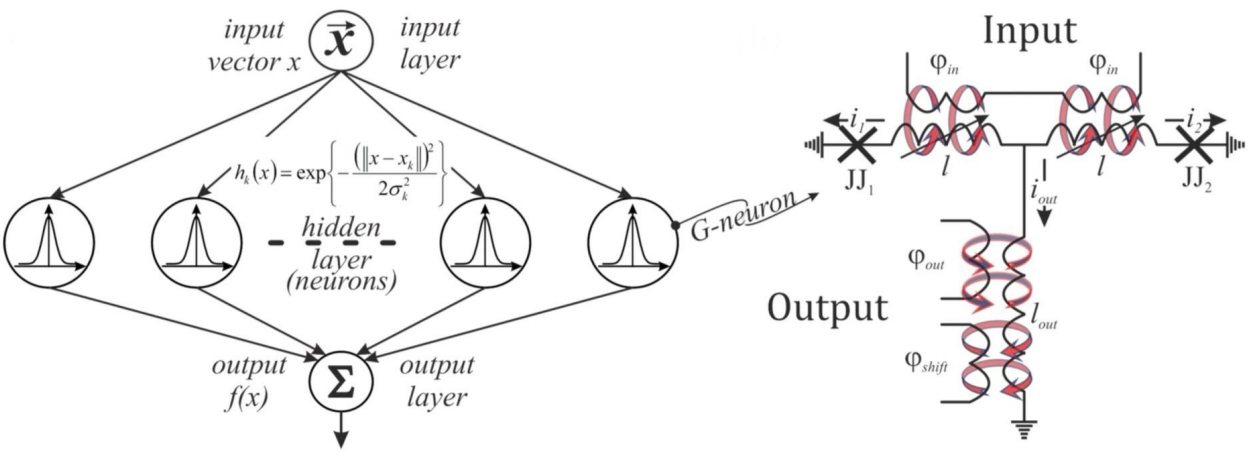
BEILSTEIN JOURNAL OF NANOTECHNOLOGY

Superconducting artificial neural networks and quantum circuits

Edited by Anatolie S. Sidorenko



Generated on 13 November 2026, 12:10

Imprint

Beilstein Journal of Nanotechnology
www.bjnano.org
ISSN 2190-4286
Email: journals-support@beilstein-institut.de

The *Beilstein Journal of Nanotechnology* is published by the Beilstein-Institut zur Förderung der Chemischen Wissenschaften.

Beilstein-Institut zur Förderung der Chemischen Wissenschaften
Trakehner Straße 7–9
60487 Frankfurt am Main
Germany
www.beilstein-institut.de

The copyright to this document as a whole, which is published in the *Beilstein Journal of Nanotechnology*, is held by the Beilstein-Institut zur Förderung der Chemischen Wissenschaften. The copyright to the individual articles in this document is held by the respective authors, subject to a Creative Commons Attribution license.

The cover image was reproduced from Beilstein J. Nanotechnol. 2022, 13, 444–454. https://doi.org/10.3762/bjnano.13.37 © 2022 Schegolev et al., published by the Beilstein-Institut, distributed under the terms of the Creative Commons Attribution 4.0 International License, https://creativecommons.org/licenses/by/4.0

BEILSTEIN JOURNAL OF NANOTECHNOLOGY

Superconducting artificial neural networks and quantum circuits

Anatolie S. Sidorenko

Editorial

Open Access

Address:
Technical University of Moldova, Chisinau 2004, Republic of Moldova

Email:
Anatolie S. Sidorenko - anatolie.sidorenko@mib.utm.md

Keywords:
artificial neural networks; high-performance computing; Josephson junctions; superconducting digital technologies; superconducting quantum circuits; ultra-low energy dissipation

Beilstein J. Nanotechnol. **2026,** *17,* 744–747.
https://doi.org/10.3762/bjnano.17.51

Received: 19 February 2026
Accepted: 11 May 2026
Published: 08 June 2026

This article is part of the thematic issue "Superconducting artificial neural networks and quantum circuits".

Editor-in-Chief: G. Wilde

© 2026 Sidorenko; licensee Beilstein-Institut.
License and terms: see end of document.

Research on artificial neural networks (ANNs) is currently one of the most rapidly developing areas of modern science and technology [1]. Neural networks have demonstrated high efficiency in solving problems of pattern recognition and classification, clustering, forecasting, approximation, and optimization.

Artificial neural networks are commonly divided into two main classes: software-based and hardware-based implementations. Software neural networks are realised as programs running on conventional computing platforms and utilizing standard computational resources. Typical examples include photo- and video-based traffic violation detection systems or face recognition in crowds [2].

Hardware neural networks, in contrast, are implemented as specialised physical devices such as chips or processors [3]. The development of such systems represents a complex physical and engineering challenge; however, it enables significantly lower energy dissipation and higher computational speed compared to conventional von Neumann architectures. A representative example is the IBM TrueNorth processor implemented using standard complementary metal–oxide–semiconductor (CMOS) technology in 2014. This processor models fully connected and recurrent neural networks and integrates one million model neurons and 256 million synaptic connections [4].

For solving more complex computational tasks that require substantial processing power, a critical challenge arises: the need for a radical reduction in energy dissipation while simultaneously increasing performance. The future of high-performance computing with reduced energy consumption is closely associated with technologies characterised by ultra-low energy dissipation. A highly promising approach is the implementation of artificial neural networks using superconducting quantum circuits and superconducting digital technologies based on Josephson junctions. The energy consumption of a basic element of superconducting digital technology is on the order of 10^{-19} J, corresponding to up to seven orders of magnitude lower energy dissipation than that of semiconductor ana-

logues [5]. Tuneable superconducting neurons and network architectures based on these principles have already been demonstrated [6].

Despite broad scientific and engineering interest in the development of artificial neural networks and quantum circuits, many fundamental problems remain unresolved. Among the most important challenges are: (i) processing of ultra-weak signals registered by highly sensitive cryogenic detectors, which is particularly relevant for deep-space communication and astronomical observations in the millimetre-wave and infrared frequency ranges [7-9]; (ii) cognitive radio and broadband signal reception, including superconducting signal processing for wideband spectrum sensing [10], as well as the development of quantum computing architectures and basic qubit technologies [11]; (iii) on-board signal processing in satellite systems, where severe constraints on power consumption and heat removal must be simultaneously addressed [12].

At present, the most energy-efficient circuit solutions are based on adiabatic superconducting logic. Such circuits do not exhibit a fundamental lower limit on energy consumption per operation. Adiabatic superconducting logic is actively developed worldwide, and recent demonstrations include a microprocessor with a total energy consumption of approximately 15 fJ per operation at a clock frequency of 5 GHz, including cooling overhead. This level of efficiency is comparable to the energy consumption of a single CMOS transistor [13].

The development of energy-efficient neuromorphic computers requires solving a broad range of fundamental, technological, engineering, and circuit-design challenges. In particular, both theoretical and experimental research is required to identify new physical phenomena suitable for novel base elements of superconducting neural networks, to develop advanced fabrication techniques for functional nanostructures, and to propose engineering solutions enabling the practical realisation of neuromorphic computing systems.

This thematic issue presents contributions from leading experts – theoreticians, experimentalists, technologists, and circuit designers – actively working in these research directions. Below, the main ideas and technical solutions discussed in this thematic issue are briefly summarised.

During the last decade, brain-inspired artificial neural networks based on superconducting elements have become the subject of intensive research [14,15]. A superconducting Gaussian neuron implemented as a two-junction interferometer and a detailed analysis of its transfer function are presented in [16]. A promising design of a neuromorphic ANN based on superconducting elements is proposed in [17]. The superconducting Josephson diode introduced in this work enforces unidirectional pulse propagation, prevents backward influence between connected neurons, and enables compact circuit designs with increased integration density.

The development of advanced technologies for the fabrication of layered functional nanostructures is a time-consuming process. To reduce the number of costly technological iterations, modelling of technological processes is essential for predicting the properties of prepared layers and multilayers. Smart computational experiments based on a mathematical model describing coordinated atomic motion predict unique magnetic properties of thin cobalt-based layers widely used in hybrid superconductor–ferromagnet structures for superconducting spintronics [18,19].

New elements of quantum circuits based on transmon “superconducting atoms” demonstrate rapid qubit control in real superconducting systems [20]. A theoretical study of the energy spectrum of a coupled single spin interacting with an infinitely coordinated Ising chain reveals a first-order phase transition between two stable phase-symmetric states, resulting in a splitting of the energy minima of the Ising chain. This phenomenon may be useful for engineering improved qubits for quantum computation [21].

Novel microwave quantum detectors [22], ultra-high-frequency receivers [23], and terahertz-range on-chip oscillators [24] based on superconducting heterostructures demonstrate significant potential for various applications of superconducting devices.

Geometry-controlled engineering of superconducting systems shows that geometric factors, such as interface curvature in normal metal–superconductor junctions, strongly influence the proximity effect and the decay length of Cooper-pair correlations [25]. For superconducting systems with complex topology, such as Fibonacci chains, enhanced spatial oscillations of the superconducting order parameter lead to a pronounced reduction of the critical temperature [26]. These findings are important for the design and optimisation of superconducting circuits, hybrid devices, and superconducting materials with complex and fractal topology [27,28].

Proximity-coupled superconductor/ferromagnet heterostructures demonstrate a number of novel phenomena, including the Fulde–Ferrell–Larkin–Ovchinnikov nonuniform superconducting state with singlet pairing [29], nonuniform superconducting states with triplet pairing [30], and fast vortex dynamics and relaxation processes in NbRe-based heterostructures,

which may serve as a basis for devices requiring ultrafast relaxation times [31].

The concept of this thematic issue emerged during the 10th International Conference on Superconductivity and Magnetism (ICSM2025) and the 3rd International Conference on Quantum Materials and Technologies (ICQMT2025), held from 26 April to 3 May 2025 in Fethiye–Ölüdeniz, Turkey. The ideas, physical phenomena, technological approaches, and engineering solutions presented by invited speakers at these conferences constitute the scientific core of this issue.

As Guest Editor of this thematic issue, I thank all contributors and the Beilstein Journals Production Team for their professional editorial support. This work was supported by the HSE University project “International academic cooperation”. Financial support from the RM project (G.A. No. O2.02.01) “Nanostructures and advanced materials for applications in spintronics, thermoelectricity and optoelectronics” is gratefully acknowledged.

Anatolie S. Sidorenko

Chisinau, February 2026

ORCID® iDs

Anatolie S. Sidorenko - https://orcid.org/0000-0001-7433-4140

Data Availability Statement

Data sharing is not applicable as no new data was generated or analyzed in this study.

References

1. Merolla, P. A.; Arthur, J. V.; Alvarez-Icaza, R.; Cassidy, A. S.; Sawada, J.; Akopyan, F.; Jackson, B. L.; Imam, N.; Guo, C.; Nakamura, Y.; Brezzo, B.; Vo, I.; Esser, S. K.; Appuswamy, R.; Taba, B.; Amir, A.; Flickner, M. D.; Risk, W. P.; Manohar, R.; Modha, D. S. *Science* **2014,** *345,* 668–673. doi:10.1126/science.1254642
2. Kattan, A.; Abdullah, R.; Geem, Z. W. *Artificial Neural Network Training and Software Implementation Techniques;* Noca Science Publishers: New York, NY, USA, 2011.
3. Misra, J.; Saha, I. *Neurocomputing* **2010,** *74,* 239–255. doi:10.1016/j.neucom.2010.03.021
4. Akopyan, F.; Sawada, J.; Cassidy, A.; Alvarez-Icaza, R.; Arthur, J.; Merolla, P.; Imam, N.; Nakamura, Y.; Datta, P.; Nam, G.-J.; Taba, B.; Beakes, M.; Brezzo, B.; Kuang, J. B.; Manohar, R.; Risk, W. P.; Jackson, B.; Modha, D. S. *IEEE Trans. Comput.-Aided Des. Integr. Circuits Syst.* **2015,** *34,* 1537–1557. doi:10.1109/tcad.2015.2474396
5. Soloviev, I. I.; Klenov, N. V.; Bakurskiy, S. V.; Kupriyanov, M. Y.; Gudkov, A. L.; Sidorenko, A. S. *Beilstein J. Nanotechnol.* **2017,** *8,* 2689–2710. doi:10.3762/bjnano.8.269
6. Schegolev, A. E.; Klenov, N. V.; Bakurskiy, S. V.; Soloviev, I. I.; Kupriyanov, M. Y.; Tereshonok, M. V.; Sidorenko, A. S. *Beilstein J. Nanotechnol.* **2022,** *13,* 444–454. doi:10.3762/bjnano.13.37
7. Tucker, J. R. *Appl. Phys. Lett.* **1980,** *36,* 477–479. doi:10.1063/1.91513
8. Kerr, A. R.; Feldman, M. J.; Pan, S. K. Receiver Noise Temperature, the Quantum Noise Limit, and the Role of the Zero-Point Fluctuations. In *Proceedings of the Eighth International Symposium on Space Terahertz Technology,* 1997; pp 101–109.
9. Revin, L. S.; Pimanov, D. A.; Chiginev, A. V.; Blagodatkin, A. V.; Zbrozhek, V. O.; Samartsev, A. V.; Orlova, A. N.; Masterov, D. V.; Parafin, A. E.; Safonova, V. Y.; Gordeeva, A. V.; Pankratov, A. L.; Kuzmin, L. S.; Sidorenko, A. S.; Masi, S.; de Bernardis, P. *Beilstein J. Nanotechnol.* **2024,** *15,* 26–36. doi:10.3762/bjnano.15.3
10. Quan, Z.; Cui, S.; Sayed, A. H.; Poor, H. V. Wideband Spectrum Sensing in Cognitive Radio Networks. In *2008 IEEE International Conference on Communications,* Beijing, China, May 19–23, 2008; IEEE, 2008; pp 901–906. doi:10.1109/icc.2008.177
11. Chae, E.; Choi, J.; Kim, J. *Nano Convergence* **2024,** *11,* 11. doi:10.1186/s40580-024-00418-5
12. Ortiz, F.; Monzon Baeza, V.; Garces-Socarras, L. M.; Vásquez-Peralvo, J. A.; Gonzalez, J. L.; Fontanesi, G.; Lagunas, E.; Querol, J.; Chatzinotas, S. *Aerospace* **2023,** *10,* 101. doi:10.3390/aerospace10020101
13. Ayala, C. L.; Tanaka, T.; Saito, R.; Nozoe, M.; Takeuchi, N.; Yoshikawa, N. *IEEE J. Solid-State Circuits* **2021,** *56,* 1152–1165. doi:10.1109/jssc.2020.3041338
14. Schegolev, A. E.; Bastrakova, M. V.; Sergeev, M. A.; Maksimovskaya, A. A.; Klenov, N. V.; Soloviev, I. *Mesosci. Nanotechnol.* **2024,** *1,* 01005. doi:10.64214/jmsn.01.01005
15. Sidorenko, A.; Klenov, N.; Soloviev, I.; Bakurskiy, S.; Boian, V.; Morari, R.; Savva, Y.; Lomakin, A.; Sidorenko, L.; Sidorenko, S.; Sidorenko, I.; Severyukhina, O.; Fedotov, A.; Salamatina, A.; Vakhrushev, A. *Int. J. Circuits, Syst. Signal Process.* **2023,** *17,* 177–183. doi:10.46300/9106.2023.17.21
16. Razorenov, F. A.; Ionin, A. S.; Shuravin, N. S.; Karelina, L. N.; Sidel’nikov, M. S.; Egorov, S. V.; Bol’ginov, V. V. *Beilstein J. Nanotechnol.* **2025,** *16,* 1160–1170. doi:10.3762/bjnano.16.85
17. Ruzhickiy, V. I.; Maksimovskaya, A. A.; Bakurskiy, S. V.; Schegolev, A. E.; Tereshonok, M. V.; Kupriyanov, M. Y.; Klenov, N. V.; Soloviev, I. I. *Beilstein J. Nanotechnol.* **2025,** *16,* 1883–1893. doi:10.3762/bjnano.16.131
18. Fedotov, A.; Severyukhina, O.; Salomatina, A.; Sidorenko, A. *Beilstein J. Nanotechnol.* **2025,** *16,* 1557–1566. doi:10.3762/bjnano.16.110
19. Fedotov, A.; Severyukhina, O.; Salomatina, A.; Boian, V.; Sidorenko, A. *Mesosci. Nanotechnol.* **2025,** *1,* 02003. doi:10.64214/jmsn.01.02003
20. Koch, J.; Yu, T. M.; Gambetta, J.; Houck, A. A.; Schuster, D. I.; Majer, J.; Blais, A.; Devoret, M. H.; Girvin, S. M.; Schoelkopf, R. J. *Phys. Rev. A* **2007,** *76,* 042319. doi:10.1103/physreva.76.042319
21. Seidov, S.; Pugach, N.; Sidorenko, A. *Beilstein J. Nanotechnol.* **2025,** *16,* 1668–1676. doi:10.3762/bjnano.16.117
22. Tarasov, M.; Fominskii, M.; Gunbina, A.; Krasilnikov, A.; Mansfeld, M.; Kukushkin, D.; Maruhno, A.; Ievleva, V.; Strelkov, M.; Zhogov, D.; Arutyunov, K.; Vdovin, V.; Stolyarov, V.; Edelman, V. *Beilstein J. Nanotechnol.* **2025,** *16,* 1931–1941. doi:10.3762/bjnano.16.134
23. Matrozova, E. A.; Chiginev, A. V.; Revin, L. S.; Pankratov, A. L. *Beilstein J. Nanotechnol.* **2025,** *16,* 2199–2206. doi:10.3762/bjnano.16.152

24. Khan, F. V.; Filippenko, L. V.; Ermakov, A. B.; Fominsky, M. Y.; Koshelets, V. P. *Beilstein J. Nanotechnol.* **2025,** *16,* 2296–2305. doi:10.3762/bjnano.16.158
25. Tomayeva, M. A.; Neverov, V. D.; Krasavin, A. V.; Vagov, A.; Croitoru, M. D. *Beilstein J. Nanotechnol.* **2025,** *16,* 2265–2273. doi:10.3762/bjnano.16.155
26. Nikonov, E. G.; Chen, Y.; Doria, M. M.; Shanenko, A. A. *Beilstein J. Nanotechnol.* **2025,** *16,* 2177–2182. doi:10.3762/bjnano.16.150
27. Sidorenko, A. S. *Fractals* **1997,** *5* (Suppl. 2), 101–117. doi:10.1142/s0218348x97000851
28. Sidorenko, A. S. *Mold. J. Phys. Sci.* **2002,** *1,* 102–105.
29. Sidorenko, A. S. *Low Temp. Phys.* **2017,** *43,* 766–771. doi:10.1063/1.4995623
30. Lenk, D.; Zdravkov, V. I.; Kehrle, J.-M.; Obermeier, G.; Ullrich, A.; Morari, R.; Krug von Nidda, H.-A.; Müller, C.; Kupriyanov, M. Y.; Sidorenko, A. S.; Horn, S.; Deminov, R. G.; Tagirov, L. R.; Tidecks, R. *Beilstein J. Nanotechnol.* **2016,** *7,* 957–969. doi:10.3762/bjnano.7.88
31. De Chiara, F.; Makhdoumi Kakhaki, Z.; Avitabile, F.; Colangelo, F.; Kumar, A.; Attanasio, C.; Cirillo, C. *Beilstein J. Nanotechnol.* **2026,** *17,* 292–302. doi:10.3762/bjnano.17.20

License and Terms

This is an open access article licensed under the terms of the Beilstein-Institut Open Access License Agreement (https://www.beilstein-journals.org/bjnano/terms), which is identical to the Creative Commons Attribution 4.0 International License (https://creativecommons.org/licenses/by/4.0). The reuse of material under this license requires that the author(s), source and license are credited. Third-party material in this article could be subject to other licenses (typically indicated in the credit line), and in this case, users are required to obtain permission from the license holder to reuse the material.

The definitive version of this article is the electronic one which can be found at:
https://doi.org/10.3762/bjnano.17.51

BEILSTEIN JOURNAL OF NANOTECHNOLOGY

Transfer function of an asymmetric superconducting Gauss neuron

Fedor A. Razorenov*[1,2], Aleksander S. Ionin[1,2,3], Nikita S. Shuravin[1], Liubov N. Karelina[1], Mikhail S. Sidel'nikov[1], Sergey V. Egorov[1] and Vitaly V. Bol'ginov[1]

Full Research Paper

Open Access

Address:
[1]Osipyan Institute of Solid State Physics RAS, Chernogolovka, Moscow District, 2 Academician Osipyan str., 142432, Russian Federation, [2]Moscow Institute of Physics and Technology, 9 Institutskiy per., Dolgoprudny, Moscow Region, 141701, Russian Federation and [3]Joint Venture Quantum Technologies, 121205, Moscow, Russian Federation

Email:
Fedor A. Razorenov* - razorenov.fa@phystech.edu

* Corresponding author

Keywords:
Josephson interferometers; superconducting neural network; superconductivity

Beilstein J. Nanotechnol. **2025,** *16,* 1160–1170.
https://doi.org/10.3762/bjnano.16.85

Received: 10 March 2025
Accepted: 03 July 2025
Published: 21 July 2025

This article is part of the thematic issue "Superconducting artificial neural networks and quantum circuits".

Guest Editor: A. S. Sidorenko

© 2025 Razorenov et al.; licensee Beilstein-Institut.
License and terms: see end of document.

Abstract

The Gauss neuron is a nonlinear signal converter, whose transfer function (TF) is described by the derivative of some sigmoidal dependence. A superconducting Gauss neuron can be implemented as a two-junction interferometer shunted symmetrically by an additional inductance. This work analyzes three cases of asymmetry that can occur in the experimental samples of Gauss neurons, that is, unequal critical currents of the interferometer's Josephson junctions, asymmetric inductive shunting, and asymmetry of the input signal supply. We illustrate the modifications in equations and the shape of the TF compared to the symmetric case. The analysis performed provides an explanation for the key features observed in a previously conducted experiment.

Introduction

Over the past decade, artificial neural networks have demonstrated their effectiveness and versatility in tasks related to processing large volumes of data, prediction, pattern recognition, and image and video generation. The increasing number of tasks and the growing volume of processed information highlight the relevance of using superconducting elements, which offer the advantages of high clock frequency and energy efficiency [1,2]. Studies [3-6] describe neuromorphic elements based on superconducting interferometers that emulate the signal response of biological neurons in various real-world scenarios. In [1,7-15], adiabatic neuromorphic interferometers were presented, whose energy consumption can be reduced to the fundamental limit of $kT\cdot\ln 2$ [16]. These devices contain one or two Josephson junctions (JJs) enclosed in a superconducting loop with three inductive elements. Such devices' design is much simpler than that of a neuromorphic CMOS element, that

contains about 20 transistors per cell [7,8], which also speaks in favor of superconducting neuromorphic devices.

The subject of this study is the Gauss neuron [1,7-9,11,12,14], schematically depicted in Figure 1. It consists of three arms connected at a common point O and grounded to a shared electrode (Gnd). Two arms ("Josephson" or "input" ones) each contain a Josephson junction $JJ_{A,B}$ and an inductance $L_{A,B}$, which is also used for receiving input signal. It is assumed that the input arms of the neuron are identical, including equal sensitivity to the input signal. These arms form the two-junction interferometer, and each of them is shunted by the third (output) arm. The latter consists of an inductive element L_{out}, which generates a magnetic flux $\Phi_{out} = L_{out}I_{out}$ when a current I_{out} flows through it (currents in the input arms are denoted as $I_{A,B}$ in Figure 1). The input signal of the neuron is the magnetic flux Φ_{in}, created using a control line (CL, shown as a dashed line in Figure 1), an external solenoid, or another method. An additional magnetic flux Φ_b is also introduced into the neuron, influencing the shape of the neuron's transfer function (TF) [1,12,14].

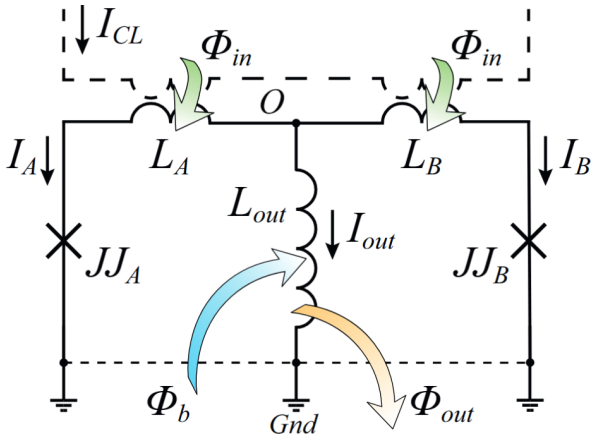


Figure 1: Schematic representation of a Gauss neuron, adapted from [14] (see details in the text).

When developing experimental superconducting neurons [17,18], it is essential to understand how the TF transforms when certain basic assumptions are violated. This can be important for improving device design and diagnosing potential faults. In this work, we consider three possible violations of the equivalence principle ("symmetry") of the input arms of the Gauss neuron. The most expected violation is the imbalance of the critical currents of the JJs, i.e., $I_{cA} \neq I_{cB}$. Indeed, during the fabrication of Josephson devices, variations in critical currents of around 5% are observed, even among leading manufacturers [19]. We will refer to this violation as Josephson asymmetry (it can also be called critical current asymmetry or Josephson inductance asymmetry). Another possible violation involves asymmetry in the input arm inductances with $L_A \neq L_B$. This asymmetry may be referred to as "inductive" or "geometric" as it arises from differences in the shape of the input arms due to, for example, defects in the thin-film structure. The third type of asymmetry may be associated with unequal signal supply into the input arms of the neuron. Below, we analyze the transformation of the TF in each of these cases and compare it with experimental results [18].

Symmetric Gauss Neuron

For clarity and systematic exposition, let us first consider the case of a symmetric Gauss neuron [8,12,14]. The equations of state consist of Kirchhoff's law in the node O (Equation 1) and two phase balance equations in the partial loops of the neuron:

$$I_{cA}\sin\varphi_A + I_{cB}\sin\varphi_B + I_{out} = 0, \tag{1}$$

$$\frac{\Phi_0}{2\pi}\varphi_A + L_A I_{cA}\sin\varphi_A + \Phi_{in} = \Phi_{out} + \Phi_b, \tag{2}$$

$$\frac{\Phi_0}{2\pi}\varphi_B + L_B I_{cB}\sin\varphi_B - \Phi_{in} = \Phi_{out} + \Phi_b. \tag{3}$$

Here, $\varphi_{A,B}$ is the phase difference across the junctions $JJ_{A,B}$, $I_{cA,B}$ are the critical currents, and Φ_0 is the magnetic flux quantum. Equation 2 is written for the left input loop, consisting of the left input and output arms (see Figure 1); Equation 3 is for the loop consisting of the right input and output arms (right input loop). The positive directions of currents (indicated by arrows in Figure 1) and the directions of loop traversal (counterclockwise and clockwise for the left and right loops, respectively) are chosen according to [14]. The phase balance equation for the full input loop, consisting of both input arms, is obtained by subtracting Equation 2–Equation 3. The symmetric case assumes $L_A = L_B = L$ and $I_{cA} = I_{cB} = I_c$.

The next step is to adopt dimensionless units: the magnetic flux is normalized by $\Phi_0/2\pi$, the current is normalized by the critical current I_c, and the inductance is normalized by the Josephson inductance $L_J = \Phi_0/2\pi I_c$. Thus,

$$\frac{2\pi}{\Phi_0}\Phi_{in} = \phi_{in}, \quad \frac{2\pi}{\Phi_0}\Phi_{out} = \phi_{out}, \quad \frac{2\pi}{\Phi_0}\Phi_b = \phi_b, \tag{4}$$

$$L/L_J = l, \quad L_{out}/L_J = l_{out}, \quad L_J = \Phi_0/2\pi I_c. \tag{5}$$

The normalized system of equations takes the form [14]:

$$\sin\varphi_A + \sin\varphi_B + \phi_{out}/l_{out} = 0, \tag{6}$$

$$\varphi_A + l\sin\varphi_A + \phi_{in} = \phi_{out} + \phi_b, \quad (7)$$

$$\varphi_B + l\sin\varphi_B - \phi_{in} = \phi_{out} + \phi_b. \quad (8)$$

By solving this system for the input and output fluxes, we obtain the TF of the Gauss neuron $\phi_{out}(\phi_{in})$, which can be written as a two-parameter dependence:

$$\phi_{in} = \frac{\varphi_B - \varphi_A}{2} + \frac{l}{2}\left(\sin\varphi_B - \sin\varphi_A\right), \quad (9)$$

$$\phi_{out} = \frac{\varphi_A + \varphi_B}{2} + \frac{l}{2}\left(\sin\varphi_A + \sin\varphi_B\right) - \phi_b, \quad (10)$$

$$\phi_b = \frac{\varphi_A + \varphi_B}{2} + \left(l_{out} + \frac{l}{2}\right)\left(\sin\varphi_A + \sin\varphi_B\right). \quad (11)$$

Equation 10 and Equation 9 are derived as the sum and the difference of Equation 7 and Equation 8, respectively. Equation 11 is obtained by substituting Equation 10 into Equation 6 to eliminate the output signal ϕ_{out}. By using the common method of introducing half-sum and half-difference of phases [1,8,9,12,14], $\varphi_+ = (\varphi_A + \varphi_B)/2$, $\varphi_- = (\varphi_B - \varphi_A)/2$, the system of Equation 10 and Equation 11 can be represented as:

$$\phi_{in} = \varphi_- + lg_-, \quad (12)$$

$$\phi_{out} = \frac{2l_{out}}{l + 2l_{out}}\left(\varphi_+ - \phi_b\right), \quad (13)$$

$$\frac{\phi_b - \varphi_+}{l + 2l_{out}} - g_+ = 0, \quad (14)$$

where, for brevity, we have introduced the notation $g_\pm = \sin\varphi_\pm\cos\varphi_\mp$. Equation 12 and Equation 13 determine the dependence of the input and output fluxes on the parameters $\varphi_\pm$, while Equation 14 links these parameters. One may also note the linear relationship between the output signal and the mean phase φ_+ according to Equation 13.

The TF (Equation 12–Equation 14) is obviously periodic with respect to ϕ_{in}. Within the first period, the TF of the Gauss neuron represents a symmetric bell-shaped curve that "rests" on a horizontal line (Figure 2a). The symmetry of the TF allows for the use of such neurons in radial basis function networks [20], with the position of the baseline being taken as the zero value of the TF when designing neural networks based on this element. This value can be determined from the system of Equation 12–Equation 14 as the value of ϕ_{out} at zero ϕ_{in}. By

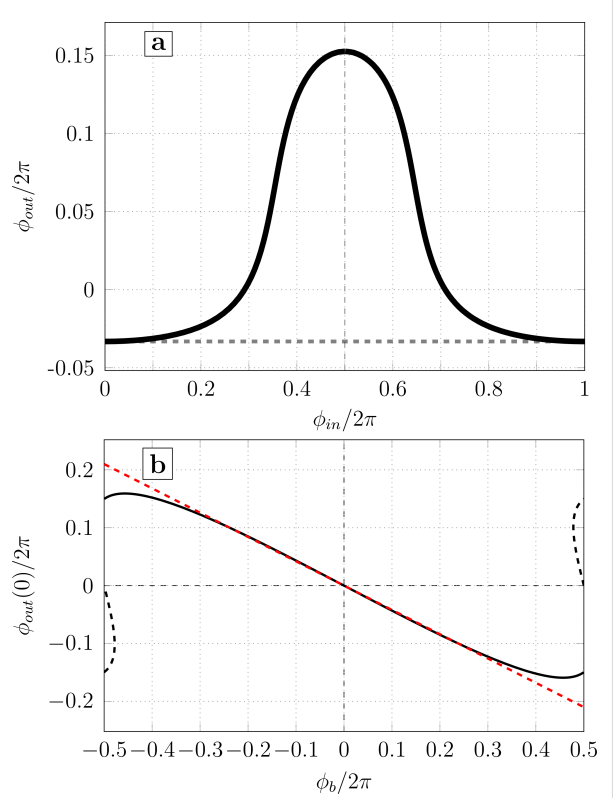


Figure 2: (a) Transfer function of the symmetric Gauss neuron according to Equation 12–Equation 14 for $l = 0.29$, $l_{out} = 0.48$, and $\phi_b = 0.155\pi$. The calculation parameters correspond to the experimental work [18]. (b) Dependence of the baseline $\phi_{out}(0)$ on the bias flux ϕ_b for the same sample (solid black line). The red dashed line shows the linear approximation of the central part of the dependence (see discussions in Sections *Symmetric Gauss Neuron* and *Results (C)*). The black dashed line shows the secondary solution that does not provide a bell-shaped response.

symmetry, we obtain $\varphi_- = 0$ according to Equation 12 and

$$f\left(\phi_{out}\right) = \frac{\phi_{out}}{2l_{out}} + \sin\left(\phi_b + \frac{l + 2l_{out}}{2l_{out}}\phi_{out}\right) = 0, \quad (15)$$

according to Equation 13 and Equation 14. The solution of this transcendental equation can be represented as a parameterized integral [8]:

$$\phi_{out}\left(0\right) = \int_0^{-\pi\mathrm{sgn}\phi_b} \theta\left[f\left(\phi_{out}\right)\mathrm{sgn}\left(\phi_b\right)\right]\mathrm{d}\phi_{out}, \quad (16)$$

where $\theta(x)$ is the Heaviside step function. The numerical solution of Equation 15 is shown in Figure 2b. The solution is 2π-periodic, and the dashed black line depicts the secondary branch of the solution that does not allow for a bell-shaped TF and cannot be obtained from Equation 16. Such a solution

appears for sufficiently large ϕ_b when $(l + 2l_{out}) > 1$. The calculation parameters correspond to the experimental sample investigated in our previous work [18]. It can be seen that in a sufficiently wide range, the graph is close to linear: deviations from the linear approximation are observed only for sufficiently large $|\phi_b| \gtrsim 0.6\pi$.

Results

A. Josephson asymmetry

Now, let us assume that, for whatever reason, the critical currents of the neuron's JJs have become unequal, $I_{cA} \neq I_{cB}$. First of all, a difficulty arises when introducing dimensionless parameters in the system of Equation 1–Equation 3 as it is unclear which value of $I_{cA,B}$ should be used for normalization in Equation 5. We begin by normalizing the magnetic flux and dividing Equation 2 and Equation 3 (which have the corresponding dimensions) by the quantity $\Phi_0/2\pi$. They will immediately take the normalized form (similar to Equation 7 and Equation 8) if we define

$$l_{A,B} = \frac{L}{L_{J_{A,B}}}, \quad L_{J_{A,B}} = \frac{\Phi_0}{2\pi I_{cA,B}}. \tag{17}$$

Thus, it can be said that in the case of Josephson asymmetry, the system of Equation 1–Equation 3 allows for the normalization of the inductances of the input arms to individual Josephson inductances $L_{J_{A,B}}$. Note that the quantities $l_{A,B}$ can also be introduced in Equation 1. To do this, we multiply it by the inductance L and notice that $LI_{cA,B}\sin\varphi_{A,B}$ are the magnetic fluxes created by the Josephson currents in the elements $L_{A,B}$. Therefore, the resulting equation should also be divided by the unit of magnetic flux $\Phi_0/2\pi$. The normalized system of equations thus takes the form

$$l_A \sin\varphi_A + l_B \sin\varphi_B + \phi_{out}/\tilde{l}_{out} = 0, \tag{18}$$

$$\varphi_A + l_A \sin\varphi_A + \phi_{in} = \phi_{out} + \phi_b, \tag{19}$$

$$\varphi_B + l_B \sin\varphi_B - \phi_{in} = \phi_{out} + \phi_b, \tag{20}$$

where $\tilde{l}_{out} = L_{out}/L$. By performing transformations similar to those in Section *Symmetric Gauss Neuron*, we obtain

$$\phi_{in} = \frac{\varphi_B - \varphi_A}{2} + \frac{1}{2}\left(l_B \sin\varphi_B - l_A \sin\varphi_A\right), \tag{21}$$

$$\phi_{out} = \frac{\varphi_B + \varphi_A}{2} + \frac{1}{2}\left(l_B \sin\varphi_B + l_A \sin\varphi_A\right) - \phi_b, \tag{22}$$

$$\frac{\varphi_B + \varphi_A}{2} + \frac{1 + 2\tilde{l}_{out}}{2}\left(l_B \sin\varphi_B + l_A \sin\varphi_A\right) = \phi_b. \tag{23}$$

The transition to the half-sum and half-difference of phases in Equation 21–Equation 23 naturally exposes the "asymmetry angle" α according to

$$\tan\alpha = \frac{l_A}{l_B} = \frac{I_{cA}}{I_{cB}}. \tag{24}$$

The normalized inductances of the arms are expressed through the asymmetry angle as follows:

$$l_A = \ell \sin\alpha, \quad l_B = \ell\cos\alpha, \quad \ell = \sqrt{l_A^2 + l_B^2}. \tag{25}$$

Thus, the parameter $\ell/\sqrt{2}$ characterizes the effective inductance of the input circuit, and tanα represents the imbalance of the critical currents. Introducing (φ_+, φ_-) and performing some simple trigonometric transformations, we obtain the two-parameter solution in the form:

$$\phi_{in} = \varphi_- + \frac{\ell}{\sqrt{2}}\left[g_- \cos\tilde{\alpha} - g_+ \sin\tilde{\alpha}\right], \tag{26}$$

$$\phi_{out} = \frac{2\tilde{l}_{out}}{1 + 2\tilde{l}_{out}}\left(\varphi_+ - \phi_b\right), \tag{27}$$

$$\frac{2\tilde{l}_{out}}{1 + 2\tilde{l}_{out}}\left(\varphi_+ - \phi_b\right) + \sqrt{2}\ell\tilde{l}_{out}\left[g_+ \cos\tilde{\alpha} - g_- \sin\tilde{\alpha}\right] = 0. \tag{28}$$

Here, for brevity, we introduce the notation $\tilde{\alpha} = \alpha - \pi/4$. In general, the system of Equation 26–Equation 28 resembles the form of the solution in Equation 12–Equation 14 with the exception of the terms containing $\sin\tilde{\alpha}$. Equation 27 coincides with Equation 13. This is possible because in Equation 22 and Equation 23, the coefficients before the sine terms in the parentheses are the same. Josephson asymmetry leads to the replacement of g_+ and g_- in Equation 12–Equation 14 with linear combinations of the $g_\pm$ terms, as indicated in the square brackets in Equation 26–Equation 28. The functions of Equation 12–Equation 14 and Equation 26–Equation 28 coincide when $\alpha = \pi/4$, which occurs in the symmetric case $I_{cA} = I_{cB}$. The range of variation for the parameter $\tilde{\alpha}$ is $\pm\pi/4$ when, for example, I_{cA} changes within $0 \le I_{cA} < \infty$. Exceeding these limits is possible if one of the Josephson junctions is a π-junction with a negative sign of the current–phase relation (see, for example, [21,22]).

The use of π-junctions in the context of developing adiabatic Josephson logic is discussed, for example, in [23,24].

Figure 3 shows the calculated TF for different cases of Josephson asymmetry. The calculation parameters ($\tilde{l}_{\text{out}}$, l_{B}, ϕ_{b}) were chosen according to the experimental work in [18]. It is assumed that the parameter I_{cA} changes while I_{cB} remains constant. It can be seen that as tanα increases, the curve becomes asymmetric, that is, the left part becomes flatter, and the right one steeper (Figure 3a). For sufficiently large asymmetry ($\tan\alpha \gtrsim 1.4$ for the parameters in Figure 3a), the transfer function becomes multivalued, and hysteresis should be observed during the experiment. In the case of reverse asymmetry (tanα < 1), the right wing of the transfer function becomes flatter (Figure 3b). The baseline remains horizontal ($\phi_{\text{out}}(0) = \phi_{\text{out}}(2\pi)$), but it may intersect the distorted transfer function. Note that a significant distortion of the bell-shaped transfer function is observed when the critical currents diverge by a factor of 1.3 or more, while an asymmetry of the order of 1.05 is unlikely to be noticeable to the naked eye. The difference between Figure 3a and Figure 3b is due to the different meaning of zero and infinite tanα limits: the first one corresponds to the break of the junction JJ_{A}, while the second corresponds to shorting of the junction JJ_{A}. In the first case, the inductance l_{A} turns to infinity and the neuron becomes a single-junction SQUID, whose multistability condition is $(L + L_{\text{out}}) < L_{J_{\text{B}}}$. The screening current circulates mainly in the JJ_{B}–L–L_{out} partial loop. In the case of infinite tanα, the Gauss neuron becomes a shunted single-junction interferometer (in fact, a Sigma neuron [7]), whose multistabitity condition can be expressed as $(L + \text{LL}_{\text{out}}/(L + L_{\text{out}})) < L_{\text{J}}$ (see [13,17]). In that case, the screening current circulates mainly in the JJ_{A}–L–L_{out} circuit, which defines the side the TF is tilted to.

Characterizing the Josephson asymmetry through the ratio of critical currents or the angle α is not the only possible approach. Using the definitions in Equation 24 and Equation 25, we get:

$$\cos\tilde{\alpha} = \sqrt{2}l_{+}/\ell, \quad \sin\tilde{\alpha} = -\sqrt{2}l_{-}/\ell, \tag{29}$$

where $l_{\pm}$ are defined as:

$$l_{\pm} = \left(l_{\text{B}} \pm l_{\text{A}}\right)/2, \quad l_{\text{A,B}} = l_{+} \mp l_{-}. \tag{30}$$

Using these definitions (and also the definition of the coefficient $\tilde{l}_{\text{out}}$), the transfer function of the Gauss neuron with Josephson asymmetry takes the form:

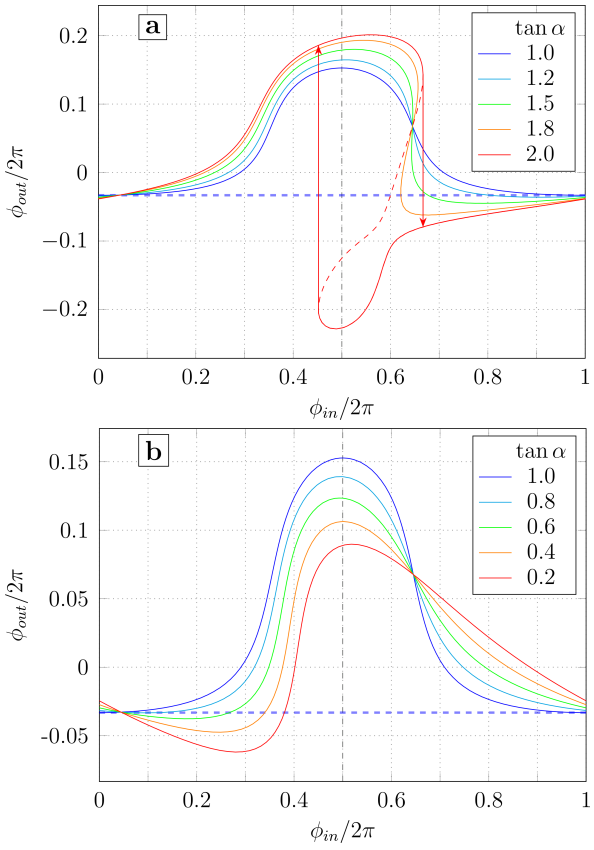


Figure 3: Transfer function of the Gauss neuron according to Equation 26–Equation 28 at different values of the Josephson asymmetry parameter $\tan\alpha = I_{\text{cA}}/I_{\text{cB}}$ for $\tan\alpha \geq 1$ (panel a) and $\tan\alpha \leq 1$ (panel b). The parameters are $\tilde{l}_{\text{out}} = 1.66$, $l_{\text{B}} = 0.29$, and $\phi_{\text{b}} = 0.155\pi$.

$$\phi_{\text{in}} = \left[\varphi_{-} + l_{+}g_{-}\right] + l_{-}g_{+}, \tag{31}$$

$$\phi_{\text{out}} = \left[\frac{2\tilde{l}_{\text{out}}}{1+2\tilde{l}_{\text{out}}}\left(\varphi_{+} - \phi_{\text{b}}\right)\right], \tag{32}$$

$$\left[\frac{\phi_{\text{b}} - \varphi_{+}}{1+2\tilde{l}_{\text{out}}} - l_{+}g_{+}\right] - l_{-}g_{-} = 0. \tag{33}$$

The form of Equation 31–Equation 33 is closest to Equation 12–Equation 14 (the matching terms are highlighted in square brackets). The parameter l_{+} characterizes the effective inductance of the input circuit, while l_{-} represents the imbalance in the normalized inductances of the Josephson circuits. Note the complete coincidence of Equation 13 and Equation 32, which define the linear relationship between the output signal and the sum phase. The influence of Josephson asymmetry reduces to the appearance of conjugate terms of the form $l_{-}g_{\pm}$ in

Equation 12 and Equation 14. The transition to the symmetric case occurs when $l_A = l_B = l_+$, $l_- = 0$.

B. Inductive asymmetry

Now let us consider the case of asymmetry in the self-inductances $L_A \neq L_B$ ("inductive asymmetry"). We will assume that the Josephson inductances are the same: $L_{J_A} = L_{J_B} = L_J$. This allows us to apply the standard normalization of the inductances of the Gauss neuron elements described in Section *Symmetric Gauss Neuron*. The normalized equations of the states described in Equation 1–Equation 3 take the form

$$\sin\varphi_A + \sin\varphi_B + \phi_{out}/l_{out} = 0, \tag{34}$$

$$\varphi_A + l_A \sin\varphi_A + \phi_{in} = \phi_{out} + \phi_b, \tag{35}$$

$$\varphi_B + l_B \sin\varphi_B - \phi_{in} = \phi_{out} + \phi_b. \tag{36}$$

It differs from the "symmetric" system (Equation 6–Equation 8) only by the different values of inductances l_A and l_B in Equation 35 and Equation 36. By adding and subtracting Equation 35 and Equation 36, we obtain the system of equations in the following form:

$$\phi_{in} = \frac{\varphi_B - \varphi_A}{2} + \frac{1}{2}\left(l_B \sin\varphi_B - l_A \sin\varphi_A\right), \tag{37}$$

$$\phi_{out} = \frac{\varphi_B + \varphi_A}{2} - \phi_b + \frac{1}{2}\left(l_B \sin\varphi_B + l_A \sin\varphi_A\right), \tag{38}$$

$$\frac{\varphi_B + \varphi_A}{2} + \left(\left(l_{out} + \frac{l_B}{2}\right)\sin\varphi_B + \left(l_{out} + \frac{l_A}{2}\right)\sin\varphi_A\right) = \phi_b. \tag{39}$$

A transition to phases φ_+ and φ_- is hindered by the fact that the coefficients in front of the Josephson currents $\sin\varphi_{A,B}$ in Equation 39 differ from the coefficients in Equation 37 and Equation 38 (unlike in the system of Equation 21–Equation 23). In this case, using the asymmetry angle appears unreasonable. By introducing the quantities $l_\pm$ according to the definition in Equation 30, we obtain the following system after simple transformations:

$$\phi_{in} = \left[\varphi_- + l_+ g_-\right] + l_- g_+, \tag{40}$$

$$\phi_{out} = \frac{2l_{out}}{l_+ + 2l_{out}}\left(\left[\varphi_+ - \phi_b\right] + l_- g_-\right), \tag{41}$$

$$\left[\frac{\phi_b - \varphi_+}{l_+ + 2l_{out}} - g_+\right] - \frac{l_-}{l_+ + 2l_{out}} g_- = 0. \tag{42}$$

The terms inside square brackets are those present in the "symmetric" system (Equation 12–Equation 14). Note that in the case of inductive asymmetry, the linear relationship between ϕ_{out} and φ_+ is not preserved (unlike in the Josephson asymmetry case). The condition relating the parameters of the phase differences $\varphi_\pm$ is also different (compared to the system of Equation 31–Equation 33). The symmetric case is obtained when $l_A = l_B = l_+$, and $l_- = 0$.

Figure 4 shows the family of transfer functions for different values of l_A/l_B. The calculation parameters (l_B, l_{out}, ϕ_b) correspond to the sample studied experimentally in [18]. It is assumed that L_A changes while L_B remains constant. As in the previous section, inductive asymmetry causes a tilt of the transfer function, bending one wing of the transfer function and

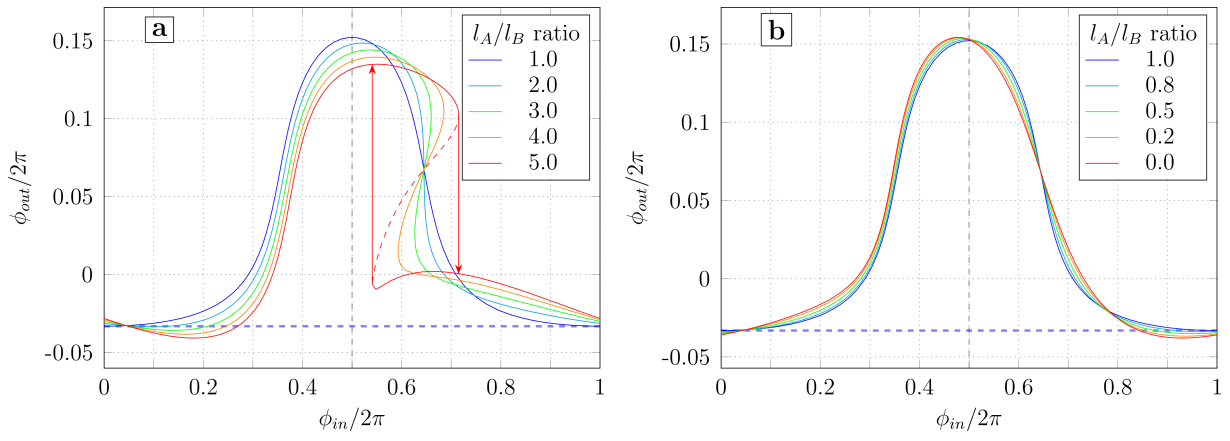


Figure 4: Transfer function of the Gauss neuron with different inductance ratios for the receiving arms (given in the legend) at a constant value of I_B in case of increasing (panel a) or decreasing (panel b) I_A.

widening the other. As l_A/l_B increases, the distortion of the transfer function increases (Figure 4a), which leads to its multivaluedness (and hence to hysteresis). This is related to the increase in the inductance of the overall receiving circuit $2l_+$ as l_A increases. The opposite change (reducing l_A while keeping l_B constant) weakly affects the shape of the transfer function, mainly leading to a slight distortion of the right half of the graph (Figure 4b). The difference between Figure 4a and Figure 4b can be understood by analogy with Josephson asymmetry. Note that all the distortions in Figure 3 and Figure 4 have slightly different shapes, which allows them to be distinguished during the initial analysis of experimental data.

In recent years, a number of superconducting devices have been proposed based on very thin superconducting films whose kinetic inductance may be comparable to the magnetic one [11,25,26]. Indeed, the inductance of a superconducting film carrying an electric current consists of two components, namely, the magnetic inductance (originating from the magnetic field energy) and the kinetic inductance (originating from the kinetic energy of the superconducting electrons). Should one want to account for the kinetic inductance, the initial Equation 1–Equation 3 remain unchanged, as it is the total inductance value that determines the phase balance conditions in Equation 2 and Equation 3. However, the value of ϕ_{out} in Equation 13 has then the meaning of the phase difference across the output arm, which cannot be directly measured in an experiment. The measurable output signal is defined only by the component of ϕ_{out} that originates from the magnetic flux generated by the output current I_{out}. To account for this, one can simply rescale ϕ_{out} in Equation 2 and Equation 3 by the factor $L_{out}^{(M)}/L_{out}$, where $L_{out}^{(M)}$ is the magnetic part of total inductance L_{out}. Therefore, the use of ultrathin superconducting films is not a promising approach for implementing a superconducting Gauss neuron.

C. Input asymmetry

One more possible type of asymmetry is related to the unequal input signal supply to the neuron's receiving arms. To parameterize this asymmetry, we introduce the parameter t, such that the magnetic fluxes in the left and right partial loops of the neuron are $(1 \pm t)\Phi_{in}$. Then the total flux in the neuron is $2\Phi_{in}$ (as in previous sections), and $\Phi_{in} = \Phi_{in}^{+}$ is simply the half-sum of the input fluxes in the partial loops. The imbalance (half-difference) of the input fluxes is the asymmetry term $\Phi_{in}^{-} = t\Phi_{in}^{+}$. In a practical situation, the magnetic flux is supplied into the neuron via a CL, inductively coupled to the receiving elements in some manner. Therefore, input asymmetry effectively means that the mutual inductances $M_{in}^{A,B}$ between the CL and the Josephson arms of the neuron are different. In this case, we can express the coefficient t through these inductances. Writing the input fluxes in the partial loops as $\Phi_{in}^{A,B} = M_{in}^{A,B} I_{CL}$ (where I_{CL} is the current in the CL), we get

$$t = \frac{\Phi_{in}^{-}}{\Phi_{in}^{+}} = \frac{M_{in}^{A} - M_{in}^{B}}{M_{in}^{A} + M_{in}^{B}}. \tag{43}$$

Let us assume that the arms of the neuron are symmetric, meaning that there is no inductive or Josephson asymmetry. Then, the system of equations of state for the Gauss neuron in the standard normalization can be written as

$$l_{out}\left(\sin\varphi_A + \sin\varphi_B\right) + \phi_{out} = 0, \tag{44}$$

$$\varphi_A + l\sin\varphi_A + (1+t)\phi_{in} = \phi_{out} + \phi_b, \tag{45}$$

$$\varphi_B + l\sin\varphi_B - (1-t)\phi_{in} = \phi_{out} + \phi_b. \tag{46}$$

Upon transformations analogous to those made in Section *Symmetric Gauss Neuron*, the first equation of the new system (compare with the system of Equation 12–Equation 14) remains unchanged. The other two acquire new terms proportional to the asymmetry term $t\phi_{in}$:

$$\phi_{in} = \left[\varphi_- + lg_-\right], \tag{47}$$

$$\phi_{out} = \left[\frac{2l_{out}}{l+2l_{out}}\left(\varphi_+ - \phi_b\right)\right] + \frac{2l_{out}}{l+2l_{out}}t\phi_{in}, \tag{48}$$

$$\left[\frac{\phi_b - \varphi_+}{l+2l_{out}} - g_+\right] - \frac{1}{l+2l_{out}}t\phi_{in} = 0. \tag{49}$$

One may note the mixing of the asymmetry term to the output flux according to Equation 47–Equation 49. If $t = 0$, the system of Equation 47–Equation 49 transforms into Equation 12–Equation 14.

The TF plots for different values of the asymmetry parameter t are shown in Figure 5. The calculation parameters (l, l_{out}, ϕ_b) correspond to the sample studied experimentally in [18]. For $t = 0$, the TF is a (blue) bell on a horizontal baseline, as demonstrated in Section *Symmetric Gauss Neuron*. However, for nonzero t, the baseline becomes slanted and the transfer function essentially acquires a "linear component". This behavior can be understood by noticing that the input signal is essentially

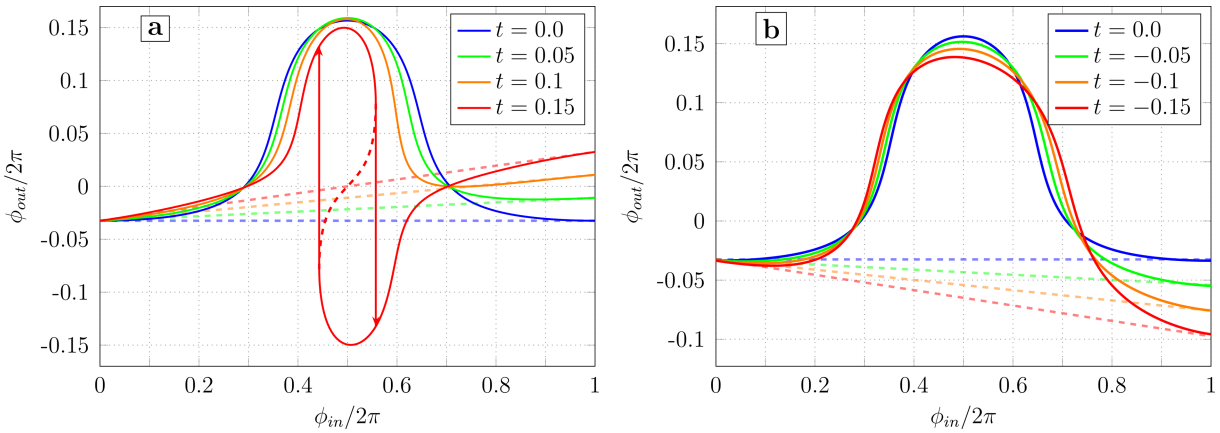


Figure 5: Transfer function of the neuron according to Equation 47–Equation 49 with different imbalance coefficients of the input signal t (positive on panel a and negative on panel b). Dashed lines represent the asymptotic baselines.

"mixed" into the bias flux: to obtain Equation 47–Equation 49 from Equation 12–Equation 14, one should make a substitution $\phi_b \to \phi_b - t\phi_{in}$. This can be seen in Equation 44–Equation 46 by moving the asymmetry terms to the right-hand side. In other words, when ϕ_{in} is swept in the positive direction, the effective bias flux $\tilde{\phi}_b = \phi_b - t\phi_{in}$ (which determines the imbalance of the magnetic flux in the receiving loops ofthe Gauss neuron) decreases for $t > 0$. The decrease in $\tilde{\phi}_b$, in turn, leads to a shift in the TF's baseline value linearly with $\tilde{\phi}_b$ (Figure 2b) for sufficiently small $\tilde{\phi}_b$. Linearity requires correspondingly small t ($|t| \lesssim 0.2$ for Figure 5) since within one period of the input signal, the shift of ϕ_b reaches $2\pi t$.

The increase in the slope of the baseline as t grows (in absolute value) makes the left branch of the transfer function ($\phi_{in} \le 0.5$) flatter, and the right branch ($\phi_{in} \ge 0.5$) steeper. As t increases, the right branch becomes vertical, and at $t \approx 0.13$, the transfer function becomes hysteretic (see the red curve in Figure 5a). The slope of the linear component is inverted when the sign of t is changed (Figure 5b).

Discussion

All the asymmetry types considered are "independent", meaning they cannot be reduced to one another through algebraic transformations. This statement is evident for input asymmetry, which leads to a slope of the baseline, unlike the other two cases. As for Josephson and inductive asymmetries, the corresponding equations of state (Equation 18–Equation 20 and Equation 34–Equation 36) differ only in the form of the first equation in the system (which originates from Kirchhoff's law) and can be reduced to a common form only in the case $l_A = l_B$ (that is, for a symmetric Gauss neuron). Moreover, the three types of symmetry breaking for the Gauss neuron presented here exhaust the list of possible asymmetries of its arms. Indeed, each receiving arm of the Gauss neuron (Figure 6) is formed by two elements (a JJ and an inductance) and is characterized by three quantities, namely, its own (geometric) inductance, the critical current of the JJ (Josephson inductance), and the sensitivity to the input signal (i.e., mutual inductance with the CL). The fluxes ϕ_{out} and ϕ_b cannot be a direct source of asymmetry in our model, since they are generated through a single element L_{out}, common to both receiving loops. Nevertheless, L_{out} can lead to an effective asymmetry of the input signal supply, as will be shown below.

Let us try to apply the results obtained above to the experimental data presented in our work [18]. The experimental curve (see Figure 6a) represents a flat bell over a slanted baseline, which indicates the presence of input asymmetry. This is surprising because both receiving areas of the Gauss neuron are identical in shape (Figure 6b). However, the effective input asymmetry may arise due to direct interaction of the input and readout elements (which does not involve the neuron as a non-linear converter) as was shown in [27]. Despite the use of a superconducting screen in experiments [17,18], such an interaction can occur due to the finite size of the screen. The interaction is mediated by circulating currents in the screen, which may be non-zero even at a significant distance from the CL [17,28].

To take this effect into consideration, one should consider the method of measuring the output flux Φ_{out} by stabilizing the magnetic flux Φ_{sq} via the measuring SQUID. The latter consists of an inductive element L_{sq}, closed onto a superconducting screen through JJs $JJ_{I,II}$ (an asymmetric two-junction SQUID, Figure 6b). The output signal is the current in the feedback loop of the SQUID I_{fb} that compensates the change in the output flux

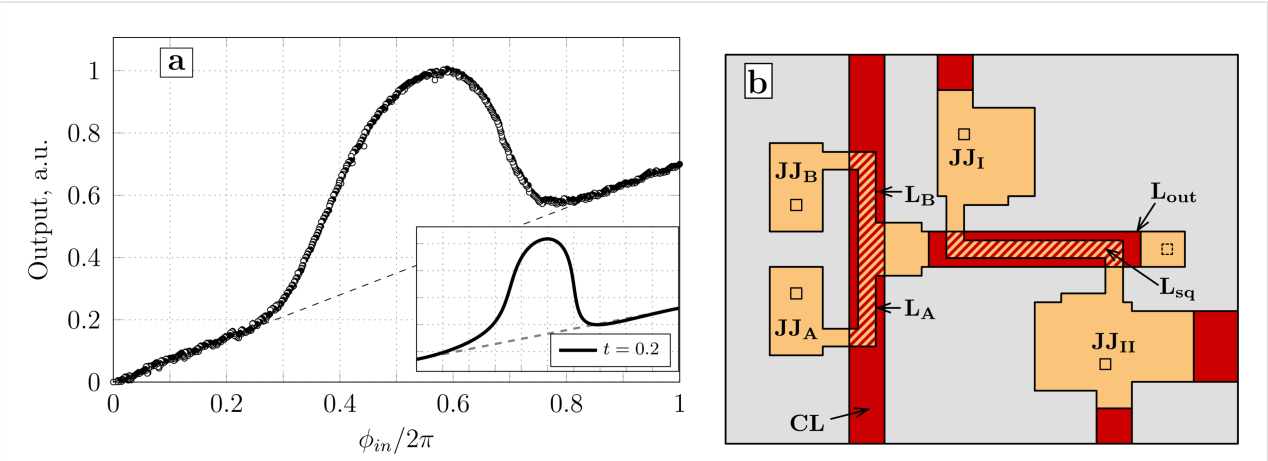


Figure 6: (a) Experimental transfer function of the superconducting Gauss neuron prototype according to [18]. The dashed lines show the baseline (see discussion in Sections *Symmetric Gauss Neuron* and *Results (C)*). The inset shows the calculated TF with t = 0.2 and ϕ_b = 0.3π. The dashed lines show the baseline (see discussion in Sections *Symmetric Gauss Neuron* and *Results (C)*). (b) Schematic of the structure of the studied sample. $L_{A,B}$ denote receiving arms, L_{out} is the output arm, $JJ_{A,B}$ are the JJs of the neuron, $JJ_{I,II}$ are the JJs of the measuring element (i.e.,SQUID), and L_{sq} is the loop of the measuring element. Different colors represent elements in different layers of the multilayer structure. Hatching indicates the areas of inductive coupling with the input and readout elements. The boundaries of the drawing coincide with the boundaries of the superconducting screen, shown in gray.

while sweeping Φ_{in}. In other words, the current $I_{fb} = I_{sq}^{(0)} - I_{sq}$ represents the difference between the initial and current values of the current flowing through the loop of the measuring element. So, the transfer function of the experimental sample has a somewhat different ("current") representation compared to the earlier proposed ("flux") one. The relationship between I_{fb} and Φ_{out} is given by

$$\Phi_{out} = L_{out} I_{out} + M_{out}\left(I_{sq}^{(0)} - I_{fb}\right), \tag{50}$$

where M_{out} is the mutual inductance between the SQUID and the output element. The variable I_{out} can be eliminated from Equation 50 using the invariance condition for the magnetic flux in the SQUID [17]:

$$\Phi_{sq} = M_{out} I_{out} + L_{sq} I_{sq} + M_{sq} I_{CL} = \text{const}\left(I_{CL}\right). \tag{51}$$

After some straightforward transformations, one can obtain:

$$\Phi_{out} = \frac{L_{sq} L_{out}^{*}}{M_{out}} I_{fb} + \left[\frac{L_{out}}{M_{out}}\Phi_{sq} - \frac{L_{sq} L_{out}^{*}}{M_{out}} I_{sq}^{(0)}\right] - \frac{L_{out} M_{sq}}{M_{out}} I_{CL}, \tag{52}$$

where

$$L_{out}^{*} = L_{out} - \frac{M_{out}^{2}}{L_{sq}}$$

is the inductance of the output element renormalized due to the interaction with the reading element [17,18,27].

Equation 52 defines the relation between "flux-type" and "current-type" output signals. It is linear but contains three terms. The first one illustrates a linear type of $I_{fb}(\Phi_{out})$ dependence. The second one represents a "shift term" that ensures a non-zero value of the bias flux even if Φ_b = 0. This can be verified by substituting Equation 52 into Equation 2 and Equation 3. Note that no special signal line to provide a bias flux into output inductance was realized in the experimental work [18], which, however, did not prevent us from observing a noticeable output signal. However, the effective bias is hard to control during the experiment, so it was estimated as a fitting parameter in [18]. Finally, the third term in Equation 52 arises due to the direct interaction between the input (CL) and readout (SQUID) elements (Equation 51). Upon substitution into Equation 2–Equation 3, the third term will cause the appearance of terms characteristic of input asymmetry with $t = L_{out}M_{sq}/M_{out}M_{in}$ (with $M_{in} = M_{in}^{A} = M_{in}^{B}$). Substituting further the values L_{out} = 7.2 pH, M_{sq} = 0.1 pH, M_{out} = 2.7 pH, and M_{in} = 2.4 pH given in [17,18], we get t = 0.2. Calculations based on Equation 52 give a similar shape of the TF (compared to Figure 6a) at ϕ_b = 0.3π. Thus, experimental results correspond to the expected ones, and a quantitative analysis shall be the subject of our subsequent publications.

The problem with cross-talk mentioned above (i.e., screen-mediated interaction) may become more and more severe when one connects more neurons together. This is why the search for

the ways to suppress the cross-talk remains one of the main directions of the neuron's design optimization. It is worth noting that the expression for the t-factor implies that it is possible to change its value by changing L_{out}. However, the change of the output arm's length is not the best way to suppress the input asymmetry. Indeed, the unlimited decrease in L_{out} is impossible at constant values of M_{out} as its length cannot be smaller than the overlap region with the SQUID-sensor loop. Therefore, the t-factor can be just increased with no practical meaning. The most promising ways to dump the effective input asymmetry are the increase of input mutual inductance M_{in} and the suppression of the screen-mediated interaction (a decrease of the M_{sq} value). Some methods of suppressing this interaction are discussed in [26]. The simplest ones include increasing the size of the screen and creating a reverse CL that is not coupled to the neuron (except screen-mediated coupling) and carries the control current in the opposite direction. Calculations show that this decreases M_{sq} by about five times. It is also useful to eliminate sections of the SQUID that are parallel to the CL. This is the main direction of optimization of the Gauss neuron design at the present time.

Conclusion

In this work, the changes in the form of the transfer function (TF) of a Gauss neuron under various violations of the equivalence condition of its receiving loops were investigated. It was shown that the imbalance of the self or Josephson inductances of the neuron's receiving arms leads to a "tilt" in the TF. The distortion of the TF shape in these cases is somewhat different, which provides an opportunity for visual diagnostics of experimental sample faults. The imbalance of the input signal results in the tilting of the baseline, which is not observed in other cases. Comparison with the experiment indicates the presence of input imbalance, which can arise even in a symmetric sample design due to the direct interaction between the input and readout elements.

Acknowledgements

We thank V.N. Shilov and N.S. Stepakov for their help in making the samples and conducting the experiment. Equations 31–33 were obtained by postgraduate students of the Moscow Institute of Physics and Technology (National Research University) A.S. Ionin and F.A. Razorenov within their practical training program. Equation 15, Equation 16 and Figure 2b were obtained as a part of A.S. Ionin's collaboration with "Joint Venture Quantum Technologies".

Funding

The work was carried out at the Osipyan Institute of Solid State Physics, Russian Academy of Sciences, and was supported by the Russian Science Foundation, project no. 23-72-00053.

ORCID® iDs

Fedor A. Razorenov - https://orcid.org/0009-0008-2681-5722
Aleksander S. Ionin - https://orcid.org/0009-0004-0249-1234
Nikita S. Shuravin - https://orcid.org/0009-0004-2612-0366
Liubov N. Karelina - https://orcid.org/0000-0003-4981-6599
Mikhail S. Sidel'nikov - https://orcid.org/0000-0003-2215-6703
Sergey V. Egorov - https://orcid.org/0000-0003-4258-7172
Vitaly V. Bol'ginov - https://orcid.org/0000-0002-6948-7975

Data Availability Statement

All data that supports the findings of this study is available in the published article and/or the supporting information of this article.

References

1. Schegolev, A. E.; Klenov, N. V.; Soloviev, I. I.; Gudkov, A. L.; Tereshonok, M. V. *Nanobiotechnol. Rep.* **2021,** *16,* 811–820. doi:10.1134/s2635167621060227
2. Soloviev, I. I.; Klenov, N. V.; Bakurskiy, S. V.; Kupriyanov, M. Y.; Gudkov, A. L.; Sidorenko, A. S. *Beilstein J. Nanotechnol.* **2017,** *8,* 2689–2710. doi:10.3762/bjnano.8.269
3. Schegolev, A. E.; Klenov, N. V.; Gubochkin, G. I.; Kupriyanov, M. Y.; Soloviev, I. I. *Nanomaterials* **2023,** *13,* 2101. doi:10.3390/nano13142101
4. Skryabina, O. V.; Schegolev, A. E.; Klenov, N. V.; Bakurskiy, S. V.; Shishkin, A. G.; Sotnichuk, S. V.; Napolskii, K. S.; Nazhestkin, I. A.; Soloviev, I. I.; Kupriyanov, M. Y.; Stolyarov, V. S. *Nanomaterials* **2022,** *12,* 1671. doi:10.3390/nano12101671
5. Semenov, V. K.; Golden, E. B.; Tolpygo, S. K. *IEEE Trans. Appl. Supercond.* **2021,** *31,* 1302207. doi:10.1109/tasc.2021.3067231
6. Semenov, V. K.; Golden, E. B.; Tolpygo, S. K. *IEEE Trans. Appl. Supercond.* **2023,** *33,* 1400308. doi:10.1109/tasc.2023.3252495
7. Schegolev, A. E.; Klenov, N. V.; Soloviev, I. I.; Tereshonok, M. V. *Beilstein J. Nanotechnol.* **2016,** *7,* 1397–1403. doi:10.3762/bjnano.7.130
8. Klenov, N. V.; Schegolev, A. E.; Soloviev, I. I.; Bakurskiy, S. V.; Tereshonok, M. V. *IEEE Trans. Appl. Supercond.* **2018,** *28,* 1301006. doi:10.1109/tasc.2018.2836903
9. Soloviev, I. I.; Schegolev, A. E.; Klenov, N. V.; Bakurskiy, S. V.; Kupriyanov, M. Y.; Tereshonok, M. V.; Shadrin, A. V.; Stolyarov, V. S.; Golubov, A. A. *J. Appl. Phys.* **2018,** *124,* 152113. doi:10.1063/1.5042147
10. Klenov, N. V.; Kuznetsov, A. V.; Schegolev, A. E.; Soloviev, I. I.; Bakurskiy, S. V.; Kupriyanov, M. Yu.; Tereshonok, M. V. *Low Temp. Phys.* **2019,** *45,* 769–775. doi:10.1063/1.5111305
11. Bakurskiy, S.; Kupriyanov, M.; Klenov, N. V.; Soloviev, I.; Schegolev, A.; Morari, R.; Khaydukov, Y.; Sidorenko, A. S. *Beilstein J. Nanotechnol.* **2020,** *11,* 1336–1345. doi:10.3762/bjnano.11.118
12. Schegolev, A.; Klenov, N.; Soloviev, I.; Tereshonok, M. *Supercond. Sci. Technol.* **2021,** *34,* 015006. doi:10.1088/1361-6668/abc569
13. Bastrakova, M.; Gorchavkina, A.; Schegolev, A.; Klenov, N.; Soloviev, I.; Satanin, A.; Tereshonok, M. *Symmetry* **2021,** *13,* 1735. doi:10.3390/sym13091735

14. Schegolev, A. E.; Klenov, N. V.; Bakurskiy, S. V.; Soloviev, I. I.; Kupriyanov, M. Y.; Tereshonok, M. V.; Sidorenko, A. S. *Beilstein J. Nanotechnol.* **2022,** *13,* 444–454. doi:10.3762/bjnano.13.37
15. Bastrakova, M. V.; Pashin, D. S.; Rybin, D. A.; Schegolev, A. E.; Klenov, N. V.; Soloviev, I. I.; Gorchavkina, A. A.; Satanin, A. M. *Beilstein J. Nanotechnol.* **2022,** *13,* 653–665. doi:10.3762/bjnano.13.57
16. Takeuchi, N.; Yamanashi, Y.; Yoshikawa, N. *Sci. Rep.* **2014,** *4,* 6354. doi:10.1038/srep06354
17. Ionin, A. S.; Shuravin, N. S.; Karelina, L. N.; Rossolenko, A. N.; Sidel'nikov, M. S.; Egorov, S. V.; Chichkov, V. I.; Chichkov, M. V.; Zhdanova, M. V.; Shchegolev, A. E.; Bol'ginov, V. V. *J. Exp. Theor. Phys.* **2023,** *137,* 888–898. doi:10.1134/s1063776123120191
18. Ionin, A. S.; Karelina, L. N.; Shuravin, N. S.; Sidel'nikov, M. S.; Razorenov, F. A.; Egorov, S. V.; Bol'ginov, V. V. *JETP Lett.* **2023,** *118,* 766–772. doi:10.1134/s002136402360324x
19. Rapid Single Flux Quantum (RSFQ) – Design Rules for Nb/Al2O3-Al/Nb-Process at Leibniz IPHT. https://www.fluxonics.org/foundry/#process (accessed Feb 7, 2025).
20. Orr, M. J. Introduction to radial basis function networks, April 1996, Centre for Cognitive Science, University of Edinburgh, Edinburgh, Scotland. https://faculty.cc.gatech.edu/~isbell/tutorials/rbf-intro.pdf (accessed Feb 7, 2025).
21. Golubov, A. A.; Kupriyanov, M. Y.; Il'ichev, E. *Rev. Mod. Phys.* **2004,** *76,* 411–469. doi:10.1103/revmodphys.76.411
22. Stoutimore, M. J. A.; Rossolenko, A. N.; Bolginov, V. V.; Oboznov, V. A.; Rusanov, A. Y.; Baranov, D. S.; Pugach, N.; Frolov, S. M.; Ryazanov, V. V.; Van Harlingen, D. J. *Phys. Rev. Lett.* **2018,** *121,* 177702. doi:10.1103/physrevlett.121.177702
23. Khismatullin, G. S.; Klenov, N. V.; Soloviev, I. I. *JETP Lett.* **2023,** *118,* 220–229. doi:10.1134/s0021364023601331
24. Soloviev, I. I.; Khismatullin, G. S.; Klenov, N. V.; Schegolev, A. E. *J. Commun. Technol. Electron.* **2022,** *67,* 1479–1491. doi:10.1134/s106422692212021x
25. Neilo, A. A.; Bakurskiy, S. V.; Klenov, N. V.; Soloviev, I. I.; Kupriyanov, M. Yu. *JETP Lett.* **2025,** *121,* 58–66. doi:10.1134/s0021364024604391
26. Luomahaara, J.; Vesterinen, V.; Grönberg, L.; Hassel, J. *Nat. Commun.* **2014,** *5,* 4872. doi:10.1038/ncomms5872
27. Shuravin, N. S.; Karelina, L. N.; Ionin, A. S.; Razorenov, F. A.; Sidel'nikov, M. S.; Egorov, S. V.; Bol'ginov, V. V. *JETP Lett.* **2024,** *120,* 829–836. doi:10.1134/s0021364024603427
28. Ionin, A. S.; Egorov, S. V.; Sidelnikov, M. S.; Karelina, L. N.; Shuravin, N. S.; Khapaev, M. M.; Bolginov, V. V. *Phys. Solid State* **2024,** *66,* 987–993.

License and Terms

This is an open access article licensed under the terms of the Beilstein-Institut Open Access License Agreement (https://www.beilstein-journals.org/bjnano/terms), which is identical to the Creative Commons Attribution 4.0 International License (https://creativecommons.org/licenses/by/4.0). The reuse of material under this license requires that the author(s), source and license are credited. Third-party material in this article could be subject to other licenses (typically indicated in the credit line), and in this case, users are required to obtain permission from the license holder to reuse the material.

The definitive version of this article is the electronic one which can be found at: https://doi.org/10.3762/bjnano.16.85

BEILSTEIN JOURNAL OF NANOTECHNOLOGY

Modeling magnetic properties of cobalt nanofilms used as a component of spin hybrid superconductor–ferromagnetic structures

Aleksey Fedotov*[1], Olesya Severyukhina[1], Anastasia Salomatina[1,2] and Anatolie Sidorenko[3,4]

Full Research Paper

Open Access

Address:
[1]Modeling Structures and Functional Materials Group, Institute of Mechanics, Udmurt Federal Research Center, Ural Division, Russian Academy of Sciences, Baramzinoy 34, Izhevsk 426067, Russia, [2]Nanotechnology and Microsystems Engineering Department, Kalashnikov Izhevsk State Technical University, Studencheskaya 7, Izhevsk 426069, Russia, [3]Institute of Electronic Engineering and Nanotechnologies, Technical University of Moldova, 3/3 Academiei St., Chisinau, 2028, Moldova and [4]Moscow Institute of Physics and Technology, 9, Institutskiy per., Dolgoprudny, 141701, Russia

Email:
Aleksey Fedotov* - alezfed@gmail.com

* Corresponding author

Keywords:
ferromagnetic properties; LAMMPS; mathematical modeling; MEAM; molecular dynamics; spin dynamics

Beilstein J. Nanotechnol. **2025,** *16,* 1557–1566.
https://doi.org/10.3762/bjnano.16.110

Received: 04 February 2025
Accepted: 08 August 2025
Published: 08 September 2025

Associate Editor: J. M. van Ruitenbeek



© 2025 Fedotov et al.; licensee Beilstein-Institut.
License and terms: see end of document.

Abstract

The paper presents a mathematical model for studying the magnetic behavior of atoms, which takes into account spin and interatomic interactions. Two problems were solved by means of mathematical modeling. At the first stage, the problem of modeling a small nanoscale system (500 atoms) consisting of cobalt atoms was solved. The purpose of this stage of computational experiment was to check the convergence of the solution and compare the obtained data with the results of other studies. The performed calculations and satisfactory correspondence to the previously obtained data confirmed the adequacy of the applied mathematical model. The second stage of numerical studies was devoted to the analysis of the magnetic behavior of cobalt nanofilms of different thicknesses. It was shown that the film thickness has a significant influence on the magnetic parameters of the modeled nanoscale systems. It was found that the magnetic energy and magnetization norm of the system change in a nonlinear manner with increasing number of crystalline layers of the nanofilm. The peaks found on the graph of the magnetization rate change can be caused by surface effects in thin films and the formation of Neel domain walls.

Introduction

Thin film structures [1,2] are increasingly employed each year in a wide range of applications, serving as functional [3,4], reinforcing, light-reflecting, conductive, and dielectric materials. Their utilization extends to contacts, printed circuit boards, and integrated circuit elements in microelectronics, as well as to the fabrication of optical filters, the component base of optoelec-

tronics, and advanced lithographic processes. Due to active experimental and theoretical research on thin films, significant progress has been made in recent years. Since the information in the field of thin film technologies is updated quite rapidly, there is a need for a thorough study and optimization of the main technological processes that are currently used, as well as fundamental features of the thin film formation processes with new composition and coatings of various types. These types of nanomaterials are very promising (in terms of computational performance and energy dissipation efficiency) for use in superconducting digital technologies [5-7] based on Josephson junctions.

It is well established that the properties of nanostructures can significantly differ from those of bulk samples. Currently, close attention is paid to thin-film magnetic structures, which include cobalt and iron [8-10]. Thus, in [1], the crystal structure and composition of Co–Ni–Fe films were evaluated, and it was found out how the deposition rate affects the conversion of a weak magnetic field into magnetic induction. In addition, thin-film structures based on Fe and Co are among the most promising materials that can be applied in the creation of magnetic heads for recording and reading information, memory cells, and other devices [11] which utilize magnetic properties of materials. Magnetic properties of nanofilms [12,13], in particular cobalt nanofilms, represent an important subject of research in both theoretical and practical fields of materials science. These properties depend not only on the composition, but also on factors such as film thickness, which in turn affects their application in microelectronics, spintronics, and other high-tech fields.

The aim of this article is to model the magnetic properties of cobalt nanofilms of different thicknesses and to reveal the main interdependence mechanisms of dimensional, structural, and magnetic subsystems. The proposed modeling methodology and the conducted studies make it possible to analyze the regularities determining the magnetic properties of thin films, which will further make it possible to optimize them for specific applications and tasks. The present work is a development of earlier publications by the authors [14-16].

The cobalt thin films studied in this work can be a component of superconductor–ferromagnetic hybrid nanostructures, which are the basis for the formation of Josephson contacts [13]. These nanomaterials are widely used [17-19] in the creation of individual qubits and quantum computers in general, superconducting microcircuits and interferometers, single photon detectors [20] and other devices of quantum electronics and spintronics.

Mathematical Model for Studying the Magnetic Behavior of Atoms

To conduct computational experiments, we used a mathematical model describing the coordinated motion of atoms and the change of their spin vectors. The spin vector of an atom in this case was understood as the intrinsic magnetic moment associated with the momentum of the atom, which was calculated as a vector sum of the spins of individual electrons included in its structure and their orbital moments.

The mathematical model of atomic displacement and changes in their magnetic moments is based on the Langevin [21] and Landau–Lifshitz–Hilbert [22,23] equations:

$$m_i \frac{\mathrm{d}\mathbf{v}_i}{\mathrm{d}t} = -\frac{\partial U^{\mathrm{MEAM}}(\mathbf{r})}{\partial \mathbf{r}_i} - \frac{\partial H^{\mathrm{ex}}(\mathbf{r})}{\partial \mathbf{r}_i} - \kappa \mathbf{v}_i + \boldsymbol{\chi}(t), \quad (1)$$

$$\frac{\mathrm{d}\mathbf{s}_i}{\mathrm{d}t} = \frac{1}{\left(1+\lambda^2\right)}\left(\left(\boldsymbol{\omega}_i + \boldsymbol{\eta}(t)\right)\times \mathbf{s}_i + \lambda \mathbf{s}_i \times \left(\boldsymbol{\omega}_i \times \mathbf{s}_i\right)\right), \quad i = 1,2,...,N \quad (2)$$

where $U^{\mathrm{MEAM}}(\mathbf{r})$ is the force potential, the modified embedded atom method (MEAM) potential was used in this work; $H^{\mathrm{ex}}(\mathbf{r})$ is the exchange interaction energy of spins; $\mathbf{r} = \{\mathbf{r}_1,\mathbf{r}_2,\ldots,\mathbf{r}_N\}$ is the generalized variable showing the dependence on the whole set of radial vectors of atoms; κ,λ are viscous friction force parameter and damping spin coefficient, respectively; $\boldsymbol{\chi}(t)$, $\boldsymbol{\eta}(t)$ are white noise present in the description of atom motion processes and the behavior of their spins, respectively; and $\boldsymbol{\omega}_i$ is the multiplication value of the gyromagnetic ratio and the local magnetic field [22].

It has been known for quite a long time [24,25] that the fluctuations of thermal and magnetic energy of an atomistic system can be described in the framework of the Langevin theory. To solve stochastic differential equations, which are the basis of this theory, random forces $\boldsymbol{\chi}(t)$ and $\boldsymbol{\eta}(t)$, characterized by the following properties, are used:

$$\left\langle \boldsymbol{\chi}(t) \right\rangle = 0, \left\langle \chi_\alpha(t)\chi_\beta(t') \right\rangle = \frac{2k_{\mathrm{B}}T_l}{B}\delta_{\alpha\beta}\delta(t-t'), \quad (3)$$

$$\left\langle \boldsymbol{\eta}(t) \right\rangle = 0, \left\langle \eta_\alpha(t)\eta_\beta(t') \right\rangle = \frac{2\pi\lambda k_{\mathrm{B}}T_s}{\hbar}\delta_{\alpha\beta}\delta(t-t'), \quad (4)$$

where t and t' are different time points; α and β are components of the random force vector, for the three-dimensional case $\{\alpha,\beta\} = \{x,y,z\}$; $\delta(t - t')$ is the Dirac delta measure; k_{B} is the Boltzmann constant; $\hbar$ is the reduced Planck constant; B is the mobility value of the Brownian particle; and T_l and T_s are

values of the thermodynamic and spin temperatures, respectively [26,27].

The potential of the modified embedded atom method [28,29] was based on the electron density functional theory. The magnitude of the potential U^{MEAM} depends on the set of atomic positions, which makes the potential multi-body model:

$$U^{\mathrm{MEAM}}\left(\mathbf{r}\right)=\sum_{i}\left(F_i\left(\bar{\rho}_i\right)+\frac{1}{2}\sum_{j,j\neq i}\phi_{ij}\left(r_{ij}\right)\right),\ i=1,2,...,N, \quad (5)$$

where F_i is the immersion function of each atom in the electron gas created by electrons of all other atoms of the system; $\phi_{ij}(r_{ij})$ is the pair potential function; $r_{ij} = |\mathbf{r}_{ij}| = |\mathbf{r}_j - \mathbf{r}_j|$ is the distance between two atoms with numbers $_i$ and $_j$; and $\bar{\rho}_i$ is the background electron density. When describing the electron density, different types of electron clouds of the atoms under consideration are taken into account, and a sufficiently large set of potential parameters is involved, which makes MEAM sufficiently accurate and allows it to be used in solving a wide range of atomistic modeling problems.

The exchange interaction energy of spins is used in mathematical models to describe the magnetic behavior of systems and allows us to reproduce their ferromagnetic and antiferromagnetic ordering. The total energy value is calculated according to the following expression:

$$H^{\mathrm{ex}}\left(\mathbf{r}\right)=-\sum_{j,i\neq j}^{N}J\left(r_{ij}\right)\mathbf{s}_i\cdot\mathbf{s}_j, \quad (6)$$

where $J(r_{ij})$ is the exchange integral, the sign of which determines the type of interaction (ferromagnetic or antiferromagnetic); and $\mathbf{s}_i$ and $\mathbf{s}_j$ are spin vectors of individual atoms. Equation 6 provides a connection between the spatial and spin degrees of freedom of the system through the exchange integral in the form of the Bethe–Slater curve:

$$J\left(r_{ij}\right)=4\varepsilon\left(\frac{r_{ij}}{\delta}\right)^2\left(1-\gamma\left(\frac{r_{ij}}{\delta}\right)^2\right)e^{-\left(\frac{r_{ij}}{\delta}\right)^2}\Theta\left(R_c-r_{ij}\right), \quad (7)$$

where ε,δ,γ are parametric coefficients of the model; $\Theta(R_c - r_{ij})$ is the piecewise constant of the Heaviside function; and R_c is the distance at which the exchange integral is clipped.

The processes of atomic motion and changes in their magnetic moments were modeled in the LAMMPS software package [30]. This software package was created by a team of authors from Sandia National Laboratories and is distributed under the GPL license (i.e., it is freely available in the form of source codes). The additional package LAMMPS SPIN allows to perform numerical studies of magnetic systems and calculate the spin dynamics of atoms [22,31].

Results and Discussion

The present paper deals with the solution of two problems related to the modeling of magnetic properties of cobalt nanostructures. The first problem was focused on confirming the adequacy of the used mathematical model and checking the convergence of the obtained numerical solutions. The second task investigated the self-organization of atomic spins in cobalt thin films and analyzed the dependence of nanofilm magnetic properties on their thickness. In both problems, there was no external magnetic field in the system, and the material structure corresponded to a face-centered cubic crystal lattice (fcc).

The size of the system in the first problem was small at 500 atoms (5 × 5 × 5 elementary crystal cells) and was due to the study of a similar system in [22]. The appearance of the modeled cobalt crystallite and the magnetic moments of its atoms are shown in Figure 1. Periodic boundary conditions were applied to the computational cell along all coordinate directions. The system was symmetric along all coordinate axes. The magnetic parameters of the exchange integral (Equation 7) were also chosen according to [22]. The magnetic behavior of the cobalt crystallite was considered in two stages. At the first stage (50 ps), relaxation of the system was performed, which resulted in mutual ordering of the spins of the atoms and orientation of the magnetization vector of the whole crystallite in

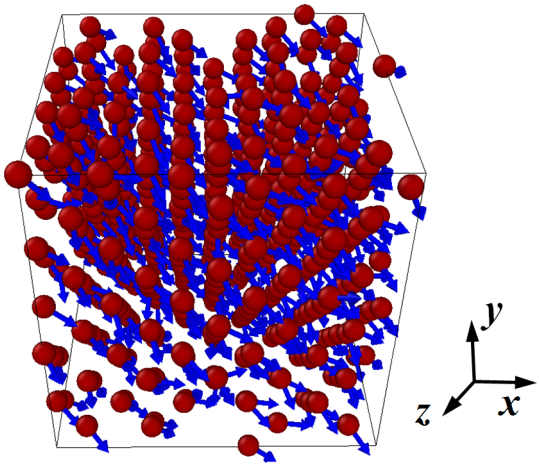


Figure 1: Appearance of a cobalt fcc crystallite (500 atoms) together with the orientation of atomic spins at the final relaxation stage for thermodynamic and spin temperatures of 300 K.

some specific direction. At the second stage (10 ps), fluctuations of the magnetic values of the system stabilized after the relaxation stage were analyzed.

For the stage of fluctuations of magnetic quantities, the graphs of changes in magnetic energy and reduced magnetization modulus (takes values from 0 to 1) of a cobalt crystallite for integration steps dt = 0.1–10.0 fs were plotted. These graphs are selectively illustrated in Figure 2. For the other integration steps, the dependences have similar behavior. The dotted line in Figure 2 shows the average values of energy and magnetization modulus for an integration step of 0.1 fs. For simplicity in comparing the results with previously known data of other authors, the magnetic energy and magnetization modulus analyzed in this work were normalized with respect to the total number of atoms in the system.

Analysis of the plots in Figure 2 shows that small integration steps are characterized by smaller fluctuations of magnetic energy and magnetization modulus. The steps dt = 0.1 fs and dt = 1.0 fs lead to changes in the instantaneous values of the magnetic parameters near the average values of E = −4.5936 eV and |**M**| = 0.8747, respectively. Comparison of the average normalized magnetic energy and normalized magnetization modulus of a similar cobalt crystallite system from [22] gives values of E = −4.4900 eV and |**M**| = 0.9019, which correspond to a relative error value of 2% for energy and 3% for the magnetization modulus. The level of deviation of the parameters may be related to the fact that in [22] the modeling was carried out within the framework of the microcanonical ensemble, while in the present work a stochastic approach based on the Landau–Lifshitz–Hilbert equation was used.

For further analysis of the convergence of the numerical solutions and the influence of the time step on the fluctuations of the magnetic properties of the system, the relative deviations of the normalized magnetic energy $\Delta E(\Delta t)$ and magnetization modulus $\Delta M(\Delta t)$ were calculated. At the same time, additional averaging over the already performed time steps was performed for the considered quantities:

$$\Delta E(\Delta t) = \frac{1}{N_{\text{step}}} \sum_{k=1}^{N_{\text{step}}} \left| \frac{E_k(\Delta t) - \langle E \rangle(\Delta t)}{\langle E \rangle(\Delta t)} \right|, \quad (8)$$

$$\Delta M(\Delta t) = \frac{1}{N_{\text{step}}} \sum_{k=1}^{N_{\text{step}}} \left| \frac{M_k(\Delta t) - \langle M \rangle(\Delta t)}{\langle M \rangle(\Delta t)} \right|, M = |\mathbf{M}|, \quad (9)$$

where N_{step} is the previously performed number of time steps; $E_k(\Delta t)$ and $M_k(\Delta t)$ are magnetic energy and magnetization modulus at the current time step; $\langle E \rangle(\Delta t)$ and $\langle M \rangle(\Delta t)$ are average values of the considered parameters over the entire time period.

The deviations of the magnetic parameters from Equation 8 and Equation 9 as a function of different integration steps are shown in Figure 3. For convenience in analyzing the data in Figure 3, the values along the abscissa and ordinate axes are given in logarithmic scale. The black dashed lines represent linear approximation functions, since the calculated points of the graphs are nearly a straight line. The approximation value for the deviation of magnetic energy $\Delta E(\Delta t)$ was R^2 = 0.96, for the deviation of magnetization modulus $\Delta M(\Delta t)$ was R^2 = 0.93.

A comparison of $\Delta E(\Delta t)$ and $\Delta M(\Delta t)$, obtained from the simulations in this work and the values from [22] indicates a satisfactory qualitative and quantitative agreement of the values. This analysis confirms that the modeling of magnetic properties and behavior of nanomaterials at the atomistic level should be

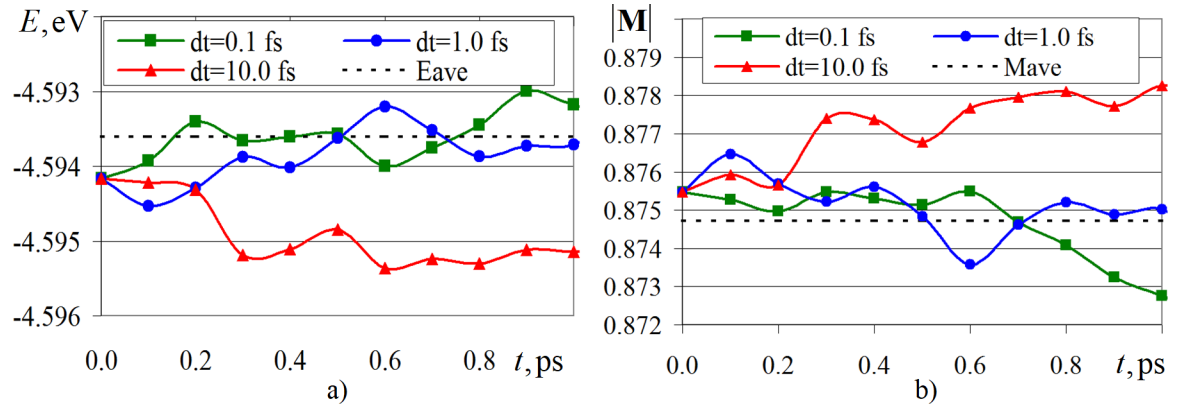


Figure 2: Variation of magnetic energy (a) and magnetization modulus (b) of a cobalt fcc crystallite (500 atoms) for different steps of integrating the systems of Equation 1 and Equation 2.

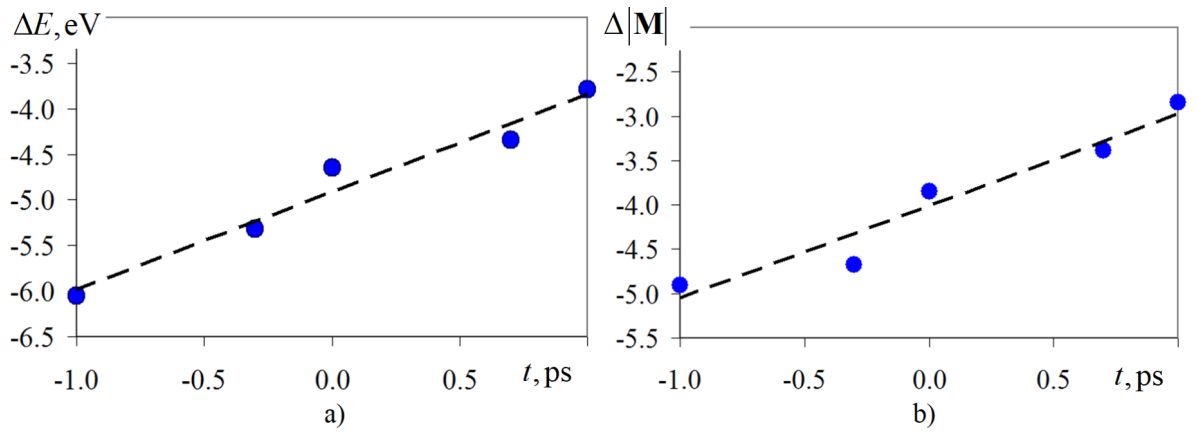


Figure 3: Dependences of the deviation of the relative normalized magnetic energy (a) and magnetization modulus (b) from different time steps of integration. The scales on the abscissa and ordinate axes are presented in decimal logarithm values.

carried out at integration time steps of no more than 1.0 fs. Typical spin dynamics models use a time step 0.1 fs, but the algorithm remains sufficiently accurate up to a time step of 10.0 fs. Therefore, for conducting computational experiments, an integration step of up to 10.0 fs can be used. According to [22], numerical results obtained with a time step of 0.1 fs show the greatest stability and robustness, since the characteristic time scales of changes in the magnetic moments of atoms are much smaller compared to their spatial counterparts. In the second problem, a unified integration step of 0.1 fs was used for all computational experiments.

In the second problem, crystalline cobalt (fcc) nanofilms containing 20 elementary crystal cells along the x and y axes were considered. The thickness of the films in the z-axis direction was varied in the range from 5 to 20 in steps of one elementary crystal cell. As studies show, the magnetic ordering in cobalt nanofilms with a thickness of less than 1.8 nm becomes unstable, and in the monolayer limit, it can be completely destroyed. When the film thickness is less than 1–2 monolayers (≈0.2–0.4 nm), the nanofilm ceases to be continuous, forming islands. This leads to random fluctuations in magnetization. Additionally, in monolayers and sub-monolayers, the number of nearest neighbors for cobalt atoms sharply decreases. This weakens the exchange interaction that stabilizes the ferromagnetic order. Disruption of lattice periodicity and a high density of defects exacerbate this problem. For these reasons, such studies are not included in this article. Thus, 16 computational experiments were realized in the second task, in which the thickness of the nanofilms was gradually increased and the investigated systems contained from 8,800 to 32,800 cobalt atoms. Along the horizontal axes (x and y), periodic boundary conditions were applied along the edges of the nanofilm, while vertically (z coordinate axis) the boundaries of the computational cell remained free.

The numerical realization of each individual computational experiment included two stages. At the first stage, the system proceeded through the stage of partial ordering of magnetic moments from the initial random distribution of spins and subsequent relaxation within 50 ps. This stage was necessary to exclude the influence of initial conditions on the magnetic characteristics further investigated. In the second stage, the magnetic properties of the previously energetically equilibrated cobalt nanofilm were investigated. The duration of the second stage was 10 ps. In both stages, there were no external influences on the system. The thermodynamic and spin temperatures were maintained at 300 K, with temperature damping parameters of $\tau_t = \tau_s = 0.01$ ps.

Magnetic energy and reduced magnetization modulus were considered as the investigated properties of cobalt nanofilms. As in the first problem, these quantities were normalized compared to the total number of atoms of the system for convenience of comparison. Figure 4 and Figure 5 are plots of the time variation of magnetic energy and magnetization modulus for the whole series of computational experiments. For clarity, the shade of the lines in the graphs is depicted in a darker color with increasing film thickness L_z, where L_z = 1.8 nm corresponds to five elementary crystal cells, and L_z = 7.1 nm to 20 elementary crystal cells.

As can be seen from the graphs in Figure 4 and Figure 5, the magnetic energy of the systems at this stage of the computational experiment stabilizes and does not significantly change over time; only its insignificant fluctuations are noticeable. In-

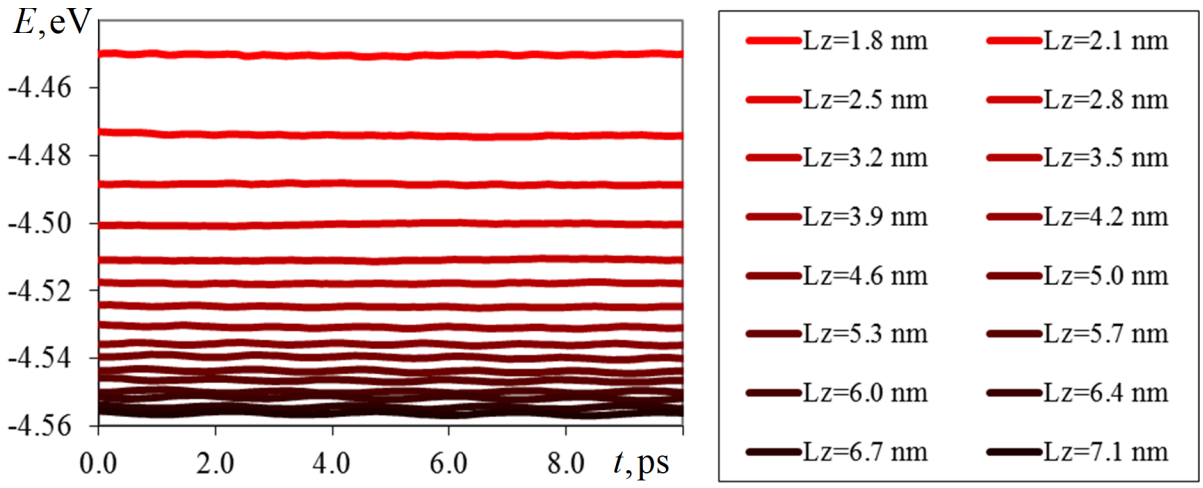


Figure 4: Variation of the magnetic energy of cobalt (fcc) normalized by the number of atoms in the system for nanofilms with thicknesses of 1.8–7.1 nm and thermodynamic and spin temperatures of 300 K.

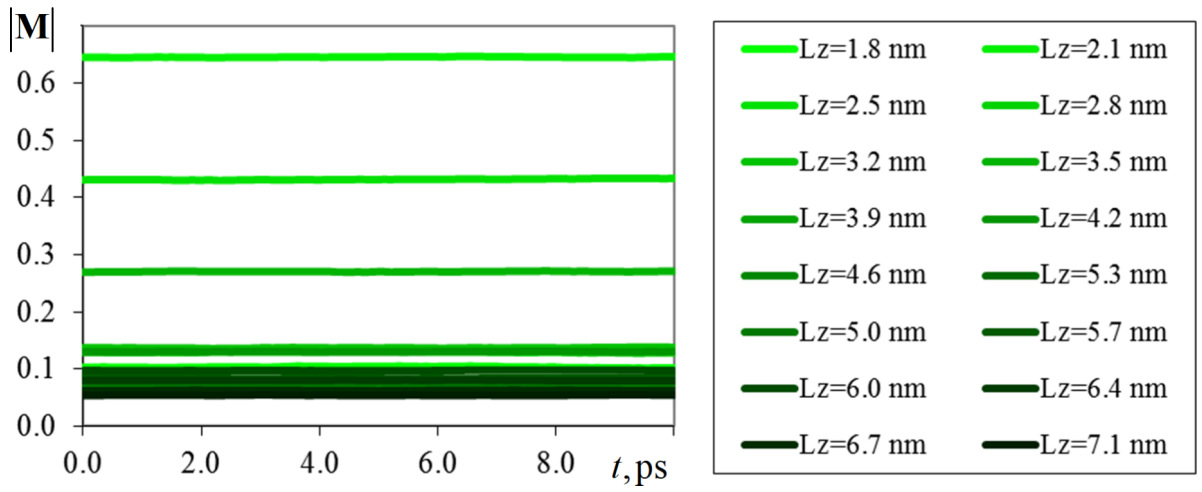


Figure 5: Variation of the magnetization modulus of cobalt (fcc) normalized by the number of atoms in the system, for nanofilms of thicknesses 1.8–7.1 nm and thermodynamic and spin temperatures of 300 K.

creasing the thickness of the nanofilm, in turn, leads to a decrease in the value of magnetic energy, in connection with which a gradient change of colors in the graphs in Figure 4 is observed. The most significant differences in the magnetic energy values were obtained for thin films L_z = 1.8–3.2 nm. For thicker cobalt nanofilms, the values of normalized magnetic energy are in the range of −4.56 to −4.53 eV. Such behavior of the magnetic energy can be related to the fact that with increasing thickness of the nanofilm, the fraction of its surface atoms decreases and the influence of various surface effects decreases. As the number of crystalline layers of the nanofilm increases, the modeled system approaches a bulk material in terms of its physical properties. That is why, from the point of view of functional characteristics, thin-film ferromagnetic nanostructures are of the greatest interest.

Analysis of the graphs in Figure 5 shows that for the whole series of computational experiments after the relaxation stage, the magnetization modulus value also slightly changes in time. The simulation results indicate that as the thickness of the nanofilm increases, there is a tendency to decrease the value of its magnetization modulus. Most of the values are concentrated in the range from 0.05 to 0.13. However, there are a number of exceptions to the smooth gradient variation of the magnetization modulus in Figure 5, indicating its nonlinear dependence on the thickness of the investigated nanofilm. Since on the basis

of Figure 5 it is difficult to speak about the type of the obtained dependence, we have plotted graphs of changes in the individual components of the magnetization vector (in absolute values), which are presented in Figure 6. In a separate inset in Figure 6, the behavior of the magnetization modulus for cobalt nanofilms of different thicknesses is shown. As M_α in Figure 6, the time-averaged value of the components of the magnetization vector was used.

The study of the dependences plotted in Figure 6 indicates that the film thickness has a significant effect on the magnetization value. A three-modal distribution of the magnetization vector components with peaks is observed at nanofilm thicknesses of 6, 10, and 12 crystal cells. The intensity of the peaks decreases with increasing thickness of the cobalt layers, which is clearly visible in Figure 6. The value of each next mode decreased in absolute value by more than 50% compared to the previous one. It is also interesting to notice that all three modal values were obtained for nanofilms with an even value of crystalline layers. The influence of the nanofilm thickness on the magnetization value significantly decreases for film thicknesses above 4.5 nm. In this range of values, local oscillations of the magnetization vector components occur, but they do not significantly affect the final modulus value.

The presence of the obtained peaks of the magnetization vector components distribution in Figure 6 may be due to surface effects in thin films and the formation of domain walls. Depending on the symmetry of the modeled crystalline structures, the joint orientation of magnetic moments of atoms and their way of turning on the boundary, the types of domain walls may differ. For example, Bloch-type domain walls, Neel-type domain walls, walls with reduced angle, and cylindrical domain walls are known. Analysis of magnetic moments of atoms mutually ordered as a result of modeling has shown that, for some cases of calculations for thin films of cobalt, the formation of Neel domain walls is typical [32-34]. An illustration of the resulting Neel domain wall is given in Figure 7, which shows the orientation of atomic spins obtained by numerical simulation after the relaxation and equilibration of the system.

As can be seen in Figure 7, the reversal of the magnetic moments of individual atoms occurs in the plane of the nanofilm. After the reversal, the spins of the atoms are oriented in the opposite direction, which is demonstrated in the right part of Figure 7. For nanofilms with a thickness of 13–20 crystalline layers, the formation of Neel walls dividing the modeled sample into domains with opposite directions of magnetic moments is observed. As a result, the total magnetization of the nanofilm is formed in the range of 0.07–0.01. It is known that the Neel domain walls occur in thin films with a thickness of 100 nm or less, which agrees well with the simulation results obtained. Since it is typical for ferromagnetic materials to form domains and domain walls due to the strong interaction of spin moments of nearby atoms, the data of computational experiments confirm the ferromagnetic nature of the magnetic behavior of cobalt nanofilms.

For nanofilms with thicknesses of 6, 10, and 12 crystalline cells, which corresponded to the peaks and maximum values of the

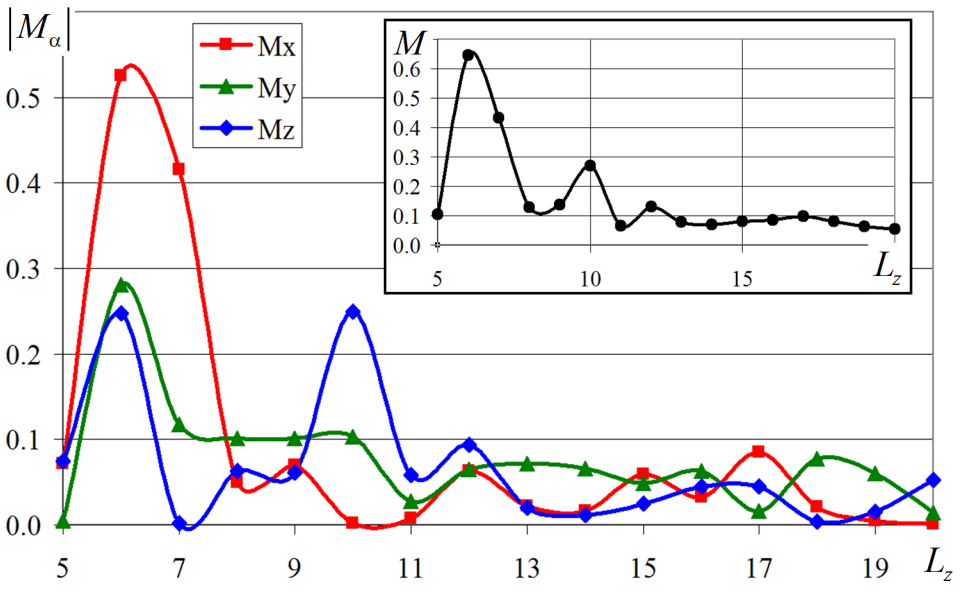


Figure 6: Variation of magnetization vector components (in absolute values) M_α,α = {*x*,*y*,*z*} as a function of cobalt nanofilm thickness measured in crystalline layers L_z, $M = |\mathbf{M}|$.

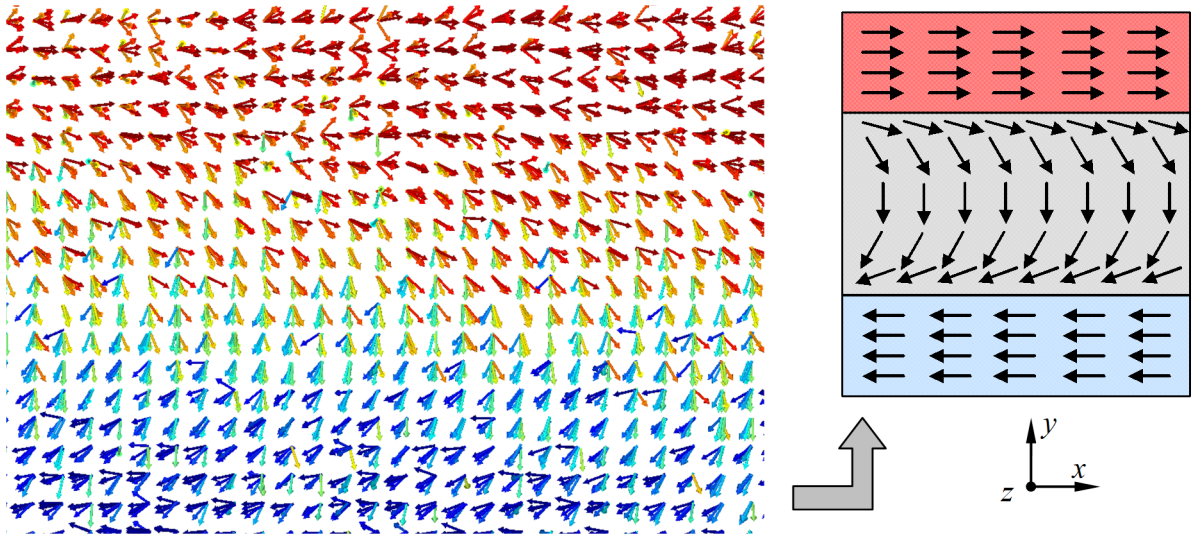


Figure 7: Formation of Neel domain walls in a cobalt nanofilm after the relaxation stage.

magnetization vector, the formation of domains of approximately the same size with antiparallel spin distribution was not observed. The predominant orientation of magnetic moments of cobalt atoms in a certain direction led to bursts and jumps in the values of individual components (x, y, z) of the magnetization vector and its modulus as a whole, which is clearly visible in the graphs in Figure 6. Due to the fact that it is difficult to assess the peculiarities of the connection between the magnetic energy of the modeled nanofilms and their thickness in Figure 4, the graph for these values was separately plotted. Figure 8 shows a nonlinear dependence of the magnetic energy on the thickness of the modeled nanofilm. The given values of magnetic energy were pre-averaged over time for a period of 10 ps after the relaxation step. The smooth change of the graph in Figure 8 may be due to a gradual and uniform decrease in the fraction of surface atoms of the nanofilms as their thicknesses increase.

The graph of calculated magnetic energy values is well approximated by a polynomial dependence of the fifth degree (the

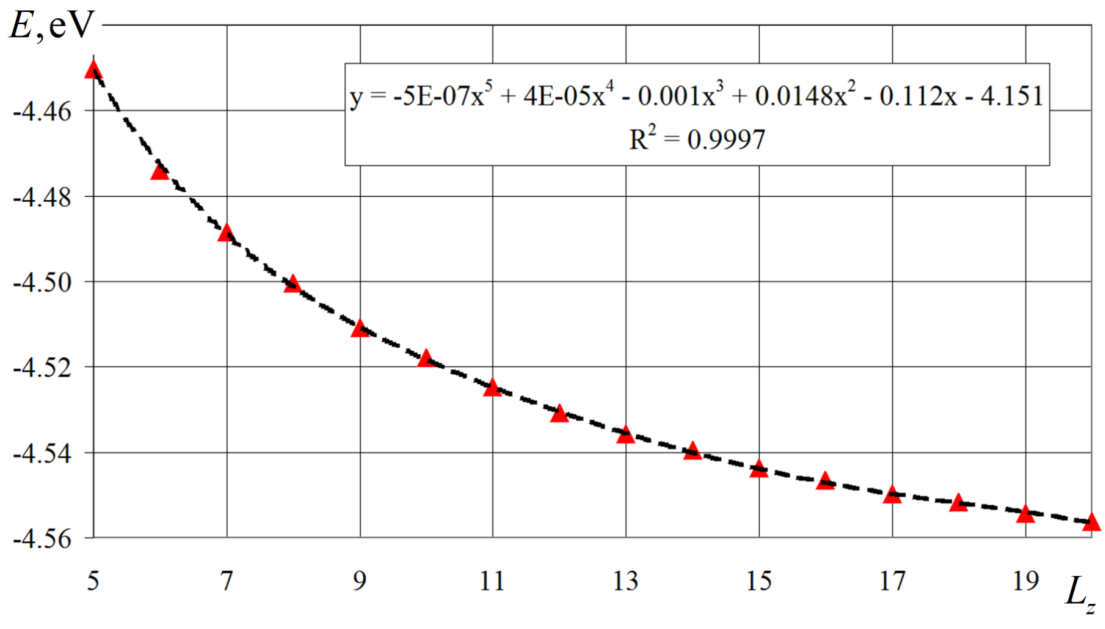


Figure 8: Variation of cobalt magnetic energy as a function of nanofilm thickness measured in crystalline layers.

equation is shown in the frame in Figure 8). The value of reliability of the constructed trend line is 0.9997. Simplification of the approximating function to a polynomial of the third degree (the coefficients in front of the 4th and 5th order terms are quite small) also brings about good results of the trend line at the reliability level of 0.9978. Linear approximation gives a lower indicator of the reliability level (i.e., 0.8848).

Conclusion

The mathematical model considered in this work allows us to investigate the magnetic behavior of a nanoscale system taking into account spin and interatomic interactions. The mathematical model is based on the joint solution of the Langevin and Landau–Lifshitz–Hilbert equations. In this work, the multi-particle potential of the modified immersed atom method, which is well established for solving such problems, is used to describe the interatomic interaction.

Numerical studies of the magnetic behavior of cobalt-based nanofilms were carried out in two stages. Analysis of the convergence of numerical solutions and evaluation of the time step effect on the fluctuations of the magnetic properties of the system showed that modeling of magnetic properties and behavior of nanomaterials at the atomistic level should be carried out at integration time steps of no more than 1.0 fs. A time step of 0.1 fs was used for the main series of computational experiments.

The study of the influence of the cobalt nanofilm thickness on the magnetic behavior of the system showed a decrease in the magnetic energy with increasing film thickness. It should be noted that the magnetic energy nonlinearly changes with increasing thickness of the cobalt nanofilm. The magnetization rate of the modeled systems also does not significantly change with time. The analyzed dependence of the magnetization norm on the thickness of the studied nanofilms illustrate the nonlinear change of this magnetic characteristic with peaks at nanofilm thicknesses of 6, 10, and 12 crystal cells. The effect of the nanofilm thickness on the magnetization value is leveled off at nm. The effects observed in the investigated films can be due to surface effects in thin films and the formation of Neel domain walls.

The dependence of the magnetic energy on the thickness of the modeled nanofilm has a nonlinear form and is well approximated by a polynomial of degree 5. Due to insignificant coefficients in front of the 4th and 5th order terms, the approximation function can be simplified to a 3rd order polynomial without significant decrease in the accuracy level. The gradual nonjump-like change of magnetic energy with increasing thickness of the studied cobalt nanofilms can be associated with a uniform and proportional decrease in the fraction of surface atoms in the thickened films.

Funding

The work was carried out within the framework of the state assignment No. FUUE-2025-0001 “Modeling and experimental studies of the structure and magnetic parameters of a Josephson contact from a multilayer nanostructure” (methodology for modeling magnetic properties) and with the financial support of the Russian Science Foundation (project No. 23-72-30004) (research at ultra-low temperatures) and the project No. 020201 of the Moldova State Program “Nanostructures and advanced materials for implementation in spintronics, thermoelectricity, and optoelectronics” (samples preparation and investigation of Nb/Co interfaces).

Author Contributions

Aleksey Fedotov: conceptualization; project administration; writing – review & editing. Olesya Severyukhina: formal analysis; investigation; writing – original draft. Anastasia Salomatina: software; validation; visualization. Anatolie Sidorenko: conceptualization; funding acquisition; writing – review & editing.

ORCID® iDs

Aleksey Fedotov - https://orcid.org/0000-0002-0463-3089
Olesya Severyukhina - https://orcid.org/0000-0001-6014-9462
Anatolie Sidorenko - https://orcid.org/0000-0001-7433-4140

Data Availability Statement

Data generated and analyzed during this study is available from the corresponding author upon reasonable request.

Preprint

A non-peer-reviewed version of this article has been previously published as a preprint: https://doi.org/10.3762/bxiv.2025.6.v1

References

1. Tikhonov, R. D.; Cheremisinov, A. A.; Tikhonov, M. R. *Perspect. Mater.* **2024,** *1,* 20–29. doi:10.30791/1028-978x-2024-1-20-29
2. Beagle, L. K.; Fang, Q.; Tran, L. D.; Baldwin, L. A.; Muratore, C.; Lou, J.; Glavin, N. R. *Mater. Today* **2021,** *51,* 427–448. doi:10.1016/j.mattod.2021.08.007
3. Shalygina, E.; Svalov, A.; Kharlamova, A.; Ganshina, E.; Doronin, D.; Kurlyandskaya, G. *Jpn. J. Appl. Phys.* **2016,** *55,* 07MF01. doi:10.7567/jjap.55.07mf01
4. Patrin, G. S.; Yakovchuk, V. Y.; Yarikov, S. A.; Shiyan, Y. G.; Furdyk, V. P. *Tech. Phys. Lett.* **2019,** *45,* 507–510. doi:10.1134/s1063785019050262
5. Likharev, K. K. *Phys. C (Amsterdam, Neth.)* **2012,** *482,* 6–18. doi:10.1016/j.physc.2012.05.016
6. Krylov, G.; Kawa, J.; Friedman, E. G. *IEEE Nanotechnol. Mag.* **2021,** *15,* 54–67. doi:10.1109/mnano.2021.3113218

7. Soloviev, I. I.; Bakurskiy, S. V.; Ruzhickiy, V. I.; Klenov, N. V.; Kupriyanov, M. Y.; Golubov, A. A.; Skryabina, O. V.; Stolyarov, V. S. *Phys. Rev. Appl.* **2021,** *16,* 044060. doi:10.1103/physrevapplied.16.044060
8. Shalygina, E.; Kharlamova, A.; Makarov, A.; Kurlyandskaya, G.; Svalov, A. *EPJ Web Conf.* **2018,** *185,* 03009. doi:10.1051/epjconf/201818503009
9. Kamashev, A. A.; Garif'yanov, N. N.; Validov, A. A.; Kataev, V.; Osin, A. S.; Fominov, Y. V.; Garifullin, I. A. *Beilstein J. Nanotechnol.* **2024,** *15,* 457–464. doi:10.3762/bjnano.15.41
10. Pashin, D. S.; Pikunov, P. V.; Bastrakova, M. V.; Schegolev, A. E.; Klenov, N. V.; Soloviev, I. I. *Beilstein J. Nanotechnol.* **2023,** *14,* 1116–1126. doi:10.3762/bjnano.14.92
11. Sidorenko, A. S.; Hahn, H.; Krasnov, V. *Beilstein J. Nanotechnol.* **2023,** *14,* 79–82. doi:10.3762/bjnano.14.9
12. Kamzin, A. S.; Wei, F.; Ganeev, V. R.; Valiullin, A. A.; Zaripova, L. D.; Tagirov, L. R. *Phys. Solid State* **2014,** *56,* 948–954. doi:10.1134/s1063783414050114
13. Voronova, N.; Grudinina, A.; Panico, R.; Trypogeorgos, D.; De Giorgi, M.; Baldwin, K.; Pfeiffer, L.; Sanvitto, D.; Ballarini, D. *Nat. Commun.* **2025,** *16,* 466. doi:10.1038/s41467-024-55119-8
14. Vakhrushev, A.; Fedotov, A.; Boian, V.; Morari, R.; Sidorenko, A. *Beilstein J. Nanotechnol.* **2020,** *11,* 1776–1788. doi:10.3762/bjnano.11.160
15. Vakhrushev, A.; Fedotov, A.; Severyukhina, O.; Sidorenko, A. *Beilstein J. Nanotechnol.* **2023,** *14,* 23–33. doi:10.3762/bjnano.14.3
16. Vakhrushev, A.; Fedotov, A.; Sidorenko, A. *Key Eng. Mater.* **2021,** *888,* 57–65. doi:10.4028/www.scientific.net/kem.888.57
17. Huang, Z.; Lotfizadeh, N.; Elfeky, B. H.; Kisslinger, K.; Cuniberto, E.; Yu, P.; Hatefipour, M.; Taniguchi, T.; Watanabe, K.; Shabani, J.; Shahrjerdi, D. *Appl. Phys. Lett.* **2022,** *121,* 243503. doi:10.1063/5.0135034
18. Pellegrino, F. M. D.; Falci, G.; Paladino, E. *Commun. Phys.* **2022,** *5,* 265. doi:10.1038/s42005-022-01042-7
19. Pal, B.; Chakraborty, A.; Sivakumar, P. K.; Davydova, M.; Gopi, A. K.; Pandeya, A. K.; Krieger, J. A.; Zhang, Y.; Date, M.; Ju, S.; Yuan, N.; Schröter, N. B. M.; Fu, L.; Parkin, S. S. P. *Nat. Phys.* **2022,** *18,* 1228–1233. doi:10.1038/s41567-022-01699-5
20. Walsh, E. D.; Jung, W.; Lee, G.-H.; Efetov, D. K.; Wu, B.-I.; Huang, K.-F.; Ohki, T. A.; Taniguchi, T.; Watanabe, K.; Kim, P.; Englund, D.; Fong, K. C. *Science* **2021,** *372,* 409–412. doi:10.1126/science.abf5539
21. Paquet, E.; Viktor, H. L. *BioMed Res. Int.* **2015,** 183918. doi:10.1155/2015/183918
22. Tranchida, J.; Plimpton, S. J.; Thibaudeau, P.; Thompson, A. P. *J. Comput. Phys.* **2018,** *372,* 406–425. doi:10.1016/j.jcp.2018.06.042
23. Gilbert, T. L. *IEEE Trans. Magn.* **2004,** *40,* 3443–3449. doi:10.1109/tmag.2004.836740
24. Brown, W. F., Jr. *Phys. Rev.* **1963,** *130,* 1677–1686. doi:10.1103/physrev.130.1677
25. García-Palacios, J. L.; Lázaro, F. J. *Phys. Rev. B* **1998,** *58,* 14937–14958. doi:10.1103/physrevb.58.14937
26. Rugh, H. H. *Phys. Rev. Lett.* **1997,** *78,* 772–774. doi:10.1103/physrevlett.78.772
27. Nurdin, W. B.; Schotte, K.-D. *Phys. Rev. E* **2000,** *61,* 3579–3582. doi:10.1103/physreve.61.3579
28. Lee, B.-J.; Baskes, M. I.; Kim, H.; Koo Cho, Y. *Phys. Rev. B* **2001,** *64,* 184102. doi:10.1103/physrevb.64.184102
29. Baskes, M. I. *Phys. Rev. B* **1992,** *46,* 2727–2742. doi:10.1103/physrevb.46.2727
30. Plimpton, S. *J. Comput. Phys.* **1995,** *117,* 1–19. doi:10.1006/jcph.1995.1039
31. Beaujouan, D.; Thibaudeau, P.; Barreteau, C. *Phys. Rev. B* **2012,** *86,* 174409. doi:10.1103/physrevb.86.174409
32. Trunk, T.; Redjdal, M.; Kákay, A.; Ruane, M. F.; Humphrey, F. B. *J. Appl. Phys.* **2001,** *89,* 7606–7608. doi:10.1063/1.1355357
33. DeJong, M. D.; Livesey, K. L. *Phys. Rev. B* **2015,** *92,* 214420. doi:10.1103/physrevb.92.214420
34. Catalan, G.; Seidel, J.; Ramesh, R.; Scott, J. F. *Rev. Mod. Phys.* **2012,** *84,* 119–156. doi:10.1103/revmodphys.84.119

License and Terms

This is an open access article licensed under the terms of the Beilstein-Institut Open Access License Agreement (https://www.beilstein-journals.org/bjnano/terms), which is identical to the Creative Commons Attribution 4.0 International License (https://creativecommons.org/licenses/by/4.0). The reuse of material under this license requires that the author(s), source and license are credited. Third-party material in this article could be subject to other licenses (typically indicated in the credit line), and in this case, users are required to obtain permission from the license holder to reuse the material.

The definitive version of this article is the electronic one which can be found at:
https://doi.org/10.3762/bjnano.16.110

BEILSTEIN JOURNAL OF NANOTECHNOLOGY

Few-photon microwave fields for superconducting transmon-based qudit control

Irina A. Solovykh[1,2], Andrey V. Pashchenko[1,3,4], Natalya A. Maleeva[5], Nikolay V. Klenov[*1,3], Olga V. Tikhonova[1,2,6] and Igor I. Soloviev[1,6]

Full Research Paper

Open Access

Address:
[1]Lomonosov Moscow State University, Faculty of Physics, Moscow, 119991, Russia, [2]Lomonosov Moscow State University, Skobeltsyn Institute of Nuclear Physics, Moscow, 119991, Russia, [3]All-Russian Research Institute of Automatics n.a. N.L. Dukhov (VNIIA), 127055, Moscow, Russia, [4]Moscow Technical University of Communications and Informatics (MTUCI), 111024, Moscow, Russia, [5]National University of Science and Technology "MISIS", 119049, Moscow, Russia and [6]Kotel'nikov Institute of Radio Engineering and Electronics of RAS, 125009 Moscow, Russia

Email:
Nikolay V. Klenov[*] - nvklenov@mail.ru

* Corresponding author

Keywords:
Josephson "atoms"; non-classical fields; quantum state control; superconducting qubits

Beilstein J. Nanotechnol. **2025,** *16,* 1580–1591.
https://doi.org/10.3762/bjnano.16.112

Received: 01 May 2025
Accepted: 19 August 2025
Published: 11 September 2025

This article is part of the thematic issue "Superconducting artificial neural networks and quantum circuits".

Guest Editor: A. S. Sidorenko



© 2025 Solovykh et al.; licensee Beilstein-Institut.
License and terms: see end of document.

Abstract

Increasing the efficiency of quantum processors is possible by moving from two-level qubits to elements with a larger computational base. An example would be a transmon-based superconducting atom, but the new basic elements require new approaches to control. To solve the control problem, we propose the use of nonclassical fields in which the number of photons is comparable to the number of levels in the computational basis. Using theoretical analysis, we have shown that (i) our approach makes it possible to efficiently populate on demand even relatively high energy levels of the qudit starting from the ground state; (ii) by changing the difference between the characteristic frequencies of the superconducting atom and a single field mode, we can choose which level to populate; and (iii) even the highest levels can be effectively populated on a sub-nanosecond time scale. We also propose the quantum circuit design of a real superconducting system in which the predicted rapid control of the transmon-based qudit can be demonstrated.

Introduction

Currently, quantum computing is under active development, opening new horizons for solving a number of problems that are difficult for classical processors, including modeling the behavior of quantum systems, optimization problems, breaking cryptographic systems, solving large systems of linear equations, and analyzing heat conduction equations [1-6].

The basis for the physical implementation of these computations is a quantum processor consisting of computational cells called qudits, whose states can be represented with satisfactory accuracy in the form of a decomposition into n basis states. Today, the main focus is on processors based on qubits (a special case of qudits with $n = 2$) on a superconducting, ionic, or other platform. However, it is still not easy to create the necessary number of qubits and control channels to implement really useful quantum algorithms. A promising solution to this problem is to expand the computational basis of an element by switching to qutrits ($n = 3$), ququarts ($n = 4$), and so on [7-12].

We believe that an additional synergistic effect can be achieved by using quantum electromagnetic fields with a comparable (with n) number of photons to control such quantum multilevel systems. The coexistence of different photons in a single waveguide should make it possible to use the scarce control circuits on a quantum chip more efficiently. In the future, the analysis of the behavior of "qudits + multiphoton quantum field" systems will form the basis for the practical implementation of quantum internet and telecommunication systems [13-16].

Among the many possibilities, we will focus on a superconducting platform; it allows one to create sources and mixers for microwave photons, qubits, and qudits with corresponding characteristic frequencies of transitions between basis states, as well as radiation detectors with the claim of being quantum-sensitive [17-26].

So far, the most common artificial atom among the superconducting ones is considered to be a charge qubit with a large shunt capacity, namely a transmon [27-29]. The transmon is technically simple to fabricate, easy to operate, and resistant to decoherence from various sources. Transmon-based qudits are already being used to detect microwave fields [30]. The latter feature makes it possible to achieve a long lifetime of this artificial atom; in a recent work [29] "coherence" times of T_1 = 64–13 μs, Ramsey periods of T_{2R} = 85–16 μs, and Hahn echo times T_{2E} = 93–22 μs for levels of n = 2–10, respectively, have been achieved.

It should be noticed that the spectrum of eigenvalues of the Hamiltonian of a real transmon (a slightly nonlinear oscillator) is quite close to the equidistant one; however, a number of widely used theoretical models describing its evolution in an external electromagnetic field (the Jaynes–Cummings model) do not take into account the high-lying energy levels of the artificial atom, nor the nonlinearity existing in a real solid-state system [31-33]. In our fully quantum analysis of the "atom"–field interaction, the nonlinearity of transmon will be taken into account.

This article presents the results of a theoretical description of the interaction between a few-photon microwave non-classical field and a transmon-based qudit with several, even high-lying, levels being taken into account. We develop methods of rapid quantum control of the designed transmon-based qudit and its state population dynamics. The structure of the article is as follows: First, the model of the system under study is described in more detail, followed by a theoretical description of the Fock-based control of the qudit states and a discussion of possible practical implementations.

Results

Model description

The system under consideration consists of a high-quality superconducting resonator (the quality factor is about 10^5–10^6 and depends mainly on the external coupling $C_{in/out}$) connected to a transmon [34] by a capacitance C_g (see Figure 1). The resonator in this system is a quantum harmonic oscillator with a fully equidistant energy spectrum described by the bosonic ladder operators $\hat{a}$ and $\hat{a}^+$, and the photon number operator $\hat{n}_a = \hat{a}^+\hat{a}$. The transmon is considered as an anharmonic oscillator (with ladder operators $\hat{b}$ and $\hat{b}^+$) with the number of excitations in the solid-state system similarly introduced as $\hat{n}_b = \hat{b}^+\hat{b}$. In a transmon, the inductance is created using a nonlinear element, that is, a nanoscale Josephson junction (JJ), or a pair of JJs forming an interferometer-like circuit, so the spectrum is no longer equidistant. In the case where the JJ pair is used, the characteristic (plasma) frequency of the transmon can be quickly adjusted in 10–20 ns in the range of 1 GHz by an external magnetic field [35]. In practice, researchers try to reduce the transmon frequency dependence on the external magnetic field to get rid of parasitic flux fluctuations. A large shunt capacitance C_B is needed to increase resistance to parasitic charge fluctuations [36].

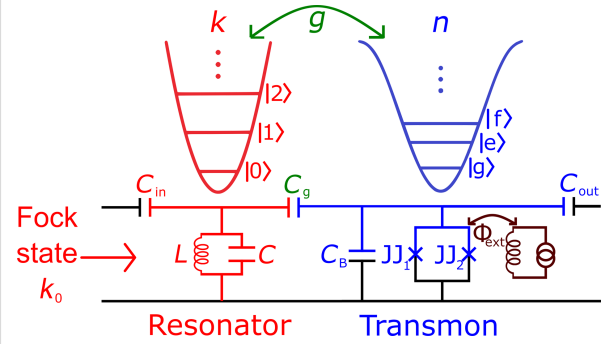


Figure 1: Schematic representation of the model under discussion: A few-photon microwave field from a high-quality resonator (red) affects an artificial transmon-based atom (blue). The potential energies and energy spectra for harmonic (resonator) and anharmonic (transmon) oscillators are shown above. Crosses mark the Josephson junctions in the transmon interferometer. The external magnetic flux Φ_{ext} is used to tune the spectrum of a transmon.

A few-photon non-classical microwave field (with a certain number of photons, k_0) enters the resonator [37-42] with variable frequency detuning Δω between the resonator and the artificial atom. The time evolution of the quantum state of the transmon qudit, the populations of its eigenstates, and the number n of excitations induced in the superconducting system by the quantum field is studied. By taking into account the nonlinearities in the system, it will be shown that there is a certain value of the frequency detuning at which the dynamics of the energy transition from the field to the solid-state system and vice versa is most efficient.

Theoretical description of Fock-based qudit control

First, we need to quantize the field in the harmonic oscillator that corresponds to a high-quality resonator. The energy of the electric field stored in the capacitor and the energy of the magnetic field stored in the inductor can be written as follows:

$$H_{LC} = \frac{Q^2}{2C} + \frac{\Phi^2}{2L} \rightarrow \hat{H}_{LC} = \hbar\omega_0\left(\hat{a}^+\hat{a} + \frac{1}{2}\right), \quad (1)$$

with operators of quantum charge and flux introduced by:

$$\hat{Q} = iQ_{\text{zpf}}\left(\hat{a}^+ - \hat{a}\right), \quad \hat{\Phi} = \Phi_{\text{zpf}}\left(\hat{a}^+ + \hat{a}\right), \quad (2)$$

where

$$Q_{\text{zpf}} = \sqrt{\frac{\hbar}{2Z_0}}, \ \Phi_{\text{zpf}} = \sqrt{\frac{\hbar Z_0}{2}}$$

are the vacuum fluctuations of charge and flux, Z_0 is the characteristic impedance, and $\omega_0 = 1/\sqrt{LC}$ is the resonator angular frequency. The transmon is treated almost the same way, but, in this case, the number of Cooper pairs on the shunt capacitor C_B (island) and the phase on the JJ/(interferometer) are quantized as follows:

$$\hat{n}_{\text{CP}} = \frac{i}{2}\left(\frac{E_J}{2E_C}\right)^{\frac{1}{4}}\left(\hat{b}^+ - \hat{b}\right), \hat{\varphi} = \left(\frac{2E_C}{E_J}\right)^{\frac{1}{4}}\left(\hat{b}^+ + \hat{b}\right), \quad (3)$$

where charge energy $E_C = e^2/2C_B$ and Josephson energy $E_J = (\Phi_0 I_c)/2\pi$ are used (I_c is the critical current flowing through the Josephson junction). The Hamiltonian for the transmon part of our system can be written in the following form, taking into account the nonlinearity [6]:

$$\hat{H}_0 = \hbar\omega_p\hat{b}^+\hat{b} - \frac{E_C}{12}\left(\hat{b} + \hat{b}^+\right)^4, \quad (4)$$

where $-E_C/12$ is the nonlinearity parameter and $\omega_p = \sqrt{8E_J E_C}/\hbar$ is the plasma frequency of the transmon.

The first term in the Hamiltonian describes a free linear evolution of the photon operators, characterized by their oscillations in time in the Heisenberg representation. The nonlinear term in the Hamiltonian can be averaged over high-frequency oscillations, leaving only smoothly varying terms. This procedure actually corresponds to the so-called rotating wave approximation, in which the following type of nonlinear term can be obtained:

$$\left(\hat{b} + \hat{b}^+\right)^4 \approx 6\hat{n}_b^2 + 6\hat{n}_b + 3. \quad (5)$$

The expression for the nonlinear term obtained in Equation 5 indicates that the nonlinearity of the transmon is similar to the type of Kerr phase modulation $\gamma\hat{n}_b(\hat{n}_b + 1)$, with $\gamma = -E_C/2\hbar$. Thus, the Hamiltonian in Equation 4 can be rewritten as follows:

$$\hat{H}_0 = \hbar\omega_p\hat{n}_b + \hbar\gamma\hat{n}_b\left(\hat{n}_b + 1\right). \quad (6)$$

Note that, for such a system, the operator $\hat{n}_b$ is found to be independent on time (being an integral of motion). This means that this nonlinearity itself leads only to phase modulation without changing the excitation statistics.

In our case, the dynamics of the excitations of a Josephson nanosystem (transmon) under the action of a nonclassical electromagnetic field is studied. The interaction of the photonic and superconducting subsystems is investigated by direct solution of the nonstationary Schrödinger equation:

$$i\hbar\frac{\partial\Psi}{\partial t} = \hat{H}\Psi. \quad (7)$$

The Hamiltonian of such a system, taking into account both the nonlinearity of the transmon and the transmon–field coupling, can be written as follows:

$$\begin{aligned}\hat{H} = {} & \hbar\omega_0\left(\hat{n}_a + \frac{1}{2}\right) + \hbar\left(\omega_0 + \Delta\omega\right)\left(\hat{n}_b + \frac{1}{2}\right) \\ & + \hbar\gamma\hat{n}_b\left(\hat{n}_b + 1\right) + \hbar\frac{g}{2}\left(\hat{b}^+\hat{a} + \hat{b}\hat{a}^+\right),\end{aligned} \quad (8)$$

where $\omega_0 + \Delta\omega = \omega_p$ is the transmon frequency. The interaction strength of the resonator mode with the Josephson subsystem is taken as $g = (d_0\varepsilon_0)/\hbar$, where $d_0 = 2el(E_J/32E_C)^{1/4}$ is the dipole moment of the transmon,

$$\varepsilon_0 = \frac{\omega_0}{l}\frac{C_g}{C_B}\sqrt{\frac{\hbar Z_0}{2}}$$

is the vacuum electric field in the resonator that affects the transmon, and l is the distance that the Cooper pair travels when tunneling through JJ [43]. The conditions for the application of the rotating wave approximation, which makes it possible to use the relation in Equation 5, are $\Delta\omega \ll \omega_0$ and $g \ll \omega_0$ [44].

Here, the efficiency of the interaction between two subsystems is determined by the average photon density $\langle N\rangle/V_{res}$, which is large enough to allow field-induced transitions to occur significantly faster than any decoherence processes in the system [29]. This actually corresponds to the strong-field regime and makes it possible to correctly describe the dynamics of a quantum system in terms of the nonstationary Schrödinger equation without taking dissipations into account [45].

The developed theoretical approach appears to be very powerful and allows one to describe the mutual influence between the superconducting and field subsystems beyond the perturbation regime with efficient excitation of transmon being taken into account. For the case of few photons in the field mode, the analytical solution of the problem is found. In the general case, the nonstationary Schrödinger equation (Equation 7) was solved numerically using the expansion of the total non-stationary wave function in terms of the interaction-free eigenfunctions of the Josephson, ϕ_n, and field, $\tilde{\phi}_k$, subsystems:

$$\Psi = \Sigma C_{n,k}(t)\phi_n\tilde{\phi}_k e^{-\frac{iE_{nk}t}{\hbar}}, \tag{9}$$

where the designation of the total energy in the system is

$$E_{n,k} = \hbar(\omega_0 + \Delta\omega)\left(n + \frac{1}{2}\right) + \hbar\omega_0\left(k + \frac{1}{2}\right).$$

Substituting the solution in Equation 9 into Equation 7 leads to a system of differential equations for probability amplitudes $C_{n,k}(t)$ to find k photons in the field mode and n-fold excitation of the transmon:

$$i\dot{C}_{n,k} = n\Delta\omega C_{n,k} + \gamma n(n+1)C_{n,k} + \sqrt{\frac{n(k+1)}{4}}gC_{n-1,k+1} + \sqrt{\frac{k(n+1)}{4}}gC_{n+1,k-1}. \tag{10}$$

Based on the obtained solution, the probability of detecting a transmon in the state with the number n is given by:

$$P_n(t) = \Sigma_k\left|C_{n,k}(t)\right|^2. \tag{11}$$

The probability of finding k photons in the field mode can be found similarly to Equation 11 as follows:

$$W_k(t) = \Sigma_n\left|C_{n,k}(t)\right|^2. \tag{12}$$

The initial state is considered to be the Fock state of the resonator with the number of photons k_0 denoted as $\tilde{\phi}_{in} = |k_0\rangle$.

Discussion

Different regimes of transmon population dynamics

The first feature demonstrated for the interacting superconducting subsystem and a single-mode quantum field is a significant influence of the Josephson nonlinearity (which is similar to the Kerr self-phase modulation) on the dynamics of the transmon excitation. Figure 2 shows 2D distributions characterizing the time dynamics of the population of different transmon states in the case of strong and weak nonlinearity in the system. Here we see Rabi-like oscillations [46-48] between different transmon states, and the amplitude of these oscillations is characterized by slow modulation resulting from the nonlinearity effect. It is shown that even a small nonlinearity leads to the appearance of amplitude modulation, and different numbers of states are characterized by different modulation and frequency. Moreover, it is found that significantly different regimes of dynamics take place in dependence on the value of the key parameter K, which combines the characteristics of both the nonlinearity and coupling with the quantum field:

$$K = \frac{\gamma k_0(k_0+1)}{g}. \tag{13}$$

Actually, this parameter represents the ratio between the efficient nonlinearity of the transmon and the strength of its coupling with the quantum field. It is very important that the efficient nonlinearity is calculated for maximal possible transmon excitation directly determined by the initial number of photons in the field k_0. For relatively small values of the nonlinearity parameter ($K \ll 1$), a strong coupling between the field and the Josephson subsystem gives rise to periodic transition of the transmon to high-energy states, as can be clearly seen in Figure 2a. Here, all the energy initially stored in the field can be

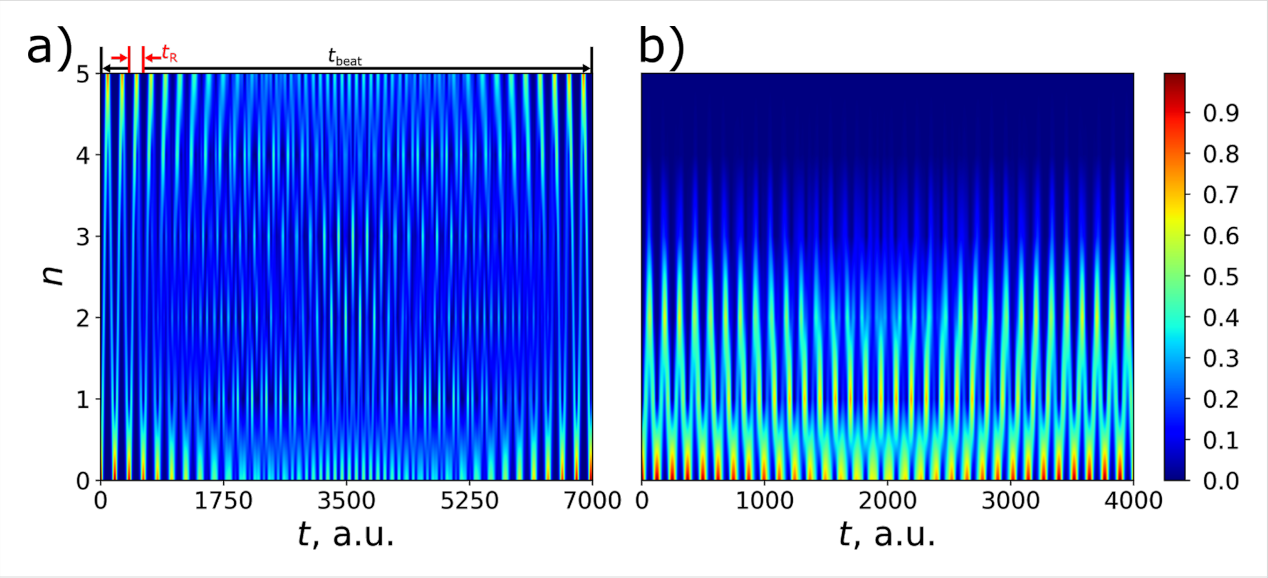


Figure 2: Distribution (colored) of the probability of transmon state excitation versus time with initial state $\psi_{in} = |0\rangle_b |5\rangle_a$ for nonlinearity parameters (a) $\gamma = -0.001\omega_0$ and (b) $\gamma = -0.01\omega_0$ for $g = 0.03\omega_0$, $\Delta\omega = 0$. The dimensionless time unit is t, which is converted to dimensional units via the formula $\tau = 2\pi t/\omega_0$.

transferred to the transmon with periodic maximal population of the highest possible excited transmon state with $n = k_0$.

An increase in the nonlinearity of the transmons leads to a significant reduction in the period of Rabi oscillations, t_R, and the beat frequency, t_{beat}, as shown in Figure 2a. When nonlinear interactions dominate, high-energy excitations are strongly suppressed. This fact is illustrated in Figure 2b.

Population control through frequency detuning

As it was shown in the previous section, the regime of strong nonlinearity, when the parameter $K > 1$, leads to suppression of excitation of high-energy transmon states. However, here we propose and discuss a method how to overcome this effect. We have found out that it is possible to controllably manage the excitations in the Kerr nonlinear transmon by varying the frequency detuning of $\Delta\omega$. Using the law of energy conservation in the case of the initial state $\psi_{in} = |0\rangle_b |k_0\rangle_a$, we have analytically found the formula to determine the optimal value of the frequency detuning that produces the maximum excitation of a certain transmon state "on demand":

$$\hbar\omega_0 k_0 + \langle W_{int}\rangle_{in} = \hbar(\omega_0 + \Delta\omega)n + \hbar\omega_0(k_0 - n) + \hbar\gamma n(n+1) + \langle W_{int}\rangle_{fin}, \quad (14)$$

where $\langle W_{int}\rangle_{in/fin}$ denotes the average value of the interaction energy in the initial and final states of the system, respectively. For an exact number of exitations in the system, the average interaction energy is zero, which means that for the case of the initial state of the transmon, $\langle W_{int}\rangle_{in} = 0$. In addition, under the condition of ensuring the maximum possible excitation, no energy should be involved in the interaction in the final state, so $\langle W_{int}\rangle_{fin} = 0$. Thus, Equation 14 implies an expression for the optimal frequency detuning at which the maximum excitation of the state with the highest number $n = k_0$ can be achieved:

$$\Delta\omega_{opt_n} = -\gamma(n+1). \quad (15)$$

It should also be emphasized that this analytical method, based on finding the integral of motion, makes it possible to predict the optimal frequency detuning without solving the system of Equation 10. Equation 15 is explicitly confirmed by the numerically calculated 2D probability distribution of the excitation of different transmon states shown in Figure 3 in dependence on frequency detuning and time.

A very well-pronounced maximum of the probability is found at optimal frequency detuning at each of the three presented distributions. It is important to note that Equation 15 is valid and can also be applied in the case of any intermediate transmon state, but in this case the characteristic peak width for the level population can be large enough to lead to some overlapping and interference patterns in the distribution (see Figure 3a,b). Physically, these lateral peaks occur in other settings when not only the desired state is involved in the excitation, but also some other neighbors. In this case, the average interaction energy in Equation 14 becomes non-zero, providing a different energy

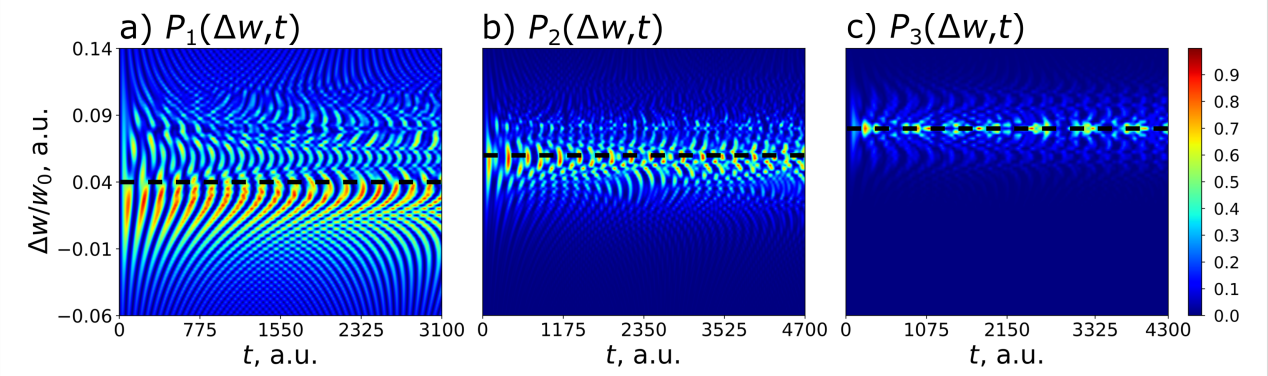


Figure 3: Distribution (colored) of the probability of transmon state excitation versus time of (a) the first, (b) the second, and (c) the third of the transmon states at $g = 0.025\omega_0$ and $\gamma = -0.02\omega_0$ as a function of the frequency detuning $\Delta\omega$ for the initial state $\psi_{in} = |0\rangle_b |3\rangle_a$. The horizontal black dashed lines correspond to the theoretical values of the detuning $\Delta\omega_{opt_n}$ obtained from Equation 15. As the transmon levels n increase, the theoretical detuning match the maximum detunings from numerical simulations $\Delta\omega_n$.

state that leads to additional preferred values of the frequency detuning.

To demonstrate more precisely the possibility of highly efficient excitation of any transmon state "on demand" by frequency detuning, we calculate the time-dependent populations of transmon levels at optimal points. The results are shown in Figure 4. In the resonance case (Figure 4a), the excitation of high-energy transmon states is strongly suppressed due to significant influence of the Kerr nonlinearity ($K = 9.6$). However, it is clearly seen that the frequency adjustments found by Equation 15 for the first (Figure 4b), second (Figure 4c), and third (Figure 4d) Fock states are indeed optimal values, providing increased excitation of the considered states. The effect of possible maximum excitation is especially pronounced for the highest transmon level when all the input energy of the quantum field is transferred to the superconducting subsystem. Thus, the optimal frequency detuning allows one to overcome the suppression of excitation induced by strong nonlinearity and to achieve a periodically maximum population of a certain transmon state "on demand".

Quantum circuit design

The optimal frequency detuning opens the possibility to achieve maximum excitation of a certain transmon state even under strong nonlinearity. In practice, however, the case where K is close to unity may be strongly demanded. This regime corresponds to a rather strong coupling between the transmon and the quantum field and can be attractive due to the possibility of much faster transmon dynamics. Moreover, as will be discussed below, the experimental control of the excitation is much easier in this case. This regime is difficult to achieve in traditional qubit-based experiments, where everyone deals with the weak coupling regime when $g/2\pi \approx 10$ MHz and $\gamma/2\pi \approx -100$ MHz. Devoret et al. [49] showed that the coupling of the JJ system with the resonator can be significantly enhanced by placing it in the gap of the central conductor of the coplanar waveguide. In this case, the JJ system will interact directly with the current (magnetic field) in the cavity, and the coupling strength will change from $g/\omega_0 \approx \sqrt{\alpha}$ to $g/\omega_0 \approx 1/\sqrt{\alpha}$, where α is a fine structure constant. This case corresponds to the so-called "ultrastrong coupling regime" [50,51], which is beyond the scope of this article.

Later, it was shown that this system is inconvenient for practical implementation because the low nonlinearity of $E_C/h \approx 5$ MHz and the huge intrinsic capacitance of JJ $C_J \approx 4$ pF are difficult to achieve. The reason was that the JJ system was located in the center of the resonator and inductive coupling prevailed. The problem can be solved by using the so-called "in-line transmon" design, that is, one should move the JJ system closer to the edge of the resonator in the area of the maximum voltage in the standing wave, where capacitive coupling will be implemented. At the same time, the value of the coupling strength will decrease, but will still remain quite large in comparison to the characteristic nonlinearity, that is, $E_C/h \approx 300$ MHz [52,53].

In this article, we turned this concept into a realistic design to demonstrate the experimental feasibility of the proposed qudit control with microwave photons. In our case, the characteristic magnitude of the nonlinearity $\gamma/2\pi = -E_C/2h = -100$ MHz is directly proportional to the charge energy E_C of the transmon, which is determined by the capacitance of the remaining part of the resonator $l_q = 549$ μm (Figure 5, the red part of the resonator). The coupling strength can be estimated as:

$$\frac{g}{2\pi} = \sqrt{\frac{2\pi Z_0 \alpha}{Z_{vac}}} \left(\frac{E_J}{2E_C}\right)^{\frac{1}{4}} \frac{\omega_p}{2\pi}, \qquad (16)$$

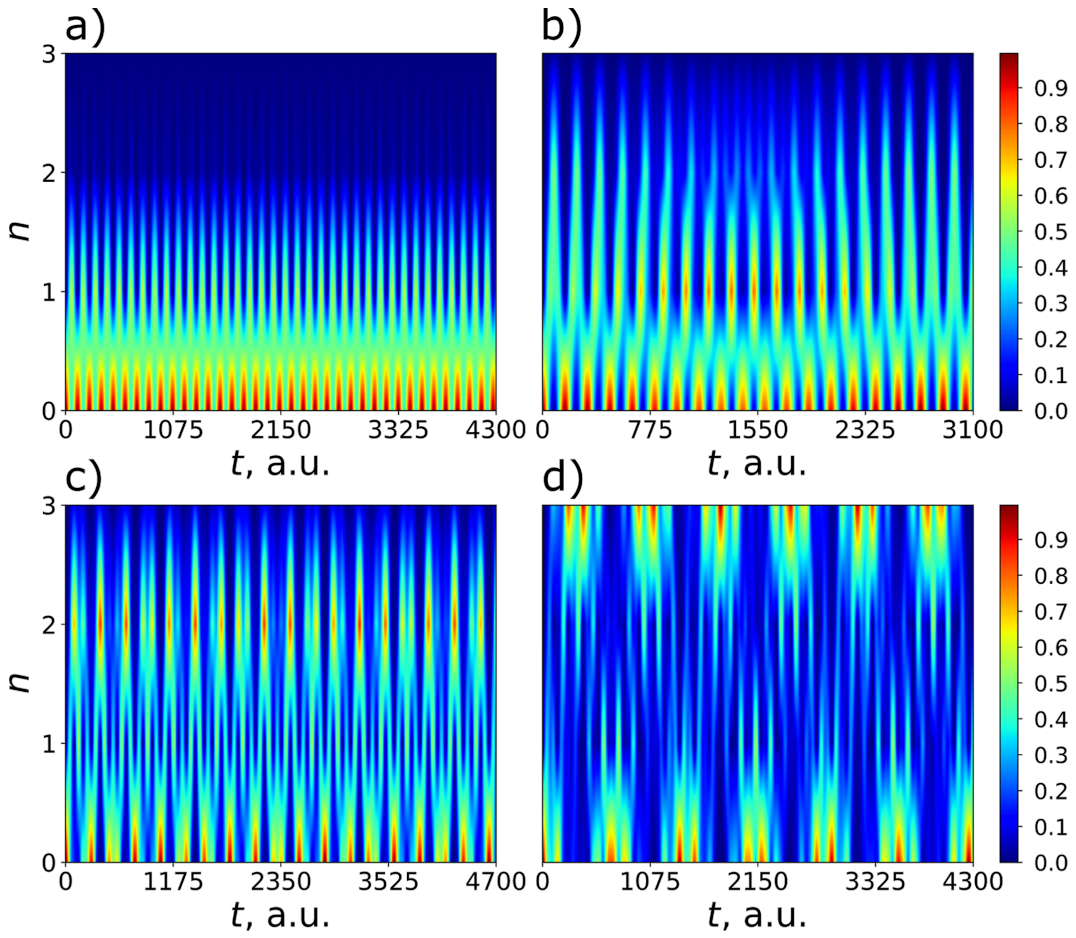


Figure 4: Distribution (colored) of the probability of transmon state excitation versus time, obtained in the case of the initial state $\psi_{in} = |0\rangle_b |3\rangle_a$ in the regime with predominant nonlinear interaction (K = 9.6) for $g = 0.025\omega_0$ and $\gamma = -0.02\omega_0$. Panel (a) corresponds to the resonant case at $\Delta\omega = 0$, panel (b) corresponds to the optimal frequency for efficient population of the first state $\Delta\omega = 0.04\omega_0$, panel (c) corresponds to the optimal frequency for efficient population of the second state $\Delta\omega = 0.06\omega_0$, and panel (d) corresponds to the optimal frequency for efficient population of the third state $\Delta\omega = 0.08\omega_0$.

and it will vary depending on the external magnetic flux ($E_J(\Phi_{ext})$ and $\omega_p/2\pi(\Phi_{ext})$). Here, $Z_{vac} \approx 377\ \Omega$ and $Z_0 = 50\ \Omega$. Taking this expression into account, at a typical plasma transmon frequency of $\omega_p/2\pi$ = 5–6 GHz, the coupling strength will be $g/2\pi \approx 1.2$ GHz, and efficient state control of the qudit will be possible for low-energy levels, n = 1–3.

Switching between effectively populated states is carried out when an external magnetic flux Φ_{ext} is applied to the interferometer, taking into account the condition $\Delta\omega_{opt_n} = -\gamma(n+1)$ (Figure 6). The tuning of the plasma frequency is regulated by the interferometric arm asymmetry, and the values of E_J determine the magnitude of the critical current and the area of each JJ: $I_{c1} \approx 39.44$ nA, $S_1 = 200 \times 197$ nm^2, $I_{c2} \approx 22.21$ nA, and $S_2 = 149 \times 149$ nm^2, with the usual critical current density of j = 1 μA·μm^{-2}. The frequency of the resonator was chosen to be $\omega_0/2\pi$ = 5.348 GHz to provide simultaneously strong coupling with the quantum field and optimal detuning from the resonance. In addition, this frequency determines the total length of the system, that is, $2l$ = 11.101 mm.

Let us discuss the limitations on the values of the physical parameters in this scheme. First of all, the following relation between Josephson and charge energies should be satisfied: $E_J \gg E_C$, provided in our design by the ratio $E_J/E_C \approx 100$, which correlates well with the chosen type of superconducting artificial atom. The second constraint $C_J \ll C_s = l_q C^0 \ll 2lC^0$ is also satisfied (the capacity of JJ can be estimated as $C_J = \varepsilon\varepsilon_0 S/d$, ε = 10, and d = 2 nm for an AlO_x film).

This implementation has a number of significant drawbacks; the system takes up a lot of space on the chip, and the impedance matching for the JJ system and the resonator is a problem. Nevertheless, for this discussed in-line transmon design, all

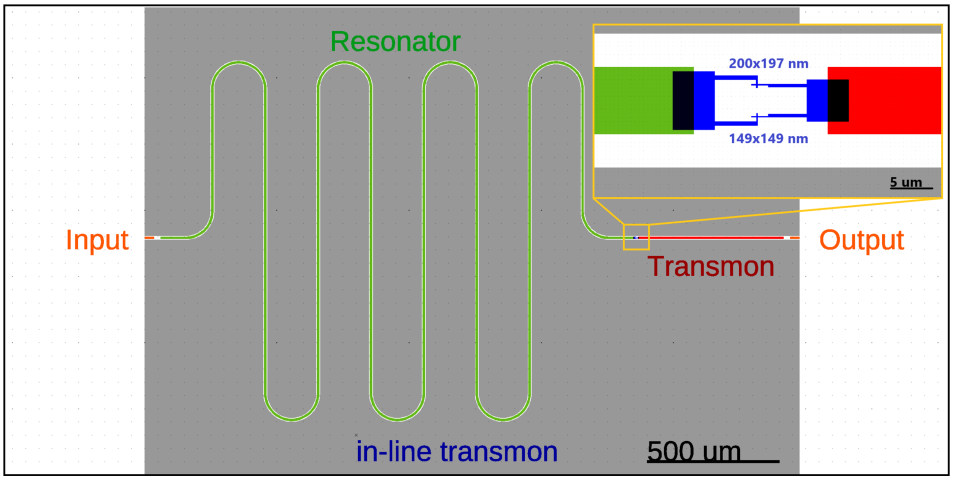


Figure 5: In-line transmon design for efficient transmission of the quantum state. The red part of the central conductor of the resonator and the blue SQUID form a transmon, the total length of the resonator (green and red parts) forms the main resonant mode ω_0.

necessary parameters are calculated and values of the coupling strength g corresponding to the optimal transmon frequencies predicted by Equation 15 and providing the most efficient excitation are found for the four lowest transmon states. For each considered transmon state, its population is numerically calculated as a function of frequency detuning and time at the found coupling strength to confirm the designed optimal frequency condition. The results are shown in Figure 7 and Table 1; they obviously prove that the optimal detuning providing maximum excitation of each state explicitly coincides with the value obtained in the designed scheme according to Equation 15 by varying the external magnetic flux and represented by four pink vertical lines in Figure 6 with corresponding numbers.

Moreover, it can be easily seen that the control of states is very rapid and can be performed on the sub-nanosecond time scale. Indeed, Figure 8 demonstrates the time-dependent probability of excitation of considered transmon states calculated for each

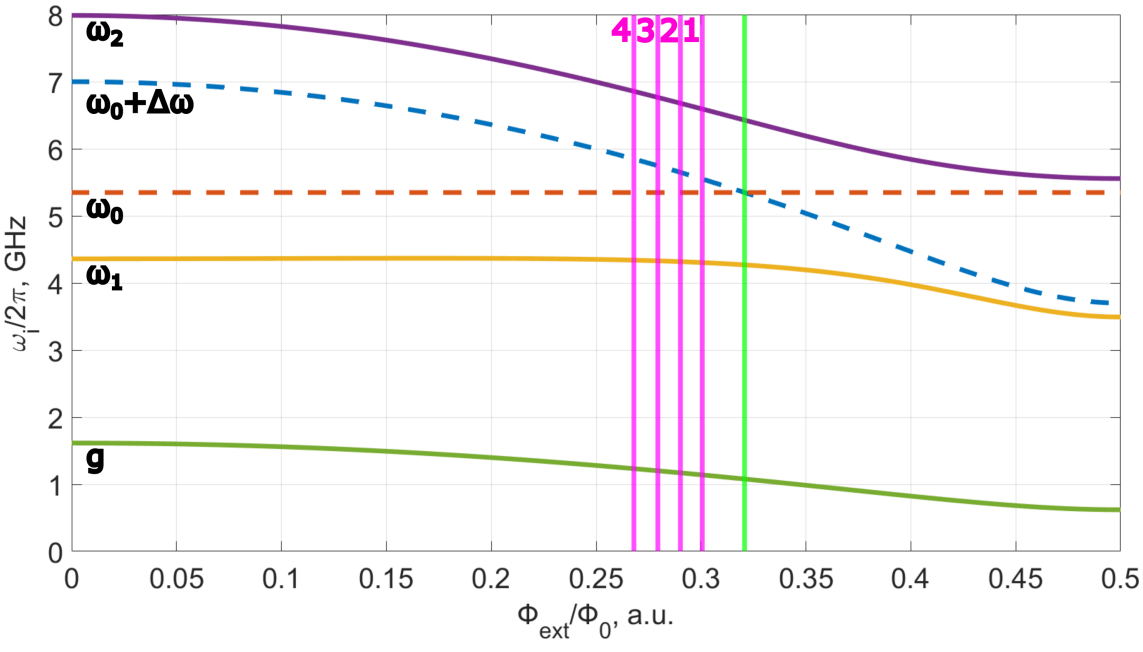


Figure 6: The dependence of the plasma frequency of the qudit $\omega_p = \omega_0 + \Delta\omega$ and coupling strength g between this two systems on the external magnetic flux Φ_{ext}. When these two systems are connected, the united system with two modes ω_1 and ω_2 appears. Anticrossing at the point when the frequencies of the two systems coincide corresponds to the green vertical line.

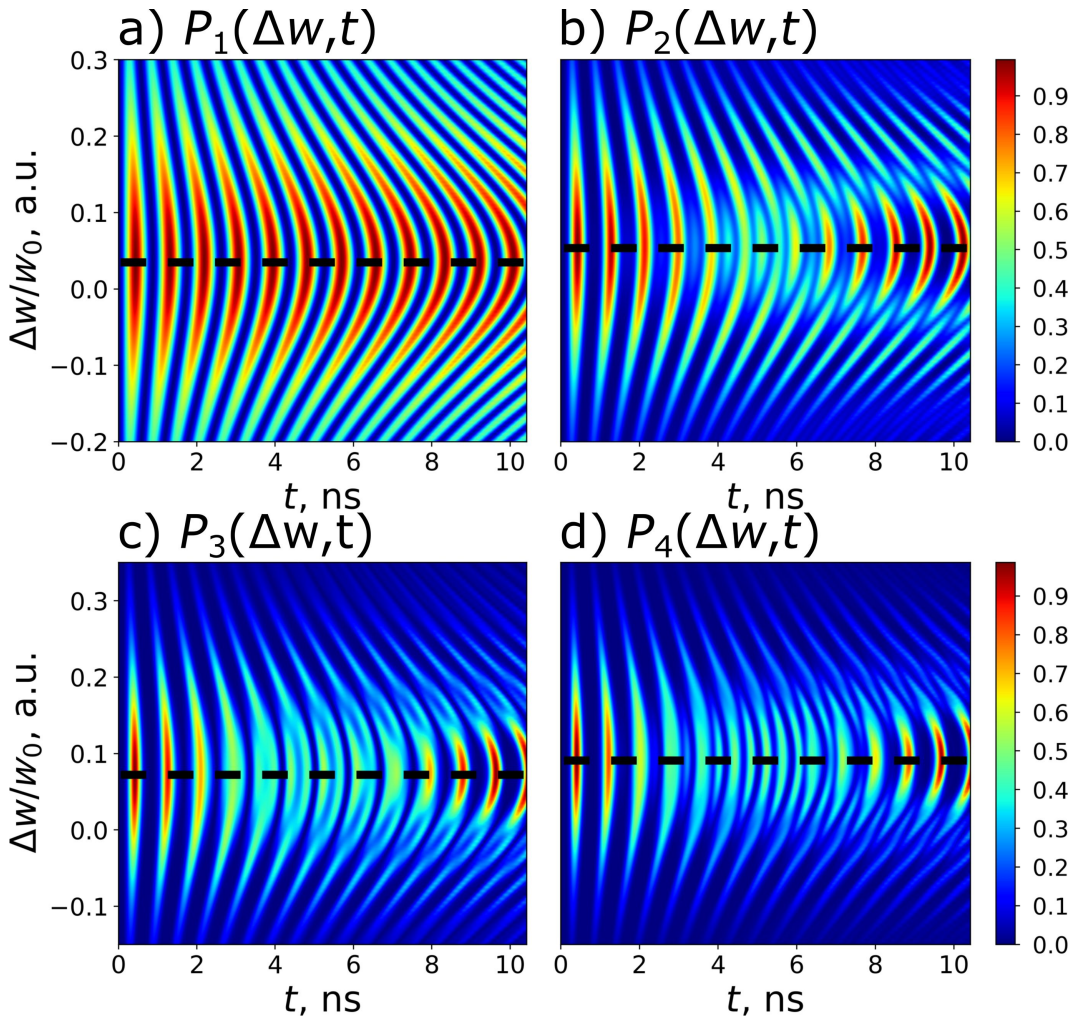


Figure 7: 2D distributions of the populations of states with n = 1–4 of the designed transmon with nonlinearity $\gamma = -0.0187\omega_0$ calculated in dependence on frequency detuning and time at certain values of the coupling strength specific for each considered state: (a) $g = 0.213\omega_0$, (b) $g = 0.219\omega_0$, (c) $g = 0.225\omega_0$, and (d) $g = 0.231\omega_0$. $k_0 = 4$ photons are chosen to be initially in the quantum field mode. The horizontal black dashed lines correspond to the theoretical values of the detuning (Equation 15), which is close enough to the numerical calculation results, see Table 1 for details.

Table 1: Comparison of theoretical detuning $\Delta\omega_{opt_n} / \omega_0$ with detuning $\Delta\omega_n$ obtained from numerical simulations.

n	1	2	3	4
$\Delta\omega_n / \omega_0$, a.u.	0.0374	0.0561	0.0748	0.0935
$\Delta\omega_{opt_n}$, a.u.	0.035	0.055	0.075	0.095

state at its own optimal detuning. The obtained results demonstrate a very fast excitation with probability equal to unity achieved for each state of the designed transmon-based qudit, even for the highest one (Table 2). Thus, the strong-coupling regime appears to be very advantageous for the rapid subnanosecond control of the designed transmon-based qudit. In this case a very fine tuning to the optimal frequency can be performed by varying the applied magnetic flux.

Conclusion

In this work, a fast, simple, and precise control of the population of an artificial atom is implemented theoretically using microwave photons (Fock states of the resonator). It is important to emphasize that, by adjusting the frequency of the nonlinear oscillator (qudit) from the linear resonator mode, we can choose which level of the solid-state subsystem is efficiently populated. Due to the nonlinearity, an efficient excitation of highly excited transmon states seems to be a challenging problem. It may be possible to excite this system “step by step” by choosing the appropriate frequency of the classical field for each stage, as was done in [54]. However, this procedure

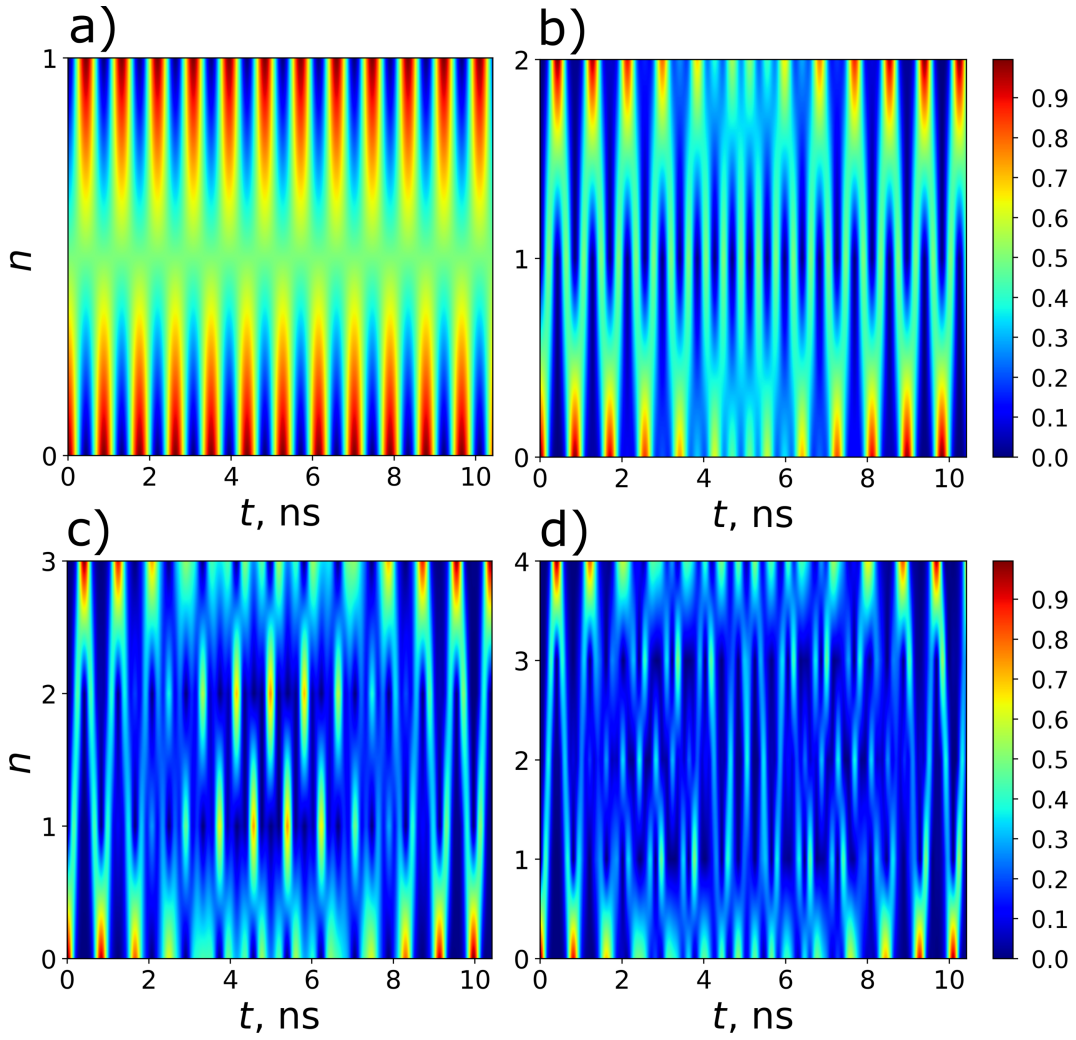


Figure 8: A demonstration of the rapid control of the states with n = 1–4 of the designed transmon (from (a) to (d), respectively). The panels show the time-dependent population of transmon states at the selected optimal frequency detuning. The parameters for each panel are the same as for the corresponding panels in Figure 7.

requires a rather complex experimental setup and takes a significant amount of time. For our particular system, we have identified and demonstrated the possibility of exciting a specific desired transmon state very quickly from the ground state (see Table 2 for details). We can significantly enhance the excitation of this specific transmon state by selecting an appropriate frequency detuning, whose value is determined analytically for each desired state. This phenomenon arises due to the interaction between nonlinearity and the coupling of quantum fields and cannot be observed when only classical fields are present.

Table 2: The maximum probability of excitation P_n of the states with n = 1–4 of the designed transmon during the time τ_n.

n	1	2	3	4
P_n, a.u.	0.999976	0.995518	0.987228	0.975867
τ_n, ns	0.438	0.427	0.417	0.405

In addition, we propose the quantum circuit design of a real superconducting scheme in which the predicted rapid control of transmon-based qudit can be demonstrated. It is important that, in a strong coupling regime, the efficient transitions in the transmon-based qudit occur on sub-nanosecond timescales [55,56]. Note that such times are not large in comparison to the decoherence process in the transmon-based qudit [29]. This circumstance makes it possible to design complex fully quantum hybrid "field + solid state" systems for quantum computing and developing a fully quantum interface between supercon-

ducting and photon platforms. Also, the developed transmon-based qudit can be used as an electromagnetic field detector, which allows one at least to determine the exact number of photons in the resonator.

Funding

The study of the basic element for quantum networking is supported by Ministry of Science and Higher Education of the Russian Federation (agreement No. 075-15-2024-538).

Author Contributions

Irina A. Solovykh: data curation; investigation; software; visualization; writing – review & editing. Andrey V. Pashchenko: formal analysis; investigation; software; visualization; writing – original draft. Natalya A. Maleeva: methodology; project administration; resources. Nikolay V. Klenov: conceptualization; methodology; validation; writing – original draft. Olga V. Tikhonova: conceptualization; data curation; investigation; methodology; writing – review & editing. Igor I. Soloviev: funding acquisition; project administration; supervision; validation.

ORCID® iDs

Irina A. Solovykh - https://orcid.org/0009-0006-2261-0055
Andrey V. Pashchenko - https://orcid.org/0000-0003-4859-6053
Nikolay V. Klenov - https://orcid.org/0000-0001-6265-3670
Olga V. Tikhonova - https://orcid.org/0000-0003-0229-5992
Igor I. Soloviev - https://orcid.org/0000-0001-9735-2720

Data Availability Statement

All data that supports the findings of this study is available in the published article and/or the supporting information of this article.

Preprint

A non-peer-reviewed version of this article has been previously published as a preprint: https://doi.org/10.3762/bxiv.2025.30.v1

References

1. Feynman, R. P. *Found. Phys.* **1986,** *16,* 507–531. doi:10.1007/bf01886518
2. Orús, R.; Mugel, S.; Lizaso, E. *Rev. Phys.* **2019,** *4,* 100028. doi:10.1016/j.revip.2019.100028
3. Kiktenko, E. O.; Pozhar, N. O.; Anufriev, M. N.; Trushechkin, A. S.; Yunusov, R. R.; Kurochkin, Y. V.; Lvovsky, A. I.; Fedorov, A. K. *Quantum Sci. Technol.* **2018,** *3,* 035004. doi:10.1088/2058-9565/aabc6b
4. Zhao, L.; Zhao, Z.; Rebentrost, P.; Fitzsimons, J. *Quantum Mach. Intell.* **2021,** *3,* 21. doi:10.1007/s42484-021-00048-8
5. Guseynov, N. M.; Zhukov, A. A.; Pogosov, W. V.; Lebedev, A. V. *Phys. Rev. A* **2023,** *107,* 052422. doi:10.1103/physreva.107.052422
6. Vozhakov, V. A.; Bastrakova, M. V.; Klenov, N. V.; Soloviev, I. I.; Pogosov, W. V.; Babukhin, D. V.; Zhukov, A. A.; Satanin, A. M. *Usp. Fiz. Nauk* **2022,** *192,* 457–476. doi:10.3367/ufnr.2021.02.038934
7. Shnyrkov, V. I.; Soroka, A. A.; Turutanov, O. G. *Phys. Rev. B* **2012,** *85,* 224512. doi:10.1103/physrevb.85.224512
8. Blok, M. S.; Ramasesh, V. V.; Schuster, T.; O'Brien, K.; Kreikebaum, J. M.; Dahlen, D.; Morvan, A.; Yoshida, B.; Yao, N. Y.; Siddiqi, I. *Phys. Rev. X* **2021,** *11,* 021010. doi:10.1103/physrevx.11.021010
9. Seifert, L. M.; Li, Z.; Roy, T.; Schuster, D. I.; Chong, F. T.; Baker, J. M. *Phys. Rev. A* **2023,** *108,* 062609. doi:10.1103/physreva.108.062609
10. Kiktenko, E. O.; Nikolaeva, A. S.; Xu, P.; Shlyapnikov, G. V.; Fedorov, A. K. *Phys. Rev. A* **2020,** *101,* 022304. doi:10.1103/physreva.101.022304
11. Liu, P.; Wang, R.; Zhang, J.-N.; Zhang, Y.; Cai, X.; Xu, H.; Li, Z.; Han, J.; Li, X.; Xue, G.; Liu, W.; You, L.; Jin, Y.; Yu, H. *Phys. Rev. X* **2023,** *13,* 021028. doi:10.1103/physrevx.13.021028
12. Nikolaeva, A. S.; Kiktenko, E. O.; Fedorov, A. K. *EPJ Quantum Technol.* **2024,** *11,* 43. doi:10.1140/epjqt/s40507-024-00250-0
13. Wehner, S.; Elkouss, D.; Hanson, R. *Science* **2018,** *362,* eaam9288. doi:10.1126/science.aam9288
14. Cacciapuoti, A. S.; Caleffi, M.; Tafuri, F.; Cataliotti, F. S.; Gherardini, S.; Bianchi, G. *IEEE Network* **2020,** *34,* 137–143. doi:10.1109/mnet.001.1900092
15. Kumar, S.; Lauk, N.; Simon, C. *Quantum Sci. Technol.* **2019,** *4,* 045003. doi:10.1088/2058-9565/ab2c87
16. Ang, J.; Carini, G.; Chen, Y.; Chuang, I.; Demarco, M.; Economou, S.; Eickbusch, A.; Faraon, A.; Fu, K.-M.; Girvin, S.; Hatridge, M.; Houck, A.; Hilaire, P.; Krsulich, K.; Li, A.; Liu, C.; Liu, Y.; Martonosi, M.; McKay, D.; Misewich, J.; Ritter, M.; Schoelkopf, R.; Stein, S.; Sussman, S.; Tang, H.; Tang, W.; Tomesh, T.; Tubman, N.; Wang, C.; Wiebe, N.; Yao, Y.; Yost, D.; Zhou, Y. *ACM Trans. Quantum Comput.* **2024,** *5,* 1–59. doi:10.1145/3674151
17. Zhou, Y.; Peng, Z.; Horiuchi, Y.; Astafiev, O. V.; Tsai, J. S. *Phys. Rev. Appl.* **2020,** *13,* 034007. doi:10.1103/physrevapplied.13.034007
18. Vozhakov, V.; Bastrakova, M.; Klenov, N.; Satanin, A.; Soloviev, I. *Quantum Sci. Technol.* **2023,** *8,* 035024. doi:10.1088/2058-9565/acd9e6
19. Pogosov, W. V.; Dmitriev, A. Y.; Astafiev, O. V. *Phys. Rev. A* **2021,** *104,* 023703. doi:10.1103/physreva.104.023703
20. Elistratov, A. A.; Remizov, S. V.; Pogosov, W. V.; Dmitriev, A. Yu.; Astafiev, O. V. *arXiv* **2023,** 2309.01444. doi:10.48550/arxiv.2309.01444
21. Zakharov, R. V.; Tikhonova, O. V.; Klenov, N. V.; Soloviev, I. I.; Antonov, V. N.; Yakovlev, D. S. *Adv. Quantum Technol.* **2024,** *7,* 2400141. doi:10.1002/qute.202400141
22. Pankratov, A. L.; Gordeeva, A. V.; Revin, L. S.; Ladeynov, D. A.; Yablokov, A. A.; Kuzmin, L. S. *Beilstein J. Nanotechnol.* **2022,** *13,* 582–589. doi:10.3762/bjnano.13.50
23. Chiarello, F.; Alesini, D.; Babusci, D.; Barone, C.; Beretta, M. M.; Buonomo, B.; D'Elia, A.; Gioacchino, D. D.; Felici, G.; Filatrella, G.; Foggetta, L. G.; Gallo, A.; Gatti, C.; Ligi, C.; Maccarrone, G.; Mattioli, F.; Pagano, S.; Piersanti, L.; Rettaroli, A.; Tocci, S.; Torrioli, G. *IEEE Trans. Appl. Supercond.* **2022,** *32,* 1–5. doi:10.1109/tasc.2022.3148693
24. Vasenko, A. S.; Hekking, F. W. J. *J. Low Temp. Phys.* **2009,** *154,* 221–232. doi:10.1007/s10909-009-9869-z
25. Ozaeta, A.; Vasenko, A. S.; Hekking, F. W. J.; Bergeret, F. S. *Phys. Rev. B* **2012,** *86,* 060509. doi:10.1103/physrevb.86.060509
26. Ozaeta, A.; Vasenko, A. S.; Hekking, F. W. J.; Bergeret, F. S. *Phys. Rev. B* **2012,** *85,* 174518. doi:10.1103/physrevb.85.174518

27. Koch, J.; Yu, T. M.; Gambetta, J.; Houck, A. A.; Schuster, D. I.; Majer, J.; Blais, A.; Devoret, M. H.; Girvin, S. M.; Schoelkopf, R. J. *Phys. Rev. A* **2007,** *76,* 042319. doi:10.1103/physreva.76.042319
28. Roth, T. E.; Ma, R.; Chew, W. C. *IEEE Antennas Propag. Mag.* **2023,** *65,* 8–20. doi:10.1109/map.2022.3176593
29. Wang, Z.; Parker, R. W.; Champion, E.; Blok, M. S. *Phys. Rev. Appl.* **2025,** *23,* 034046. doi:10.1103/physrevapplied.23.034046
30. Kristen, M.; Schneider, A.; Stehli, A.; Wolz, T.; Danilin, S.; Ku, H. S.; Long, J.; Wu, X.; Lake, R.; Pappas, D. P.; Ustinov, A. V.; Weides, M. *npj Quantum Inf.* **2020,** *6,* 57. doi:10.1038/s41534-020-00287-w
31. Houck, A. A.; Schreier, J. A.; Johnson, B. R.; Chow, J. M.; Koch, J.; Gambetta, J. M.; Schuster, D. I.; Frunzio, L.; Devoret, M. H.; Girvin, S. M.; Schoelkopf, R. J. *Phys. Rev. Lett.* **2008,** *101,* 080502. doi:10.1103/physrevlett.101.080502
32. Place, A. P. M.; Rodgers, L. V. H.; Mundada, P.; Smitham, B. M.; Fitzpatrick, M.; Leng, Z.; Premkumar, A.; Bryon, J.; Vrajitoarea, A.; Sussman, S.; Cheng, G.; Madhavan, T.; Babla, H. K.; Le, X. H.; Gang, Y.; Jäck, B.; Gyenis, A.; Yao, N.; Cava, R. J.; de Leon, N. P.; Houck, A. A. *Nat. Commun.* **2021,** *12,* 1779. doi:10.1038/s41467-021-22030-5
33. Wang, C.; Li, X.; Xu, H.; Li, Z.; Wang, J.; Yang, Z.; Mi, Z.; Liang, X.; Su, T.; Yang, C.; Wang, G.; Wang, W.; Li, Y.; Chen, M.; Li, C.; Linghu, K.; Han, J.; Zhang, Y.; Feng, Y.; Song, Y.; Ma, T.; Zhang, J.; Wang, R.; Zhao, P.; Liu, W.; Xue, G.; Jin, Y.; Yu, H. *npj Quantum Inf.* **2022,** *8,* 3. doi:10.1038/s41534-021-00510-2
34. Lvov, D. S.; Lemziakov, S. A.; Ankerhold, E.; Peltonen, J. T.; Pekola, J. P. *Phys. Rev. Appl.* **2025,** *23,* 054079. doi:10.1103/physrevapplied.23.054079
35. Rol, M. A.; Ciorciaro, L.; Malinowski, F. K.; Tarasinski, B. M.; Sagastizabal, R. E.; Bultink, C. C.; Salathe, Y.; Haandbaek, N.; Sedivy, J.; DiCarlo, L. *Appl. Phys. Lett.* **2020,** *116,* 054001. doi:10.1063/1.5133894
36. Houck, A. A.; Koch, J.; Devoret, M. H.; Girvin, S. M.; Schoelkopf, R. J. *Quantum Inf. Process.* **2009,** *8,* 105–115. doi:10.1007/s11128-009-0100-6
37. Hofheinz, M.; Weig, E. M.; Ansmann, M.; Bialczak, R. C.; Lucero, E.; Neeley, M.; O'Connell, A. D.; Wang, H.; Martinis, J. M.; Cleland, A. N. *Nature* **2008,** *454,* 310–314. doi:10.1038/nature07136
38. Hofheinz, M.; Wang, H.; Ansmann, M.; Bialczak, R. C.; Lucero, E.; Neeley, M.; O'Connell, A. D.; Sank, D.; Wenner, J.; Martinis, J. M.; Cleland, A. N. *Nature* **2009,** *459,* 546–549. doi:10.1038/nature08005
39. Peng, Z. H.; de Graaf, S. E.; Tsai, J. S.; Astafiev, O. V. *Nat. Commun.* **2016,** *7,* 12588. doi:10.1038/ncomms12588
40. Zhao, Y.-J.; Wang, C.; Zhu, X.; Liu, Y.-x. *Sci. Rep.* **2016,** *6,* 23646. doi:10.1038/srep23646
41. Dmitriev, A. Y.; Shaikhaidarov, R.; Antonov, V. N.; Hönigl-Decrinis, T.; Astafiev, O. V. *Nat. Commun.* **2017,** *8,* 1352. doi:10.1038/s41467-017-01471-x
42. Dmitriev, A. Y.; Shaikhaidarov, R.; Hönigl-Decrinis, T.; de Graaf, S. E.; Antonov, V. N.; Astafiev, O. V. *Phys. Rev. A* **2019,** *100,* 013808. doi:10.1103/physreva.100.013808
43. Blais, A.; Grimsmo, A. L.; Girvin, S. M.; Wallraff, A. *Rev. Mod. Phys.* **2021,** *93,* 025005. doi:10.1103/revmodphys.93.025005
44. Popolitova, D. V.; Tikhonova, O. V. *Laser Phys. Lett.* **2019,** *16,* 125301. doi:10.1088/1612-202x/ab570b
45. Tikhonova, O. V.; Vasil'ev, A. N. *J. Phys.: Condens. Matter* **2023,** *35,* 115301. doi:10.1088/1361-648x/acaf1f
46. Johansson, J.; Saito, S.; Meno, T.; Nakano, H.; Ueda, M.; Semba, K.; Takayanagi, H. *Phys. Rev. Lett.* **2006,** *96,* 127006. doi:10.1103/physrevlett.96.127006
47. Claudon, J.; Zazunov, A.; Hekking, F. W. J.; Buisson, O. *Phys. Rev. B* **2008,** *78,* 184503. doi:10.1103/physrevb.78.184503
48. Shevchenko, S. N.; Omelyanchouk, A. N.; Zagoskin, A. M.; Savel'ev, S.; Nori, F. *New J. Phys.* **2008,** *10,* 073026. doi:10.1088/1367-2630/10/7/073026
49. Devoret, M. H.; Girvin, S.; Schoelkopf, R. *Ann. Phys. (Berlin, Ger.)* **2007,** *519,* 767–779. doi:10.1002/andp.200751910-1109
50. Andersen, C. K.; Blais, A. *New J. Phys.* **2017,** *19,* 023022. doi:10.1088/1367-2630/aa5941
51. Frisk Kockum, A.; Miranowicz, A.; De Liberato, S.; Savasta, S.; Nori, F. *Nat. Rev. Phys.* **2019,** *1,* 19–40. doi:10.1038/s42254-018-0006-2
52. Bourassa, J.; Beaudoin, F.; Gambetta, J. M.; Blais, A. *Phys. Rev. A* **2012,** *86,* 013814. doi:10.1103/physreva.86.013814
53. Hyyppä, E.; Kundu, S.; Chan, C. F.; Gunyhó, A.; Hotari, J.; Janzso, D.; Juliusson, K.; Kiuru, O.; Kotilahti, J.; Landra, A.; Liu, W.; Marxer, F.; Mäkinen, A.; Orgiazzi, J.-L.; Palma, M.; Savytskyi, M.; Tosto, F.; Tuorila, J.; Vadimov, V.; Li, T.; Ockeloen-Korppi, C.; Heinsoo, J.; Tan, K. Y.; Hassel, J.; Möttönen, M. *Nat. Commun.* **2022,** *13,* 6895. doi:10.1038/s41467-022-34614-w
54. Peterer, M. J.; Bader, S. J.; Jin, X.; Yan, F.; Kamal, A.; Gudmundsen, T. J.; Leek, P. J.; Orlando, T. P.; Oliver, W. D.; Gustavsson, S. *Phys. Rev. Lett.* **2015,** *114,* 010501. doi:10.1103/physrevlett.114.010501
55. Klenov, N. V.; Kuznetsov, A. V.; Soloviev, I. I.; Bakurskiy, S. V.; Tikhonova, O. V. *Beilstein J. Nanotechnol.* **2015,** *6,* 1946–1956. doi:10.3762/bjnano.6.199
56. Bastrakova, M.; Klenov, N.; Ruzhickiy, V.; Soloviev, I.; Satanin, A. *Supercond. Sci. Technol.* **2022,** *35,* 055003. doi:10.1088/1361-6668/ac5505

License and Terms

This is an open access article licensed under the terms of the Beilstein-Institut Open Access License Agreement (https://www.beilstein-journals.org/bjnano/terms), which is identical to the Creative Commons Attribution 4.0 International License (https://creativecommons.org/licenses/by/4.0). The reuse of material under this license requires that the author(s), source and license are credited. Third-party material in this article could be subject to other licenses (typically indicated in the credit line), and in this case, users are required to obtain permission from the license holder to reuse the material.

The definitive version of this article is the electronic one which can be found at:
https://doi.org/10.3762/bjnano.16.112

BEILSTEIN JOURNAL OF NANOTECHNOLOGY

Energy spectrum and quantum phase transition of the coupled single spin and an infinitely coordinated Ising chain

Seidali Seidov*[1,2], Natalia Pugach[1] and Anatolie Sidorenko[3,4]

Full Research Paper

Open Access

Address:
[1]HSE University, Moscow, Russia, [2]NUST MISIS, Moscow, Russia, [3]Technical University of Moldova, Institute of Electronic Engineering and Nanotechnologies, Republic of Moldova and [4]Moscow Institute of Physics and Technology, Dolgoprudny, Russia

Email:
Seidali Seidov* - alikseidov@yandex.ru

* Corresponding author

Keywords:
Ising chain; Lipkin–Meshkov–Glick model; quantum phase transitions

Beilstein J. Nanotechnol. **2025,** *16,* 1668–1676.
https://doi.org/10.3762/bjnano.16.117

Received: 29 April 2025
Accepted: 22 August 2025
Published: 24 September 2025

This article is part of the thematic issue "Superconducting artificial neural networks and quantum circuits".

Associate Editor: J. M. van Ruitenbeek

© 2025 Seidov et al.; licensee Beilstein-Institut.
License and terms: see end of document.

Abstract

In this work we consider a spin model composed of a single spin and connected to an infinitely coordinated Ising chain. Theoretical models of this type arise from various fields of theoretical physics, such as theory of open systems, quantum control, and quantum computations. In the thermodynamic limit of an infinite chain, we map the chain Hamiltonian to the Hamiltonian of the Lipkin–Meshkov–Glik model, and the system as a whole is described by a generalized Rabi Hamiltonian. Next, the effective Hamiltonian is obtained using the Foulton–Gouterman transformation. In the thermodynamic limit we obtain the spectrum of the whole system and study the properties of the ground-state quantum phase transition.

Introduction

In the present manuscript, we consider a single spin connected to an infinitely coordinated Ising chain. From a purely theoretical point of view, this model arises when studying the physics of open systems [1,2]. In this case, the chain is modelling the external environment to which the single spin is connected. In such models, it is convenient to study not only Markovian dynamics of the single spin, but also non-Markovian dynamics going beyond the limitations of the Lindblad master equation [3-6]. The approach is to find the dynamics of the whole system (i.e., the chain and the single spin) and then trace out the chain degrees of freedom, ending up with the master equation for the single-spin density matrix. One might choose to make or not to make the Markov approximation, obtaining different types of master equations. Given that the exact solution is known, different master equation solutions can be compared against it. This allows to study the limits of applicability of the Markovian approximation, and also the correct way of introducing the Lindblad dissipation operators. These problems remain important in the general field of open quantum systems, extending beyond spin models [7-9].

One of the practical applications is modelling of certain quantum computing layouts, if one considers spins as qubits. In particular, we have previously proposed a method for implementing a CCZ (control–control–Z) quantum gate on a system composed of three logical qubits, which are connected to another coupler qubit [10]. This approach allows to increase the fidelity of the operation, and it has technical benefits such as simplicity of calibration and suppression of the unwanted longitudinal ZZ interaction. One of the important quantities is the shift of the coupler qubits energy levels depending on the state of the logical qubits. In the present manuscript, we find the energy levels of such system in the limit of infinitely many logical qubits, and find the energy spectrum of the coupler qubit depending on the state of the logical qubits ensemble.

We start our theoretical analysis by mapping the Ising chain Hamiltonian to a Lipkin– Meshkov–Glik (LMG) Hamiltonian [11-13]. The Hamiltonian of the whole system then becomes akin to the Hamiltonian of the generalized Rabi model, but with the bosonic field replaced by the collective spin of the LMG model. Next, it is diagonalized in the spin space using the Fulton–Gouterman transformation and we obtain an effective Hamiltonian. In the limit of infinite Ising chain, or equivalently of the infinite total spin, the LMG Hamiltonian can be solved exactly. We exploit this fact and analytically obtain the energy spectrum of the whole system. Based on this result, we study the structure of the extrema of the ground state energy and the consequent properties of different phases of the system.

Model

We consider a single spin coupled to a fully connected Ising chain with the Hamiltonian

$$\begin{aligned} H &= \frac{\omega}{2}\tau_z + \frac{\Delta}{2}\tau_x + H_{\text{chain}} + H_{\text{int}} \\ H_{\text{chain}} &= \frac{1}{2}\sum_{i=1}^{N}\left(\tilde{\omega}\sigma_z^i + \tilde{\Delta}\sigma_x^i\right) + \frac{J}{4N}\sum_{i\neq j}^{N}\sigma_z^i\sigma_z^j \\ H_{\text{int}} &= \frac{\tilde{J}}{2}\tau_z\sum_{i=1}^{N}\sigma_z^i. \end{aligned} \tag{1}$$

Here, $\tau_{x,z}$ are the Pauli matrices describing the single spin, and $\sigma_{x,z}^i$ are the Pauli matrices describing spins in the Ising chain. This model arises when one studies spin-bath theoretical models in studies of quantum control and design of qubit layouts in quantum computation. The coupling between the spins in the chain is rescaled by $1/N$ factor in order to obtain a finite energy per spin $\langle H\rangle/N$ in the thermodynamic limit.

Let us first consider the Hamiltonian $H_{\text{chain}} + H_{\text{int}}$. By introducing collective spin operators

$$S_{x,z} = \frac{1}{2}\sum_{i=1}^{N}\sigma_{x,z}^i \tag{2}$$

the Hamiltonian is brought in the following form [14,15]:

$$H_{\text{chain}} + H_{\text{int}} = \left(\tilde{\omega} + \frac{\tilde{J}}{2}\tau_z\right)S_z + \tilde{\Delta}S_x + \frac{J}{2S}S_z^2. \tag{3}$$

Here, $S = N/2$ is the total spin of the chain. This is a well-known Lipkin–Meshkov–Glick (LMG) Hamiltonian which we will further denote as $H_{\text{LMG}} = H_{\text{chain}} + H_{\text{int}}$. The total Hamiltonian now can be written as a 2×2 block matrix in the single-spin Hilbert space:

$$H = \frac{1}{2}\begin{pmatrix}\omega & \Delta \\ \Delta & -\omega\end{pmatrix} + \begin{pmatrix}H_{\text{LMG}}^{+} & 0 \\ 0 & H_{\text{LMG}}^{-}\end{pmatrix}. \tag{4}$$

Here $H_{\text{LMG}}^{\pm}$ are the Hamiltonians H_{LMG} corresponding to eigenvalues ± 1 of τ_z. These types of Hamiltonians are the Hamiltonians of the generalized Rabi models. These describe a two-level system connected not to a single bosonic mode, but to a more complicated environment [16-18].

Diagonalization in the Spin Space

The Hamiltonian in the spin space can be diagonalized using the formula for the determinant of a 2×2 block matrix. This is also known as the Fulton–Gouterman transformation [19]. This leads to two effective Hamiltonians in the chain Hilbert space, corresponding to the state of the single spin. These are:

$$\begin{aligned} H_{\text{eff}}^{\pm} &= \pm\frac{\omega}{2} + H_{\text{LMG}}^{\pm} - \frac{\Delta^2}{4}G_{\mp} \\ G_{\pm} &= \left(\pm\frac{\omega}{2} + H_{\text{LMG}}^{\pm} - E\right)^{-1}. \end{aligned} \tag{5}$$

Operators $G_{\pm}$ are the Green functions of the Hamiltonians $\pm\omega/2 + H_{\text{LMG}}^{\pm}$. Both of these Hamiltonians contain full information about the system, so it is sufficient to consider only one of them. We will choose the Hamiltonian $H_{\text{eff}} = H_{\text{eff}}^{+}$ as the effective Hamiltonian. Given the eigenenergies $\varepsilon_n^{\pm}$ and eigenstates $|n^{\pm}\rangle$ of the Hamiltonian $\pm\omega/2 + H_{\text{LMG}}^{\pm}$, the effective Hamiltonian can be written as:

$$H_{\text{eff}} = \sum_{n=1}^{N} \varepsilon_n^+ \left|n^+\right\rangle\left\langle n^+\right| - \frac{\Delta^2}{4} \sum_{n=1}^{N} \frac{\left|n^-\right\rangle\left\langle n^-\right|}{\varepsilon_n^- - E}. \tag{6}$$

The eigenenergies of the whole system are solutions of the equation $\lambda(E) = E$, where $\lambda(E)$ are the eigenvalues of H_{eff}. In principle, solutions of this equation are exactly the energy levels of the corresponding physical system. However, given that in practice an analytical solution is impossible in most cases, a usual approach is to substitute some values of energy E_0 on the left hand side and look for corrections. Our approach will be to find some kind of relation between the Hamiltonians H^+_{LMG} and H^-_{LMG}, which will allow us to express the eigenstates of one Hamiltonian via the eigenstates of the other. Then, the equation $\lambda(E) = E$ will be quadratic with two solutions, corresponding to two states of the single spin.

Limit of Strong Single-Spin–Chain Coupling

We focus on the limit of large coupling between the single spin and the chain (i.e., large $\tilde{J}$). In practice, this can be realized by coupling a single spin to an ensemble of noninteracting spins, such that the ensemble interacts only indirectly through the external spin. In this case, spins in the chain are mostly aligned along the z-axis due to the large $\tilde{J}\tau_z S_z$ term. Effectively, an interaction with the single spin creates a strong magnetic field parallel to the single spin direction. Thus, the perpendicular component of the "magnetic field" $\tilde{\Delta} S_x$ can be considered as a small perturbation. Formally, this means that we can divide the LMG Hamiltonian into the main part

$$H^0_{\text{LMG}} = \left(\tilde{\omega} + \frac{\tilde{J}}{2}\tau_z\right) S_z + \frac{J}{2S} S_z^2 \tag{7}$$

and the perturbation $V = \tilde{\Delta} S_x$. With the standard perturbation theory approach, we find the energy levels of H_{LMG} up to second order in $\tilde{\Delta}$:

$$\begin{aligned} \varepsilon^{\pm}_{\sigma} &= \varepsilon^{(0)}_{\pm,\sigma} + \sum_{\sigma' \neq \sigma} c_{\sigma\sigma'} \\ \varepsilon^{(0)}_{\pm,\sigma} &= \left(\tilde{\omega} \pm \frac{\tilde{J}}{2}\right)\sigma + \frac{J}{2S}\sigma^2 \\ c^{\pm}_{\sigma\sigma'} &= \tilde{\Delta}^2 \frac{\left|\langle \sigma' | S_x | \sigma \rangle\right|^2}{E^{(0)}_{\pm,\sigma} - E^{(0)}_{\pm,\sigma'}}. \end{aligned} \tag{8}$$

Here, $S_z|\sigma\rangle = \sigma|\sigma\rangle$. Accordingly, the eigenstates are

$$\left|\psi^{\pm}_{\sigma}\right\rangle \approx |\sigma\rangle + \sum_{\sigma' \neq \sigma} c^{\pm}_{\sigma\sigma'} |\sigma'\rangle. \tag{9}$$

As discussed earlier, we aim to relate H^+_{LMG} and H^-_{LMG}. Let us express the projectors on states $\left|\psi^+_\sigma\right\rangle$ via projectors on $\left|\psi^-_\sigma\right\rangle$. Up to the second order in $\tilde{\Delta}$:

$$\begin{aligned} \left|\psi^+_\sigma\right\rangle\left\langle\psi^+_\sigma\right| = \left|\psi^-_\sigma\right\rangle\left\langle\psi^-_\sigma\right| \\ + \sum_{\sigma'} \left(c^+_{\sigma\sigma'} - c^-_{\sigma\sigma'}\right)\left(\left|\psi^-_\sigma\right\rangle\langle\sigma| + |\sigma\rangle\left\langle\psi^-_\sigma\right|\right). \end{aligned} \tag{10}$$

The Hamiltonians $H^{\pm}_{\text{LMG}}$ now can be written as:

$$\begin{aligned} H^+_{\text{LMG}} &= \sum_{\sigma} E^+_\sigma \left|\psi^-_\sigma\right\rangle\left\langle\psi^-_\sigma\right| \\ &\quad + \sum_{\sigma\sigma'} \varepsilon^+_\sigma \left(c^+_{\sigma\sigma'} - c^-_{\sigma\sigma'}\right)\left(\left|\psi^-_\sigma\right\rangle\langle\sigma| + |\sigma\rangle\left\langle\psi^-_\sigma\right|\right) \\ H^-_{\text{LMG}} &= \sum_{\sigma} \varepsilon^-_\sigma \left|\psi^-_\sigma\right\rangle\left\langle\psi^-_\sigma\right|. \end{aligned} \tag{11}$$

One can see that the leading order H^+_{LMG} is expressed via projectors on the eigenstates of H^-_{LMG}. The extra terms, when substituted in the effective Hamiltonian, will lead to higher order corrections and will be insignificant. Indeed, substituting in (Equation 6) we find:

$$\begin{aligned} H_{\text{eff}} = \sum_{\sigma} \left(\frac{\omega}{2} + \varepsilon^+_\sigma - \frac{\Delta^2}{4\left(E^-_\sigma - \omega/2 - E\right)}\right)\left|\psi^-_\sigma\right\rangle\left\langle\psi^-_\sigma\right| \\ + \sum_{\sigma\sigma'} \varepsilon^+_\sigma \left(c^+_{\sigma\sigma'} - c^-_{\sigma\sigma'}\right)\left(\left|\psi^-_\sigma\right\rangle\langle\sigma| + |\sigma\rangle\left\langle\psi^-_\sigma\right|\right). \end{aligned} \tag{12}$$

The first term is diagonal in the basis $\left|\psi^-_\sigma\right\rangle$, so its contribution to the eigenvalues of the effective Hamiltonian eigenvalues will be of second order in $\tilde{\Delta}$ (as it is the order to which we have expanded $\varepsilon^{\pm}_\sigma$). The second term is of second order in $\tilde{\Delta}$ and off-diagonal, so its contribution will be of fourth order in $\tilde{\Delta}$. Thus, up to the second order in $\tilde{\Delta}$, the energy E of the whole system is defined by the following equation:

$$\frac{\omega}{2} + \varepsilon^+_\sigma - \frac{\Delta^2}{4\left(\varepsilon^-_\sigma - \omega/2 - E\right)} = E, \tag{13}$$

from which follows

$$E_{\sigma}^{\pm}=\frac{1}{2}\left(\varepsilon_{\sigma}^{+}+\varepsilon_{\sigma}^{-}\pm\sqrt{\left(\omega+\varepsilon_{\sigma}^{+}-\varepsilon_{\sigma}^{-}\right)^{2}+\Delta^{2}}\right). \tag{14}$$

Also, from these calculations follows that the eigenstates are $\left|\psi_{\sigma}^{-}\right\rangle$. One might wonder why there is no contribution from $\left|\psi_{\sigma}^{+}\right\rangle$, given that our choice between expanding the Hamiltonian (Equation 13) in $\left|\psi_{\sigma}^{-}\right\rangle\left\langle\psi_{\sigma}^{-}\right|$ or $\left|\psi_{\sigma}^{+}\right\rangle\left\langle\psi_{\sigma}^{+}\right|$ was arbitrary. In fact, there is indeed no difference between choosing one over the other, because $\left\langle\psi_{\sigma}^{-}\middle|\psi_{\sigma}^{+}\right\rangle=\delta_{\sigma\sigma'}+\mathcal{O}\left(\tilde{\Delta}^{4}\right)$.

We also note that the same spectrum corresponds to the single-spin Hamiltonian

$$H=\frac{1}{2}\begin{pmatrix}\omega & \Delta\\ \Delta & -\omega\end{pmatrix}+\begin{pmatrix}\varepsilon_{\mathrm{LMG}}^{+} & 0\\ 0 & \varepsilon_{\mathrm{LMG}}^{-}\end{pmatrix}. \tag{15}$$

This Hamiltonian can be obtained if one replaces $H_{\mathrm{LMG}}^{\pm}$ by their eigenvalues $\varepsilon_{\mathrm{LMG}}^{\pm}$ in Equation 4. This is a Born–Oppenheimer approximation in which the chain is considered to be a fast subsystem relative to the single spin. In particular, the energy of the spin chain is a contribution to the potential energy of the single spin.

Phase Transition in the Thermodynamic Limit

Phase transition of the bare LMG model

In the thermodynamic classical limit, the spin operators in the LMG model can be replaced by classical expectation values (i.e., $S_z = S\cos\theta$, $S_x = S\sin\theta\cos\varphi$, $S_y = S\sin\theta\sin\varphi$). The Hamiltonian is then replaced by its classical energy profile, which is defined according to [12] as:

$$\begin{aligned}\varepsilon^{\pm}(\theta,\varphi)&=\lim_{S\to\infty}\frac{\left\langle H_{\mathrm{LMG}}^{\pm}\right\rangle}{S}\\&=\left(\tilde{\omega}\pm\frac{\tilde{J}}{2}\right)\cos\theta+\frac{J}{2}\cos^{2}\theta+\tilde{\Delta}\sin\theta\cos\varphi.\end{aligned} \tag{16}$$

The average is taken over a spin coherent state $|\theta,\varphi\rangle$. It is known that the LMG Hamiltonian has two distinct phases in the thermodynamic limit [12,20-22]. The symmetric phase, in which $|\langle S_z\rangle| = S$, is realized when the linear part in S_z term in the Hamiltonian dominates over the quadratic one. In our particular case, this means competition between the values of coefficients $\tilde{\omega}+\tilde{J}\tau_z/2$ and J in the Hamiltonian (Equation 3). The second broken symmetry phase, in which the energy profile has two minima at $\langle S_z\rangle=\pm S_z^0$, is realized in the opposite case, when the S_z^2 term dominates over the ~S_z term. These minima are degenerate if $\tilde{\Delta} = 0$, otherwise one is lower than the other. The plot of the LMG model energy as a function of the angle θ is presented in Figure 1.

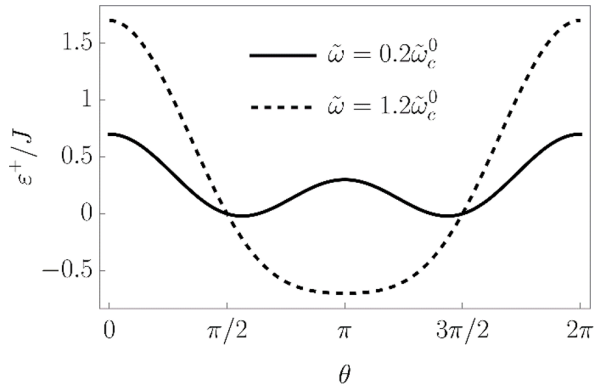


Figure 1: Energy profile (Equation 16) of the LMG model in the thermodynamic limit as a function of θ at φ = 0 and $\tilde{\Delta}$ = 0. The solid line corresponds to the broken symmetry phase with two stable minima, and the dashed line to the symmetric phase with a single minimum at θ = π.

We wished to study the phase transition of the bare LMG model (i.e., decoupled from the external spin) and in the next section we will compare the results with the ones for the LMG model coupled to the external spin. First, we have to find the extrema of the LMG model energy $\varepsilon=\varepsilon^{+}\left(\tilde{J}=0\right)$. They are defined by the following equations:

$$\begin{aligned}&\frac{\partial\varepsilon}{\partial\theta}=0\Rightarrow\sin\theta\left(J\cos\theta+\tilde{\omega}\right)-\tilde{\Delta}\cos\theta\cos\varphi=0\\&\frac{\partial\varepsilon}{\partial\varphi}=0\Rightarrow\tilde{\Delta}\sin\theta\sin\varphi=0.\end{aligned} \tag{17}$$

One of the solutions is sinθ = 0 and cosφ = 0; it corresponds to the symmetric phase in which $|\langle S_z\rangle| = |S\cos\theta| = S$. The second solution corresponds to sinφ = 0 and

$$\cos\theta+\frac{\tilde{\omega}\sin\theta}{J\sin\theta-\tilde{\Delta}}=0. \tag{18}$$

It describes the broken symmetry phase in which $|\langle S_z\rangle| \neq S$.

We found the critical values of the parameters, at which the phase transition occurs, by checking the stability of the symmetric phase. Namely, if it is stable, the sinθ = 0 and cosφ = 0 extremum is a minimum in the θ direction, and the second de-

rivative of $\varepsilon^+(\theta,\varphi)$ with respect to θ is positive. Otherwise, the said extremum is a maximum and the stable phase is the broken symmetry one. When carrying out the calculations, we should choose the $\theta = \pi$ solution of the equation $\sin\theta = 0$, since the $\sim S_z$ contribution to the energy is positive and the ground state corresponds to $S_z = \cos\pi = -S$. The $\theta = 0$ solution corresponds to the maximum of the energy profile. Thus, we find:

$$\frac{\partial^2}{\partial\theta^2}\varepsilon^+\Big|_{\theta=\pi,\varphi=0} = \tilde{\omega} - J. \tag{19}$$

Therefore, the broken symmetry phase exists (i.e., the expression above is negative) for $\tilde{\omega} < \tilde{\omega}_c^0 = J$. The projection of the spin on the z-axis in the broken symmetry phase is $S_z^0 = S\cos\theta_0$, where θ_0 is the solution of Equation 18. If $\tilde{\Delta} = 0$, the solutions are $\cos\theta_0 = \tilde{\omega}/J = \tilde{\omega}/\tilde{\omega}_c^0$. The plots of the energy profile $\varepsilon^+(\theta,\varphi)$ in symmetric and broken symmetry phases are presented in Figure 1.

Phase transition of the LMG model coupled to a single spin

Next, we study the properties of the phase transition if the chain is coupled to the external single spin. In this case, we have to minimize the ground state energy of the whole system. From Equation 14 we find the spectrum:

$$E^{\pm}(\theta,\varphi) = \frac{1}{2}\left(\varepsilon^+(\theta,\varphi) + \varepsilon^-(\theta,\varphi) \pm\sqrt{\left[\omega + \varepsilon^+(\theta,\varphi) - \varepsilon^-(\theta,\varphi)\right]^2 + \Delta^2}\right). \tag{20}$$

These functions also have nontrivial minima structure depending on the values of the parameters, see Figure 2. Again, from equations $\partial_\theta E^- = 0$ and $\partial_\varphi E^- = 0$ we find that the extrema of the ground state energy are defined by equations

$$\sin\varphi\sin\theta = 0$$
$$\left(\tilde{\Delta}\cos\varphi - J\sin\theta\right)\cos\theta - \tilde{\omega}\sin\theta = \frac{\tilde{J}\left(\omega + \tilde{J}\cos\theta\right)\sin\theta}{2\sqrt{\left(\omega + \tilde{J}\cos\theta\right)^2 + \Delta^2}}. \tag{21}$$

The second equation defines $\langle S_z\rangle$ in the broken symmetry phase, analogously to Equation 18. In general, it has up to nine real solutions on the interval $\theta \in [0,2\pi]$ depending on the values of the parameters. For $\tilde{\Delta} = 0$, three of them are $\theta = 0, \pi, 2\pi$ as it follows from the condition $\sin\theta = 0$. Nonzero $\tilde{\Delta}$ will shift these solutions and corrections due to small $\tilde{\Delta}$ which can be found by expanding the equation at said points. Six other solutions cannot be analytically found; however, we can study the properties of the energy profile exploiting the following facts: 1) due to the 2π-periodicity of $E^{\pm}(\theta,\varphi)$, the extrema at $\theta = 0, 2\pi$ are of the same type. 2) Three of unknown extrema are on the interval $\theta \in (0,\pi)$ and the other three are on the interval $\theta \in (\pi,2\pi)$. 3) A maximum should be followed by a minimum and vice versa.

Additional extrema arise due to hybridization between the energy levels $\varepsilon^{\pm}(\theta,\varphi)$ of the bare LMG model with the single spin directed up or down, leading to the appearance of avoided crossings and richer extremum structure of the ground state energy. The extrema at $\theta = 0, \pi, 2\pi$ always exist and could be either minima or maxima and the six other ones might be minima, maxima, or not exist. This allows us to list all possible extrema configurations of the energy profile. We group them into two types: either minima at $\theta = 0, 2\pi$ and $\theta = \pi$ are of different types or the same, see Figure 2a and Figure 2b, respectively.

Let us first start with "different type" configurations in Figure 2a. Configurations 1 and 2 have no additional extrema and in both of them the symmetric phase is stable. The difference is that in configuration 1 the total spin of the chain is aligned along the positive direction of the z-axis, and in configuration 2 – along the negative direction. Remarkably, configuration 1 is unstable for the bare LMG model. Configuration 3 is not realized and in configuration 4 both symmetric and broken symmetry extrema are minima, meaning that one of the phases is stable and the other is metastable. This means that coupling to the external spin can change the type of the phase transition between two phases from the second to the first one. The corresponding plots of the energy levels are presented in Figure 3.

Now we consider the "same type" configurations in Figure 2b. In configuration 1, two minima correspond to symmetric phases with the total spin aligned along the positive and negative directions of the z-axis. One of the phases is stable and the other is metastable, so a first order phase transition between them is possible. In configuration 2, the broken symmetry phase is stable, resembling the case of the bare LMG model. The configuration 3 is again not realized. The most interesting one is the configuration 4 in which the minima, corresponding to the stable broken symmetry phase, split into two. The plots of the energy levels, corresponding to described extrema configurations, can be found in Figure 4.

We also derive the conditions for stability of the points $\theta = 0, \pi, 2\pi$. Calculating the second derivatives we find:

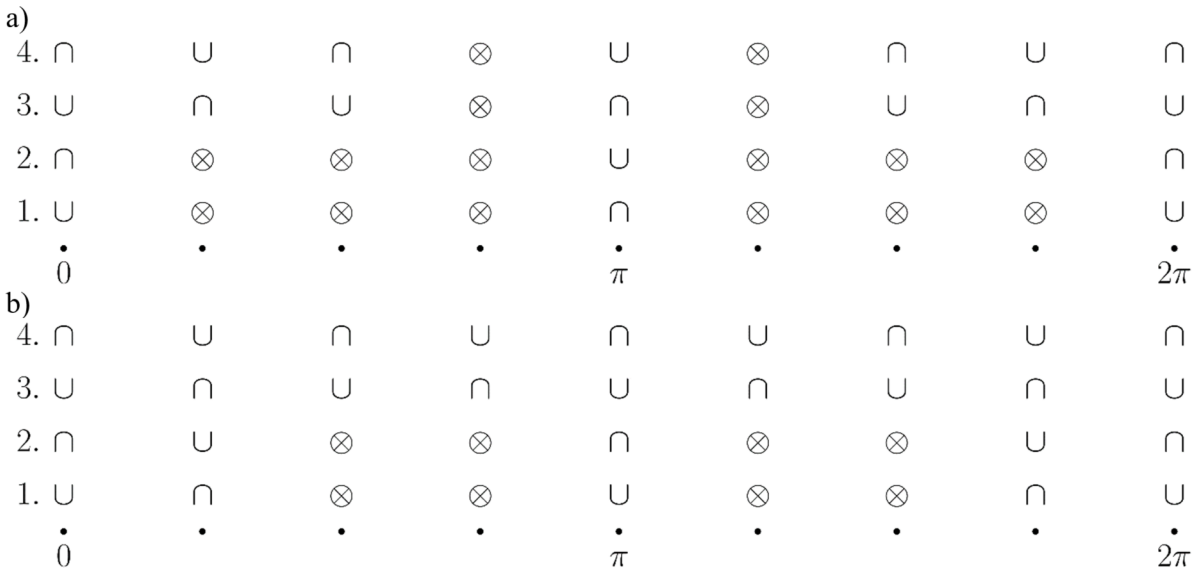


Figure 2: Possible configurations of the extrema of the ground state energy $E^{-}(\theta,\varphi)$. The symbol ∪ denotes a minimum, ∩ – a maximum, and ⊗ – absence of the extremum. In (a) "different type" configurations are presented and in (b) "same type" configurations are presented.

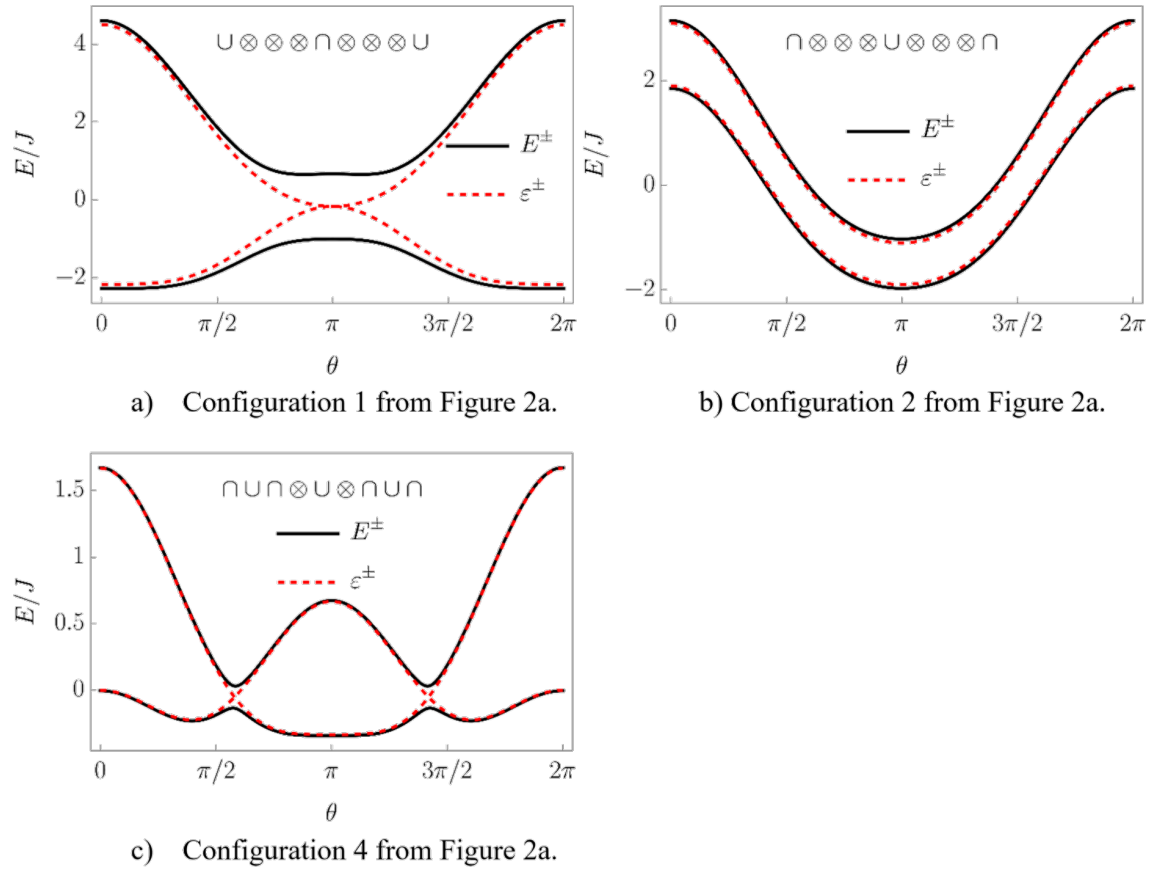


Figure 3: The energy levels of the system corresponding to configurations 1, 2, and 4 from Figure 2a. In plots a) and b) the symmetric phases with spin aligned along positive and negative directions of the *z*-axis, respectively, are stable. In plot c) one can observe a stable symmetric phase and a metastable broken symmetry phase.

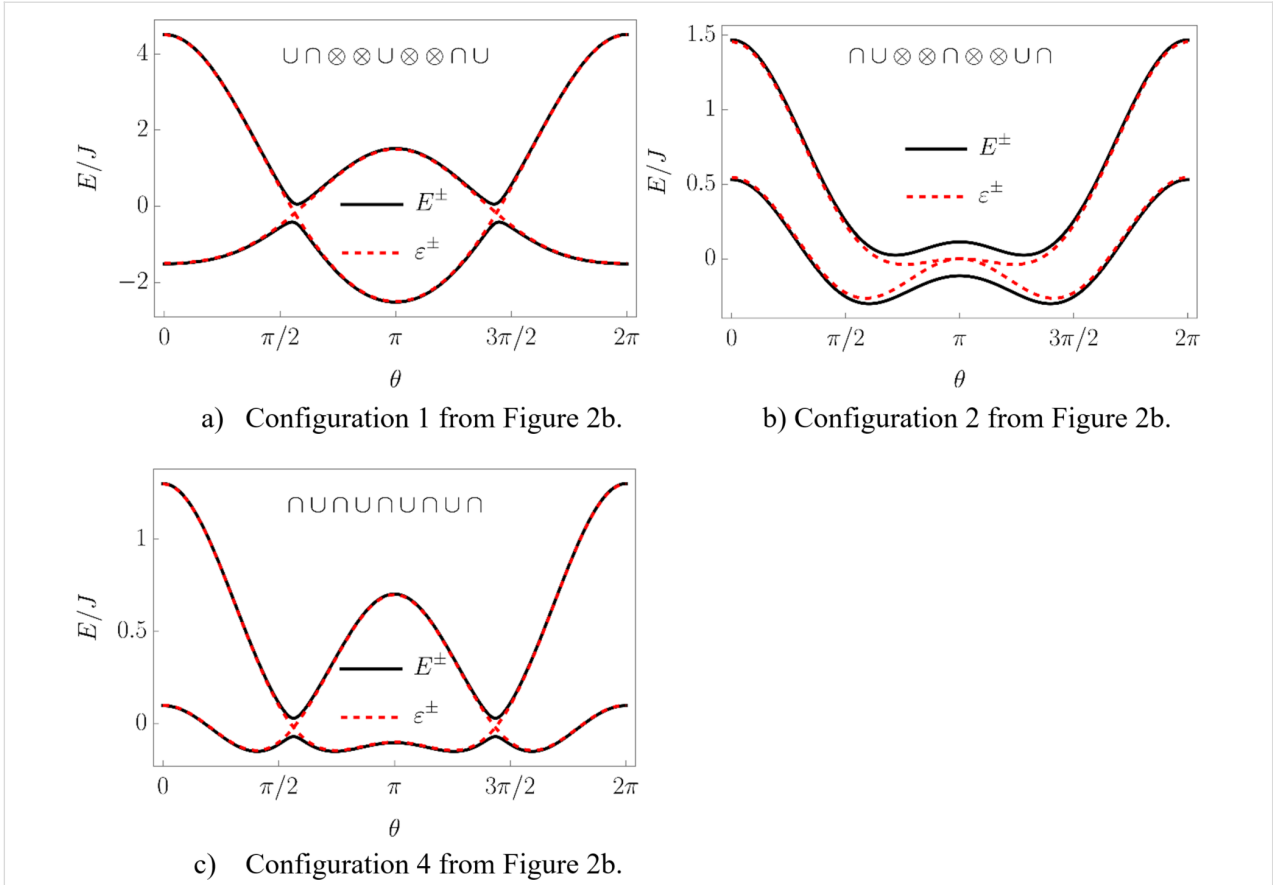


Figure 4: The energy levels of the system corresponding to configurations 1, 2, and 4 from Figure 2b. In plot a) the symmetric phases with spin aligned along negative direction of the *z*-axis is stable and the one with spin aligned along the positive direction is metastable. In plot c) the minima corresponding to the stable broken symmetry phase are split into two.

$$\left.\frac{\partial^2}{\partial\theta^2}E^-\right|_{\theta=\pi} = \tilde{\omega} - J + \frac{\tilde{J}\left(\tilde{J}-\omega\right)}{2\sqrt{\left(\tilde{J}-\omega\right)^2+\Delta^2}}$$
$$\left.\frac{\partial^2}{\partial\theta^2}E^-\right|_{\theta=0,2\pi} = -\tilde{\omega} - J + \frac{\tilde{J}\left(\tilde{J}+\omega\right)}{2\sqrt{\left(\tilde{J}+\omega\right)^2+\Delta^2}}. \quad (22)$$

Accordingly, the point θ = π is a minimum if

$$\tilde{\omega} > J - \frac{\tilde{J}\left(\tilde{J}-\omega\right)}{2\sqrt{\left(\tilde{J}-\omega\right)^2+\Delta^2}} \quad (23)$$

and points θ = 0, 2π are stable if

$$\tilde{\omega} < -J + \frac{\tilde{J}\left(\tilde{J}+\omega\right)}{2\sqrt{\left(\tilde{J}+\omega\right)^2+\Delta^2}}. \quad (24)$$

Two important observations can be made here. First, the right-hand side of Equation 23 can be negative for large enough values of $\tilde{J}$ (i.e., single spin–chain coupling) making the symmetric state always stable. Second, at certain range of parameters, both conditions (Equation 23) and Equation 24 might be true or not true simultaneously, which leads to the appearance of the "same type" configurations. More detailed analysis of transitions between different phases requires knowing the conditions of existence of intermediate extrema at θ = 0, π, 2π. This boils down to finding all solutions of Equation 21 and one has to resort to numerical calculations. In Figure 5, the phase diagram, obtained numerically, is presented on the J–$\tilde{J}$ plane for fixed values of the rest of the parameters.

Results and Discussion

We have theoretically studied the infinitely coordinated Ising chain, coupled to a single external spin. We have written down the effective Hamiltonian in the Ising chain space by diagonalizing the Hamiltonian of the whole system in the space of the external spin. In the thermodynamic limit, when the chain Hamiltonian is exactly solvable, the energy spectrum of the

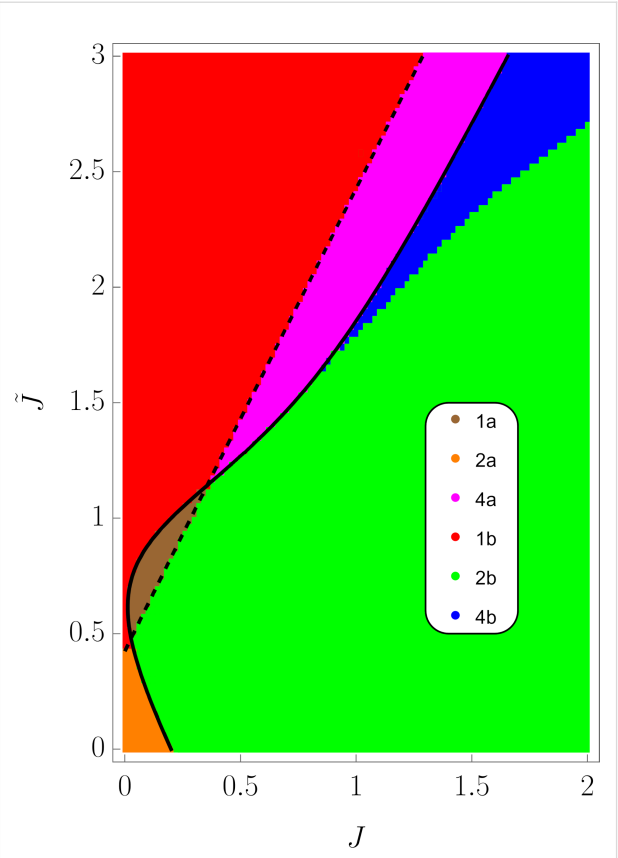


Figure 5: The phase diagram of the considered model on the J–$\tilde{J}$ plane. The legend notation coincides with the configurations in Figure 2 (e.g., 1a is the configuration 1 in Figure 2a). The black solid line is the contour given by Equation 23, and the dashed black line is given by Equation 24. The rest of the parameters are chosen as $\omega = 1$, $\tilde{\omega} = 0.2$, $\Delta = 0.5$, and $\tilde{\Delta} = 0$.

system was found. It is demonstrated that coupling to an external spin drastically changes the properties of the phases relative to the bare LMG model. In particular, it leads to the appearance of a new stable phase-symmetric one, but with the total spin of the chain oriented in the reverse direction compared to the symmetric state of the bare LMG model. This phase might be stable as well as metastable, and the first order phase transition between two stable phases is possible. The broken symmetry phase might also become metastable at certain values of the parameters, which means that the corresponding phase transition becomes of first order as opposed to the second order in the case of the bare LMG model. Finally, coupling to the external spin might change the properties of the broken symmetry phase by splitting the corresponding minima of energy into two.

In case of an experimental attempt, it is possible to check the spin configuration of the coordinated Ising chain by using a well-developed and very sensitive method of polarized neutron reflectometry (PNR) [23-26] to improve the qubit quality, which is an important task [27,28].

The considered model is relevant in the field of quantum computation, as the layout is used for a certain realization of the CCZ gate [10]. Although, admittedly, the thermodynamic limit approximation made during the analysis is far from a feasible experimental setup involving only several qubits.

Funding

The publication was prepared with the support of the Russian Science Foundation (Grant No. 23–72–01067).

Author Contributions

Seidali Seidov: data curation; investigation; software. Natalia Pugach: conceptualization; formal analysis; funding acquisition; validation; writing – original draft. Anatolie Sidorenko: data curation; investigation; supervision; validation.

ORCID® iDs

Seidali Seidov - https://orcid.org/0000-0003-1946-6014
Natalia Pugach - https://orcid.org/0000-0003-4017-1667
Anatolie Sidorenko - https://orcid.org/0000-0001-7433-4140

Data Availability Statement

All data that supports the findings of this study is available in the published article and/or the supporting information of this article.

Preprint

A non-peer-reviewed version of this article has been previously published as a preprint: https://arxiv.org/abs/2504.02164

References

1. Prokof'ev, N. V.; Stamp, P. C. E. *Rep. Prog. Phys.* **2000,** *63,* 669–726. doi:10.1088/0034-4885/63/4/204
2. Arenz, C.; Gualdi, G.; Burgarth, D. *New J. Phys.* **2014,** *16,* 065023. doi:10.1088/1367-2630/16/6/065023
3. Krovi, H.; Oreshkov, O.; Ryazanov, M.; Lidar, D. A. *Phys. Rev. A* **2007,** *76,* 052117. doi:10.1103/physreva.76.052117
4. Budini, A. A. *Phys. Rev. A* **2019,** *99,* 052125. doi:10.1103/physreva.99.052125
5. Han, L.; Zou, J.; Li, H.; Shao, B. *Entropy* **2020,** *22,* 895. doi:10.3390/e22080895
6. Brenes, M.; Min, B.; Anto-Sztrikacs, N.; Bar-Gill, N.; Segal, D. *J. Chem. Phys.* **2024,** *160,* 244106. doi:10.1063/5.0207028
7. Cattaneo, M.; Giorgi, G. L.; Maniscalco, S.; Zambrini, R. *New J. Phys.* **2019,** *21,* 113045. doi:10.1088/1367-2630/ab54ac
8. Mitchison, M. T.; Plenio, M. B. *New J. Phys.* **2018,** *20,* 033005. doi:10.1088/1367-2630/aa9f70
9. Czerwinski, A. *Symmetry* **2022,** *14,* 1752. doi:10.3390/sym14081752
10. Simakov, I. A.; Mazhorin, G. S.; Moskalenko, I. N.; Seidov, S. S.; Besedin, I. S. *Phys. Rev. Appl.* **2024,** *21,* 044035. doi:10.1103/physrevapplied.21.044035

11. Lipkin, H. J.; Meshkov, N.; Glick, A. J. *Nucl. Phys.* **1965,** *62,* 188–198. doi:10.1016/0029-5582(65)90862-x
12. Ribeiro, P.; Vidal, J.; Mosseri, R. *Phys. Rev. E* **2008,** *78,* 021106. doi:10.1103/physreve.78.021106
13. Chinni, K.; Poggi, P. M.; Deutsch, I. H. *Phys. Rev. Res.* **2021,** *3,* 033145. doi:10.1103/physrevresearch.3.033145
14. Santos, L. F.; Távora, M.; Pérez-Bernal, F. *Phys. Rev. A* **2016,** *94,* 012113. doi:10.1103/physreva.94.012113
15. Vidal, J. *Phys. Rev. A* **2006,** *73,* 062318. doi:10.1103/physreva.73.062318
16. Moroz, A. *EPL* **2016,** *113,* 50004. doi:10.1209/0295-5075/113/50004
17. Eckle, H.-P.; Johannesson, H. *J. Phys. A: Math. Theor.* **2017,** *50,* 294004. doi:10.1088/1751-8121/aa785a
18. Li, Z.-M.; Batchelor, M. T. *Phys. Rev. A* **2021,** *104,* 033712. doi:10.1103/physreva.104.033712
19. Naseri, A.; Hu, Y.; Luo, W. *arXiv* **2020,** 2012.00197. doi:10.48550/arxiv.2012.00197
20. Botet, R.; Jullien, R.; Pfeuty, P. *Phys. Rev. Lett.* **1982,** *49,* 478–481. doi:10.1103/physrevlett.49.478
21. Botet, R.; Jullien, R. *Phys. Rev. B* **1983,** *28,* 3955–3967. doi:10.1103/physrevb.28.3955
22. Castaños, O.; López-Peña, R.; Hirsch, J. G.; López-Moreno, E. *Phys. Rev. B* **2006,** *74,* 104118. doi:10.1103/physrevb.74.104118
23. Khaydukov, Y. N.; Lenk, D.; Zdravkov, V.; Morari, R.; Keller, T.; Sidorenko, A. S.; Tagirov, L. R.; Tidecks, R.; Horn, S.; Keimer, B. *Phys. Rev. B* **2021,** *104,* 174445. doi:10.1103/physrevb.104.174445
24. Khaydukov, Y.; Pütter, S.; Guasco, L.; Morari, R.; Kim, G.; Keller, T.; Sidorenko, A.; Keimer, B. *Beilstein J. Nanotechnol.* **2020,** *11,* 1254–1263. doi:10.3762/bjnano.11.109
25. Khaydukov, Y.; Kravtsov, E.; Morari, R.; Lenk, D.; Mustafa, L.; Kim, G.; Trapp, M.; Zhaketov, V.; Proglyado, V.; Zrdavkov, V.; Nikitenko, Y.; Krug von Nidda, H.-A.; Keller, T.; Steitz, R.; Tideks, R.; Sidorenko, A.; Ustinov, V.; Aksenov, V.; Keimer, B. *J. Phys.: Conf. Ser.* **2019,** *1389,* 012060. doi:10.1088/1742-6596/1389/1/012060
26. Zhaketov, V. D.; Devyaterikov, D. I.; Avdeev, M. M.; Norov, D. A.; Kolupaev, E. D.; Kuzmenko, M. O.; Pugach, N. G.; Khaydukov, Yu. N.; Kravtsov, E. A.; Nikitenko, Yu. V.; Aksenov, V. L. *Phys. Solid State* **2023,** *65,* 1076. doi:10.61011/pss.2023.07.56393.35h
27. Klenov, N.; Kornev, V.; Vedyayev, A.; Ryzhanova, N.; Pugach, N.; Rumyantseva, T. *J. Phys.: Conf. Ser.* **2008,** *97,* 012037. doi:10.1088/1742-6596/97/1/012037
28. Klenov, N. V.; Kornev, V. K.; Sharafiev, A. V.; Bakurskiy, S. V.; Pugach, N. G. *J. Phys.: Conf. Ser.* **2010,** *234,* 042017. doi:10.1088/1742-6596/234/4/042017

License and Terms

This is an open access article licensed under the terms of the Beilstein-Institut Open Access License Agreement (https://www.beilstein-journals.org/bjnano/terms), which is identical to the Creative Commons Attribution 4.0 International License (https://creativecommons.org/licenses/by/4.0). The reuse of material under this license requires that the author(s), source and license are credited. Third-party material in this article could be subject to other licenses (typically indicated in the credit line), and in this case, users are required to obtain permission from the license holder to reuse the material.

The definitive version of this article is the electronic one which can be found at:
https://doi.org/10.3762/bjnano.16.117

BEILSTEIN JOURNAL OF NANOTECHNOLOGY

Programmable soliton dynamics in all-Josephson-junction logic cells and networks

Vsevolod I. Ruzhickiy[1,2], Anastasia A. Maksimovskaya[*1,2,3], Sergey V. Bakurskiy[1,4], Andrey E. Schegolev[1,5], Maxim V. Tereshonok[5], Mikhail Yu. Kupriyanov[1,4], Nikolay V. Klenov[3] and Igor I. Soloviev[1,2,4]

Full Research Paper

Open Access

Address:
[1]Lomonosov Moscow State University, Skobeltsyn Institute of Nuclear Physics, Moscow, 119991, Russia, [2]All-Russian Research Institute of Automatics n.a. N.L. Dukhov (VNIIA), 127030, Moscow, Russia, [3]Lomonosov Moscow State University, Faculty of Physics, Moscow, 119991, Russia, [4]Moscow Institute of Physics and Technology, 141700 Dolgoprudny, Russia and [5]Moscow Technical University of Communications and Informatics (MTUCI), 111024, Moscow, Russia

Email:
Anastasia A. Maksimovskaya[*] - stasyahime@gmail.com

* Corresponding author

Keywords:
Josephson-based diode; kinetic inductance; soliton dynamics; superconducting electronics; superconducting neural networks

Beilstein J. Nanotechnol. **2025,** *16,* 1883–1893.
https://doi.org/10.3762/bjnano.16.131

Received: 31 July 2025
Accepted: 30 September 2025
Published: 28 October 2025

This article is part of the thematic issue "Superconducting artificial neural networks and quantum circuits".

Guest Editor: A. S. Sidorenko



© 2025 Ruzhickiy et al.; licensee Beilstein-Institut.
License and terms: see end of document.

Abstract

We demonstrate the programmable control of kinetic soliton dynamics in all-Josephson-junction (all-JJ) networks through a novel tunable cell design. This cell enables on-demand switching of transmission lines and operates across defined parameter regimes supporting diverse dynamical modes. By introducing a structural asymmetry into a transmission line, we implement a Josephson diode that enforces unidirectional soliton propagation. The programmability of the kinetic inductance then provides a crucial mechanism to selectively enable or disable this diode functionality. By engineering artificial inhomogeneity into the circuit architecture, we enhance robustness in all-JJ logic circuits, 2D transmission line all-JJ lattices, and neuromorphic computing systems.

Introduction

The rapid advancement of Josephson junction (JJ) logic circuits [1-5] and neuromorphic networks [6-9] holds transformative potential for ultra-low-power computing. However, achieving scalable integration remains a critical bottleneck, as conventional JJ-based architectures face fundamental density constraints imposed by magnetic flux manipulation requirements and complex mutual inductive crosstalks.

Circuits composed entirely of Josephson junctions (all-JJ circuits) [10-16] represent a promising platform for energy-efficient, high-speed, and scalable computing. In these systems, the propagation of information is associated with the movement of a current wave/topological soliton, which is clearly visible in the model by a 2π jump of the so-called Josephson phase, φ. In contrast to conventional rapid single flux quantum (RSFQ)

logic, the phase drop for the considered single kinetic soliton (SKS) occurs not on the relatively large connecting geometric inductors, but on the Josephson junctions. SKS is a propagating wave of phase change with kinetic energy limited from below; the corresponding current pulse "dissipates" if its motion is interrupted, for example, by a structural inhomogeneity in a transmission line. Traditionally, this sensitivity to structural inhomogeneities has been viewed as a challenge for robust circuit design.

In this work, we propose to exploit the sensitivity mentioned above. We base our proposal on the concept of applying a small number of key cells, which should create precisely engineered tunable inhomogeneities. Such inhomogeneity may be designed as an element of tunable kinetic inductance [17]. This element has high inductance at small scales and can be controlled using currents [18,19], voltage [20], or magnetic fields [21,22]. At the same time, the use of hybrid superconductor–normal metal structures makes it possible to increase the effect of frequency tuning [23,24], while the addition of ferromagnetic layers permits the non-volatile control [25,26]. Another feature of tunable kinetic inductance element is the linear behavior for weak signals, which excludes formation of parasitic processes in the transmission line. This permits to apply tunable kinetic inductance in the resonators with shifting resonance frequency [19,21,22], as well as in sensitive all-JJ digital circuits.

This idea enables us to use the "flaws" of the structure as its important features, opening up a pathway to creating programmable and reconfigurable large circuits. An obvious and widely required application of this technology is in the development of superconductive programmable gate arrays (SPGAs) [27-30], an active area of current research. Another important application of this idea lies in the promising neuromorphic direction [31-33]. Earlier in [34], we have already proposed using kinetic inductances to control neuron dynamics in networks based on radial basis functions (RBF-networks). Moreover, this approach can be extended to hardware realizations of bio-inspired spiking neural networks [35-42] by solving the challenges of creating controllable synapses to realize the effect of spike-timing-dependent plasticity and unidirectional feedbacks for self-regulation. Furthermore, the physical resemblance between solitons and the action potentials (spikes of voltage) generated in biological nervous systems makes all-JJ structures tempting candidates for constructing neuromorphic hardware [43].

In this paper, we investigate the use of controlled kinetic inductance to create an engineered inhomogeneous medium for kinetic solitons. We demonstrate that by tuning this inhomogeneity, distinct dynamical modes can be induced, fundamentally altering the soliton's behavior. Furthermore, we explore how structural asymmetry within this medium can be exploited to achieve a diode effect, enabling non-reciprocal soliton propagation. Building upon these foundational concepts, we then propose two specific architectural solutions: a programmable switch and a versatile routing matrix, which we term the "WayMatrix". We suggest that these architectures provide a framework for the flexible configuration of advanced logic and neuromorphic circuits.

Results

Model description

To model the dynamics of kinetic solitons [43], we employ the resistively and capacitively shunted junction (RCSJ) model [1], where the total current I across a Josephson junction is the sum of the supercurrent, the quasi-particle current, and the displacement current:

$$I = I_{\mathrm{c}} \sin\left(\varphi\right) + \frac{V}{R_{\mathrm{N}}} + C\frac{\mathrm{d}V}{\mathrm{d}t}. \tag{1}$$

Here, φ is the phase difference for the complex superconducting order parameter across the junction, V is the voltage, I_{c} is the critical current, R_{N} is the resistance in the normal state and C is the capacitance. For analysis, it is convenient to express this equation in a dimensionless form. We normalize the time to the inverse of a reference plasma frequency, $\tau = \tilde{\omega}_{\mathrm{p}} t$, where $\tilde{\omega}_{\mathrm{p}} = \sqrt{2\pi \tilde{I}_{\mathrm{c}} / \left(\Phi_0 C\right)}$, and normalize the current to a reference critical current $\tilde{I}_{\mathrm{c}}$. This yields:

$$i = A \cdot \sin\left(\varphi\right) + \alpha\dot{\varphi} + \ddot{\varphi}. \tag{2}$$

In this normalized equation, the dots above the phases indicate differentiation over time with respect to τ. The dimensionless damping coefficient is $\alpha = \Phi_0 \tilde{\omega}_{\mathrm{p}} / \left(2\pi \tilde{I}_{\mathrm{c}} R_{\mathrm{N}}\right)$. The term $\dot{\varphi}$ represents the voltage normalized by the characteristic voltage $V_0 = \Phi_0 \tilde{\omega} / \left(2\pi\right)$. The parameter $A = I_{\mathrm{c}} / \tilde{I}_{\mathrm{c}}$ is the normalized amplitude of the critical current for junctions with the critical current I_{c} that differs from the reference normalization value $\tilde{I}_{\mathrm{c}}$.

To analyze the circuit dynamics, we adopt a nodal analysis approach. In this approach, the gauge-invariant phase difference across any element is expressed in terms of the nodal phases at its terminals, $\varphi = \varphi_k - \varphi_j$. The phase of the ground node is set to zero by convention. This formulation inherently satisfies Kirchhoff's current law (KCL) at each node. For any node k connected to H elements, KCL dictates that the algebraic sum of currents is zero:

$$\sum_{h=1}^{H} I_{k,j(h)} = 0, \tag{3}$$

where the index h runs over all elements connected to node k, $j(h)$ is the index of the node at the other end of element h, and $I_{k,j(h)}$ is the normalized current flowing from the node k to the node $j(h)$. Each current is described by the RCSJ model (Equation 2):

$$\frac{I_{k,j(h)}}{\tilde{I}_c} = A_h \sin\left(\varphi_k - \varphi_{j(h)}\right) + \alpha_h\left(\dot{\varphi}_k - \dot{\varphi}_{j(h)}\right) + \left(\ddot{\varphi}_k - \ddot{\varphi}_{j(h)}\right). \tag{4}$$

With this approach, the current across the inductance is defined by the expression

$$\frac{I^L_{k,j(h)}}{\tilde{I}_c} = \frac{\Phi_0}{2\pi L \tilde{I}_c}\left(\varphi_k - \varphi_{j(h)}\right) = \frac{\left(\varphi_k - \varphi_{j(h)}\right)}{l}, \tag{5}$$

where $l = L/L_J$ is inductance normalized to the Josephson inductance $L_J = \Phi_0/\left(2\pi\tilde{I}_c\right)$.

After substituting the expressions for the current into the formula for the current balance at the node, we get:

$$M_{k,k}\ddot{\varphi}_k - \sum_{h=1}^{H} M_{k,j(h)}\ddot{\varphi}_{k,j(h)} = F_k\left(\varphi_k, \varphi_{k,j(h)}, \dot{\varphi}_k, \dot{\varphi}_{k,j(h)}\right), \tag{6}$$

where $M_{k,k}$ is the sum of the coefficients before $\ddot{\varphi}_k$, $M_{k,j(h)}$ are the coefficients before $\ddot{\varphi}_{k,j(h)}$, F_k contains the sum of all summands except those that do not contain the second derivative. In F_k, all summands with φ_k are written with a minus sign, and all summands with $\varphi_{k,j(h)}$ are written with a plus sign. Additional currents (e.g., the bias current or the time-dependent current from the generator) are also included as components. After writing down Equation 6 for each node, a system of second-order diffeomorphic equations are obtained, which can be represented in matrix form:

$$\hat{M}\ddot{\varphi} = \begin{pmatrix} M_{11} & M_{12} & \dots & M_{1N} \\ M_{21} & M_{22} & \dots & M_{2N} \\ \vdots & \vdots & \ddots & \vdots \\ M_{N1} & M_{N2} & \dots & M_{NN} \end{pmatrix} \begin{pmatrix} \ddot{\varphi}_1 \\ \ddot{\varphi}_2 \\ \vdots \\ \ddot{\varphi}_N \end{pmatrix} = \mathbf{F}(\varphi, \dot{\varphi}). \tag{7}$$

The resulting system of N ordinary differential equations is expressed in the matrix form shown in Equation 7. In this equation, $\vec{\varphi}$ is the vector of nodal phases, N is the total number of non-ground nodes, and $\hat{M}$ is the $N \times N$ mass matrix (also known as the capacitance matrix), which is defined by the capacitive coupling coefficients from Equation 6. A key property of $\hat{M}$ is its sparsity, which arises directly from the local connectivity of the circuit topology; each node is connected to a small subset of other nodes. To increase computational efficiency, we exploit this sparsity when solving the system. The equations are integrated numerically using an adaptive-step-size solver based on the explicit Runge–Kutta (4th and 5th order) formula, commonly known as the Dormand–Prince pair [44,45], which is well suited for this class of non-stiff problems.

The fundamental building block of our design is the "kinetic inductance controllable key" (KICK), which is constructed from the two modified unit cells of an all-Josephson Junction Transmission Line (all-JJTL). As depicted in Figure 1a, each cell is modified by incorporating a controlled kinetic inductance in series with one of its Josephson junctions connected to the ground plane. There are some operational regimes inherent to such a KICK governed by the value of this inductance and by the damping parameter of junctions within the transmission line. The damping parameter is a critical factor as it dictates the kinetic soliton's propagation rate.

As a preliminary step, we characterized the dependence of the kinetic soliton propagation velocity on the damping parameter of the connecting junctions, α (see Figure 1b). We define the velocity as the number of grounded junctions traversed per unit of normalized time, τ. Our simulations revealed a critical damping threshold at $\alpha_{crit} \approx 0.8$; below this value, stable soliton propagation is not supported. Also, under this condition, the energy dissipation rate is too high relative to the energy transfer between adjacent junctions, causing the soliton to decay. When $\alpha > \alpha_{crit}$, the soliton velocity is a monotonically increasing function of the damping. This dependence falls into an approximately linear regime for $\alpha > 3$. The physical mechanism for this velocity increase can be understood from the RCSJ model; a higher value of α enhances the resistive quasiparticle current ($\alpha\dot{\varphi}$) that flows as a junction switches. This larger current provides a stronger driving force to the next junction in the line, causing it to reach its critical threshold and switch more rapidly, thus increasing the overall propagation velocity of the soliton.

The functionality of the KICK is determined by the interplay between the damping α and the normalized kinetic inductance L/L_J. Figure 1c summarizes the behavior of the device in a parameter map, which reveals four distinct operational regimes: (1) Open mode: The KICK is effectively transparent, allowing an incident kinetic soliton to propagate through it with minimal perturbation. (2) Close mode: The KICK acts as a terminator, blocking and destroying the incoming soliton. (3) T-mode: The

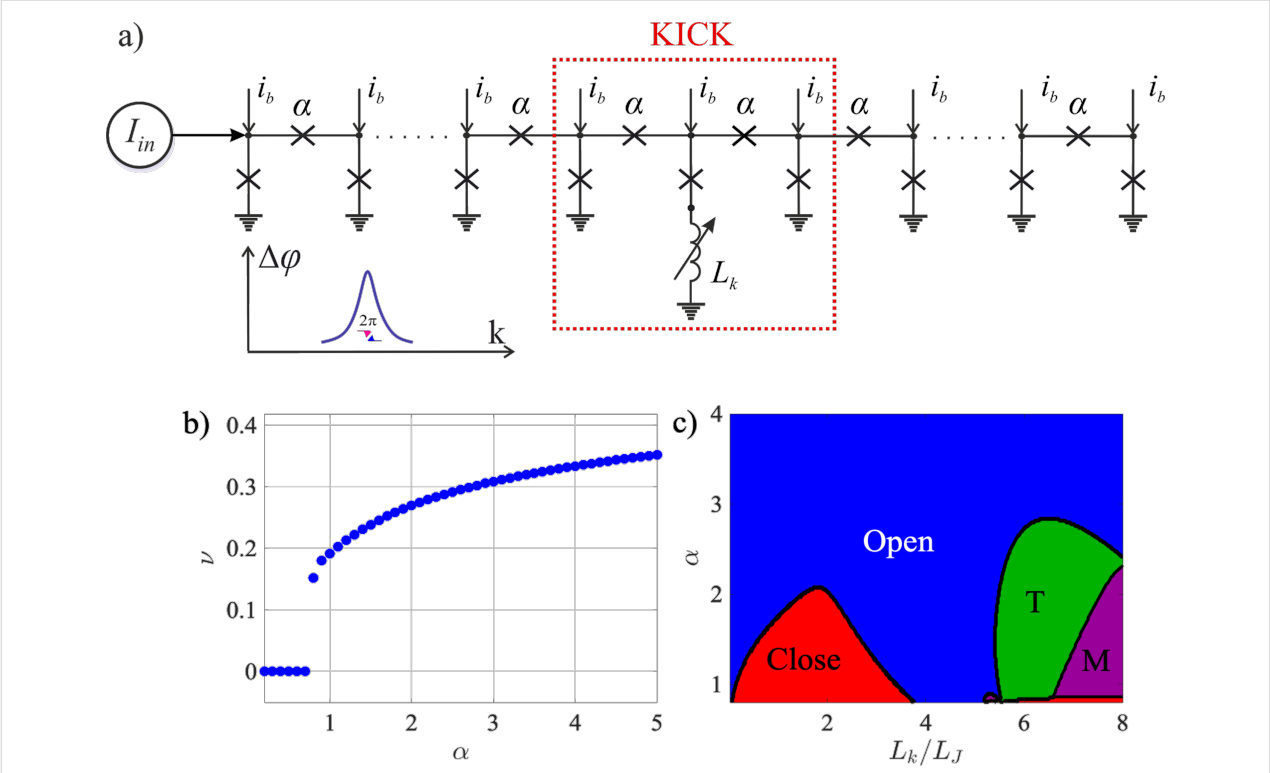


Figure 1: (a) An equivalent scheme for the "kinetic inductance controllable key" (KICK) as a part of an all-Josephson transmission line. A soliton whose dynamics is controlled by the developed key is represented schematically. (b) Dependence of the single kinetic soliton (SKS) propagation velocity, measured in Josephson junctions per normalized time unit, on the damping parameter α. (c) Map of different modes depending on the damping parameter and kinetic inductance measurement. Close mode (red zone): The KICK does not allow the SKS to pass through. Open mode (blue zone): The SKS passes through the KICK. T-mode (green zone): The KICK has two stable states, and every second SKS passes through it. M-mode (purple zone): The KICK has many stable states.

KICK functions as a T-flip-flop. It possesses two stable states, and each arriving soliton toggles the cell from its current state to the other. Every second soliton passes to the exit. (4) M-mode (Multistate mode): This regime is characterized by the formation of more than two stable states and other complex dynamics, which fall outside the scope of this study.

An essential feature of the KICK is the ability to switch between different modes at a fixed value of α; thus, by fixing α (e.g., α = 2) and varying the kinetic inductance, we can switch between all modes (Open mode → Close mode → Open mode → T-mode → M-mode) represented on the parameter map (see Figure 1).

To illustrate the operational modes of the KICK, we simulated the propagation of a kinetic soliton through the all-JJTL. The simulated line comprises 31 grounded junctions with a uniform damping parameter of connecting junctions α = 1. The KICK is implemented by inserting a controlled kinetic inductance in series with the ground junction at the line's center (node k = 16). Figure 2 presents the results for different values of this inductance, corresponding to distinct operational modes. Each panel displays two key physical quantities on dual y-axes: (1) the spatial profile of the nodal Josephson phases (φ_k) as a function of the node index k and (2) the normalized currents flowing through the series junctions connecting the nodes. The current between nodes k and k + 1 ($I_c/\tilde{I}_c \sin(\varphi_{k+1}-\varphi_k)$) is plotted at the midpoint index k + 0.5 for visual clarity.This visualization allows for a direct comparison of the system's state before and after soliton interaction. The solid lines depict the initial state (before the soliton reaches the KICK), and the dashed lines show the final state (after the soliton has passed and the system has settled).

For a low inductance of L/L_J = 0.1 (see Figure 2a), corresponding to the Open mode, the KICK causes only slight disturbance in the transmission line.The incident soliton propagates through it unimpeded, and the entire line returns to its initial physical state. However, increasing the inductance to L/L_J = 2 (see Figure 2b) switches the system to the Close mode. In this mode, the KICK serve as a significant barrier; when the soliton arrives, the large inductance impedes the necessary current dynamics, halting the propagation and causing the soliton to be annihilated. Consequently, the 2π phase slip, which signifies the

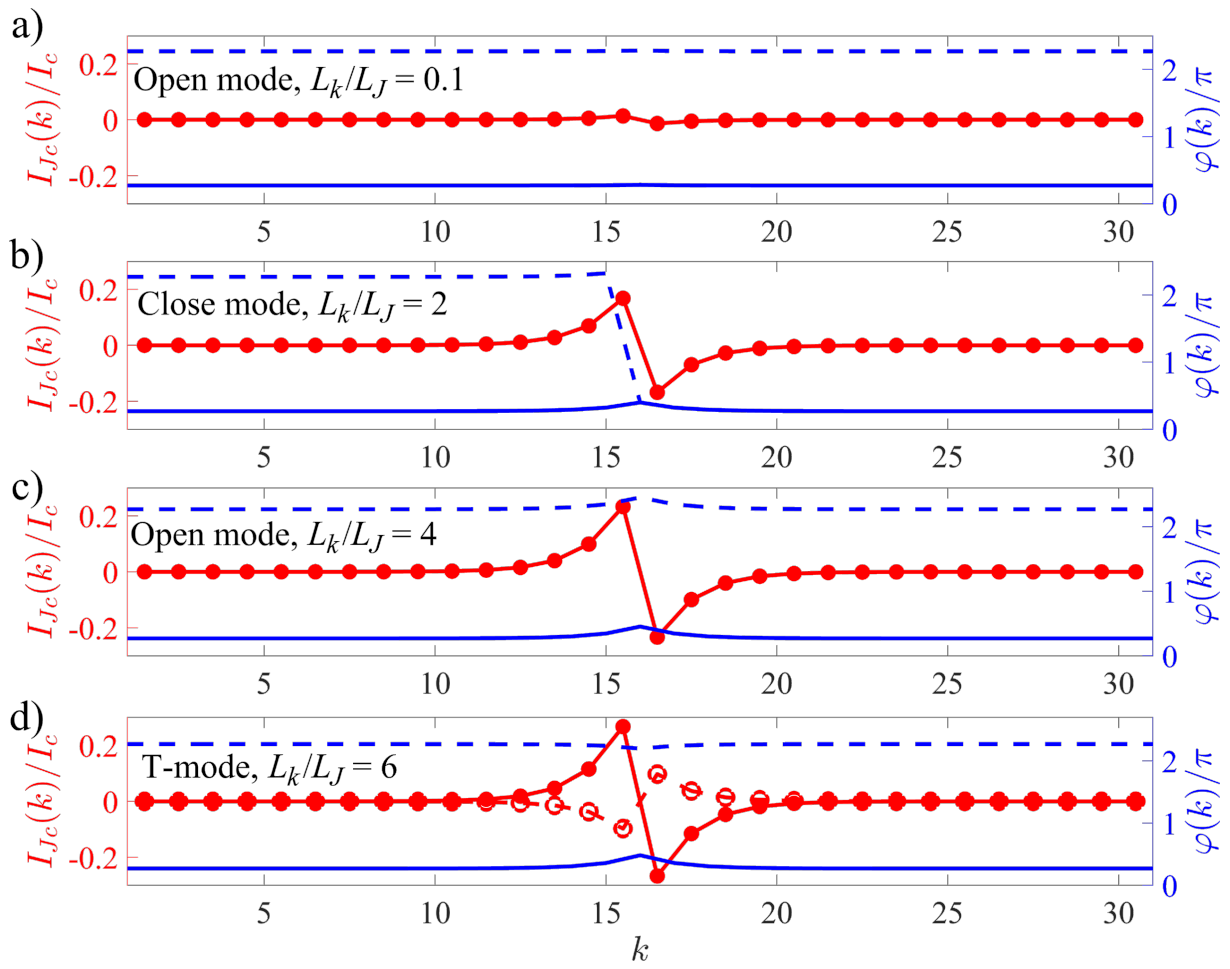


Figure 2: Spatial distributions of the Josephson phase (blue curves) and current (red curves) in (a, c) Open mode, $L_k/L_J = 0.1$ (a) and $L_k/L_J = 4$ (c); (b) Close mode, $L_k/L_J = 2$; and (d) T-mode, $L_k/L_J = 6$. Solid lines show initial profiles, and dashed lines represent distributions after soliton passage. The Josephson phase is plotted against the integer node index k, whereas the current is plotted at the midpoint index $k + 0.5$ to represent the junction between nodes k and $k + 1$, see Figure 1a.

soliton's passage, only traverses the first half of the line (nodes 1 to 15), while the segment beyond the KICK remains entirely unperturbed. Remarkably, a further increase of inductance to $L/L_J = 4$ (see Figure 2c) leads to the re-emergence of the Open mode. This non-trivial effect is governed by transient energy storage in the inductor L. Although the soliton is momentarily halted at the KICK, the subsequent release of stored magnetic energy provides the necessary "kick" to complete the phase slip at node 16. This re-initiates the propagation, allowing the soliton to effectively re-form and travel down the rest of the line. Similarly to the low-inductance case, the soliton successfully traverses the entire line, and the system returns to its initial physical state.

The behavior of the KICK in the T-Mode, which enables its use as a T-flip-flop, is detailed in Figure 2d. This mode is defined by the existence of two distinct stable states, physically corresponding to a bistable potential landscape created by the KICK architecture. These two states are distinguished by the presence of persistent, static currents of opposite polarity flowing from the central node ($k = 16$). This physical difference leads to an fundamentally state-dependent and asymmetric toggling action. When the KICK is in the first stable state, an incoming soliton successfully flips it to the second state and is transmitted, continuing its propagation down the line. Conversely, when starting from the second state, an arriving soliton again flips the KICK back to the first state, but it is annihilated in the process and does not propagate further. This state-dependent transmission and annihilation is the core mechanism that allows the KICK to function as a memory element or a dynamic routing switch.

Beyond primary operational modes, the system exhibits other notable behavior types in specific regions of its parameter

space. The M-Mode, for instance, is characterized by complex responses, depend on previous events. This can include such behavior when an initial soliton is annihilated, effectively "priming" the cell to transmit all subsequent solitons, a feature potentially useful for tasks like sequential filtering. Furthermore, in the transition regions between the primary modes, we observe phenomena such as soliton reflection back towards the source.

Finally, the asymptotic behavior in the high-damping (α) limit is particularly significant. As α increases, so does the soliton's velocity and kinetic energy. Consequently, for sufficiently high α, the soliton's energy is large enough to overcome any potential barrier presented by the KICK, ensuring transmission regardless of the inductance value. This results in a universal Open mode at high rates. Crucially, this high-energy passage is not inert; if the KICK is in a bistable regime (such as the T-Mode), the "passing" soliton can still deliver enough of an impulse to toggle the cell's state.

The soliton diode

What is even more interesting is that the KICK architecture can be engineered to function as a soliton diode, a device the function of which is similar to that of a semiconductor diode, allowing the soliton to pass in only one direction. This is achieved by introducing a structural asymmetry into the cell's design. It is important to note that such non-reciprocal behavior can be achieved even without the kinetic inductance ($L = 0$). However, the inclusion of one (i.e., a tunable inductance) is a key innovation, as it allows to dynamically switch this directional property on and off.

We demonstrate this principle through simulation of a KICK with $L/L_J = 2$. In our model, the transmission line's series junctions have a nominal critical current of $I_c = 0.7\tilde{I}_c$. The asymmetry is created by increasing the critical current of the specific junction connecting nodes 15 and 16 to $I_c = \tilde{I}_c$ (i.e., to 1 in normalized units). The effect of this asymmetric potential barrier is that a soliton initiated in the forward direction (from node 1) successfully overcomes it and is transmitted along the entire line. In contrast, a soliton propagating in the reverse direction (from node 31) is unable to pass the barrier and is annihilated at node 17.

Figure 3 demonstrates the non-reciprocal behavior of the soliton diode by showing a sequence of five snapshots of the nodal Josephson phase distribution at successive moments in time, arranged from top to bottom. The process begins with the line in its initial state (top panel), after which a soliton is initiated from the left side (node 1). As shown in the second panel, this forward-propagating soliton successfully passes through the diode, resulting in a 2π phase advance across all nodes. Immediately after, a new soliton is initiated from the right side (node 31) to test the reverse direction. The third panel reveals that this soliton is blocked; its propagation is halted at the diode, and the corresponding 2π phase slip is confined to nodes 17 through 31. The fourth panel confirms the robustness of this blocking action, as a second, subsequent reverse-propagating soliton is also annihilated in the same manner. To complete the demonstration, another forward-propagating soliton is sent from the left. The fifth panel confirms that the diode once again allows it to pass, resulting in another full 2π phase advance across the entire line. It is crucial to note that although the absolute phase values accumulate in multiples of 2π throughout this sequence, the physical state of the structure remains unchanged after each full transmission, a direct consequence of the 2π periodicity of the Josephson energy.

A significant feature of this structure is the ability to disable the diode effect. By increasing the inductance to $L/L_J = 3$, the device becomes bi-directionally transparent, effectively turning the diode function "off". This demonstrates how the introduced structural asymmetry alters the operational landscape of the device: An inductance value that would normally correspond to the Close mode in a symmetric KICK now matches to a bi-directional Open mode for the asymmetric diode structure. Furthermore, it is worth noting that the asymmetry required for diode-like behavior can be achieved through alternative means, such as by creating a local mismatch in the damping parameter, for instance, by increasing α from 1 to 3 for one of the series junctions instead of the critical current.

The ability to enforce a specific direction of soliton flow makes the soliton diode an essential component for complex circuit design. This is particularly critical in architectures involving feedback loops, where it is necessary to unambiguously define the direction of signal propagation. This concept can be extended by cascading two such tunable diodes with opposing forward directions. This configuration creates a programmable transmission line where the permitted direction of soliton travel can be pre-configured by setting the inductance values of each diode.

Discussion

Implementation of reconfigurable networks

On the basis of the operational principles of the kinetic inductance controllable key and the soliton diode, we now demonstrate how these fundamental building blocks can be integrated to create reconfigurable soliton-based logic circuits. We begin by proposing a specific proof-of-concept design for a signal routing network and then introduce a generalized, scalable architecture suitable for complex computational tasks.

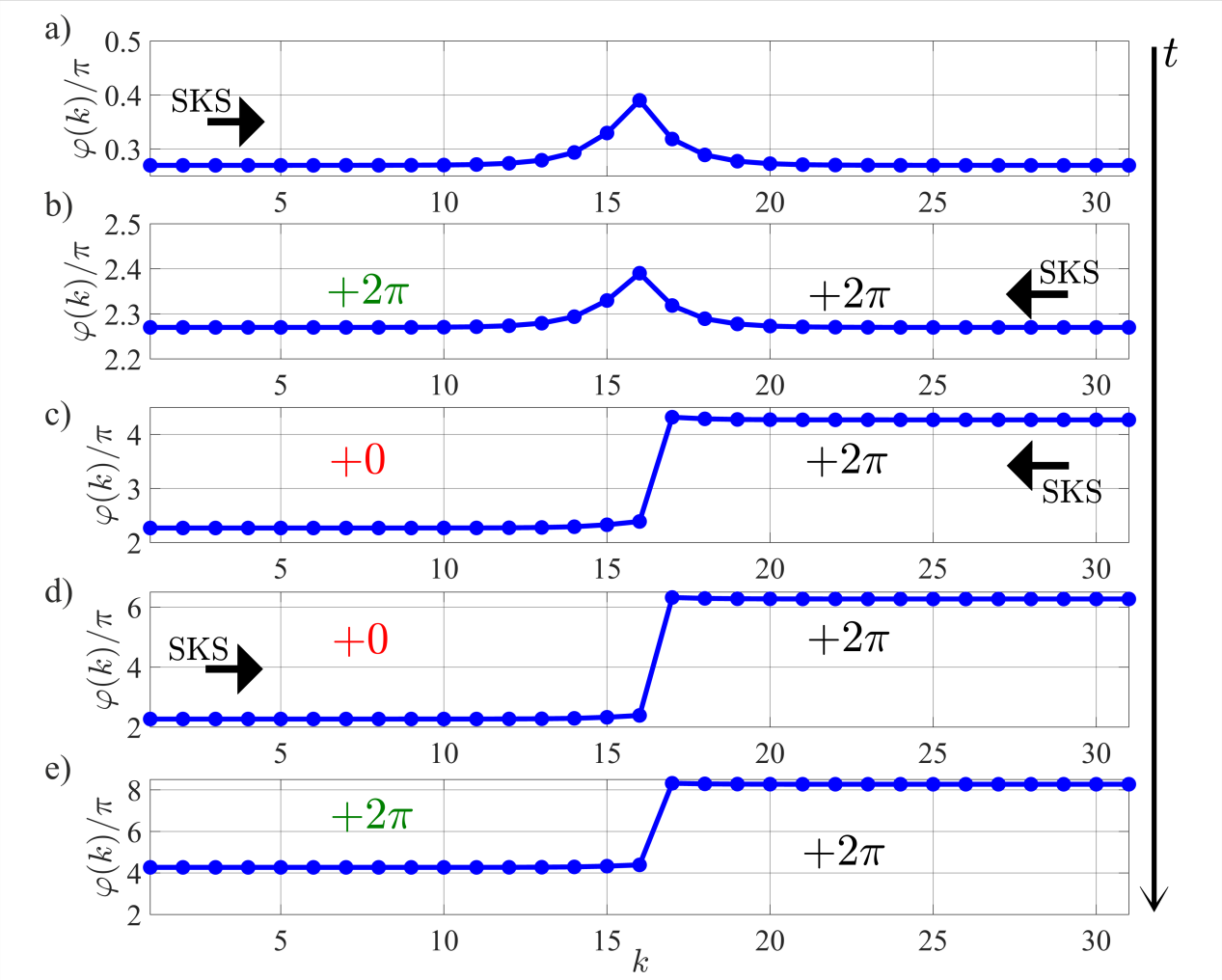


Figure 3: Temporal evolution of Josephson phase asymmetry in a soliton diode: (a) initial state; (b) after left-propagating soliton passage; (c, d) sequential right-propagating soliton interactions; (e) final left-propagating soliton recurrence.

As a direct application of the KICK's switching capabilities, we first propose the three-input, three-output routing network illustrated in Figure 4a. The proposed architecture is based on a grid where each path depicted is itself a complete all-JJTL. The routing mechanism would depend on the incorporation of KICKs into specific segments of these all-JJTLs. By programming each KICK to be in either its Open mode (transmitting) or Close mode (blocking), one could control the flow of solitons through the network and define a unique path from any input to any output. To prevent collisions between solitons traveling along different routes, the design incorporates auxiliary buffer lines. These lines make it possible to define a set of non-intersecting paths for all required connections, thus ensuring collision-free operation. This design serves to validate the fundamental principle of using KICKs as programmable switches.

With this idea, we propose a more general and powerful architecture, which we term the "WayMatrix", shown schematically in Figure 4b. This versatile $N \times M$ routing matrix is conceived as a core component of larger soliton-based processors. Its enhanced functionality would be predicated on the synergistic action of its core components. First, KICKs integrated into the line segments would act as programmable switches controlling the signal flow. Second, the directionality of soliton propagation would be rigorously enforced by integrated soliton diodes. Thus, the diodes and switches placed in the all-JJTL lines determine the direction of soliton propagation in the line. Finally, to solve the problem of collisions in a dense matrix, we propose dedicated vertical lines that enable row-skipping connections. For the same purposes, horizontal lines can also be used for column-skipping connections.

At first glance, it may seem that the proposed architecture is a complicated version of a memristive crossbar, but this is not the case. The main distinction is in the organization of interconnections between lines: In a memristive crossbar, as the name sug-

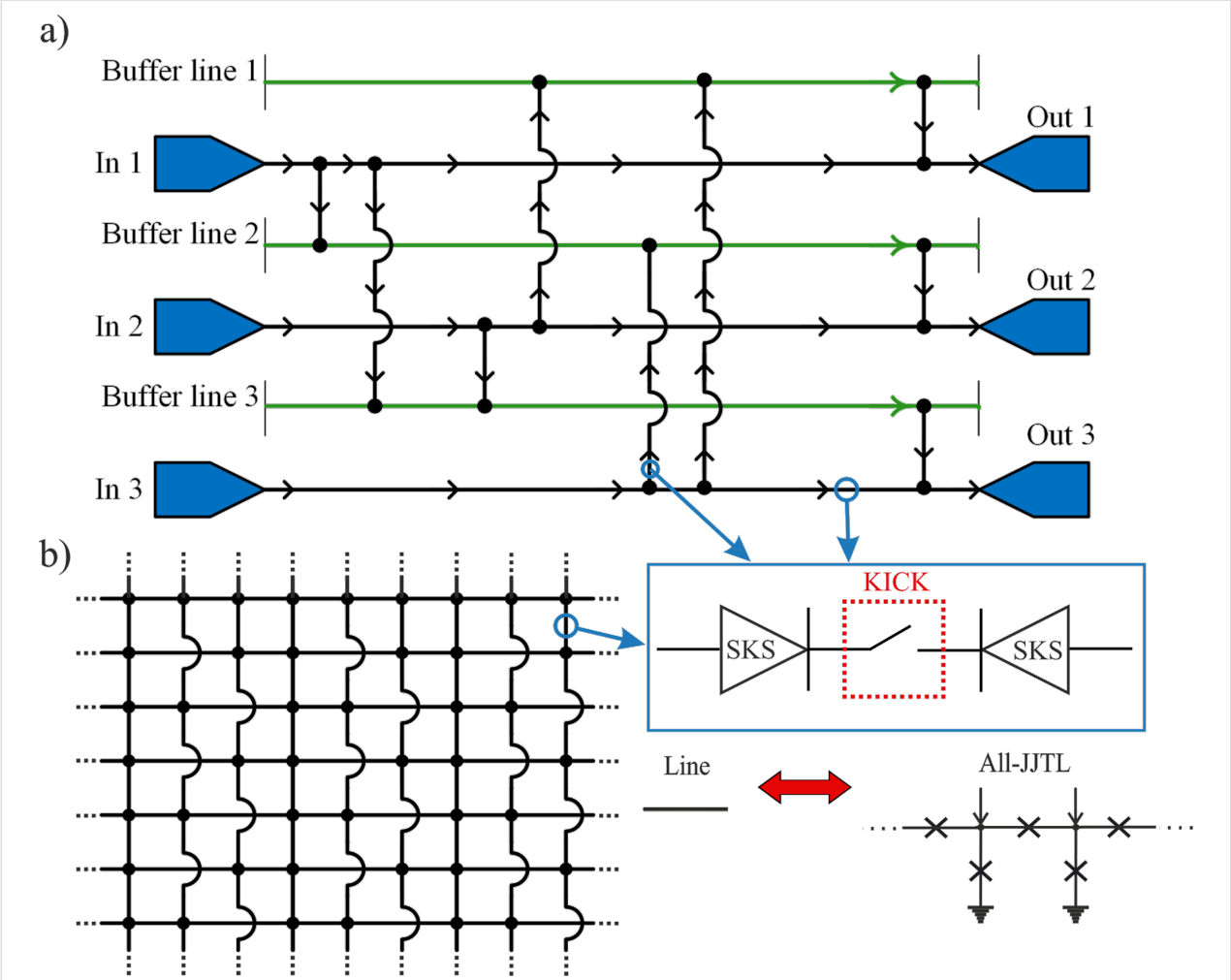


Figure 4: (a) Schematic of an all-Josephson-junction transmission line (all-JJTL) network with three inputs (In 1, In 2, In 3), three outputs (Out 1, Out 2, Out 3), and three auxiliary buffer lines. Black arrows on the lines indicate soliton propagation paths. Input–output connections are configured by setting operation modes of kinetic inductance controllable keys (KICKs), where each cell either transmits or blocks solitons based on its programmed state. (b) The schematic shows a transmission line matrix where path selection is governed by KICKs and signal directionality is ensured by soliton diodes. Specific vertical lines enable row-skipping connections to prevent soliton collisions during signal propagation.

gests, these connections are formed by the intersection of signal lines and the corresponding memristive layer. In the proposed WayMatrix, however, the lines are combined into a single node at the intersection point, the current direction of which can be controlled by switches and diodes. The power of the WayMatrix architecture lies in its potential use as a universal framework for creating programmable and reconfigurable connections between different circuit blocks. WayMatrix makes it easy to set up feedback loops between these blocks, change their connection order, and perform logical operations. We envision it serving as a reconfigurable “backbone” to link various specialized functional units within a larger integrated circuit. For example, the WayMatrix could be configured to connect arrays of memory cells to arithmetic logic units or to route data between different processing cores. Another key application is the creation of programmable clock distribution networks. In such a role, the WayMatrix could manage signal timing across a chip by introducing precise, configurable delays into the clock paths, which is crucial for asynchronous circuit design. This would allow a single hardware platform to be flexibly repurposed for different algorithms by simply re-programming the routing paths, a paradigm central to the development of SPGAs.

The true potential of this architecture, however, is most evident in its application as an axon-synaptic connection matrix for neuromorphic computing. The ability to program connections, enforce directionality, and reconfigure paths makes the WayMatrix an ideal candidate for emulating the complex and plastic connectivity of a biological neural network. In such a system, each soliton acts as a “spike”, and the WayMatrix serves as the synaptic network that routes these spikes between artificial neurons. This lays the groundwork for building power-

ful, event-driven, and energy-efficient spiking neural networks based on the principles we have outlined. In addition to using the WayMatrix, we can reconfigure the neural network itself, program connections between different neurons, implement synaptic pruning, and even "kill" parts of the artificial brain.

Human or animal brains contain a huge number of synapses, many times greater than the number of neurons (e.g., the Norwegian rat brain contains about 200 million neurons, each of which roughly has an average of about 1000 synapses [46]). The ability of a living being to solve certain tasks depends precisely on the number of interneuronal connections. In their attempts to implement such complex systems in hardware, engineers and scientists inevitably face the problem of interconnects and the implementation of a huge number of synaptic connections. The superconducting axon-synaptic matrix based on the WayMatrix concept seems to be a promising solution to the problem [47-50].

As mentioned above repeatedly, the field applications of kinetic inductance and, in particular, KICK, also extend to bio-inspired neuromorphic spiking networks. One important feature of living nervous tissues is the ability to modulate the synaptic delay of signal propagation from one neuron to another. This feature is equally important to implement in hardware artificial realizations of neuromorphic networks. The signal propagation delay is also affected by a length and a conductivity of an axon, which is quite simply imitated by means of a standard Josephson transmission line, as well as by means of all-JJTLs, discussed at the beginning of this article. A simple solution to modulate the propagation delay is to change the length (number of JTL cells) of such an artificial axon, but there is another way. The inductance connected in parallel with the Josephson junctions determines the amount of magnetic energy stored within each JTL cell. Consequently, a larger inductance value results in a longer propagation delay.

Conclusion

This study demonstrates the programmable control of kinetic soliton dynamics in all-Josephson-junction networks through a novel tunable element, the "kinetic inductance controllable key" (KICK). By engineering inhomogeneity via controlled kinetic inductance, we induce distinct dynamical modes (Open mode, Close mode, and T-mode) that fundamentally alter soliton propagation. Furthermore, the features of the proposed cell enable a soliton diode effect, achieving non-reciprocal signal transmission. Building on these principles, we propose two scalable architectures, namely, a programmable switch for reconfigurable routing and the WayMatrix, a versatile $N \times M$ routing matrix. These solutions establish a framework for robust, high-speed superconducting logic that addresses critical bottlenecks in this type of computing.

We realize that the time required to "reprogram" kinetic inductance significantly exceeds the picosecond timescales of Josephson junction dynamics. However, this re-configuration time should be considered in the context of hardware development cycles. From this point of view, the re-configuration time is orders of magnitude lower than the time required to design, fabricate, and test a new application-specific integrated circuit (ASIC), offering a compelling advantage in flexibility and prototyping rate.

The superconducting diodes proposed in this work can be used as a part of synaptic connections in neuromorphic networks to prevent the backward influence of a postsynaptic neuron on a presynaptic neuron through the same connection link. It should also be noted that the signal propagation time between neurons can be controlled by modulating the bias currents, the value of which directly affects the potential barrier in Josephson line (standard JTL or All-JJTL). Thus, the choice of a particular method of signal propagation delay influence depends on the realization of interneuron interactions and the need to adjust a particular interneuron connection. Moreover, these approaches can be combined into one by using a chain of superconductor diodes. Using cells with kinetic inductances, we can change the local propagation speed of spikes in interneuronal signal transmission circuits by smoothly adjusting the delay time. The integration of the WayMatrix will make it possible to change the length of the axonal line as a whole, and thus introduce a delay. Besides, it is really interesting to examine how the dynamics of voltage spike formation in a bio-inspired neuron, proposed in [42], will change if we substitute geometric inductances for kinetic ones. Further development of the idea presented in this article will also address this aspect.

The proposed technique allows for a more compact design and new (diode) functionality of various superconducting computing modules and makes possible further increase of integration density compared to well-known RSFQ technology.

Funding

N.K. and M.K. are grateful to Russian Science Foundation for the support of theoretical study of controlled kinetic inductance as a programmable element for superconducting logic (Project no. 25-19-00057). S.B. and I.S. are grateful the Ministry of Science and Higher Education of the Russian Federation for the support of the study of reconfigurable networks. (Agreement no. 075-15-2025-010). A.M. is grateful to the Foundation for the Advancement of Theoretical Physics and Mathematics "BASIS" (A.M. grant 24-2-10-6-1).

ORCID® iDs

Vsevolod I. Ruzhickiy - https://orcid.org/0000-0002-3411-7050
Anastasia A. Maksimovskaya - https://orcid.org/0009-0002-4197-2263
Sergey V. Bakurskiy - https://orcid.org/0000-0002-6010-6697
Andrey E. Schegolev - https://orcid.org/0000-0002-5381-3297
Maxim V. Tereshonok - https://orcid.org/0000-0003-1330-281X
Mikhail Yu. Kupriyanov - https://orcid.org/0000-0003-1204-9664
Nikolay V. Klenov - https://orcid.org/0000-0001-6265-3670
Igor I. Soloviev - https://orcid.org/0000-0001-9735-2720

Data Availability Statement

Data generated and analyzed during this study is available from the corresponding author upon reasonable request.

Preprint

A non-peer-reviewed version of this article has been previously published as a preprint: https://doi.org/10.3762/bxiv.2025.49.v1

References

1. Likharev, K. K. *Dynamics of Josephson junctions and circuits;* CRC Press: Boca Raton, FL, USA, 1986.
2. Likharev, K. K. *Phys. C (Amsterdam, Neth.)* **2012,** *482,* 6–18. doi:10.1016/j.physc.2012.05.016
3. Holmes, D. S.; Ripple, A. L.; Manheimer, M. A. *IEEE Trans. Appl. Supercond.* **2013,** *23,* 1701610. doi:10.1109/tasc.2013.2244634
4. Tolpygo, S. K. *Low Temp. Phys.* **2016,** *42,* 361–379. doi:10.1063/1.4948618
5. Ahmad, M.; Giagkoulovits, C.; Danilin, S.; Weides, M.; Heidari, H. *Adv. Intell. Syst.* **2022,** *4,* 2200079. doi:10.1002/aisy.202200079
6. Marković, D.; Mizrahi, A.; Querlioz, D.; Grollier, J. *Nat. Rev. Phys.* **2020,** *2,* 499–510. doi:10.1038/s42254-020-0208-2
7. Schneider, M.; Toomey, E.; Rowlands, G.; Shainline, J.; Tschirhart, P.; Segall, K. *Supercond. Sci. Technol.* **2022,** *35,* 053001. doi:10.1088/1361-6668/ac4cd2
8. Jardine, M. A.; Fourie, C. J. *IEEE Trans. Appl. Supercond.* **2023,** *33,* 1302409. doi:10.1109/tasc.2023.3248140
9. Karamuftuoglu, M. A.; Bozbey, A.; Razmkhah, S. *IEEE Trans. Appl. Supercond.* **2023,** *33,* 1400607. doi:10.1109/tasc.2023.3270766
10. Yamanashi, Y.; Nakaishi, S.; Sugiyama, A.; Takeuchi, N.; Yoshikawa, N. *Supercond. Sci. Technol.* **2018,** *31,* 105003. doi:10.1088/1361-6668/aad78d
11. Soloviev, I. I.; Ruzhickiy, V. I.; Bakurskiy, S. V.; Klenov, N. V.; Kupriyanov, M. Yu.; Golubov, A. A.; Skryabina, O. V.; Stolyarov, V. S. *Phys. Rev. Appl.* **2021,** *16,* 014052. doi:10.1103/physrevapplied.16.014052
12. Maksimovskaya, A. A.; Ruzhickiy, V. I.; Klenov, N. V.; Bakurskiy, S. V.; Kupriyanov, M. Y.; Soloviev, I. I. *J. Exp. Theor. Phys. Lett.* **2022,** *115,* 735–741. doi:10.1134/s0021364022600884
13. Salameh, I.; Friedman, E. G.; Kvatinsky, S. *IEEE Trans. Circuits Syst. II: Express Briefs* **2022,** *69,* 2533–2537. doi:10.1109/tcsii.2022.3162723
14. Tanemura, S.; Takeshita, Y.; Li, F.; Nakayama, T.; Tanaka, M.; Fujimaki, A. *IEEE Trans. Appl. Supercond.* **2023,** *33,* 1701305. doi:10.1109/tasc.2023.3258374
15. Jabbari, T.; Bocko, M.; Friedman, E. G. *IEEE Trans. Appl. Supercond.* **2023,** *33,* 1303807. doi:10.1109/tasc.2023.3260774
16. Razmkhah, S.; Pedram, M. *Eng. Res. Express* **2024,** *6,* 015307. doi:10.1088/2631-8695/ad27f5
17. Annunziata, A. J.; Santavicca, D. F.; Frunzio, L.; Catelani, G.; Rooks, M. J.; Frydman, A.; Prober, D. E. *Nanotechnology* **2010,** *21,* 445202. doi:10.1088/0957-4484/21/44/445202
18. Adamyan, A. A.; Kubatkin, S. E.; Danilov, A. V. *Appl. Phys. Lett.* **2016,** *108,* 172601. doi:10.1063/1.4947579
19. Mahashabde, S.; Otto, E.; Montemurro, D.; de Graaf, S.; Kubatkin, S.; Danilov, A. *Phys. Rev. Appl.* **2020,** *14,* 044040. doi:10.1103/physrevapplied.14.044040
20. Splitthoff, L. J.; Bargerbos, A.; Grünhaupt, L.; Pita-Vidal, M.; Wesdorp, J. J.; Liu, Y.; Kou, A.; Andersen, C. K.; van Heck, B. *Phys. Rev. Appl.* **2022,** *18,* 024074. doi:10.1103/physrevapplied.18.024074
21. Wang, C.-G.; Yue, W.-C.; Tu, X.; Chi, T.; Guo, T.; Lyu, Y.-Y.; Dong, S.; Cao, C.; Zhang, L.; Jia, X.; Sun, G.; Kang, L.; Chen, J.; Chen, J.; Wang, Y.-L.; Wang, H.; Wu, P. *Chin. Phys. B* **2024,** *33,* 058402. doi:10.1088/1674-1056/ad2f21
22. Li, J.; Barry, P.; Cecil, T.; Lisovenko, M.; Yefremenko, V.; Wang, G.; Kruhlov, S.; Karapetrov, G.; Chang, C. *Phys. Rev. Appl.* **2024,** *22,* 014080. doi:10.1103/physrevapplied.22.014080
23. Ustavschikov, S. S.; Levichev, M. Y.; Pashenkin, I. Y.; Klushin, A. M.; Vodolazov, D. Y. *Supercond. Sci. Technol.* **2021,** *34,* 015004. doi:10.1088/1361-6668/abc2ad
24. Levichev, M. Y.; Pashenkin, I. Y.; Gusev, N. S.; Vodolazov, D. Y. *Phys. Rev. B* **2023,** *108,* 094517. doi:10.1103/physrevb.108.094517
25. Neilo, A.; Bakurskiy, S.; Klenov, N.; Soloviev, I.; Kupriyanov, M. *Nanomaterials* **2024,** *14,* 245. doi:10.3390/nano14030245
26. Neilo, A. A.; Bakurskiy, S. V.; Klenov, N. V.; Soloviev, I. I.; Kupriyanov, M. Y. *J. Exp. Theor. Phys. Lett.* **2025,** *121,* 58–66. doi:10.1134/s0021364024604391
27. Fourie, C. J.; van Heerden, H. *IEEE Trans. Appl. Supercond.* **2007,** *17,* 538–541. doi:10.1109/tasc.2007.897387
28. Hironaka, Y.; Hosoya, T.; Yamanashi, Y.; Yoshikawa, N. *IEEE Trans. Appl. Supercond.* **2022,** *32,* 1301305. doi:10.1109/tasc.2022.3191984
29. Hosoya, T.; Yamanashi, Y.; Yoshikawa, N. *IEEE Trans. Appl. Supercond.* **2021,** *31,* 1300406. doi:10.1109/tasc.2021.3049771
30. Katam, N. K.; Mukhanov, O. A.; Pedram, M. *IEEE Trans. Appl. Supercond.* **2018,** *28,* 1300212. doi:10.1109/tasc.2018.2797262
31. Schuman, C. D.; Kulkarni, S. R.; Parsa, M.; Mitchell, J. P.; Date, P.; Kay, B. *Nat. Comput. Sci.* **2022,** *2,* 10–19. doi:10.1038/s43588-021-00184-y
32. Kudithipudi, D.; Schuman, C.; Vineyard, C. M.; Pandit, T.; Merkel, C.; Kubendran, R.; Aimone, J. B.; Orchard, G.; Mayr, C.; Benosman, R.; Hays, J.; Young, C.; Bartolozzi, C.; Majumdar, A.; Cardwell, S. G.; Payvand, M.; Buckley, S.; Kulkarni, S.; Gonzalez, H. A.; Cauwenberghs, G.; Thakur, C. S.; Subramoney, A.; Furber, S. *Nature* **2025,** *637,* 801–812. doi:10.1038/s41586-024-08253-8
33. Schegolev, A. E.; Bastrakova, M. V.; Sergeev, M. A.; Maksimovskaya, A. A.; Klenov, N. V.; Soloviev, I. *Mesosci. Nanotechnol.* **2024,** *1,* 01-01005. doi:10.64214/jmsn.01.01005
34. Schegolev, A. E.; Klenov, N. V.; Bakurskiy, S. V.; Soloviev, I. I.; Kupriyanov, M. Y.; Tereshonok, M. V.; Sidorenko, A. S. *Beilstein J. Nanotechnol.* **2022,** *13,* 444–454. doi:10.3762/bjnano.13.37

35. Merolla, P. A.; Arthur, J. V.; Alvarez-Icaza, R.; Cassidy, A. S.; Sawada, J.; Akopyan, F.; Jackson, B. L.; Imam, N.; Guo, C.; Nakamura, Y.; Brezzo, B.; Vo, I.; Esser, S. K.; Appuswamy, R.; Taba, B.; Amir, A.; Flickner, M. D.; Risk, W. P.; Manohar, R.; Modha, D. S. *Science* **2014,** *345,* 668–673. doi:10.1126/science.1254642
36. Indiveri, G.; Liu, S.-C. *Proc. IEEE* **2015,** *103,* 1379–1397. doi:10.1109/jproc.2015.2444094
37. Crotty, P.; Schult, D.; Segall, K. *Phys. Rev. E* **2010,** *82,* 011914. doi:10.1103/physreve.82.011914
38. Goteti, U. S.; Dynes, R. C. *J. Appl. Phys.* **2021,** *129,* 073901. doi:10.1063/5.0027997
39. Semenov, V. K.; Golden, E. B.; Tolpygo, S. K. *IEEE Trans. Appl. Supercond.* **2023,** *33,* 1400308. doi:10.1109/tasc.2023.3252495
40. Feldhoff, F.; Toepfer, H. *IEEE Trans. Appl. Supercond.* **2024,** *34,* 1300105. doi:10.1109/tasc.2024.3355876
41. Skryabina, O. V.; Schegolev, A. E.; Klenov, N. V.; Bakurskiy, S. V.; Shishkin, A. G.; Sotnichuk, S. V.; Napolskii, K. S.; Nazhestkin, I. A.; Soloviev, I. I.; Kupriyanov, M. Y.; Stolyarov, V. S. *Nanomaterials* **2022,** *12,* 1671. doi:10.3390/nano12101671
42. Schegolev, A. E.; Klenov, N. V.; Gubochkin, G. I.; Kupriyanov, M. Y.; Soloviev, I. I. *Nanomaterials* **2023,** *13,* 2101. doi:10.3390/nano13142101
43. Maksimovskaya, A. A.; Ruzhickiy, V. I.; Klenov, N. V.; Schegolev, A. E.; Bakurskiy, S. V.; Soloviev, I. I.; Yakovlev, D. S. *Chaos, Solitons Fractals* **2025,** *193,* 116074. doi:10.1016/j.chaos.2025.116074
44. Dormand, J. R.; Prince, P. J. *J. Comput. Appl. Math.* **1980,** *6,* 19–26. doi:10.1016/0771-050x(80)90013-3
45. Shampine, L. F.; Reichelt, M. W. *SIAM J. Sci. Comput.* **1997,** *18,* 1–22. doi:10.1137/s1064827594276424
46. Swanson, L. W. *J. Comp. Neurol.* **2018,** *526,* 935–943. doi:10.1002/cne.24381
47. Xia, Q.; Yang, J. J. *Nat. Mater.* **2019,** *18,* 309–323. doi:10.1038/s41563-019-0291-x
48. El Mesoudy, A.; Lamri, G.; Dawant, R.; Arias-Zapata, J.; Gliech, P.; Beilliard, Y.; Ecoffey, S.; Ruediger, A.; Alibart, F.; Drouin, D. *Microelectron. Eng.* **2022,** *255,* 111706. doi:10.1016/j.mee.2021.111706
49. Chakraborty, I.; Ali, M.; Ankit, A.; Jain, S.; Roy, S.; Sridharan, S.; Agrawal, A.; Raghunathan, A.; Roy, K. *Proc. IEEE* **2020,** *108,* 2276–2310. doi:10.1109/jproc.2020.3003007
50. Xu, Q.; Wang, J.; Yuan, B.; Sun, Q.; Chen, S.; Yu, B.; Kang, Y.; Wu, F. *IEEE Trans. Autom. Sci. Eng.* **2023,** *20,* 74–87. doi:10.1109/tase.2021.3125065

License and Terms

This is an open access article licensed under the terms of the Beilstein-Institut Open Access License Agreement (https://www.beilstein-journals.org/bjnano/terms), which is identical to the Creative Commons Attribution 4.0 International License (https://creativecommons.org/licenses/by/4.0). The reuse of material under this license requires that the author(s), source and license are credited. Third-party material in this article could be subject to other licenses (typically indicated in the credit line), and in this case, users are required to obtain permission from the license holder to reuse the material.

The definitive version of this article is the electronic one which can be found at:
https://doi.org/10.3762/bjnano.16.131

BEILSTEIN JOURNAL OF NANOTECHNOLOGY

Quantum circuits with SINIS structures

Mikhail Tarasov*[1], Mikhail Fominskii[1], Aleksandra Gunbina[1], Artem Krasilnikov[2,3], Maria Mansfeld[2,3], Dmitrii Kukushkin[3,4], Andrei Maruhno[3], Valeria Ievleva[5], Mikhail Strelkov[1], Daniil Zhogov[1], Konstantin Arutyunov[6,7], Vyacheslav Vdovin[2,3], Vladislav Stolyarov[3] and Valerian Edelman[7]

Full Research Paper

Open Access

Address:
[1]V. Kotelnikov Institute of Radio Engineering and Electronics RAS, Moscow, Russia, [2]Institute of Applied Physics RAS, Nizhny Novgorod, Russia, [3]Special Astrophysical Observatory RAS, Nizhnii Arkhyz, Russia, [4]ITMO University, Saint Petersburg, Russia, [5]P.N. Lebedev Physical Institute of the Russian Academy of Sciences, 119991 Moscow, [6]National Research University "Higher School of Economics," Moscow, 101000 Russia and [7]P. Kapitza Institute for Physical Problems RAS, Moscow, Russia

Email:
Mikhail Tarasov* - tarasov@hitech.cplire.ru

* Corresponding author

Keywords:
Big Telescope Alt-azimuthal; electron coolers; microwave detectors; micro- and nanotechnology; NIS tunnel junction; superconducting tunnel junctions

Beilstein J. Nanotechnol. **2025,** *16,* 1931–1941.
https://doi.org/10.3762/bjnano.16.134

Received: 12 August 2025
Accepted: 08 October 2025
Published: 04 November 2025

This article is part of the thematic issue "Superconducting artificial neural networks and quantum circuits".

Guest Editor: A. S. Sidorenko

© 2025 Tarasov et al.; licensee Beilstein-Institut.
License and terms: see end of document.

Abstract

The superconductor–insulator–normal metal–insulator–superconductor (SINIS) tunnel junction structure is the basic building block for various cryogenic devices. Microwave detectors, electron coolers, primary thermometers, and Aharonov–Bohm interferometers have been fabricated by various methods and measured at temperatures down to 100 mK. The manufacturing methods included Dolan-type shadow evaporation, Manhattan-type shadow evaporation, and magnetron sputtering with selective etching of superconducting and normal metal electrodes. Improvement in ultimate sensitivity is achieved by suspending the absorber above the substrate. Best responsivity of up to 30 electrons per photon at a frequency of 350 GHz, or 72000 A/W, and voltage responsivity up to 3.9×10^9 V/W were obtained with a black body radiation source and series of band-pass filters. The specially designed SINIS arrays are intended to detect 90 GHz radiation at the “Big Telescope Alt-azimuthal” (romanized Russian: “Bolshoi Teleskop Alt-azimutalnyi”, BTA) with noise equivalent power of less than 10^{-16} W·Hz$^{-1/2}$. The receiver in a ^{3}He cryostat with an optical window was mounted at the Nasmyth focus of the BTA and tested at a temperature of 260 mK with a IMPATT diode radiation source.

Introduction

Modern superconducting electronics is moving towards lower temperatures, lower noise levels, and higher sensitivity, which can be achieved at sub-Kelvin temperatures using aluminum-based tunnel junctions. One group of devices, such as superconducting quantum interference devices (SQUIDs) and rapid single flux quantum circuits, are based on superconductor–insu-

lator–superconductor (SIS) junctions, another uses superconductor–insulator–normal metal (SIN) junctions. Tunnel junctions based on the SIN structure are widely used, and many different devices are manufactured on their basis [1-3]. These extend from cryogenic thermometers [4-6] and electron coolers [7-10] to various detectors such as Andreev bolometers [11-13], cold electron bolometers [14,15], superconductor–insulator–normal metal–insulator–superconductor (SINIS) bolometers [16,17], and SINIS detectors [18-20]. Here, we present an overview and comparison of our SINIS devices manufactured using different methods. The advantage of Al-based technology is the presence of the intrinsic oxide on its surface, which prevents short circuits with subsequent conductive layers and ensures ease of manufacturing a tunnel barrier, in contrast to Nb-based technology, which requires the formation of an artificial anodic oxide or an additional insulating layer to prevent short circuits, as well as an additional Al layer to form an AlO_x or AlN tunnel barrier.

Results

NIS tunnel junction

In tunnel structures, the barrier is a dielectric layer between two metal films (often the oxide layer on the surface of the first metal layer is used as a dielectric). The first experimental study of a tunnel junction was carried out in 1960 [21] for an aluminum–aluminum oxide–lead contact. When tunneling from a normal metal into a superconductor, due to the presence of an energy gap (Δ), only electrons whose energy exceeds Δ can tunnel into the superconductor. Without applying an external voltage or in the case when $eV < \Delta$ ($T = 0$), tunneling does not occur. Accordingly, a tunnel current occurs when $eV > \Delta$. In the case when $T \neq 0$ the *I*–*V* curve will be smeared [22].

The current–voltage characteristic of a tunnel NIS junction is determined by the following formula [23]:

$$I = \frac{1}{eR_\mathrm{n}} \int_{-\infty}^{+\infty} N_\mathrm{S}(E)\left[n_\mathrm{N}(E-eV) - n_\mathrm{S}(E)\right] \mathrm{d}E, \qquad (1)$$

where R_n is the asymptotic resistance of the tunnel junction, $N_\mathrm{S}(E)$ is the density of states in the superconductor, n_S is the distribution function in the superconductor, and n_N is the distribution function in the normal metal. At temperatures $T \ll T_\mathrm{c}$ (T_c is the critical temperature of the superconductor), the relationship between the tunnel current and voltage can be written using a simplified formula:

$$I = \frac{2\Delta}{eR_\mathrm{n}} \sqrt{2\pi k_\mathrm{B} T \Delta} \cdot \exp\left(-\frac{\Delta}{k_\mathrm{B}T}\right) \sinh\left(\frac{eV}{k_\mathrm{B}T}\right), \qquad (2)$$

where Δ is the energy gap of the superconductor and k_B is the Boltzmann constant. The differential resistance is expressed by the following formula:

$$R_d = R_\mathrm{n} \sqrt{\frac{k_\mathrm{B}T}{2\pi\Delta}} \cdot \exp\left(\frac{\Delta}{k_\mathrm{B}T}\right) \left(\cosh\left(\frac{eV}{k_\mathrm{B}T}\right)\right)^{-1}. \qquad (3)$$

It should also be noted that, in addition to the tunnel current in NIS structures, the presence of a subgap (Andreev) current caused by the Andreev reflection effect is possible [24]. In general terms, the Andreev reflection process is as follows: An electron from a normal metal hitting the SN boundary, passes into the superconductor in the form of a Cooper pair, and a hole is reflected from the SN boundary back into the normal metal. In the simplest case, the Andreev current can be written as the sum of contributions associated with the transfer of electrons in the normal metal (I_N) and the superconductor (I_S), [25]:

$$I_\mathrm{N} = \frac{\hbar}{e^3 R_\mathrm{n}^2 S \nu_\mathrm{N} d_\mathrm{N}} \tanh\frac{eV}{k_\mathrm{B}T}, \qquad (4)$$

$$I_\mathrm{S} = \frac{\hbar}{e^3 R_\mathrm{n}^2 S \nu_\mathrm{S} d_\mathrm{S}} \frac{eV/\Delta}{2\pi\sqrt{1-eV/\Delta}}, \qquad (5)$$

where ν_N and ν_S are the densities of electron states in a normal metal and a superconductor, S is the area of the tunnel NIS junction, d_N and d_S are the thicknesses of the normal metal and superconductor films, respectively.

Another feature of the tunnel–NIS junction is the phenomenon of electron cooling. This process is a transfer of heat from a normal metal to a superconductor and is caused by the fact that charge carriers with higher energy (exceeding the value of $\Delta - eV$) move from the metal to the superconductor, and those with lower energy remain in the normal metal. As a result, a heat flow arises from the normal metal (P is the power of electron cooling) [26]:

$$P = Q - IV = \frac{1}{e^2 R_\mathrm{n}} \int_{-\infty}^{+\infty} E N_\mathrm{S}(E)\left[n_\mathrm{N}(E-eV) - n_\mathrm{S}(E)\right] \mathrm{d}E, \qquad (6)$$

where Q is the total power released in the superconductor, IV is the Joule heat, n_N and n_S are the distribution functions of electrons and holes in normal metal and superconductor, respectively. As can be seen from the formula, the electron cooling power depends on both the temperature of the normal metal and the temperature of the superconductor.

Fabrication techniques

Historically, aluminum tunnel junctions were fabricated by shadow evaporation at different angles by the so-called Dolan technology [27]. It requires the formation of a two-layer resist with suspended bridge of the top resist layer (Figure 1a). The advantage of the technique is its simplicity, drawbacks are not very high reproducibility and stability. Another fabrication method is the Manhattan technology [28] with deep orthogonal groves in the resist, see Figure 1b,c. Both methods are based on thermal evaporation at different angles and rotation of substrate, requiring rather sophisticated and expensive deposition plants with thermal or e-beam evaporation. A much more available and simple deposition equipment is magnetron sputtering, but it provides only isotropic deposition, which is incompatible with anisotropic shadow evaporation. The practical solution for a magnetron sputtering is selective etching of different layers of superconducting aluminum and normal metal (e.g., copper). In case of chemical wet etching, this is achieved through an alkali and acid pair, for dry etching, chlorine and fluorine plasmas are used. Alternatively, in the case of magnetron sputtering and separate lithography, ion etching is used before making of the insulator and sputtering of the normal metal (for details see [29]). An example of such a method is presented in Figure 1d,e. Besides SINIS structures with N-absorber on the substrate, we also developed devices with the absorber suspended above the substrate (Figure 1f, technology with wet etching) that are promising for detectors and electron coolers. More details on various technologies and specific features of the fabrication of tunnel structures are provided in a review publication [29].

Aharonov–Bohm interferometer

The Aharonov–Bohm interferometer is a hybrid nanostructure consisting of a T-shaped normal metal electrode (copper), an insulating tunnel layer (aluminum oxide), and a superconducting fork (aluminum), Figure 2a. Tunnel junction size is 0.2×0.2 μm, loop area 2, 4, 8, or 10 μm^2. The transport characteristics of the fabricated interferometers were studied in sorption ^{3}He cryostat at 0.33 K, Figure 2b. The relatively low value of the resistance ratio (R_d/R_n – dynamic resistance/normal resistance) is associated with the high sensitivity of the interferometer to external noise.

NIS thermometers

The I–V characteristic and dynamic resistance of the NIS junction are described by simple relations (Equation 2 and Equation 3), which do not contain fit parameters. In the case of negligibly small Andreev currents suppressed by the ferromagnetic sublayer, such characteristics can be used as primary thermometers [30]. A simple figure of merit for NIS thermometers is the ratio of the resistance at zero bias to the asymptotic one (Equation 7):

$$RR = \left(0.09\,T_e/T_c\right) \times \exp\left(1.76\,T_e/T_c\right), \tag{7}$$

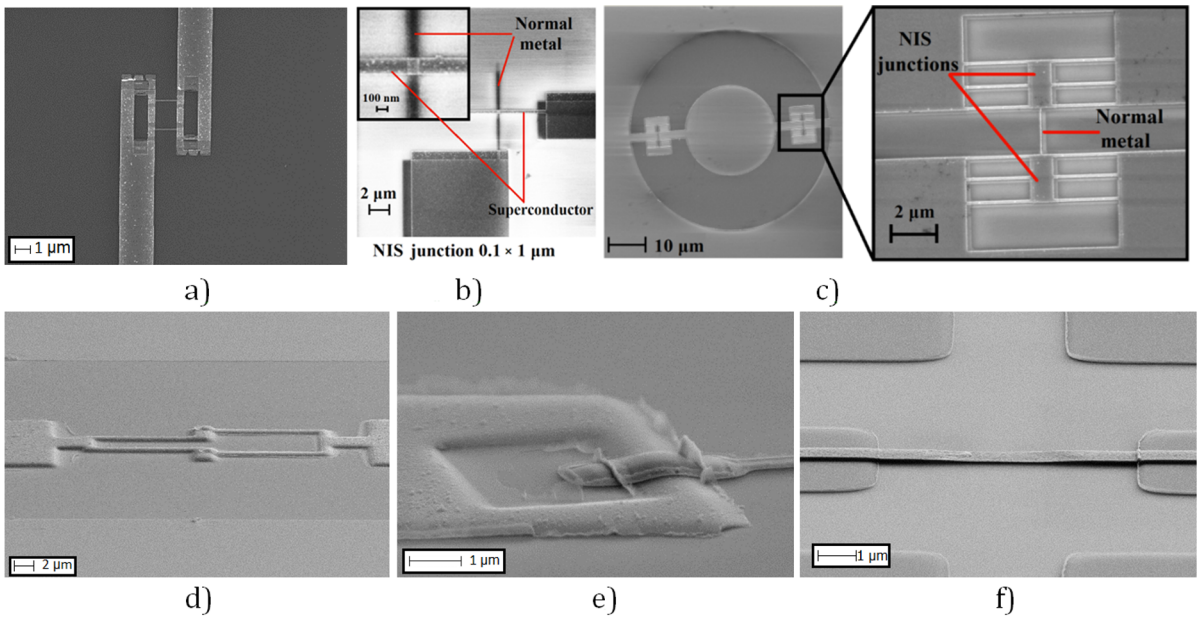


Figure 1: Photos of various tunnel structures fabricated using different technologies. (a) SINIS detector made by using Dolan technology, (b) single tunnel NIS junction and (c) circular antenna with SINIS detector made by Manhattan technology, (d) single SQUID and (e) single NIS junction made by magnetron sputtering with separate lithography, and (f) single SINIS detector with suspended Hf absorber.

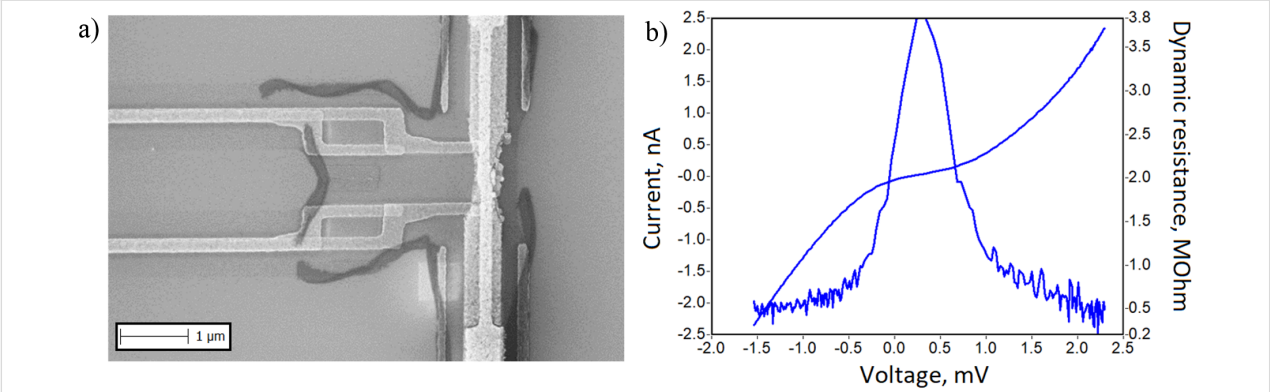


Figure 2: Aharonov–Bohm structure. (a) SEM image of the sample made by Manhattan-type SINIS fabrication and (b) *I*–*V* curve and dynamic resistance of the Aharonov–Bohm interferometer at 330 mK.

obtained from the general relation in Equation 3. For $I(V) = I_0\exp[(eV - \Delta)/kT_e]$ the temperature sensitivity at low bias current can be approximated as $dV/dT_e = (k/e)\ln(I/I_0) \approx -V_\Delta/T_e$. To reduce the influence of external noise and increase the signal-to-noise ratio, the NIS junctions are connected in series arrays (Figure 3). The temperature dependency of the resistance ratio for aluminum SIN junctions is shown in Figure 4.

Electron coolers

The tunneling current, when biased near the energy gap, carries hot quasiparticles out of the normal electrode, which leads to electron cooling, as in a Peltier element. In a single SINIS structure, it is possible to reduce the electron temperature from 260 to 90 mK [31]. Cascaded NIS coolers can be efficient refrigerators for cooling from 1 K to below 100 mK [32]. One of the

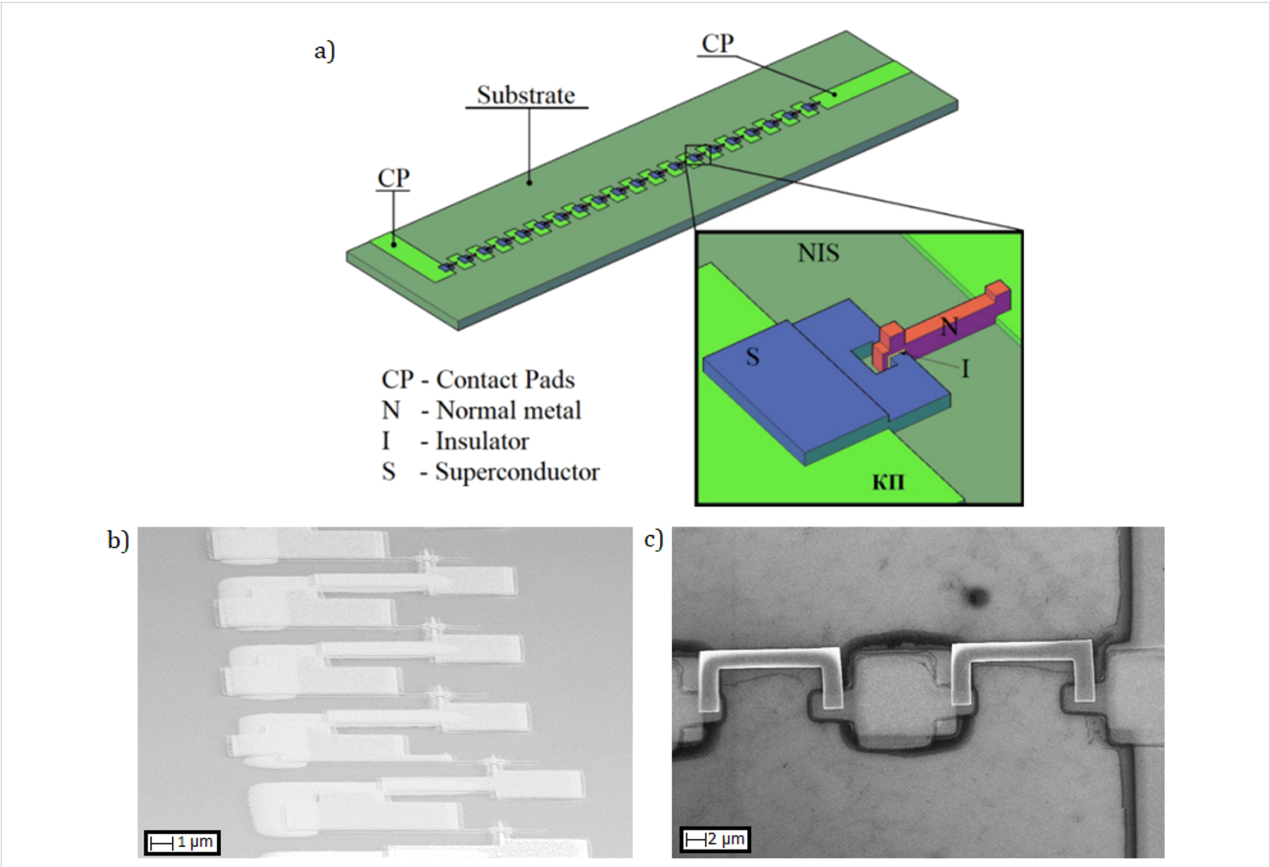


Figure 3: NIS thermometer series array. (a) Schematic view of a thermometer with a chain of 20 NIS junctions and SEM images of thermometers made by (b) Manhattan technology and (c) magnetron sputtering with separate lithography technology.

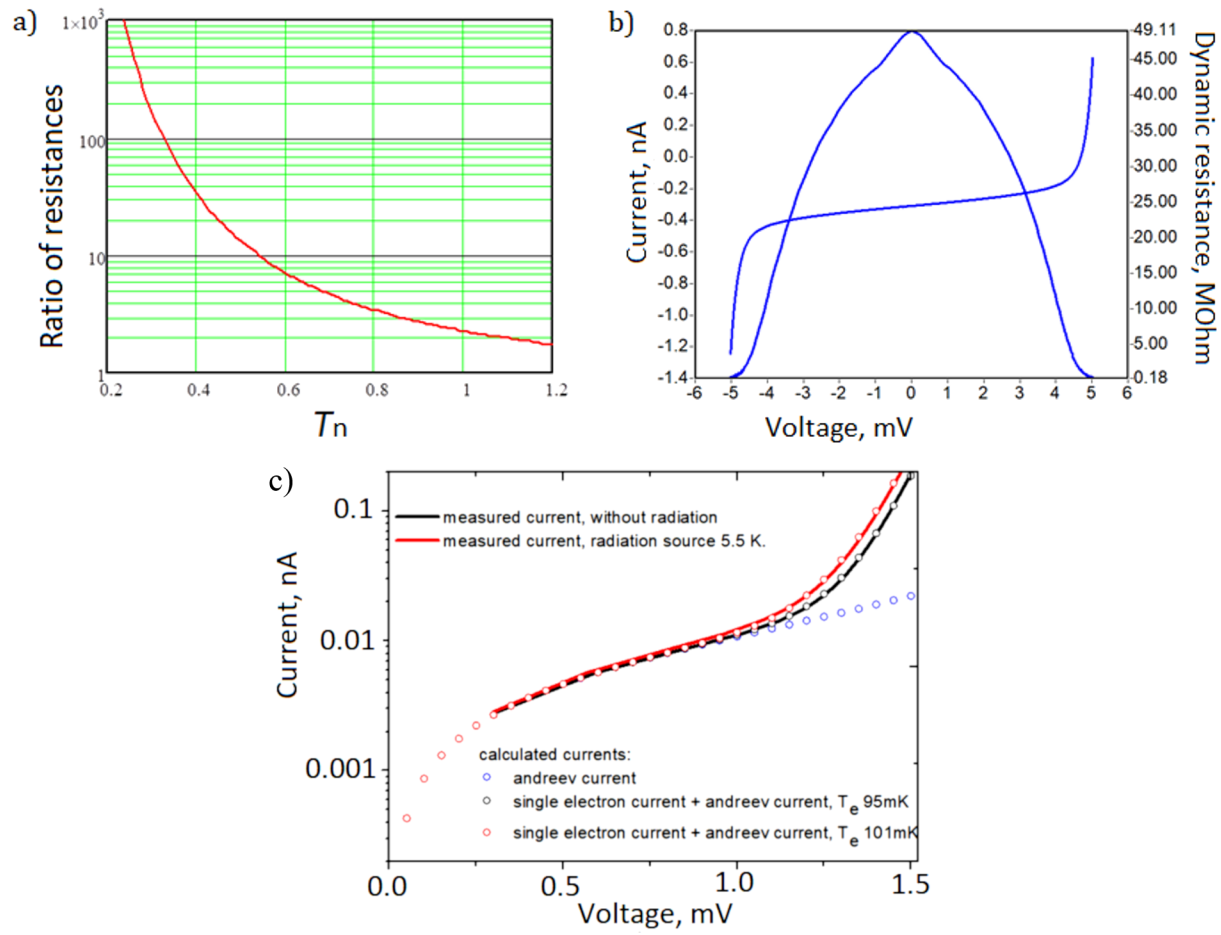


Figure 4: (a) Ratio of resistance at zero bias to the asymptotic resistance using Equation 7, obtained from the general relation in Equation 3. (b) *I–V* curve and dynamic resistance for the SINIS thermometer. (c) Measured current with and without radiation. The resistance ratio is R_d/R_n = 15000 at 95 mK and does not respond to radiation at 5.5 K.

problems in explaining results is that, when the injection rate of electrons exceeds the internal relaxation rate in the metal to be cooled, the electrons do not obey the Fermi–Dirac distribution, and the concept of temperature cannot be applied as such. This work is an exciting development towards a fully solid-state, cryogen-free microrefrigerator, which could eventually cover temperatures from the ambient down to the millikelvin range. Figure 5 shows photographs of a two-stage SINIS cooler. The performance of a single-stage SINIS cooler is presented in Figure 6.

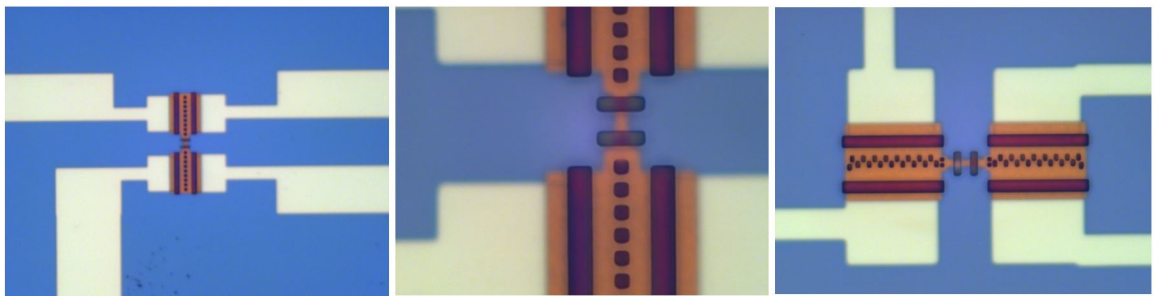


Figure 5: Copper cooler cascade.

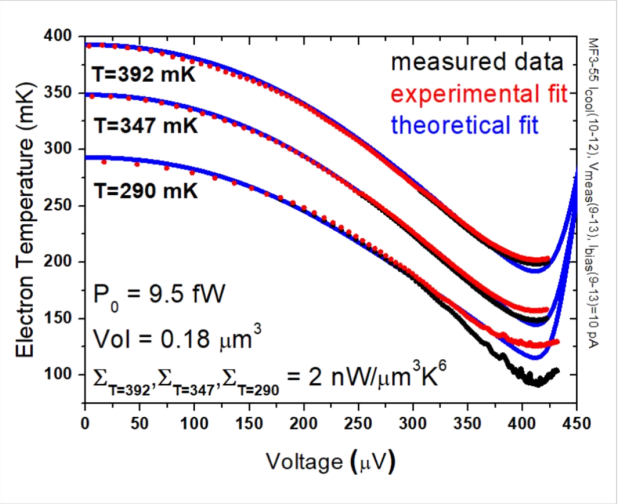


Figure 6: Electron cooling from 392, 347, and 290 mK down to 200, 150, and 95 mK, respectively.

SINIS detectors

The SINIS detector is a thin film of normal metal (the absorber is an element sensitive to incoming radiation) and two NIS junctions that act as a thermometer. An SEM view of the SINIS detector was shown in Figure 1a–f. Often SINIS detectors are considered as classical devices with the optical response equivalent to the electrical response to thermal heating of the absorber by direct current, for example, in [12,14,33-35]. But in practice, the electrical response to heating by direct current is always significantly higher than the optical response for microwave, terahertz, or IR radiation. This is explained by the fact that, in the case of heating the absorber by direct current, the electron temperature of all conduction electrons increases. In the equilibrium state, the electron temperature is determined by the incoming power and the electron–phonon interaction. However, in cases of absorption of a photon with an energy much higher than the thermal energy, the quantum absorption mechanism is already realized, and the real absorption picture becomes much more complicated [19]. It is necessary to take into account many other parameters and relaxation mechanisms. An example of the thermalization process of a radiation quantum with a radiation frequency of 350 GHz is given in [29,36,37]. When an electron absorbs a photon with an energy much higher than the thermal energy, the electron energy will correspond to the electron temperature $hf = kT_e$ of about 16 K for 350 GHz. As a result, a high-energy phonon is created. The process of electron energy relaxation continues until their characteristic times reach the tunneling time determined by the parameters of the SIN transition, that is, the transparency of the barrier, the thickness of the normal metal film, and the diffusion rate of electrons in it. For commonly used structures, this time is of the order of tens of nanoseconds. Typical relaxation times are given in [37,38].

To calculate the sensitivity in the case of heating the absorber with direct current or at low frequencies, the heat balance equation is applicable [12,14]:

$$P_{sig} + P_{bg} = \Sigma\Lambda\left(T_e^5 - T_{ph}^5\right) + P_{cool}, \tag{8}$$

where P_{sig} is the signal power, P_{bg} is the background radiation power, $\Sigma\Lambda(T_e{}^5 - T_{ph}{}^5)$ is the heat flux from electrons to phonons, Σ is the material constant, Λ is the absorber volume, T_e and T_{ph} are, respectively, the electron and phonon temperatures of the absorber, and P_{cool} is the electron cooling power. In other cases, it is necessary to move on to the analysis of collision integrals and the kinetic equation [19,20].

One of the main characteristics of the detector is the noise equivalent power (NEP) [W·Hz$^{-1/2}$], that is, the power of the useful signal in a unit of frequency band, equivalent to the noise power in the device receiving the signal. Approximately, in the simplest case, the NEP of the SINIS detector can be calculated using the following formula:

$$NEP^2 = NEP_{e-ph}^2 + NEP_{NIS}^2 + NEP_{amp}^2 \tag{9}$$

NEP_{e-ph} is the noise equivalent power of electron–phonon interaction, caused by the discreteness of energy exchange between electrons and phonons:

$$NEP_{e-ph} = \sqrt{10k_B\Lambda\Sigma\left(T_e^6 + T_{ph}^6\right)}, \tag{10}$$

where k_B is the Boltzmann constant, Λ is the volume of the absorber, Σ is the constant of electron–phonon interaction, and T_e and T_{ph} are the temperatures of the electron and phonon subsystems, respectively. NEP_{NIS} is the noise equivalent power of NIS junction. It is a combination of shot noise that occurs as a result of the charge transfer by electrons during tunneling through the tunnel SIN junction and the thermal noise of these same electrons as heat carriers:

$$NEP_{NIS} = \sqrt{\frac{\delta I_\omega^2}{S_V^2}\left(\frac{dV}{dI}\right)^2 + \delta P_\omega^2 - 2\frac{\langle \delta P_\omega \delta I_\omega \rangle}{S_V(i)}\frac{dV}{dI}}. \tag{11}$$

$\delta I_\omega{}^2$ is the power spectral density (PSD) of current fluctuations due to shot noise, $\delta P_\omega{}^2$ is the PSD of thermal fluctuations, and $\langle \delta P_\omega \delta I_\omega \rangle$ is the correlation between the two types of noise. NEP_{amp} is the noise equivalent power of the readout amplifiers. We develop typical characteristics of the detectors based on SINIS structures, namely, volt–watt responsivity no worse than

10^9 V·W^{-1}, noise equivalent power below 10^{-17} W·Hz$^{-1/2}$ (the value is given for measurements with a room-temperature JFET readout system and can be improved by upgrading the readout electronics). As an example, some measured characteristics of the SINIS detectors are given in Figure 7. The amplifier voltage noise is 20 nV·Hz$^{-1/2}$, the optimal input impedance for this amplifier is 500 kΩ, and the maximum response is measured at a bias voltage of 0.5 Δ/*e*.

The list of designed and fabricated devices contains different arrays of SINIS detectors for frequencies from below 100 GHz to above a few terahertz, broadband detectors integrated with log-periodic antennas, and narrow-band detectors integrated in twin-slot and double-dipole antennas. The miniature size of SINIS detectors allows them to be integrated into antennas of various types. Also, the detector itself is not frequency-selective, but by integrating such devices into various antennas and using additional filter elements, the detecting device can be tuned to the required frequency. Single antennas are convenient to use for test studies or for use under conditions of low background load and signal. This is due to the fact that the saturation level of a single SINIS detector is 0.5–1.0 pW. Under conditions with a high background load (for example, for ground and balloon observations), such detectors are combined into matrices; the power of incoming radiation is distributed between the matrix elements and, accordingly, the dynamic range of the detecting device can be significantly increased.

Deployment at “Big Telescope Alt-azimuthal”

Currently, work is underway to implement the SINIS detectors on a practical instrument, that is, the optical observatory “Big Telescope Alt-azimuthal” (BTA SAO RAS) for observations in the range of 75–110 GHz. The choice of an optical observatory is due to the fact that there are no large-scale subterahertz observatories in Russia, but there are agreements and the possibility of conducting research based on the BTA observatory. Estimates of the possibility of observations, a description of the receiving system, and the current status of the work are given in [39-41]. These works will allow not only to conduct full-scale tests of the SINIS detectors, but will also expand the capabilities of the BTA observatory to the subterahertz range and use it not only for observations, but also for testing new technologies of subterahertz detectors.

According to [42], the thermodynamic temperature of the planets of the solar system at a frequency of 100 GHz can be

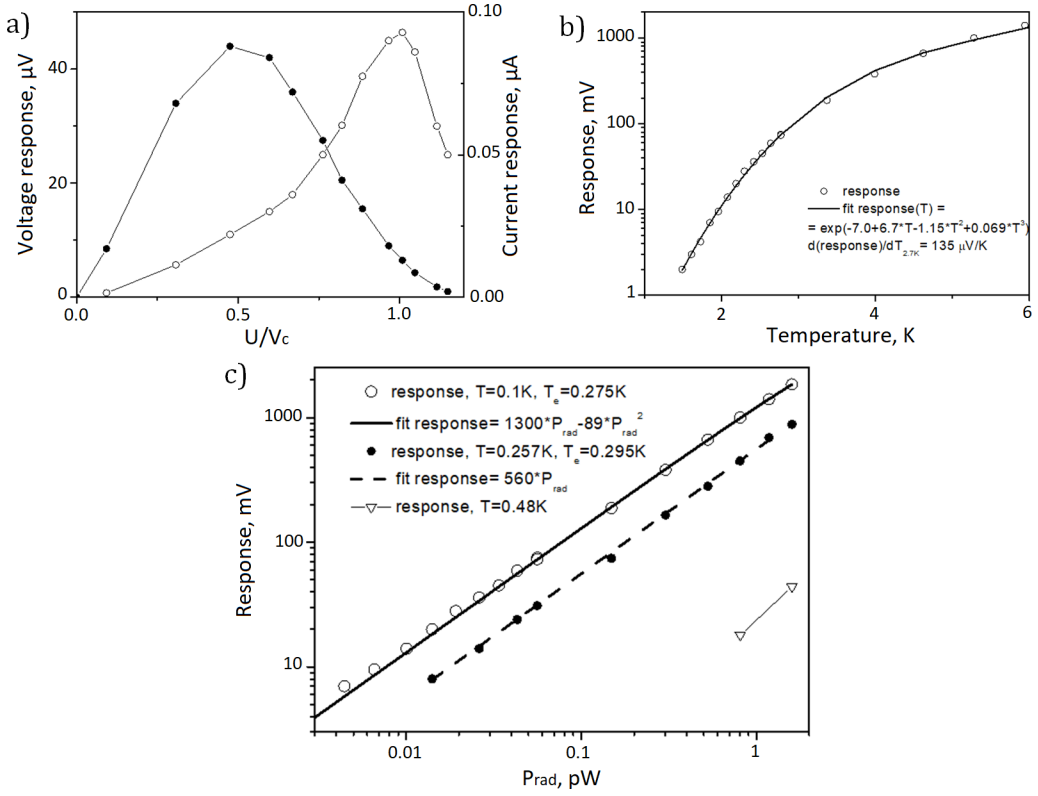


Figure 7: Some of SINIS detectors measured characteristics. (a) Current and voltage response for a parallel array for P_{rad} = 1 pW and maximum current responsivity of d*I*/d*P* = 72000 A/W. (b) Voltage response on black body temperature; at 2.7 K, it is d*V*/d*T* = 135 μV·K^{-1}, (c) voltage response at temperatures of 0.1, 0.295, and 0.48 K; the maximum response is 3.9 V/nW.

estimated as Mars 198 K, Jupiter 172.6 K, Saturn 145 K, Uranus 121 K, and Neptune 118 K; the brightness temperature of the Moon can vary from 100 to 400 K, depending on the time of day. These values exceed the sky temperature at the zenith for the BTA and can be measured with a signal-to-noise ratio greater than unity by the described receiver even without diagram.

Approximate estimates for observing Jupiter and other planets are made and compared with figures from [42] (central frequency f_c = 100 GHz, bandwidth 10%, Δf = 10 GHz. The thermodynamic temperature of Jupiter at 100 GHz is 172.6 K; the angular diameter of Jupiter is 41.68 arcsec; the BTA main mirror diameter is 6 m, and the aperture efficiency of 0.8 gives an effective area of A_{eff} = 22.6 m^2. The solid angle occupied by Jupiter is of the order of $\Omega = 3.20 \times 10^{-8}$ sr. The spectral flux density is $S = I \times \Omega$ = 1677 Jy = 1.677×10^{-23} W·m^{-2}·Hz^{-1}. For 172.6 K at 100 GHz, we have a blackbody intensity $I = 5.23 \times 10^{-16}$ W·m^{-2}·Hz^{-1}·sr^{-1}. The power density collected by a telescope with an effective aperture of 22.6 m^2 is $P = 3.79 \times 10^{-22}$ W·Hz^{-1}. The total power in the 10% band recorded by the receiver from Jupiter is $P_{tot} = 3.79 \times 10^{-12}$ W. For planets visible in November 2025 at 100 GHz, the flux densities will be as follows: Jupiter 41.68 arcsec, 172.6 K, 1677.08 Jy; Saturn 18.68 arcsec, 145.7 K, 283.63 Jy; Mars 3.87 arcsec, 192.3 K, 16.13 Jy; Uranus 3.8 arcsec, 120.5 K, 9.67 Jy; and Neptune 2.34 arcsec, 117.4 K, 3.57 Jy.

At this stage, the necessary equipment and elements of the quasi-optical path in the "Nasmyth 1" cabin of the BTA telescope have been installed. Also, primary tests of the quasi-optical path for focusing incoming radiation and irradiation of the source (IMPATT diode) of the detecting matrix in the 75–110 GHz range were carried out. Photos from the expedition are presented in Figure 8. The ratio of resistances on the presented current–voltage characteristic is about 30, which, according to Equation 3, corresponds to an electron temperature of 0.5 K with a physical temperature of 0.26 K.

The array structure was mounted in back-to-back horn matching structure with an optimum for 95 GHz and corresponding quasi-optical band-pass filters (Figure 9). *I–V* curves and dynamic resistances are presented in Figure 10a. The resistance ratio is 46, which corresponds to an electron temperature of about 0.36 K. In these measurements, there was no optical window and no strong overheating of the sample by radiation.

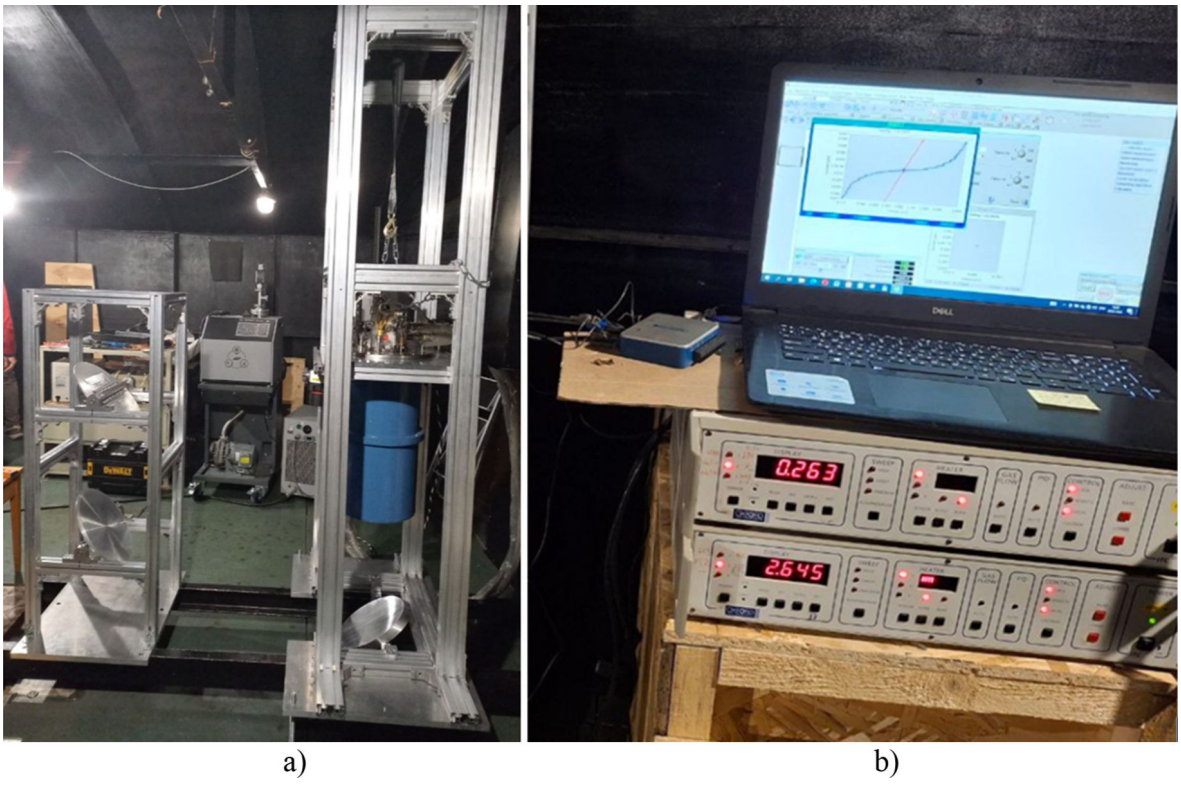


Figure 8: Installation and initial testing of the receiving system based on SINIS detectors at the BTA SAO RAS observatory. (a) Installed racks with a Heliox AC-V cryostat and (b) measured *I–V* characteristics of the SINIS detector matrix installed inside the cryostat with a closed optical window and under irradiation by the source; The lower part demonstrates a PT2 temperature of 2.6 K and a ^{3}He pot temperature of 263 mK.

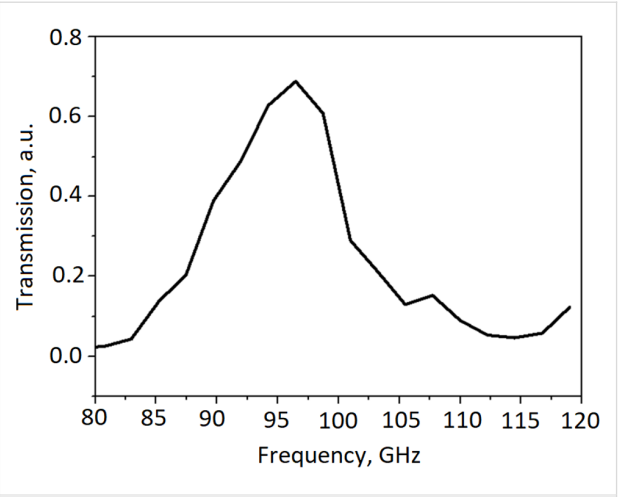


Figure 9: Transmission spectrum of the cold mesh filter.

Discussion

We have designed, fabricated, and experimentally studied a family of aluminum SINIS devices. Microwave detectors at 100 mK demonstrated responsivity up to 10^9 V·W^{-1}, array of NIS thermometers provide sensitivity down to 10 μK, electron coolers can reduce the electron temperature of a normal metal absorber from 280 mK down to 100 mK, and the SINIS receiver for a frequency of 95 GHz was installed on the BTA telescope and tested at a temperature of 260 mK.

Funding

Work is supported by grant from Ministry of science and higher education of Russian Federation No:075-15-2024-482.

Author Contributions

Mikhail Tarasov: supervision. Mikhail Fominskii: data curation. Aleksandra Gunbina: data curation. Artem Krasilnikov: methodology. Maria Mansfeld: data curation. Dmitrii Kukushkin: data curation. Andrei Maruhno: resources. Valeria Ievleva: validation. Mikhail Strelkov: visualization. Daniil Zhogov: investigation. Konstantin Arutyunov: writing – original draft. Vyacheslav Vdovin: writing – review & editing. Vladislav Stolyarov: validation. Valerian Edelman: writing – review & editing.

ORCID® iDs

Mikhail Tarasov - https://orcid.org/0000-0002-8330-9163
Mikhail Fominskii - https://orcid.org/0000-0001-6529-0465
Aleksandra Gunbina - https://orcid.org/0000-0002-0308-142X
Dmitrii Kukushkin - https://orcid.org/0009-0008-2186-3071
Valeria Ievleva - https://orcid.org/0009-0003-1448-0244
Vladislav Stolyarov - https://orcid.org/0000-0001-8151-828X

Data Availability Statement

Data generated and analyzed during this study is available from the corresponding author upon reasonable request.

References

1. Giazotto, F.; Heikkilä, T. T.; Luukanen, A.; Savin, A. M.; Pekola, J. P. *Rev. Mod. Phys.* **2006,** *78,* 217–274. doi:10.1103/revmodphys.78.217
2. Ullom, J. N. *AIP Conf. Proc.* **2002,** *605,* 135–140. doi:10.1063/1.1457613
3. Tarasov, M.; Edelman, V. Nanodevices with Normal Metal—Insulator—Superconductor Tunnel Junctions. In *Functional Nanostructures and Metamaterials for Superconducting Spintronics;* Sidorenko, A., Ed.; NanoScience and Technology; Springer International Publishing: Cham, Switzerland, 2018; pp 91–116. doi:10.1007/978-3-319-90481-8_5
4. Feshchenko, A. V.; Casparis, L.; Khaymovich, I. M.; Maradan, D.; Saira, O.-P.; Palma, M.; Meschke, M.; Pekola, J. P.; Zumbühl, D. M. *Phys. Rev. Appl.* **2015,** *4,* 034001. doi:10.1103/physrevapplied.4.034001
5. Pekola, J. *J. Low Temp. Phys.* **2004,** *135,* 723–744. doi:10.1023/b:jolt.0000029516.18146.42

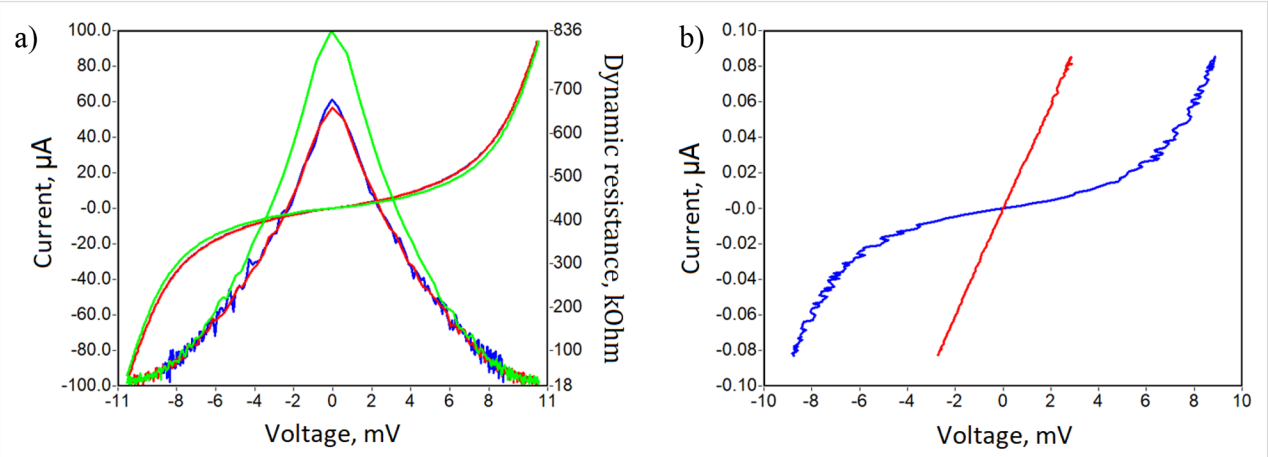


Figure 10: (a) *I–V* curves and dynamic resistance of series SINIS array and (b) *I–V* curve without (blue) and with (red) microwave radiation at 95 GHz.

6. Isosaari, E.; Holmqvist, T.; Meschke, M.; Heinonen, M.; Pekola, J. P. *Eur. Phys. J.: Spec. Top.* **2009,** *172,* 323–332. doi:10.1140/epjst/e2009-01057-y
7. Pekola, J. P.; Manninen, A. J.; Leivo, M. M.; Arutyunov, K.; Suoknuuti, J. K.; Suppula, T. I.; Collaudin, B. *Phys. B (Amsterdam, Neth.)* **2000,** *280,* 485–490. doi:10.1016/s0921-4526(99)01842-6
8. Nguyen, H. Q.; Aref, T.; Kauppila, V. J.; Meschke, M.; Winkelmann, C. B.; Courtois, H.; Pekola, J. P. *New J. Phys.* **2013,** *15,* 085013. doi:10.1088/1367-2630/15/8/085013
9. Clark, A. M.; Miller, N. A.; Williams, A.; Ruggiero, S. T.; Hilton, G. C.; Vale, L. R.; Beall, J. A.; Irwin, K. D.; Ullom, J. N. *Appl. Phys. Lett.* **2005,** *86,* 173508. doi:10.1063/1.1914966
10. O'Neil, G. C. Improving NIS Tunnel Junction Refrigerators: Modeling, Materials, and Traps. Ph.D. Thesis, Boulder, Colorado, 2011.
11. Nahum, M.; Martinis, J. M. *Appl. Phys. Lett.* **1993,** *63,* 3075–3077. doi:10.1063/1.110237
12. Nahum, M.; Richards, P. L.; Mears, C. A. *IEEE Trans. Appl. Supercond.* **1993,** *3,* 2124–2127. doi:10.1109/77.233921
13. Vystavkin, A. N.; Shuvaev, D. V.; Kuz'min, L. S.; Tarasov, M. A.; Aderstedt, E.; Willander, M.; Claeson, T. *J. Exp. Theor. Phys.* **1999,** *88,* 598–602. doi:10.1134/1.558834
14. Kuzmin, L. S.; Devyatov, I. A.; Golubev, D. *Proc. SPIE* **1998,** *3465,* 193–199. doi:10.1117/12.331165
15. Brien, T. L. R.; Ade, P. A. R.; Barry, P. S.; Dunscombe, C.; Leadley, D. R.; Morozov, D. V.; Myronov, M.; Parker, E. H. C.; Prest, M. J.; Prunnila, M.; Sudiwala, R. V.; Whall, T. E.; Mauskopf, P. D. *Appl. Phys. Lett.* **2014,** *105,* 043509. doi:10.1063/1.4892069
16. Schmidt, D. R.; Duncan, W. D.; Irwin, K. D.; Lehnert, K. W.; Miller, N. A.; Ullom, J. N. *Nucl. Instrum. Methods Phys. Res., Sect. A* **2006,** *559,* 516–518. doi:10.1016/j.nima.2005.12.043
17. Schmidt, D. R.; Lehnert, K. W.; Clark, A. M.; Duncan, W. D.; Irwin, K. D.; Miller, N.; Ullom, J. N. *Appl. Phys. Lett.* **2005,** *86,* 053505. doi:10.1063/1.1855411
18. Tarasov, M.; Gunbina, A.; Chekushkin, A.; Yusupov, R.; Edelman, V.; Koshelets, V. *Appl. Sci.* **2022,** *12,* 10525. doi:10.3390/app122010525
19. Devyatov, I. A.; Krutitskiĭ, P. A.; Kupriyanov, M. Y. *J. Exp. Theor. Phys. Lett.* **2006,** *84,* 57–61. doi:10.1134/s0021364006140037
20. Devyatov, I. A.; Kupriyanov, M. Y. *J. Exp. Theor. Phys. Lett.* **2004,** *80,* 646–650. doi:10.1134/1.1857272
21. Giaever, I. *Phys. Rev. Lett.* **1960,** *5,* 147–148. doi:10.1103/physrevlett.5.147
22. Schmidt, V. V. *Introduction to physics of superconductivity,* 2nd ed.; MCCME, 2000.
23. Giaever, I.; Megerle, K. *Phys. Rev.* **1961,** *122,* 1101–1111. doi:10.1103/physrev.122.1101
24. Andreev, A. F. *Sov. Phys. - JETP* **1964,** *19,* 1228–1231.
25. Hekking, F. W. J.; Nazarov, Yu. V. *Phys. Rev. B* **1994,** *49,* 6847–6852. doi:10.1103/physrevb.49.6847
26. Leivo, M. M.; Pekola, J. P.; Averin, D. V. *Appl. Phys. Lett.* **1996,** *68,* 1996–1998. doi:10.1063/1.115651
27. Dolan, G. J. *Appl. Phys. Lett.* **1977,** *31,* 337–339. doi:10.1063/1.89690
28. Aleksandrovich, T. M.; Vladimirovna, N. D.; Anatolevna, G. A.; Yurevich, F. M. Method of making devices with thin-film tunnel junctions. RU 2733330 C1, Oct 1, 2020.
29. Gunbina, A.; Tarasov, M.; Fominsky, M.; Chekushkin, A.; Yusupov, R.; Nagirnaya, D. Fabrication of aluminium nanostructures for microwave detectors based on tunnel junctions. In *Advances in Microelectronics Reviews;* Sergey, Y. Y., Ed.; IFSA Publishing: Barcelona, Spain, 2021; Vol. 3, pp 183–212. ISBN 978-84-09-33338-7/978-84-09-33339-4.
30. Pekola, J. P.; Holmqvist, T.; Meschke, M. *Phys. Rev. Lett.* **2008,** *101,* 206801. doi:10.1103/physrevlett.101.206801
31. Tarasov, M. A.; Kuz'min, L. S.; Fominskii, M. Yu.; Agulo, I. E.; Kalabukhov, A. S. *J. Exp. Theor. Phys. Lett.* **2003,** *78,* 714–717. doi:10.1134/1.1648293
32. Kemppinen, A.; Ronzani, A.; Mykkänen, E.; Hätinen, J.; Lehtinen, J. S.; Prunnila, M. *Appl. Phys. Lett.* **2021,** *119,* 052603. doi:10.1063/5.0060652
33. Clarke, J.; Hoffer, G. I.; Richards, P. L. *Rev. Phys. Appl.* **1974,** *9,* 69–71. doi:10.1051/rphysap:019740090106900
34. Kuzmin, L. S.; Pankratov, A. L.; Gordeeva, A. V.; Zbrozhek, V. O.; Shamporov, V. A.; Revin, L. S.; Blagodatkin, A. V.; Masi, S.; de Bernardis, P. *Commun. Phys.* **2019,** *2,* 104. doi:10.1038/s42005-019-0206-9
35. Gordeeva, A. V.; Zbrozhek, V. O.; Pankratov, A. L.; Revin, L. S.; Shamporov, V. A.; Gunbina, A. A.; Kuzmin, L. S. *Appl. Phys. Lett.* **2017,** *110,* 162603. doi:10.1063/1.4982031
36. Yusupov, R. A.; Gunbina, A. A.; Chekushkin, A. M.; Nagirnaya, D. V.; Lemzyakov, S. A.; Edel'man, V. S.; Tarasov, M. A. *Phys. Solid State* **2020,** *62,* 1567–1570. doi:10.1134/s106378342009036x
37. Tarasov, M.; Gunbina, A.; Yusupov, R.; Chekushkin, A.; Nagirnaya, D.; Lemzyakov, S.; Vdovin, V.; Edelman, V.; Kalaboukhov, A.; Winkler, D. *IEEE Trans. Appl. Supercond.* **2021,** *31,* 2300105. doi:10.1109/tasc.2021.3057327
38. Gershenson, M. E.; Gong, D.; Sato, T.; Karasik, B. S.; Sergeev, A. V. *Appl. Phys. Lett.* **2001,** *79,* 2049–2051. doi:10.1063/1.1407302
39. Balega, Y.; Bubnov, G.; Chekushkin, A.; Dubrovich, V.; Edelman, V.; Gunbina, A.; Kapustin, S.; Khabarova, T.; Kukushkin, D.; Lapkin, I.; Mansfeld, M.; Maruhno, A.; Parshin, V.; Raevskiy, A.; Stolyarov, V.; Tarasov, M.; Valyavin, G.; Vdovin, V.; Yakopov, G.; Yusupov, R.; Zemlyanukha, P.; Zinchenko, I. *Sensors* **2024,** *24,* 359. doi:10.3390/s24020359
40. Stolyarov, V. A.; Balega, Y. Y.; Mingaliev, M. G.; Sotnikova, Y. V.; Vdovin, V. F.; Gunbina, A. A.; Kukushkin, D. E.; Tarasov, M. A.; Fominsky, M. Y.; Chekushkin, A. M.; Edelman, V. S.; Yusupov, R. A. *Astrophys. Bull.* **2024,** *79,* 321–339. doi:10.1134/s1990341324600467
41. Tarasov, M. A.; Gunbina, A. A.; Checkushkin, A. M.; Markina, M. A.; Ysupov, R. A.; Fominskii, M. Y.; Filippenko, L. V.; Edelman, V. S.; Vdovin, V. F.; Stolyarov, V. A.; Zinchenko, I.; Krasilnikov, A. M.; Maruhno, A. S.; Mansfeld, M. A.; Kukushkin, D. E.; Sazonenko, D. A.; Bolshakov, O. S.; Ermakov, A. B.; Lesnov, I. V.; Valeev, A. F. *Astrophys. Bull.* **2025,** *80,* 502–518.

42. Akrami, Y.; Ashdown, M.; Aumont, J.; Baccigalupi, C.; Ballardini, M.; Banday, A. J.; Barreiro, R. B.; Bartolo, N.; Basak, S.; Benabed, K.; Bernard, J.-P.; Bersanelli, M.; Bielewicz, P.; Bonavera, L.; Bond, J. R.; Borrill, J.; Bouchet, F. R.; Boulanger, F.; Bucher, M.; Burigana, C.; Butler, R. C.; Calabrese, E.; Cardoso, J.-F.; Carron, J.; Chiang, H. C.; Colombo, L. P. L.; Comis, B.; Couchot, F.; Coulais, A.; Crill, B. P.; Curto, A.; Cuttaia, F.; de Bernardis, P.; de Rosa, A.; de Zotti, G.; Delabrouille, J.; Di Valentino, E.; Dickinson, C.; Diego, J. M.; Doré, O.; Ducout, A.; Dupac, X.; Elsner, F.; Enßlin, T. A.; Eriksen, H. K.; Falgarone, E.; Fantaye, Y.; Finelli, F.; Frailis, M.; Fraisse, A. A.; Franceschi, E.; Frolov, A.; Galeotta, S.; Galli, S.; Ganga, K.; Génova-Santos, R. T.; Gerbino, M.; González-Nuevo, J.; Górski, K. M.; Gruppuso, A.; Gudmundsson, J. E.; Hansen, F. K.; Helou, G.; Henrot-Versillé, S.; Herranz, D.; Hivon, E.; Jaffe, A. H.; Jones, W. C.; Keihänen, E.; Keskitalo, R.; Kiiveri, K.; Kim, J.; Kisner, T. S.; Krachmalnicoff, N.; Kunz, M.; Kurki-Suonio, H.; Lagache, G.; Lamarre, J.-M.; Lasenby, A.; Lattanzi, M.; Lawrence, C. R.; Le Jeune, M.; Lellouch, E.; Levrier, F.; Liguori, M.; Lilje, P. B.; Lindholm, V.; López-Caniego, M.; Ma, Y.-Z.; Macías-Pérez, J. F.; Maggio, G.; Maino, D.; Mandolesi, N.; Maris, M.; Martin, P. G.; Martínez-González, E.; Matarrese, S.; Mauri, N.; McEwen, J. D.; Melchiorri, A.; Mennella, A.; Migliaccio, M.; Miville-Deschênes, M.-A.; Molinari, D.; Moneti, A.; Montier, L.; Moreno, R.; Morgante, G.; Natoli, P.; Oxborrow, C. A.; Paoletti, D.; Partridge, B.; Patanchon, G.; Patrizii, L.; Perdereau, O.; Piacentini, F.; Plaszczynski, S.; Polenta, G.; Rachen, J. P.; Racine, B.; Reinecke, M.; Remazeilles, M.; Renzi, A.; Rocha, G.; Romelli, E.; Rosset, C.; Roudier, G.; Rubiño-Martín, J. A.; Ruiz-Granados, B.; Salvati, L.; Sandri, M.; Savelainen, M.; Scott, D.; Sirri, G.; Spencer, L. D.; Suur-Uski, A.-S.; Tauber, J. A.; Tavagnacco, D.; Tenti, M.; Toffolatti, L.; Tomasi, M.; Tristram, M.; Trombetti, T.; Valiviita, J.; Van Tent, F.; Vielva, P.; Villa, F.; Wehus, I. K.; Zacchei, A. *Astron. Astrophys.* **2017,** *607,* A122. doi:10.1051/0004-6361/201630311

License and Terms

This is an open access article licensed under the terms of the Beilstein-Institut Open Access License Agreement (https://www.beilstein-journals.org/bjnano/terms), which is identical to the Creative Commons Attribution 4.0 International License (https://creativecommons.org/licenses/by/4.0). The reuse of material under this license requires that the author(s), source and license are credited. Third-party material in this article could be subject to other licenses (typically indicated in the credit line), and in this case, users are required to obtain permission from the license holder to reuse the material.

The definitive version of this article is the electronic one which can be found at:
https://doi.org/10.3762/bjnano.16.134

BEILSTEIN JOURNAL OF NANOTECHNOLOGY

Hartree–Fock interaction in superconducting condensate fractals

Edward G. Nikonov[1,2], Yajiang Chen[*3], Mauro M. Doria[4] and Arkady A. Shanenko[*1]

Full Research Paper

Open Access

Address:
[1]HSE University, 101000 Moscow, Russia, [2]Meshcheryakov Laboratory of Information Technologies, Joint Institute for Nuclear Research, Dubna, Russia, [3]Zhejiang Key Laboratory of Quantum State Control and Optical Field Manipulation, Department of Physics, Zhejiang Sci-Tech University, 310018 Hangzhou, China and [4]Instituto de Física, Universidade Federal do Rio de Janeiro, 21941-972 Rio de Janeiro, Brazil

Email:
Yajiang Chen[*] - yjchen@zstu.edu.cn; Arkady A. Shanenko[*] - ashanenko@hse.ru

* Corresponding author

Keywords:
Fibonacci chain; fractal superconductivity; Hartree–Fock interaction; quasicrystal

Beilstein J. Nanotechnol. **2025,** *16,* 2177–2182.
https://doi.org/10.3762/bjnano.16.150

Received: 29 October 2025
Accepted: 27 November 2025
Published: 04 December 2025

This article is part of the thematic issue "Superconducting artificial neural networks and quantum circuits".

Guest Editor: A. S. Sidorenko

© 2025 Nikonov et al.; licensee Beilstein-Institut.
License and terms: see end of document.

Abstract

It is well known that the Hartree–Fock (HF) interaction does not alter observables in conventional superconductors as its effect is mainly reduced to a chemical potential shift. Deviations from this behavior can only arise in situations of translational symmetry breaking, for example, caused by the presence of external fields that induce spatial variations of the order parameter and electron density. We demonstrate that this scenario changes fundamentally in quasicrystalline systems, where the intrinsic lack of translational symmetry leads to a fractal spatial distribution of the superconducting condensate and electron density. By investigating a Fibonacci chain as a prototype quasicrystal, we numerically solve the Bogoliubov–de Gennes equations and show that, beyond the half-filling, the HF potential significantly enhances the self-similar spatial oscillations of the order parameter while simultaneously reducing its average value and altering its critical exponent. Consequently, the critical temperature is suppressed; for our chosen microscopic parameters, this suppression can reach up to 20%. Therefore, an accurate analysis of condensate distribution and related quantities in quasicrystalline superconductors requires the comparison of results obtained with and without the HF interaction.

Introduction

It is well known, dating back to the classical book by de Gennes [1], that, in conventional superconducting materials, the Hartree–Fock (HF) interaction merely reduces to a shift of the chemical potential, as the observables are not affected due to translational invariance. Hence, the HF field is a kind of “spectator” that defines the single-particle states and chemical poten-

tial but does not act on the pair formation and, thus, can be neglected, as in the standard formulation of the BCS model [2,3]. Nevertheless, the HF potential cannot be neglected in the presence of external fields [4], such as impurity potentials [5,6], quantum confinement in nanoscale superconductors [7], and potential barriers at interfaces [8]. Such external fields break the translational invariance, which is the condition for the HF field to make a contribution to the formation of the superconducting condensate.

This raises an interesting question about systems that exhibit an intrinsic lack of translational invariance even in the absence of any applied field. Among those are quasicrystals, which were first discovered in 1984 [9-11]. Quasicrystals exhibit long-range orientational order, such as the fivefold symmetry in $Al_{86}Mn_{14}$ alloys [9,10], but lack the translational invariance [11]. The superconductivity of quasicrystals was established in 2018 with the discovery of superconducting signatures in an Al–Zn–Mg alloy below a critical temperature of $T_c \sim 0.05$ K [12]. More recently, in 2024 and 2025, much higher critical temperatures of $T_c \sim 1$ K and $T_c \sim 5.47$ K were reported in van der Waals-layered dodecagonal quasicrystals $Ta_{1.6}Te$ [13] and in a monoclinic approximant to the decagonal quasicrystal $Al_{13}Os_4$[14], respectively.

Experimental observations of the superconductivity in quasicrystals ignited big interest regarding many open problems related to the superconducting condensate in quasiperiodic systems. Most of the recent results were obtained for a superconducting Fibonacci chain, being a simplified one-dimensional model for superconducting quasicrystals [15]. Using this model, researchers explored a range of phenomena in quasiperiodic systems, including proximity effects in quasicrystal–metal hybrids [16-18], enhanced superconductivity from staggered hopping amplitudes [19], and the interplay between the Josephson effect and quasiperiodicity [20]. The model has also been used to investigate topological superconductivity [21] and anomalous local critical temperatures (at the left end, at the right end, and at the chain center) in quasiperiodic chains [22]. These investigations demonstrate that the spatial distribution of the superconducting condensate in quasiperiodic chains exhibits a distinct fractal character, with significant oscillations of the order parameter along the system. A similar fractal inhomogeneous distribution of the pair condensate has been calculated for Penrose and Ammann–Beenker tilings [23], well-known representations of two-dimensional quasicrystals.

Recent studies confirm that the superconducting condensate in quasiperiodic systems possesses a highly nontrivial spatial structure. This finding naturally raises the question of how sensitive the theoretical predictions for quasicrystalline superconductors are to the inclusion of the HF potential in the fundamental microscopic equations. Our work addresses this open problem through an investigation of the superconducting Fibonacci chain, a standard prototype for quasiperiodic systems.

Bogoliubov–de Gennes Equations for Superconducting Fibonacci Chains

To investigate the superconducting properties of a Fibonacci chain, we use an attractive Hubbard model with the grand-canonical Hamiltonian (absorbing the chemical potential μ) given by [4-6,8,19,22],

$$\hat{H} = -\sum_{ij\sigma} t_{\langle ij\rangle} c_{i\sigma}^{\dagger} c_{j\sigma} - \sum_{i\sigma} \mu \hat{n}_{i\sigma} - g \sum_{i} \hat{n}_{i\uparrow} \hat{n}_{i\downarrow}, \quad (1)$$

where $c_{i\sigma}$ and $c_{i\sigma}^{\dagger}$ are, respectively, the annihilation and creation operators of an electron with the spin projection $\sigma = (\uparrow, \downarrow)$ at sites $i = 1,\ldots,N$, $t_{\langle ij\rangle}$ is the hopping amplitude between the nearest neighboring sites, $\hat{n}_{i\sigma} = c_{i\sigma}^{\dagger} c_{i\sigma}$, and $g > 0$ is the on-site attractive electron–electron interaction.

Within the mean-field approximation, the Hamiltonian in Equation 1 is reduced [4] to the effective BCS–Bogoliubov Hamiltonian in the form (for the s-wave pairing):

$$\hat{H}_{\text{eff}} = \sum_{ij\sigma} h_{ij} c_{i\sigma}^{\dagger} c_{j\sigma} + \sum_{i} \left[\Delta(i) c_{i\uparrow}^{\dagger} c_{i\downarrow}^{\dagger} + \Delta^{*}(i) c_{i\downarrow} c_{i\uparrow} \right], \quad (2)$$

where

$$h_{ij} = -t_{\langle ij\rangle} - \delta_{ij} \left[\mu - U_{\text{HF}}(i) \right], \quad (3)$$

with δ_{ij} the Kronecker delta, and $\Delta(i)$ and $U_{\text{HF}}(i)$ the superconducting order parameter and the HF interaction potential, respectively. The latter obey the self-consistency relations

$$\Delta(i) = g \left\langle c_{i\uparrow} c_{i\downarrow} \right\rangle, \quad U_{\text{HF}}(i) = -g \left\langle \hat{n}_{i\uparrow} \right\rangle = -g \left\langle \hat{n}_{i\downarrow} \right\rangle; \quad (4)$$

here, we exclude spin-imbalanced regimes in which $\langle \hat{n}_{i\uparrow} \rangle \neq \langle \hat{n}_{i\downarrow} \rangle$.

The effective Hamiltonian is diagonalized by applying the Bogoliubov–Valatin transformation [4],

$$\begin{pmatrix} c_{i\uparrow} \\ c_{i\downarrow}^{\dagger} \end{pmatrix} = \sum_{\nu} \begin{pmatrix} u_{\nu}(i) & -v_{\nu}^{*}(i) \\ v_{\nu}(i) & u_{\nu}^{*}(i) \end{pmatrix} \begin{pmatrix} \gamma_{\nu\uparrow} \\ \gamma_{\nu\downarrow}^{\dagger} \end{pmatrix}, \quad (5)$$

where $u_\nu(i)$ and $v_\nu(i)$ are, respectively, the particle-like and hole-like quasiparticle (bogolon) wavefunctions, and $\gamma_{\nu\sigma}$ and $\gamma^\dagger_{\nu\sigma}$ are the annihilation and creation operators for bogolon state ν, σ, respectively. The quasiparticle wave functions obey the Bogoliubov–de Gennes equations

$$\begin{aligned}\sum_j h_{ij}u_\nu(j)+\Delta(i)v_\nu(i)&=\varepsilon_\nu u_\nu(i),\\ \Delta^*(i)u_\nu(i)-\sum_j h^*_{ij}v_\nu(j)&=\varepsilon_\nu v_\nu(i),\end{aligned} \tag{6}$$

where ε_ν is the quasiparticle energy. As a result of the diagonalization, one obtains

$$\left\langle\gamma^\dagger_{\nu\uparrow}\gamma_{\nu\uparrow}\right\rangle=\left\langle\gamma^\dagger_{\nu\downarrow}\gamma_{\nu\downarrow}\right\rangle=f_\nu,\quad\left\langle\gamma_{\nu\uparrow}\gamma_{\nu\downarrow}\right\rangle=0, \tag{7}$$

where f_ν is the Fermi–Dirac distribution of bogolons with the quasiparticle energy ε_ν. The quantum number ν enumerates the quasiparticle states in ascending energy order. In our study, we employ the open-boundary conditions [5,8,22] for the quasiparticle wavefunctions $u_\nu(i)$ and $v_\nu(i)$, which corresponds to the physical scenario of electrons being quantum-confined within the chain.

When using Equation 5 and Equation 7, the self-consistency relations given by Equation 4 are represented in the form

$$\begin{aligned}\Delta(i)&=g\sum_\nu u_\nu(i)v^*_\nu(i)\left[1-2f_\nu\right],\\ U_{\mathrm{HF}}(i)&=-g\sum_\nu\left[|u_\nu(i)|^2 f_\nu+|v_\nu(i)|^2(1-f_\nu)\right].\end{aligned} \tag{8}$$

In addition, the averaged occupation number of electrons is given by

$$n_{\mathrm{e}}=\frac{1}{N}\sum_{i\sigma}\langle\hat{n}_{i\sigma}\rangle=2\sum_{i\nu}\left[f_\nu|u_\nu(i)|^2+(1-f_\nu)|v_\nu(i)|^2\right], \tag{9}$$

which defines the chemical potential μ. The summation in Equation 8 and Equation 9 is over the quasiparticle species with positive energies. In addition, the summation in $\Delta(i)$ is limited to the states in the Debye window around the Fermi level, that is, $0\le\varepsilon_\nu\le\hbar\omega_{\mathrm{D}}$. However, in the current study, we assume that $\hbar\omega_{\mathrm{D}}$ is much larger than the half-bandwidth. This assumption renders the Debye energy constraint ineffective as all solutions of the Bogoliubov–de Gennes (BdG) equations with positive quasiparticle energies consequently fall within the Debye window.

The self-consistent calculation procedure follows the same protocol as for the periodic Hubbard model. First, we solve the BdG equations (Equation 6) using an initial guess for μ, $\Delta(i)$, and $U_{\mathrm{HF}}(i)$. Second, using the resulting quasiparticle energies and wave functions, we compute new values for $\Delta(i)$ and $U_{\mathrm{HF}}(i)$ from Equation 8. Third, we adjust μ to achieve the desired average occupation number n_{e} from Equation 9. The new values of μ, $\Delta(i)$, and $U_{\mathrm{HF}}(i)$ are then reinserted into the BdG equations, and the entire procedure is repeated until convergence is achieved. The calculation is considered converged when the relative changes in the order parameter and the HF field are below 10^{-7}.

To model quasicrystal superconducting properties, as the first step, we consider a finite Fibonacci sequence (Fibonacci approximant) S_n, with n being the characteristic sequence number [15]. This is a sequence of symbols "A" and "B", which is the concatenation of sequences S_{n-1} and S_{n-2}, that is, $S_n = [S_{n-1}, S_{n-2}]$, where S_1 = [B] and S_2 = [A] include only one symbol [15]. Based on this Fibonacci rule, we have S_3 = [AB], S_4 = [ABA], S_5 = [ABAAB], S_6 = [ABAABABA] and so on. The number of symbols in S_n is F_n, and $\{F_1, F_2, F_3, F_4, F_5,\ldots\} = \{1, 1, 2, 3, 5,\ldots\}$, which are the Fibonacci numbers. We then map this sequence onto a physical lattice using the off-diagonal model. Each symbol A or B in the sequence defines the hopping parameters t_{A} or t_{B}, respectively, between adjacent lattice sites. This results in a one-dimensional chain with a total of $N = F_n + 1$ sites, following the well-established off-diagonal formulation of the Fibonacci model [15,19,24,25].

All energy-related quantities, that is, $\Delta(i)$, $U_{\mathrm{HF}}(i)$, μ, T, t_{A}, and g, are expressed in units of the hopping parameter t_{B}. We set $g = 2$ and consider two different values of the Fibonacci sequence index, $n = 12$ and $n = 13$, for a more detailed illustration. Furthermore, we investigate two variants of the hopping amplitudes, namely, $t_{\mathrm{A}} = 0.5$ and $t_{\mathrm{A}} = 1.5$ (in units of t_{B}). Our calculations are performed away from the half-filling as this regime was shown to produce a uniform electronic distribution in Fibonacci chains [22], where the HF potential does not alter superconducting properties. Here, we adopt an electron density of $n_{\mathrm{e}} = 0.5$. Our qualitative conclusions are robust and not sensitive to the specific choice of these model parameters.

Results and Discussion

Figure 1 shows results of numerically solving the BdG equations in a self-consistent manner for $n = 12$ and $t_{\mathrm{A}} = 1.5$. In this case, $F_{n=12} = 233$; consequently, the number of atomic sites in

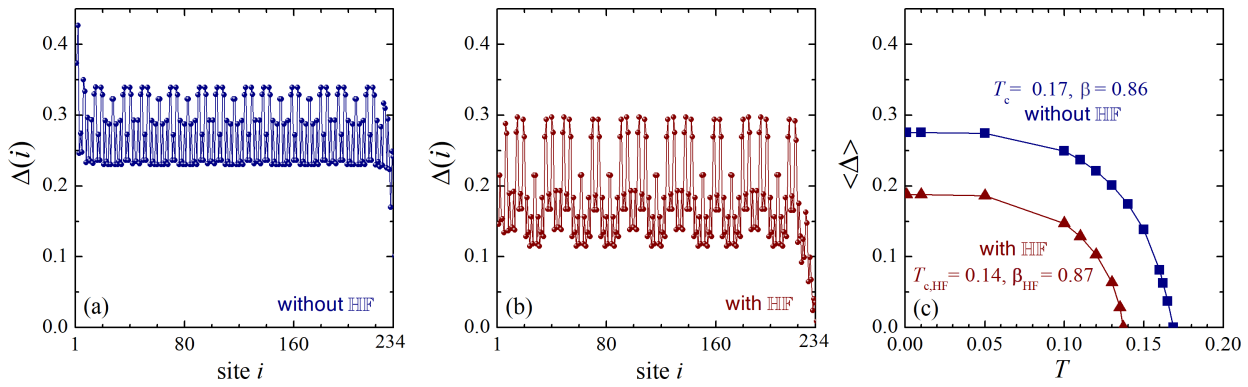


Figure 1: The spatial distribution of the order parameter in the Fibonacci chain with n = 12 and t_A = 1.5, without the HF potential (a) and with the HF potential (b). Panel (c) represents the temperature-dependence of the average order parameter in the chain center with (triangles) and without (squares) HF interaction. The critical temperatures with and without HF interaction are $T_{c,HF}$ = 0.14 and T_c = 0.17; the corresponding critical exponents of the averaged order parameter are β_{HF} = 0.87 (with HF) and β = 0.86 (without HF).

the chain is N = 234. In Figure 1a, one can see the spatial profile of the order parameter $\Delta(i)$ calculated at zero temperature by taking into account the HF interaction. The order parameter exhibits significant oscillations due to the quasiperiodic character of the system. These oscillations in the Fibonacci approximant with n = 12 are connected with the fractal distribution of the condensate in the infinite Fibonacci chain. In agreement with a previous investigation [22], there are three spatial regions with clearly different averages of the order parameter, namely, the left-end domain, the center of the chain, and the right-end region. The order parameter is enhanced up to 0.43 near the left end, while it is reduced to 0.16 near the right end. The average value of $\Delta(i)$ near the chain center (averaging in the interval from i = 70 to i = 170) is 0.28. This feature is related to the presence of three critical temperatures, that is, the left-end, the right-end, and the center (bulk) superconducting temperature, as reported in [22].

We now examine the zero-temperature order parameter for the system with the HF potential, as shown in Figure 1b. The oscillations of the order parameter are immediately apparent and are significantly more pronounced than in the system without the HF potential. In Figure 1a, the total range of the oscillations (from their minimum to their maximum in a given region) is approximately 30% of the average order parameter value, whereas in Figure 1b, this value reaches nearly 100%. Furthermore, including the HF interaction qualitatively alters the spatial distribution of the condensate near the chain edges. Specifically, the enhancement of the order parameter near the left end, which is clearly present without the HF potential, is suppressed when the HF interaction is included, as seen in Figure 1b. Concurrently, the suppression of the order parameter near the right chain end becomes even more pronounced in the system with HF interaction.

To further analyze the system, Figure 1c shows the temperature-dependence of the order parameter averaged over the center of the chain, $\langle\Delta\rangle$ (in the interval from i = 80 to i = 160). The inclusion of HF interaction results in a significant decrease of both the order parameter in the chain center and the corresponding critical temperature. When the HF potential is included, the zero-temperature order parameter is $\langle\Delta\rangle_{T=0,\mathrm{HF}}$ = 0.19, compared to a value of approximately 0.28 without it. The critical temperatures are T_c = 0.17 and $T_{c,\mathrm{HF}}$ = 0.14. The ratio $\langle\Delta\rangle_{T=0,\mathrm{HF}}/T_{c,\mathrm{HF}}$ = 1.36 is notably smaller than the corresponding ratio without the HF field, $\langle\Delta\rangle_{T=0}/T_c$ = 1.64. Furthermore, both values are smaller than the universal BCS prediction of $\Delta(0)/T_c$ = 1.76.

Finally, using the temperature-dependent data from Figure 1c, we calculate the critical exponent β of the order parameter near the critical temperature:

$$\langle\Delta\rangle \propto \tau^{\beta}, \tag{10}$$

where $\tau = 1 - T/T_c$ (or $T_{c,\mathrm{HF}}$ for the chain with the HF interaction). Our analysis shows that β = 0.86 without the HF field, while β_{HF} = 0.87 with it. These values are only slightly different. However, both of them are significantly larger than the BCS order-parameter critical exponent of 0.5. This observation agrees with previous expectations [26,27] of power-law scaling with non-standard exponents for thermodynamic properties of superconducting quasicrystals near T_c. Here, we note an early investigation of another quasiperiodic one-dimensional quantum system, namely, the Ising model on a transverse applied field, which studied the phase transition occurring in its coupling parameter and related critical indexes [28].

For a further illustration, we consider a numerical solution of the BdG equations for a different parametric set, that is, for n = 13 and t_A = 0.5 (all other microscopic parameters are the same). In this case $F_{n=13}$ = 377 and N = 378. The corresponding results are shown in Figure 2. This figure shows the order-parameter spatial distribution without (Figure 2a) and with HF interaction (Figure 2b), calculated for zero temperature. Similarly to the previous case, one observes significant oscillations of the order parameter, and these oscillations are notably enhanced when including HF interaction. The maximal difference between the order-parameter minima and maxima in Figure 2a is about 20% of the spatially averaged order parameter. In Figure 2b this values becomes about 60%.

However, despite a significant enhancement of the spatial oscillations of the order parameter in the presence of the HF interaction, its spatially averaged value (in the interval from i = 140 to i = 240) does not exhibit a significant drop and is reduced by less than 10%. An even smaller difference is observed between the two critical temperatures, T_c = 0.304 and $T_{c,HF}$ = 0.301. In addition, for the present case, we have $\langle\Delta\rangle_{T=0,HF}/T_{c,HF}$ = 1.82, which is larger than the corresponding ratio without the HF field, $\langle\Delta\rangle_{T=0}/T_c$ = 1.67. In this case, the BCS value of the ratio between the zero-temperature order parameter and the critical temperature is 1.76, that is, between the two values calculated for the Fibonacci approximant. Finally, the critical order-parameter exponents for the system with HF interaction, β_{HF} = 0.57, and without HF interaction, β = 0.65, are still larger than the corresponding BCS value of 0.5; yet, this difference is less pronounced than for the previous parametric choice.

Conclusion

Based on a numerical solution of the BdG equations for superconducting Fibonacci chains, we demonstrate that including the HF interaction significantly enhances the spatial oscillations of the order parameter when the averaged electron density is beyond the half-filling regime. These oscillations are a direct consequence of the system's quasiperiodicity, reflecting a general feature of superconducting quasicrystals. The enhancement of these oscillations leads to a reduction of the critical temperature, which can be pronounced depending on the model's microscopic parameters. We also find that the critical exponent β of the order parameter differs significantly from that of a uniform BCS condensate. Moreover, the value of β changes when the HF interaction is included. Finally, the ratio between the zero-temperature order parameter and the critical temperature is also sensitive to the HF potential and deviates notably from the universal BCS value. Consequently, a rigorous analysis of the condensate distribution in quasicrystalline superconductors requires a direct comparison of results with and without HF interaction.

Finally, we remark that our results are obtained in the regime beyond the half-filling. The half-filling is the special regime with uniform density of electrons so that the HF field appears to be just a shift of the chemical potential, not altering other thermodynamic quantities, see the discussion in [22].

Funding

This work was supported by the project "International academic cooperation" of HSE University.

Author Contributions

Edward G. Nikonov: data curation; investigation; software; validation; visualization. Yajiang Chen: conceptualization; software. Mauro M. Doria: investigation; writing – review & editing. Arkady A. Shanenko: conceptualization; investigation;

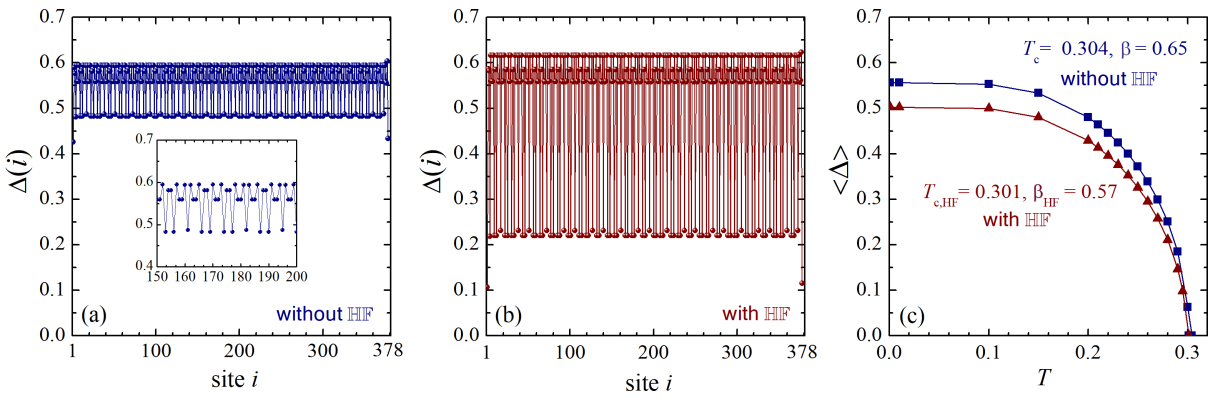


Figure 2: The same as in Figure 1 but for the Fibonacci chain with n = 13 and t_A = 0.5. Here, the critical temperatures of the systems with and without HF interaction are only slightly different: T_c = 0.304 and $T_{c,HF}$ = 0.301. However, the order-parameter critical exponent for the case with the HF potential, β_{HF} = 0.57, is notably smaller than the value of β = 0.65 for the chain without the HF interaction.

project administration; writing – original draft; writing – review & editing.

ORCID® iDs

Edward G. Nikonov - https://orcid.org/0000-0001-7162-0344
Yajiang Chen - https://orcid.org/0000-0003-1442-4448
Mauro M. Doria - https://orcid.org/0000-0001-7207-7697
Arkady A. Shanenko - https://orcid.org/0000-0002-6031-5106

Data Availability Statement

Data generated and analyzed during this study is available from the corresponding author upon reasonable request.

Preprint

A non-peer-reviewed version of this article has been previously published as a preprint: https://doi.org/10.3762/bxiv.2025.60.v1

References

1. De Gennes, P. G. *Superconductivity of metals and alloys;* W. A. Benjamin: New York, NY, USA, 1966.
2. Bardeen, J.; Cooper, L. N.; Schrieffer, J. R. *Phys. Rev.* **1957,** *108,* 1175–1204. doi:10.1103/physrev.108.1175
3. Ketterson, J. B.; Song, S. N. *Superconductivity;* Cambridge University Press: Cambridge, UK, 1999.
4. Zhu, J.-X. *Bogoliubov-de Gennes Method and Its Applications,* 1st ed.; Lecture notes in physics; Springer International Publishing: Cham, Switzerland, 2016. doi:10.1007/978-3-319-31314-6
5. Tanaka, K.; Marsiglio, F. *Phys. Rev. B* **2000,** *62,* 5345–5348. doi:10.1103/physrevb.62.5345
6. Ghosal, A.; Randeria, M.; Trivedi, N. *Phys. Rev. B* **2001,** *65,* 014501. doi:10.1103/physrevb.65.014501
7. Chen, Y.; Croitoru, M. D.; Shanenko, A. A.; Peeters, F. M. *J. Phys.: Condens. Matter* **2009,** *21,* 435701. doi:10.1088/0953-8984/21/43/435701
8. Chen, Y.; Zhu, Q.; Zhang, M.; Luo, X.; Shanenko, A. A. *Phys. Lett. A* **2024,** *494,* 129281. doi:10.1016/j.physleta.2023.129281
9. Shechtman, D.; Blech, I.; Gratias, D.; Cahn, J. W. *Phys. Rev. Lett.* **1984,** *53,* 1951–1953. doi:10.1103/physrevlett.53.1951
10. Levine, D.; Steinhardt, P. J. *Phys. Rev. Lett.* **1984,** *53,* 2477–2480. doi:10.1103/physrevlett.53.2477
11. Senechal, M. *Quasicrystals and geometry;* Cambridge University Press: Cambridge, MA, USA, 1995.
12. Kamiya, K.; Takeuchi, T.; Kabeya, N.; Wada, N.; Ishimasa, T.; Ochiai, A.; Deguchi, K.; Imura, K.; Sato, N. K. *Nat. Commun.* **2018,** *9,* 154. doi:10.1038/s41467-017-02667-x
13. Tokumoto, Y.; Hamano, K.; Nakagawa, S.; Kamimura, Y.; Suzuki, S.; Tamura, R.; Edagawa, K. *Nat. Commun.* **2024,** *15,* 1529. doi:10.1038/s41467-024-45952-2
14. Meena, P. K.; Verma, R.; Arushi; Jangid, S.; Kushwaha, R. K.; Stewart, R.; Hillier, A. D.; Singh, B.; Singh, R. P. *Commun. Mater.* **2025,** *6,* 226. doi:10.1038/s43246-025-00949-2
15. Jagannathan, A. *Rev. Mod. Phys.* **2021,** *93,* 045001. doi:10.1103/revmodphys.93.045001
16. Rai, G.; Haas, S.; Jagannathan, A. *Phys. Rev. B* **2019,** *100,* 165121. doi:10.1103/physrevb.100.165121
17. Rai, G.; Haas, S.; Jagannathan, A. *Phys. Rev. B* **2020,** *102,* 134211. doi:10.1103/physrevb.102.134211
18. Rai, G.; Haas, S.; Jagannathan, A. *J. Phys.: Conf. Ser.* **2020,** *1458,* 012013. doi:10.1088/1742-6596/1458/1/012013
19. Sun, M.; Čadež, T.; Yurkevich, I.; Andreanov, A. *Phys. Rev. B* **2024,** *109,* 134504. doi:10.1103/physrevb.109.134504
20. Sandberg, A.; Awoga, O. A.; Black-Schaffer, A. M.; Holmvall, P. *Phys. Rev. B* **2024,** *110,* 104513. doi:10.1103/physrevb.110.104513
21. Kobiałka, A.; Awoga, O. A.; Leijnse, M.; Domański, T.; Holmvall, P.; Black-Schaffer, A. M. *Phys. Rev. B* **2024,** *110,* 134508. doi:10.1103/physrevb.110.134508
22. Zhu, Q.; Zha, G.-Q.; Shanenko, A. A.; Chen, Y. *Phys. Rev. B* **2025,** *112,* 134503. doi:10.1103/j8tj-82ty
23. Nagai, Y. *Phys. Rev. B* **2022,** *106,* 064506. doi:10.1103/physrevb.106.064506
24. Piéchon, F.; Benakli, M.; Jagannathan, A. *Phys. Rev. Lett.* **1995,** *74,* 5248–5251. doi:10.1103/physrevlett.74.5248
25. Rüdinger, A.; Piéchon, F. *J. Phys. A: Math. Gen.* **1998,** *31,* 155–164. doi:10.1088/0305-4470/31/1/017
26. Karkut, M. G.; Triscone, J.-M.; Ariosa, D.; Fischer, Ø. *Phys. Rev. B* **1986,** *34,* 4390–4393. doi:10.1103/physrevb.34.4390
27. Kitaev, A. Y.; Levitov, L. S. *Sov. Phys. - JETP* **1989,** *68,* 176–181.
28. Doria, M. M.; Satija, I. I. *Phys. Rev. Lett.* **1988,** *60,* 444–447. doi:10.1103/physrevlett.60.444

License and Terms

This is an open access article licensed under the terms of the Beilstein-Institut Open Access License Agreement (https://www.beilstein-journals.org/bjnano/terms), which is identical to the Creative Commons Attribution 4.0 International License (https://creativecommons.org/licenses/by/4.0). The reuse of material under this license requires that the author(s), source and license are credited. Third-party material in this article could be subject to other licenses (typically indicated in the credit line), and in this case, users are required to obtain permission from the license holder to reuse the material.

The definitive version of this article is the electronic one which can be found at:
https://doi.org/10.3762/bjnano.16.150

BEILSTEIN JOURNAL OF NANOTECHNOLOGY

Electromagnetic study of a split-ring resonator metamaterial with cold-electron bolometers

Ekaterina A. Matrozova[1], Alexander V. Chiginev[1,2], Leonid S. Revin[1,2] and Andrey L. Pankratov[*1,2]

Full Research Paper

Open Access

Address:
[1]Nizhny Novgorod State Technical University n.a. R.E. Alekseev, MininStreet, 24, Nizhny Novgorod, 603155, Russia and [2]Institute for Physics of Microstructures of the Russian Academy of Sciences, Akademicheskaya Street, 7, Nizhny Novgorod, 603950, Russia

Email:
Andrey L. Pankratov[*] - alp@ipmras.ru

* Corresponding author

Keywords:
cold-electron bolometer; metamaterial; split-ring resonator

Beilstein J. Nanotechnol. **2025,** *16,* 2199–2206.
https://doi.org/10.3762/bjnano.16.152

Received: 02 October 2025
Accepted: 18 November 2025
Published: 05 December 2025

This article is part of the thematic issue "Superconducting artificial neural networks and quantum circuits".

Guest Editor: A. S. Sidorenko

© 2025 Matrozova et al.; licensee Beilstein-Institut.
License and terms: see end of document.

Abstract

We present an electromagnetic study of a metamaterial receiver based on split-ring resonators with integrated cold-electron bolometers. We suggest a modified antenna design that allows one to significantly increase the absorbed power and the bandwidth. The trade-off between the bandwidth expansion due to miniaturization and the reduction in absorption efficiency determined by the Airy spot size of the coupling lens is investigated. To solve this issue, a simultaneous miniaturization of the size of the entire structure with an increase in the number of array elements is proposed. The design with a 37-element array demonstrates an increase in power absorption by a factor of 1.4 compared to the original 19-element single-ring array, as well as an increase in operating bandwidth from 160 to 820 GHz.

Introduction

Highly sensitive receivers with broadband antennas are of significant interest for advanced spectroscopic applications and various radioastronomy tasks [1-5]. In particular, broadband receiving systems are required for use with a Fourier-transform spectrometer based on the Martin–Paplett interferometer that is planned to be used in future missions such as BISOU (Balloon Interferometer for Spectral Observations of the Universe) [3,4] and Millimetron [2,5]. The use of cold-electron bolometers (CEBs) is particularly advantageous for such systems, enabling operation in a wide frequency range from gigahertz frequencies to X-rays [6-8] due to a normal-metal absorber. CEBs offer several advantages over other types of receivers such as transition edge sensors [9-11]. These advantages include their micrometer-scale size, which facilitates direct integration into antenna slots without the need for microwave feed lines (e.g., microstrip or coplanar lines), thus simplifying the design and preventing signal degradation at higher frequencies [12]. Furthermore, the natural electron cooling mechanism in CEBs [13-15] is highly suitable for operation with cryogenic systems such as ^{3}He sorption fridges. Perhaps most critically, CEBs

demonstrate exceptional hardness against cosmic rays [16], a paramount requirement for balloon and space missions.

Our group has recently designed, fabricated, and characterized a metamaterial receiver with integrated CEBs, operating in a broad frequency range [17]. In that work, each element represented a ring antenna with two embedded CEBs connected parallel in DC, whereas the antennas in the array were connected in series. In the present work, we propose and numerically investigate a new design of a CEB metamaterial receiver based on double split-ring resonators (SRRs) [18] to increase both the magnitude of the absorbed signal and the working bandwidth. We consider various geometrical modifications of this design and perform a comparative analysis.

Design and Simulation Approach

In our previous work [17], a metamaterial comprising 19-ring antennas enabled the reception of external electromagnetic signals in the broad band from 150 to 550 GHz, as well as in the band from 900 to 1300 GHz. To further enhance signal absorption, we propose replacing simple ring antennas with SRRs [18-21]. The SRR is a well-established magnetic metamaterial element whose resonant properties are governed by its internal inductance and capacitance, allowing for a strong magnetic response and associated current loops at the designed resonance frequency.

The simulations of the metamaterial arrays were performed in the time-domain solver of CST MWS in 3D mode. The simulated receiving structure is placed on a 500 μm thick silicon substrate. A 4 mm-diameter silicon hyperhemispherical lens is placed on the rear side of the substrate to efficiently couple the incident radiation into the planar structure. The external signal is incident from the H_{11} mode of the round waveguide port located behind the Si lens, simulating a realistic excitation source. The electric field of the incident wave is directed perpendicularly to the gaps in the receiving elements.

The signal is received by an array of the proposed ring resonators. Two CEBs are embedded into the outer ring of each SRR element. In the simulations, each CEB is modeled as an RC circuit (see inset in Figure 1), where R_{abs} = 75 Ω represents the resistance of the CEB's normal-metal absorber, and C_{SIN} = 20 fF is the capacitance of the two SIN junctions of the CEB connected in series. The total absorbed power is calculated as the sum of the powers absorbed in these discrete ports repre-

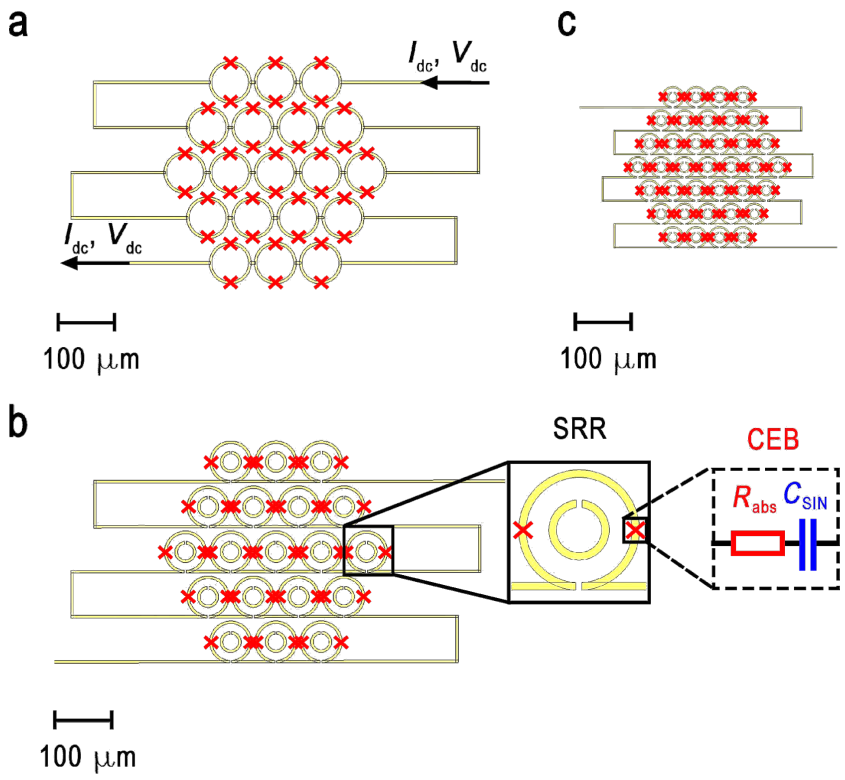


Figure 1: Schematic layout of the investigated metamaterial arrays. (a) 19-element array of single-ring antennas; (b) 19-element array of split-ring resonators; (c) 37-element array of miniaturized SRRs. Inset: a single unit cell with two embedded CEBs represented as an RC circuit.

senting the CEBs. The power in our modeling is normalized to the power outgoing from the waveguide port, which is equal to 0.5 in arbitrary units.

Results

The design of the previously studied metamaterial with CEBs and single-ring antennas is shown in Figure 1a. To increase the absorbed power and the working frequency band, we propose and analyze a new design based on SRRs (Figure 1b,c). The geometric parameters of the structures are as follows: A single ring has an outer ring diameter of d_{ext} = 80 μm and an inner ring diameter of d_{int} = 70 μm. The lattice constant (period) of the metamaterial array is P = 86 μm. The total size of the structure is 424 μm. A large-scale SRR has an outer ring with an external diameter of $d_{ext,1}$ = 80 μm and an internal diameter of $d_{int,1}$ = 70 μm. The inner ring has an external diameter of $d_{ext,2}$ = 40 μm and an internal diameter of $d_{int,2}$ = 30 μm. The period of the metamaterial array is P = 86 μm. The total size of the structure is 424 μm. A small-scale SRR is a scaled-down version with $d_{ext,1}$ = 40 μm, $d_{int,1}$ = 35 μm; $d_{ext,2}$ = 20 μm, $d_{int,2}$ = 15 μm. The lattice period for this dense array is P = 43 μm. The total size of the structure is reduced to 298 μm. This scaling of the SRR geometry is intended to shift the central frequency of the metamaterial to a higher value while maintaining the increasing absorption of the double-ring design.

The transition from a single-ring antenna to a double split-ring resonator design, while keeping the number of elements constant, resulted in a significant improvement in performance. The addition of the inner ring, which increases the total capacitance of the resonant element, leads to a slight reduction of the central frequency [20]. More importantly, it yielded a 1.5-fold increase in the total absorbed power.

The amplitude–frequency characteristics (AFC) for the simulated single-ring and SRR designs are presented in Figure 2. For the single-ring array, the absorbed power in the first resonance maximum reached a value of 0.18 (normalized units, with 0.5 maximal total power) with the bandwidth at half maximum (FWHM) spanning from 100 to 545 GHz (Figure 2, red curve). In contrast, the SRR array demonstrated a higher absorbed power of 0.27 within a bandwidth of 105 to 440 GHz (Figure 2, blue curve). Parameters of metamaterials with CEBs and different designs are given in Table 1.

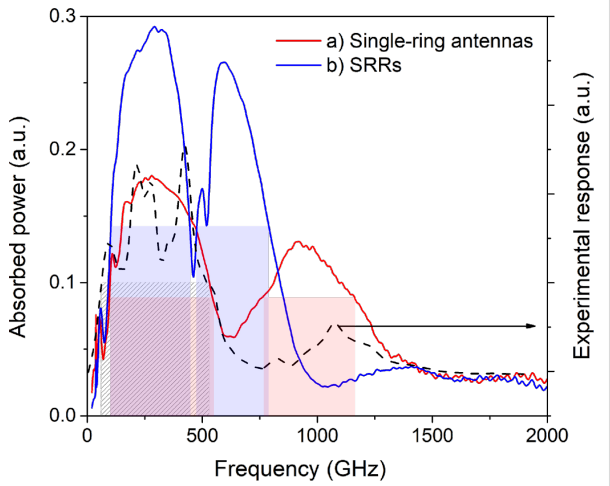


Figure 2: Amplitude–frequency characteristics of the metamaterial receiver. (a) 19-element array of single-ring antennas with a lattice period of P = 86 μm (red curve); (b) 19-element array of SRRs with P = 86 μm (blue curve). The dashed black curve shows the experimentally measured response of the single-ring metamaterial.

As an experimental reference for our simulations, Figure 2 also shows the frequency response measured for a fabricated sample consisting of a 19-element single-ring metamaterial (black dashed curve). This sample had the design described in [17] and was characterized using the same experimental setup described there. This setup employs a YBaCuO Josephson junction oscillator as a broadband source, with the signal delivered to the sample via an oversized waveguide. Therefore, the measured frequency response is the combined frequency response of the entire path (oscillator, waveguide-feeder, lens and the CEB metamaterial itself), with "fingers" due to the used log-periodic antenna of the Josephson oscillator, which was not fully matched to the antenna. Despite this convolution, the experimental data clearly confirm the calculated dual-band behavior of the metamaterial, showing two broad peaks centered at approximately 350 and 1100 GHz. This agreement validates our simulation model.

Table 1: Parameters of metamaterial structures with CEBs.

Design (according to Figure 1)	Type of unit cell	Number of cells	Period of structure, μm	Peak absorption, a.u.	Frequency band, GHz
a	single-ring antennas	19	86	0.18	100–545
b	split-ring resonators	19	86	0.27	105–440
c	split-ring resonators	37	43	0.25	160–820

The AFC of the single-ring and SRR metamaterials with various scaling factors are presented in Figure 3. The optimal number and size of the resonators are governed by the requirement to fill the Airy spot of the silicon lens. If the total array size is smaller than the Airy spot, a portion of the incident signal will not interact with the metamaterial, instead scattering into the surrounding space. Our simulations confirm this principle: A reduction in the SRR dimensions and the array period by 20% led to a broadening of the absorption bandwidth and a small shift of the first resonance maximum towards higher frequencies. A further reduction of dimensions by 40% resulted in an even wider bandwidth; however, the peak absorbed power began decreasing, indicating that the array size was becoming insufficient relative to the Airy spot. A drastic 60% size reduction caused a severe deterioration of absorption.

To achieve the widest possible bandwidth using SRRs, our results shown in Figure 3 suggest prioritizing somewhat smaller unit cell sizes. Simply scaling down a fixed 19-element array leads to less efficient signal reception since the array is becoming smaller than the Airy spot. As an efficient alternative, we propose to halve the SRR dimensions and array period while simultaneously increasing the number of elements from 19 to 37 (Figure 1c). This approach successfully increased the absorbed power to 0.25, which is by a factor of 1.4 higher than that of the single-ring array, while also achieving an ultrawide receiving band from 160 to 820 GHz (Figure 4, black line). If the 37-element array structure occupies the same area as the original single-ring structure, larger absorption efficiency at the first peak can be achieved (Figure 4, red line), but the working bandwidth will be narrower than for the structure with smaller

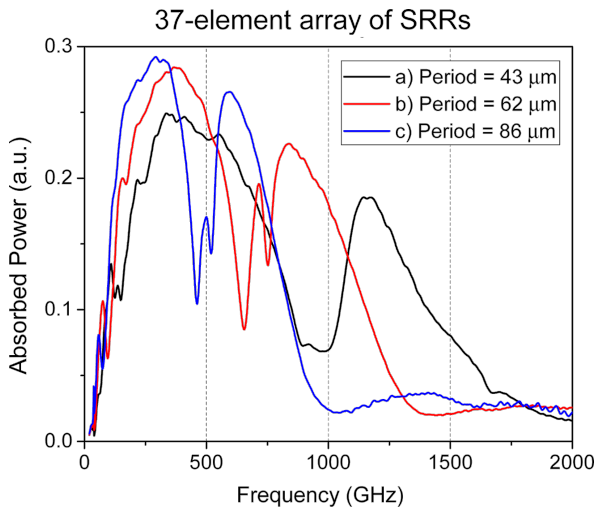


Figure 4: The amplitude–frequency characteristics of the 37-element array of SRR-based metamaterial for different periods of the lattice.

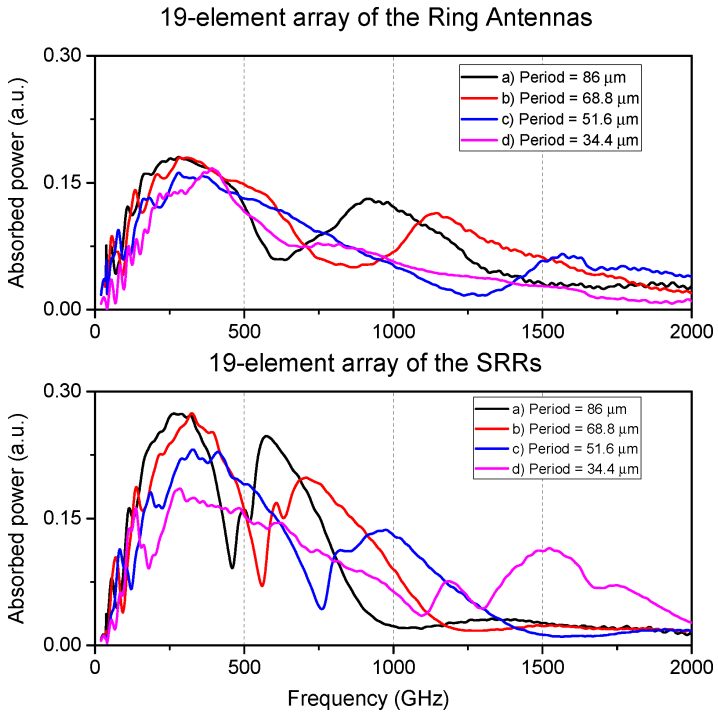


Figure 3: Top: AFC of the 19 single-ring antenna metamaterial for different geometric scaling factors. (a, black curve) outer ring diameter d_{out} = 80 μm, inner ring diameter d_{in} = 70 μm, period P = 86 μm; (b, red curve) d_{out} = 64 μm, d_{in} = 56 μm, P = 68.8 μm; (c, blue curve) d_{out} = 48 μm, d_{in} = 42 μm, P = 51.6 μm; (d, purple curve) d_{out} = 32 μm, d_{in} = 28 μm, P = 34.4 μm. Bottom: AFC of the 19 SRR-based metamaterial for different geometric scaling factors. The design parameters and scaling factors (0%, 20%, 40%, and 60%) correspond to the upper plot.

rings. Thus, by selecting the overall structure size, a compromise can be found between the maximum absorption efficiency and the widest receiving bandwidth.

It is important to note that the choice of the number of receiving antennas should be in a proper balance. Although a larger array can better fill the Airy spot, it also increases the total number of bolometers. This, in turn, increases the differential resistance of the structure at the operating point and increases the current noise contribution of the readout amplifier [17,22]. Furthermore, a larger number of elements increases the fabrication complexity. Crucially, nearly doubling the number of elements (from 19 to 37) does not produce a proportional increase in the absorbed power (Figure 5).

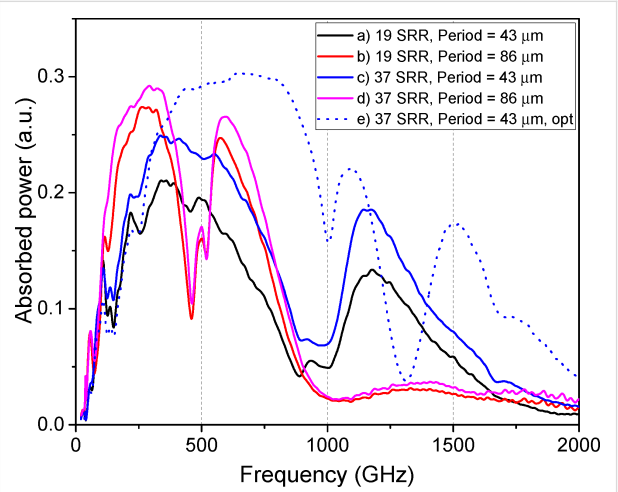


Figure 5: Dependence of the absorbed power on the number of elements in the SRR array.

Figure 5 shows the AFC of the SRR metamaterial with a different number of elements. For the large-scale design (period P = 86 μm, rings: $d_{out,1}/d_{in,1}$ = 80/70 μm, $d_{out,2}/d_{in,2}$ = 40/30 μm), doubling the number of elements increases the absorbed power by about 7% only, with a minor increase in bandwidth. The same doubling for the miniaturized design (P = 43 μm, rings: $d_{out,1}/d_{in,1}$ = 40/35 μm, $d_{out,2}/d_{in,2}$ = 20/15 μm) is more efficient, leading to 17% increase in power. This higher efficiency is directly linked to the Airy spot coverage: Adding elements to the smaller array more effectively increases its total area towards the optimal size. For the already large array, new elements are added at the periphery or outside the most intense part of the Airy spot, which does not actually help.

The obtained results can be further enhanced through optimized design parameters of the structure. Specifically, increasing the substrate thickness to 700 μm enables an increase in absorbed power up to 0.3 a.u. across an ultrabroad frequency range of 200–1200 GHz (Figure 5e). Such a thick substrate can be realized by using commercially available substrates with greater thickness (or by stacking and bonding multiple thinner substrates), or by employing a lens with a pedestal structure.

Discussion

Solving the problem of broadband high-sensitivity reception for terahertz applications naturally entails comparing the metamaterial-based approach presented here with traditional broadband antenna solutions such as the log-periodic [23-25] or spiral antennas [26,27]. These antennas are indeed a well-established technology, providing wideband frequency response and high detection/radiation efficiency. However, their widespread use is subject to a fundamental limitation: The active receiving element is typically a single detector unit located at the antenna's feed point. This configuration can become a bottleneck when detecting ultralow power signals in the presence of high background radiation, as the single detector must handle the entire power load, potentially limiting the dynamic range and complicating the optimization of noise-equivalent power (NEP).

There have been proposals to integrate multiple sensing elements directly into the structure of a log-periodic antenna [28-30]. While promising, such designs face significant challenges in implementation. The complex geometry of the antenna makes it difficult to integrate a large number of detectors and to design complex series–parallel electrical networks necessary for optimal power distribution and impedance matching. In contrast, the metamaterial approach offers a fundamentally more flexible paradigm. A periodic array of resonators, such as our SRR-based design, inherently functions as a multiabsorber system. This architecture allows for the precise engineering of the detector network, that is, the number of CEBs, their individual connection (series or parallel), and the overall array configuration to achieve an optimal balance between power load, responsivity, and total noise [17,22].

This capability is particularly critical for applications like cosmic microwave background polarimetry or high-resolution spectroscopy, where the detector must operate photon-noise-limited under a specific background power load. For CEBs, we have previously demonstrated that the optimal configuration for minimizing the total NEP with a given readout amplifier involves a specific series–parallel combination of bolometers. The metamaterial platform is ideal for implementing such an optimized multiabsorber receiver. By adapting the array geometry and the electrical connection scheme between CEBs, one can precisely control the power absorbed per bolometer and the resulting differential resistance, thereby achieving photon-noise-limited performance across a wide bandwidth. This level

of design control is considerably more challenging to realize within the constrained geometry of a single-feed log-periodic antenna.

Conclusion

In this work, we have presented a comprehensive electromagnetic study on the design and optimization of a metamaterial receiver based on split-ring resonators integrated with cold-electron bolometers. The transition from a conventional single-ring antenna design to a double SRR configuration has been demonstrated to be a highly efficient strategy to enhance the receiver performance. This design improvement resulted in a substantial 1.5-fold increase in the absorbed power, confirming the theoretical advantage of SRRs in providing a stronger magnetic resonance and greater field concentration within the capacitive gaps where the CEBs are located.

Our investigation of the scaling of the metamaterial array revealed a critical design trade-off. While reducing the dimensions of the SRR unit cells effectively broadens the operational bandwidth, it also reduces the total absorbed power if the array's physical size becomes smaller than the Airy spot of the coupling lens. We successfully resolved this issue by implementing a strategy of simultaneous miniaturization and increasing the array density. By halving the SRR dimensions and lattice period while nearly doubling the number of elements (from 19 to 37), we achieved an optimal compromise. The resulting receiver exhibits both enhanced absorption (by a factor of 1.4 larger than the original single-ring design) and an ultrawide bandwidth spanning from 160 to 820 GHz.

Furthermore, we quantified the non-linear relationship between the number of array elements and the absorbed power, showing that the benefit of adding elements is significantly higher for a miniaturized array that initially underfills the Airy spot. This provides a crucial practical guideline for designing efficient multiabsorber receivers, balancing performance gains against the increased technological complexity and noise considerations associated with a larger number of bolometers.

This work solidifies the position of CEB-based SRR metamaterials as a highly promising platform for constructing ultrabroadband, high-sensitivity receivers essential for next-generation spectroscopic and radioastronomical applications, particularly in demanding space and balloon-borne environments. One more important potential application for such broadband receiving system is the use for axion search experiments with broadband coaxial dish antennas [31,32]. Future work will focus on the experimental fabrication and characterization of the proposed miniaturized 37-element SRR array to validate these simulation results.

Funding

The work is supported by Russian Science Foundation Grant No. 21-79-20227.

Author Contributions

Ekaterina A. Matrozova: data curation; formal analysis; investigation; methodology; software; visualization; writing – original draft; writing – review & editing. Alexander V. Chiginev: conceptualization; data curation; formal analysis; investigation; methodology; software; validation; writing – original draft; writing – review & editing. Leonid S. Revin: conceptualization; formal analysis; investigation; methodology; software; validation; visualization; writing – original draft; writing – review & editing. Andrey L. Pankratov: conceptualization; formal analysis; funding acquisition; investigation; methodology; project administration; resources; supervision; validation; writing – review & editing.

ORCID® iDs

Ekaterina A. Matrozova - https://orcid.org/0000-0003-1013-1365
Alexander V. Chiginev - https://orcid.org/0000-0002-6676-9141
Andrey L. Pankratov - https://orcid.org/0000-0003-2661-2745

Data Availability Statement

Data generated and analyzed during this study is available from the corresponding author upon reasonable request.

Preprint

A non-peer-reviewed version of this article has been previously published as a preprint: https://doi.org/10.3762/bxiv.2025.58.v1

References

1. Ajito, K.; Nakamura, M.; Tajima, T.; Ueno, Y. Terahertz Spectroscopy Methods and Instrumentation. In *Encyclopedia of Spectroscopy and Spectrometry,* 3rd ed.; Lindon, J. C.; Tranter, G. E.; Koppenaal, D. W., Eds.; Academic Press: Oxford, UK, 2017; pp 432–438. doi:10.1016/b978-0-12-409547-2.12092-x
2. Likhachev, S. F.; Larchenkova, T. I. *Phys.-Usp.* **2024,** *67,* 768–778. doi:10.3367/ufne.2024.03.039662
3. Maffei, B.; Aghanim, N.; Aumont, J.; Battistelli, E.; Beelen, A.; Besnard, A.; Borgo, B.; Calvo, M.; Catalano, A.; Chluba, J.; Coulon, X.; de Bernardis, P.; De Jabrun, C.; Douspis, M.; Errard, J.; Grain, J.; Guiot, P.; Hill, J. C.; Ishino, H.; Kogut, A.; Lagache, G.; Macias-Perez, J.; Masi, S.; Matsumura, T.; Monfardini, A.; O'Sullivan, C.; Pagano, L.; Patanchon, G.; Pisano, G.; Pitre, L.; Ponthieu, N.; Remazeilles, M.; Ritacco, A.; Savini, G.; Sauvage, V.; Shitvov, A.; Stever, S. L.; Tartari, A.; Thiele, L.; Trappe, N.; Aubrun, J.-F.; Bray, N.; Louvel, S. BISOU: a balloon pathfinder for CMB spectral distortions studies. In *Millimeter, Submillimeter, and Far-Infrared Detectors and Instrumentation for Astronomy XII,* Yokohama, Japan, June 18–22, 2024; Zmuidzinas, J.; Gao, J.-R., Eds.; SPIE, 2024; 131020N. doi:10.1117/12.3018371
4. Coulon, X.; Maffei, B.; Aghanim, N. *EPJ Web Conf.* **2024,** *293,* 00012. doi:10.1051/epjconf/202429300012

5. Novikov, D. I.; Doroshkevich, A. G.; Larchenkova, T. I.; Malinovsky, A. M.; Mihalchenko, A. O.; Osipova, A. M.; Parfenov, K. O.; Pilipenko, S. V. *Phys.-Usp.* **2025,** *68,* 987–1000. doi:10.3367/ufne.2025.08.040006
6. Anghel, D. V.; Kuzmin, L. S. *Phys. Rev. Appl.* **2020,** *13,* 024028. doi:10.1103/physrevapplied.13.024028
7. Pimanov, D. A.; Pankratov, A. L.; Gordeeva, A. V.; Chiginev, A. V.; Blagodatkin, A. V.; Revin, L. S.; Razov, S. A.; Safonova, V. Yu.; Fedotov, I. A.; Skorokhodov, E. V.; Orlova, A. N.; Tatarsky, D. A.; Gusev, N. S.; Trofimov, I. V.; Mumlyakov, A. M.; Tarkhov, M. A. *Supercond. Sci. Technol.* **2025,** *38,* 035026. doi:10.1088/1361-6668/adb942
8. Nahum, M.; Martinis, J. M. *Appl. Phys. Lett.* **1995,** *66,* 3203–3205. doi:10.1063/1.113723
9. Irwin, K. D.; Hilton, G. C. Transition-Edge Sensors. *Cryogenic Particle Detection;* Topics in Applied Physics, Vol. 99; Springer: Berlin, Germany, 2005; pp 63–150. doi:10.1007/10933596_3
10. Withington, S. *Contemp. Phys.* **2022,** *63,* 116–137. doi:10.1080/00107514.2023.2180179
11. Safonova, V. Y.; Gordeeva, A. V.; Blagodatkin, A. V.; Pimanov, D. A.; Yablokov, A. A.; Pankratov, A. L. *Beilstein J. Nanotechnol.* **2024,** *15,* 1353–1361. doi:10.3762/bjnano.15.108
12. O'Brient, R.; Ade, P.; Arnold, K.; Edwards, J.; Engargiola, G.; Holzapfel, W. L.; Lee, A. T.; Myers, M. J.; Quealy, E.; Rebeiz, G.; Richards, P.; Suzuki, A. *Appl. Phys. Lett.* **2013,** *102,* 063506. doi:10.1063/1.4791692
13. Gordeeva, A. V.; Pankratov, A. L.; Pugach, N. G.; Vasenko, A. S.; Zbrozhek, V. O.; Blagodatkin, A. V.; Pimanov, D. A.; Kuzmin, L. S. *Sci. Rep.* **2020,** *10,* 21961. doi:10.1038/s41598-020-78869-z
14. Pimanov, D. A.; Frost, V. A.; Blagodatkin, A. V.; Gordeeva, A. V.; Pankratov, A. L.; Kuzmin, L. S. *Beilstein J. Nanotechnol.* **2022,** *13,* 896–901. doi:10.3762/bjnano.13.80
15. Lemziakov, S. A.; Karimi, B.; Nakamura, S.; Lvov, D. S.; Upadhyay, R.; Satrya, C. D.; Chen, Z.-Y.; Subero, D.; Chang, Y.-C.; Wang, L. B.; Pekola, J. P. *J. Low Temp. Phys.* **2024,** *217,* 54–81. doi:10.1007/s10909-024-03144-8
16. Salatino, M.; de Bernardis, P.; Kuzmin, L. S.; Mahashabde, S.; Masi, S. *J. Low Temp. Phys.* **2014,** *176,* 323–330. doi:10.1007/s10909-013-1057-5
17. Revin, L. S.; Pimanov, D. A.; Pankratov, A. L.; Blagodatkin, A. V.; Matrozova, E. A.; Chiginev, A. V.; Gordeeva, A. V.; Fedotov, I. A.; Skorokhodov, E. V.; Gusev, N. S.; Masterov, D. V.; Parafin, A. E.; Sobolev, A. S. *Phys. Rev. Appl.* **2024,** *22,* 064040. doi:10.1103/physrevapplied.22.064040
18. Sydoruk, O.; Tatartschuk, E.; Shamonina, E.; Solymar, L. *J. Appl. Phys.* **2009,** *105,* 014903. doi:10.1063/1.3056052
19. Pendry, J. B.; Holden, A. J.; Robbins, D. J.; Stewart, W. J. *IEEE Trans. Microwave Theory Tech.* **1999,** *47,* 2075–2084. doi:10.1109/22.798002
20. Reddy, A. N.; Raghavan, S. Split ring resonator and its evolved structures over the past decade: This paper discusses the nuances of the most celebrated composite particle (split-ring resonator) with which novel artificial structured materials (called metamaterials) are built. In *2013 IEEE International Conference ON Emerging Trends in Computing, Communication and Nanotechnology (ICECCN),* Tirunelveli, India, March 25–26, 2013; IEEE, 2013; pp 625–629. doi:10.1109/ice-ccn.2013.6528575
21. Marqués, R.; Martín, F.; Sorolla, M. *Metamaterials with Negative Parameters: Theory, Design and Microwave Applications;* John Wiley & Sons: Hoboken, NJ, USA, 2008. doi:10.1002/9780470191736
22. Kuzmin, L. S.; Pankratov, A. L.; Gordeeva, A. V.; Zbrozhek, V. O.; Shamporov, V. A.; Revin, L. S.; Blagodatkin, A. V.; Masi, S.; de Bernardis, P. *Commun. Phys.* **2019,** *2,* 104. doi:10.1038/s42005-019-0206-9
23. Tarasov, M.; Kuzmin, L.; Stepantsov, E.; Kidiyarova-Shevchenko, A. Quasioptical Terahertz Spectrometer Based on a Josephson Oscillator and a Cold Electron Nanobolometer. *Nanoscale Devices - Fundamentals and Applications; NATO Science Series*, Vol. 233; Springer: Dordrecht, Netherlands, 2006; pp 325–335. doi:10.1007/978-1-4020-5107-4_22
24. Stepantsov, E.; Tarasov, M.; Kalabukhov, A.; Kuzmin, L.; Claeson, T. *J. Appl. Phys.* **2004,** *96,* 3357–3361. doi:10.1063/1.1782273
25. Gao, X.; Zhang, T.; Du, J.; Weily, A. R.; Guo, Y. J.; Foley, C. P. *Supercond. Sci. Technol.* **2017,** *30,* 095011. doi:10.1088/1361-6668/aa7cc1
26. Tretyakov, I. V.; Khudchenko, A. V.; Rudakov, K. I.; Ivashentseva, I. V.; Kaurova, N. S.; Voronov, B. M.; Kirsanova, M. S.; Larchenkova, T. I.; Goltsman, G. N.; Baryshev, A. M.; Hesper, R.; Khan, F. V.; Zhukova, E. S.; Chekushkin, A. M.; Melentev, A. V.; Zhivetev, K. V.; Terentiev, A. V.; Koshelets, V. P.; Likhachev, S. F. *IEEE Trans. Terahertz Sci. Technol.* **2025,** *15,* 191–199. doi:10.1109/tthz.2024.3505592
27. Malnou, M.; Luo, A.; Wolf, T.; Wang, Y.; Feuillet-Palma, C.; Ulysse, C.; Faini, G.; Febvre, P.; Sirena, M.; Lesueur, J.; Bergeal, N. *Appl. Phys. Lett.* **2012,** *101,* 233505. doi:10.1063/1.4769441
28. Yu, M.; Geng, H.; Hua, T.; An, D.; Xu, W.; Chen, Z. N.; Chen, J.; Wang, H.; Wu, P. *Supercond. Sci. Technol.* **2020,** *33,* 025001. doi:10.1088/1361-6668/ab5e13
29. Sharafiev, A.; Malnou, M.; Feuillet-Palma, C.; Ulysse, C.; Wolf, T.; Couëdo, F.; Febvre, P.; Lesueur, J.; Bergeal, N. *Supercond. Sci. Technol.* **2018,** *31,* 035003. doi:10.1088/1361-6668/aa9d48
30. Glushkov, E. I.; Chiginev, A. V.; Kuzmin, L. S.; Revin, L. S. *Beilstein J. Nanotechnol.* **2022,** *13,* 325–333. doi:10.3762/bjnano.13.27
31. Knirck, S.; Hoshino, G.; Awida, M. H.; Cancelo, G. I.; Di Federico, M.; Knepper, B.; Lapuente, A.; Littmann, M.; Miller, D. W.; Mitchell, D. V.; Rodriguez, D.; Ruschman, M. K.; Sawtell, M. A.; Stefanazzi, L.; Sonnenschein, A.; Teafoe, G. W.; Bowring, D.; Carosi, G.; Chou, A.; Chang, C. L.; Dona, K.; Khatiwada, R.; Kurinsky, N. A.; Liu, J.; Pena, C.; Salemi, C. P.; Wang, C. W.; Yu, J. *Phys. Rev. Lett.* **2024,** *132,* 131004. doi:10.1103/physrevlett.132.131004
32. Hoshino, G.; Knirck, S.; Awida, M. H.; Cancelo, G. I.; Corrodi, S.; Di Federico, M.; Knepper, B.; Lapuente, A.; Littmann, M.; Miller, D. W.; Mitchell, D. V.; Rodriguez, D.; Ruschman, M. K.; Salemi, C. P.; Sawtell, M. A.; Stefanazzi, L.; Sonnenschein, A.; Teafoe, G. W.; Winter, P. *Phys. Rev. Lett.* **2025,** *134,* 171002. doi:10.1103/physrevlett.134.171002

License and Terms

This is an open access article licensed under the terms of the Beilstein-Institut Open Access License Agreement (https://www.beilstein-journals.org/bjnano/terms), which is identical to the Creative Commons Attribution 4.0 International License (https://creativecommons.org/licenses/by/4.0). The reuse of material under this license requires that the author(s), source and license are credited. Third-party material in this article could be subject to other licenses (typically indicated in the credit line), and in this case, users are required to obtain permission from the license holder to reuse the material.

The definitive version of this article is the electronic one which can be found at:
https://doi.org/10.3762/bjnano.16.152

BEILSTEIN JOURNAL OF NANOTECHNOLOGY

Geometry-controlled engineering of the low-temperature proximity effect in normal metal–superconductor junctions

Munisa A. Tomayeva[1,2], Vyacheslav D. Neverov[2,3], Andrey V. Krasavin[*1,2], Alexei Vagov[2] and Mihail D. Croitoru[2,4]

Full Research Paper

Open Access

Address:
[1]National Research Nuclear University MEPhI, Moscow 115409, Russian Federation, [2]HSE University, Moscow 101000, Russian Federation, [3]Moscow Institute of Physics and Technology, 141700 Dolgoprudny, Russian Federation and [4]Departamento de Física, Universidade Federal de Pernambuco, 50740-560,Recife-PE, Brazil

Email:
Andrey V. Krasavin[*] - avkrasavin@gmail.com

* Corresponding author

Keywords:
Bogoliubov–de Gennes equations; normal metal–superconductor junction; order parameter; proximity effect; superconductivity

Beilstein J. Nanotechnol. **2025,** *16,* 2265–2273.
https://doi.org/10.3762/bjnano.16.155

Received: 30 July 2025
Accepted: 26 November 2025
Published: 12 December 2025

This article is part of the thematic issue "Superconducting artificial neural networks and quantum circuits".

Guest Editor: A. S. Sidorenko



© 2025 Tomayeva et al.; licensee Beilstein-Institut.
License and terms: see end of document.

Abstract

In the ballistic regime at finite temperatures, the proximity effect diminishes following an exponential pattern; however, at low or zero temperatures, this transition alters to a decay characterized by a power law with a dimensionality-dependent exponent. Here, we extend the current understanding of the proximity effect by exploring the role of normal metal–superconductor (NS) junction geometry in altering the spatial propagation of the superconducting order. Specifically, we demonstrate that geometric factors, such as interface curvature, significantly affect the decay exponent of the Cooper pair wave function, with negative curvature increasing the proximity range exponent and positive curvature shortening it. Furthermore, we discuss how the geometry of the NS interface governs the transparency of the clean NS junction and thus influences the proximity effect. These results deepen our understanding of how geometry and the proximity effect interact, which is important for the design and optimization of superconducting hybrid devices.

Introduction

When a superconductor (SC) is brought into contact with a normal metal (NM) or a ferromagnet (FM), Cooper pairs penetrate the adjacent material, imparting superconducting properties to it. This phenomenon, known as the proximity effect, enables normal material to support supercurrents and to exhibit a reduced density of states near the Fermi level, where a gap opens in the single-particle spectrum as electrons form into Cooper pairs [1-4].

At the same time, unpaired electrons from the normal side scatter into the superconductor, suppressing the superconducting order parameter near the interface [5-7]. In the normal region, the absence of intrinsic attractive electron–electron interaction causes Cooper pairs to break up beyond a characteristic length scale, namely, the normal-metal coherence length, $\xi_n = \sqrt{\hbar D_n / 2\pi k T_c}$, where D_n is the electron diffusion coefficient and T_c is the critical temperature [8,9]. In a FM,

the exchange field E_{ex} further suppresses superconducting correlations, resulting in a shorter coherence length, $\xi_f = \sqrt{\hbar D_f / E_{ex}}$ [10-13].

This gradual decay of superconducting correlations in the NM is a hallmark of the proximity effect [14-16]. The pair correlations continuously decrease from their bulk value deep inside the superconductor, leak into the normal material, and eventually vanish at a distance much larger than ξ_n far inside the NM [7,17,18]. The spatial dependence of the superconducting pair correlations is characterized by the pair amplitude $F(z)$, which varies on both sides of the interface [7,8].

The proximity effect in normal metal–superconductor (NS) junctions has been thoroughly studied through experimental [19-21] and theoretical works [7,22-24], which include both pristine and disordered systems [25,26] across a range of temperatures from near absolute zero to higher finite temperatures [27]. A key aspect is the spatial variation of $F(z)$ at the NS interface and its decay within the normal metal [7].

At temperatures near T_c, in the ballistic regime, the pair amplitude decays exponentially in a NM according to the expression

$$F(z) \propto \exp\left(-K|z|\right), \tag{1}$$

where the characteristic decay length is given by $K^{-1} = \hbar v_n / 2\pi k_B T_c$ in clean metals and $K^{-1} = \xi_n$ in dirty metals. Here, v_n is the Fermi velocity in the NM, and z is the distance from the NS interface [2,7,26-28].

However, at low or zero temperatures, self-consistent Bogoliubov–de Gennes calculations show that the decay is no longer exponential. In the ballistic regime, the pair amplitude instead follows a power-law decay [7,29-32],

$$F(z) \propto \left(\frac{\xi}{|z|}\right)^{\alpha}, \tag{2}$$

where ξ is the proximity length. The exponent α depends on the spatial dimensionality of the system [33], taking values of $\alpha = 1$ in 3D [7,29,32], $\alpha = 1/2$ in 2D [34,35], and $\alpha = 0$ in 1D [36]. This behavior holds for distances z smaller than both the thermal decay length $\xi_T = \hbar v_n / k_B T$ and the mean free path $l = v_n \tau$, where τ is the impurity scattering time [32]. Beyond these scales, the proximity effect is determined by the shorter of these two length scales [37-39]. These results have been obtained for materials and samples with strictly defined dimensionality.

In systems with quasi-low dimensionality or multiband materials, where the single-particle density of states departs from simple integer-dimensional behavior, the power-law decay exponent α can continuously vary between values typical for 3D and 1D systems. This transition reflects how the size and shape of the Cooper pair adapt to the dimensionality of the system [33]. The effective dimensionality of the proximity effect can also be influenced by the geometry of the NS interface. As first shown in [40], the curvature of the interface can significantly affect the proximity effect, that is, a negative curvature (concave, viewed from the SC) enhances the proximity range, while a positive curvature (convex) suppresses it.

Another critical factor is the interface transparency. A perfectly reflective interface (zero transparency) completely decouples SC and NM, suppressing proximity-induced correlations and producing an abrupt change in the Cooper pair density [7,27,41]. Conversely, a perfectly transparent interface yields a continuous order parameter profile across the interface. In realistic systems, finite reflectivity due to band mismatch leads to partial suppression of Andreev reflection and reduced proximity strength [6,42]. Even small interface imperfections can significantly impact superconducting hybrid devices by enhancing normal quasiparticle scattering at the expense of Cooper pair transport [42].

Although interface transparency can be tuned by chemical surface treatments or in situ growth [43], an alternative and less explored approach is to control the proximity effect via the geometry of the NS junction. In this work, we systematically investigate how geometrical characteristics of the NS interface, such as local curvature and morphology, affect both the spatial decay of the superconducting order parameter in the NM and the effective interface transparency. We aim to elucidate how geometric variations modify the amplitude and spatial profile of the Cooper pair wave function, as well as the effective barrier potential at the interface. These geometric effects influence the balance between Andreev reflection and quasiparticle scattering, modulate pair-breaking mechanisms, and thus control the proximity effect. This geometric degree of freedom provides a novel route for engineering and optimizing the performance of superconducting hybrid devices.

Results and Discussion

Model

We perform the calculations on a system described by the two-dimensional Hubbard model, defined through the following lattice Hamiltonian [44]:

$$\hat{H} = \sum_{\mathbf{i},\mathbf{j},\sigma} t_{\mathbf{ij}} \hat{c}^{\dagger}_{\mathbf{i}\sigma} \hat{c}_{\mathbf{j}\sigma} - g \sum_{\mathbf{i}} \hat{n}_{\mathbf{i}\uparrow} \hat{n}_{\mathbf{i}\downarrow}, \tag{3}$$

with $\hat{n}_{\mathbf{i}\sigma} = \hat{c}^{\dagger}_{\mathbf{i}\sigma}\hat{c}_{\mathbf{i}\sigma}$, where $\hat{c}^{\dagger}_{\mathbf{i}\sigma}$ ($H^{(0)}_{\mathbf{ij}}$) represent electron creation (annihilation) operators for spin σ at site **i** on the lattice. The tunneling amplitude $t_{\mathbf{ij}}$ is non-zero only between nearest neighbors ($t_{\mathbf{ij}} = -t$), $g > 0$ is the superconducting pairing constant on the superconducting side of the heterojunction, and $g = 0$ in the normal region [45].

The effective mean-field Hamiltonian associated with Equation 3 is written as [44,46]:

$$H_{\text{eff}} = \sum_{\mathbf{i},\mathbf{j},\sigma} H^{(0)}_{\mathbf{ij}}\hat{c}^{\dagger}_{\mathbf{i}\sigma}\hat{c}_{\mathbf{j}\sigma} + \sum_{\mathbf{i},\mathbf{j}}\left(\Delta_{\mathbf{ij}}\hat{c}^{\dagger}_{\mathbf{i}\uparrow}\hat{c}^{\dagger}_{\mathbf{j}\downarrow} + \Delta^{*}_{\mathbf{ij}}\hat{c}_{\mathbf{j}\downarrow}\hat{c}_{\mathbf{i}\uparrow}\right). \quad (4)$$

Here $H^{(0)}_{\mathbf{ij}}$ is the single-particle Hamiltonian,

$$H^{(0)}_{\mathbf{ij}} = t_{\mathbf{ij}} + \left(V_{\mathbf{i}} + U_{\mathbf{i}}\right)\delta_{\mathbf{ij}} \quad (5)$$

with $\delta_{\mathbf{ij}}$ as the Kronecker delta and $U_{\mathbf{i}}$ as the Hartree potential.

The eigenstates and eigenvalues of H_{eff} can be obtained by solving the Bogoliubov–de Gennes matrix equations [5,47-49]:

$$\begin{pmatrix} H^{(0)} - \mu & \Delta \\ \Delta^{\dagger} & -H^{(0)\dagger} + \mu \end{pmatrix}\begin{pmatrix} u \\ v \end{pmatrix} = E\begin{pmatrix} u \\ v \end{pmatrix}, \quad (6)$$

where u and v are eigenvectors, and E the corresponding eigenvalues, μ represents the chemical potential of the system, which is adjusted to have the electron density below half-filling, $n_{\text{e}} = (1/N)\sum_{\sigma\mathbf{i}} n_{\mathbf{i}\sigma} = 0.75$, where N is the number of lattice sites, to avoid being in resonance with the peak in the single-particle density of states at $n_{\text{e}} = 1$.

The order parameter $\Delta_{\mathbf{ij}} = \Delta_{\mathbf{i}}\delta_{\mathbf{ij}}$ and the Hartree potential $U_{\mathbf{i}}$ are determined from the self-consistency equations. For the order parameter, we have [50]

$$\Delta_{\mathbf{i}} = gF_{\mathbf{i}} = g\left\langle \hat{c}_{\mathbf{j}\downarrow}\hat{c}_{\mathbf{i}\uparrow}\right\rangle, \quad (7)$$

where F_i is a pair amplitude, and for the Hartree potential

$$U_{\mathbf{i}} = -\frac{g}{2}\sum_{\sigma}\left\langle \hat{c}^{\dagger}_{\mathbf{i}\sigma}\hat{c}_{\mathbf{i}\sigma}\right\rangle, \quad (8)$$

with $\langle\ldots\rangle$ denoting the quantum mechanical averaging.

The Equations Equation 6 are solved numerically through a self-consistent iteration process that produces the eigenvectors u and v. These eigenvectors are then used to calculate updated values of the order parameter and Hartree potential, and the process is repeated until convergence is reached at each site [51-53]. In the following, all energy values are given in terms of the hopping amplitude t, and all distances in terms of the lattice constant.

To investigate the influence of NS junction geometry on the superconducting proximity effects, we consider a 2D interface between NM and SC given by a parabolic line in x–z plane,

$$z = \eta x^2, \quad (9)$$

where the parameter η can be interpreted as the curvature of the interface at $x = 0$. By varying η, we explore how the curvature affects the spatial decay of superconducting correlations in NM. In the limiting case of $\eta = 0$, the NS interface is flat, representing a standard planar junction. For large positive values $\eta \gg 1$, the geometry approaches a quasi-1D NM channel embedded in a superconducting background, effectively forming a "normal wire in a superconducting sea" [54]. In contrast, for $\eta \ll -1$, the system represents a quasi-1D superconducting wire (which can only exist for moderate $|\eta|$ due to fluctuations) immersed in the NM, essentially a "superconducting wire in a normal sea" [55,56]. Representative configurations for different η values used in subsequent calculations are schematically illustrated by white dashed lines in Figure 1.

For numerical simulations, we used a discretized lattice model with a system size of 128 unit cells along the z-direction (the principal axis of the NS transition) and 64 unit cells in the perpendicular x-direction. A total of twelve different geometries were modeled by varying η in the set $\eta \in \{0, \pm0.05, \pm0.1, \pm0.25, \pm0.5, 1, 2, 4\}$.

Figure 1 illustrates the spatial distribution of the superconducting pair amplitude across the NS interface for several selected interface geometries with both negative and positive values of η. Consistent with previous studies [33], the spatial decay of superconducting correlations in the normal and superconducting regions, corresponding to the proximity and antiproximity effects, respectively, exhibits distinct qualitative behaviors. Moreover, both effects are found to be strongly influenced by the interface curvature η, particularly by its sign. For instance, in the normal region, the spatial correlations decay more rapidly when $\eta < 0$. In what follows, we present a detailed quantitative analysis of how the decay rate varies as a function of η.

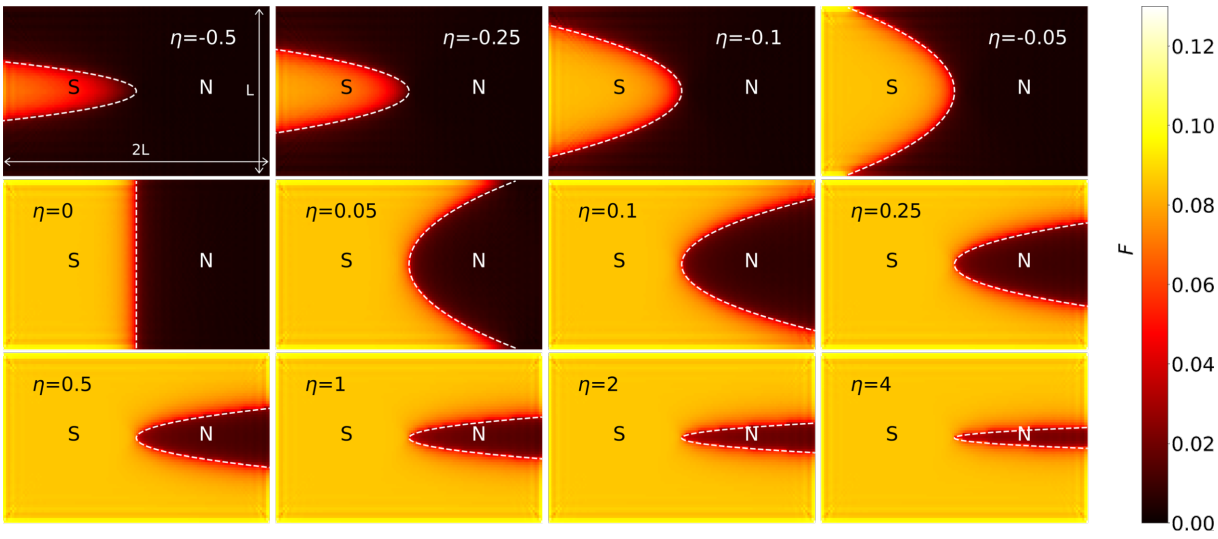


Figure 1: Superconducting correlations in a superconductive sample (S) with normal (N) region of a parabolic shape as a function of the coefficient η characterizing the parabola curvature, $z = \eta x^2$. The white dashed lines show the interface between the superconductor and the normal metal. The dimensions of the sample are $2L \times L$ with $L = 64$.

The proximity effect is further quantified in Figure 2, which illustrates the suppression of the density of states (DOS) at low energies in the NM, that is, the proximity gap, induced by its proximity to the SC. The magnitude of the gap depends on the curvature parameter η. The proximity gap sets the lowest quasiparticle excitation energy scale in the NM region, crucial for coherence and stability of superconducting hybrid devices. For NS junctions with large positive curvature, that is, for quasi-low-dimensional structures, a robust proximity gap emerges, persisting over extended distances because of enhanced superconducting correlations. However, real systems often exhibit a soft gap in experiments, where the DOS remains nonzero at low energies. This broadening arises from inelastic scattering, interface imperfections, and finite quasiparticle lifetimes [46,53,57]. Experimentally, the proximity gap can be probed by tunneling spectroscopy by measuring the differential conductance $\mathrm{d}I/\mathrm{d}V$ on the NM side.

Power-law decay of the pair amplitude

To quantify the decay of superconducting correlations in the normal region, we analyze the spatial profile of the pair amplitude $F(z)$ along the symmetry axis (z-direction). The results show that, as η increases, the superconducting region progressively envelopes the NM region, strengthening the proximity effect. In particular, for large positive values of η, the amplitude of the pair penetrates deeper into the NM, indicating significantly increased superconducting correlations in this region [33,36].

To extract quantitative information about the decay behavior of superconducting correlations into the NM, we fit the computed pair amplitude profiles to a generalized power-law decay function of the form

$$F\left(z>0\right)=F\left(z\to+0\right)\left(\frac{z_0}{z_0+z}\right)^{\alpha}, \tag{10}$$

where z_0 is a characteristic length scale (proximity length, related to superconducting length [32]), $F(z\to+0)$ is the numerical value of the pair amplitude in the vicinity of the interface, and α is the power-law decay exponent. Representative fits of

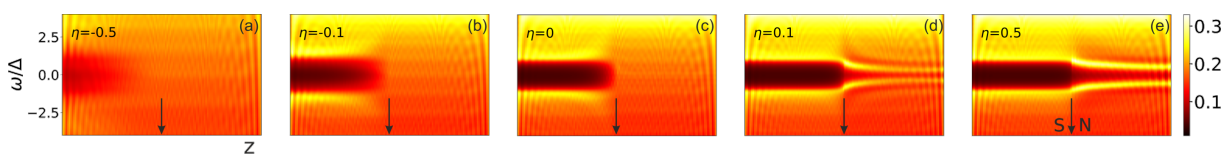


Figure 2: Local density of states normalized to the value of Δ_{bulk} along the symmetry axis. (a) η = −0.5; (b) η = −0.1; (c) η = 0; (d) η = 0.1; (e) η = 0.5. The black arrows show the location of the S–N interface on the z-axis.

the numerical data to this functional form are shown by the solid lines in Figure 3c. The fitting results for all values of η are summarized in Figure 3d,e, where the extracted parameters z_0 and α are plotted as functions of η. From Figure 3e, we observe that z_0 increases with increasing η. This implies that the proximity length grows as the geometry becomes more confining for the NM (i.e., as the system approaches a quasi-1D "normal wire embedded in a superconductor"). This is consistent with the physical picture that the Cooper pair wavefunction becomes more spatially squeezed in the normal region [33,58].

Figure 3d is particularly informative, showing how the power-law decay exponent α varies with η. For negative values of η (i.e., when the superconductor forms a quasi-1D wire), α increases, indicating a faster decay of the pair amplitude in the normal region. For positive η, the exponent decreases, corresponding to slower decay and enhanced superconducting correlations. Interestingly, at η = 0, the pair amplitude reaches a maximum value of approximately α(η = 0) ≈ 0.6, consistent with previous studies of clean two-dimensional systems, where values near 0.5 were reported [33-35]. As η increases, α(η) decays and asymptotically approaches the typical values of effectively one-dimensional systems, as expected [36].

Exponential recovery of the pair amplitude in the inverse proximity effect

In a SC, superconductivity is intrinsic. The suppression of the order parameter, that is, the inverse proximity effect, is a localized response to the boundary condition or interface, and the pairing potential $\Delta_s(z)$ must recover to its self-consistent bulk value Δ_{bulk} on a characteristic length scale set by the superconducting coherence length ξ_s[5,59,60].

In the SC, near the NS boundary, the superconducting order parameter $\Delta_s(z)$ is governed by the self-consistent Bogoliubov–de Gennes equations. Linearizing these equations under the assumption of a weak perturbation (i.e., $\Delta_s(z) \approx \Delta_{bulk}$), one finds that

$$\Delta_s(z) \approx \Delta_{bulk}\left[1 - Ae^{-z/\xi_s}\right], \tag{11}$$

where A is a constant determined by interface transparency (γ_{NS}) and material mismatch (γ). This exponential recovery arises from the mean-field self-consistency in the BCS theory and the gapped quasiparticle spectrum of the superconductor. The system energetically favors a homogeneous pairing amplitude, and any deviation from it decays on a characteristic scale ξ_s, as subgap quasiparticles cannot propagate far into the bulk. Consequently, even at zero temperature, the antiproximity effect is a short-range phenomenon, in contrast to the long-range power-law decay of proximity-induced pairing in the normal metal.

We quantitatively investigate how the curvature of the NS interface modifies this behavior by analyzing the spatial profile of the pair amplitude $F_s(z)$ inside the superconducting region near the interface for various values of η. The results shown in Figure 3c for $z < 0$ reveal that in certain geometrical configurations, particularly for highly negative values of η, where a narrow superconducting channel is surrounded by a normal metal, the suppression of superconducting order can be substantial. To quantify this dependence, we fit the numerical results in the phenomenological form:

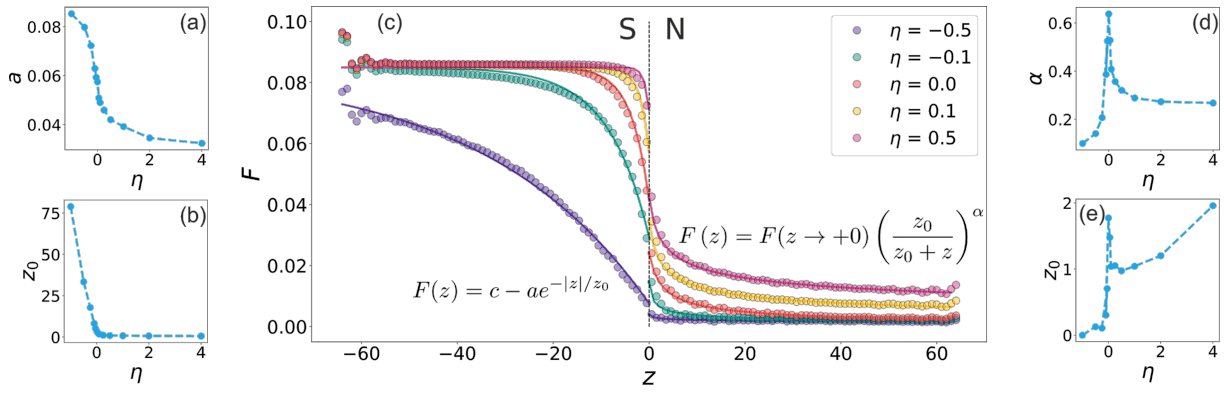


Figure 3: Spatial distribution of the superconducting pair amplitude across the NS junction. (a, b) Fitting coefficients a, z_0 as functions of the curvature η for the functional dependence of the superconducting pair amplitude $F(z<0) = c - ae^{-z/|z_0|}$ in the superconducting region. (c) The value of the superconducting pair amplitude along the z-axis at $x = 0$; circles represent numerical data, and solid lines correspond to fitted dependencies. (d, e) Fit coefficients α, z_0 as functions of the curvature η for the functional dependence of the superconducting pair amplitude $F(z > 0) = F(z \to +0)[(z_0)/(z_0 + z)]^{\alpha}$ in the normal region.

$$F(z) = c - ae^{-z/|z_0|}. \tag{12}$$

The parameter c is almost curvature-independent, and its value is $c \approx F_{S,bulk}$. Other fit results are shown in Figure 3a,b. The parameter z_0 is a decay length that decreases with η: For positive curvature, z_0 remains small and constant, while for negative curvature, it increases monotonically with |η|. We also observe that the parameter a, which mimics A, exhibits a strong curvature-dependence, reflecting changes in the transparency of the interface and in the local density of states near the interface.

We quantify this suppression of the order parameter/pair function amplitude in the SC due to the proximity effect in terms of a pair-breaking parameter,

$$\gamma = 1 - \frac{F(z \to -0)}{F_{S,bulk}}, \tag{13}$$

which effectively describes how the boundary to the normal metal acts as a source of pair breaking. Figure 4b illustrates the dependence of γ on the geometry of the NS junction, as extracted from the numerical calculations of the spatial dependence of the superconducting gap shown in Figure 3c. The results show a monotonic decrease in pair breaking as the geometry changes from $\eta \ll -1$ to $\eta \gg 1$. This trend is expected since, for a "normal wire in a superconducting sea", the influence of the boundary to NM diminishes.

Proximity-induced gap and interface transparency

The proximity-induced gap (mini-gap) on the NM side of a NS junction, shown in Figure 3c, is generally smaller than the superconducting gap $\Delta_s(0)$ at the interface. This mismatch or jump between the gaps on both sides of the interface grows at larger value of curvature η. This is shown in Figure 4a, which reveals a monotonically increasing dependence $\delta\Delta(\eta)$.

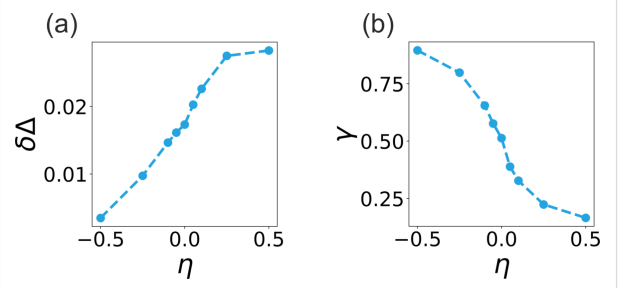


Figure 4: (a) The difference in gaps at the NS junction as a function of the NS junction curvature parameter. (b) The interface pair-breaking parameter as a function of the NS junction curvature parameter.

The obtained monotonic increase of the mismatch in the gaps is consistent with the earlier results obtained for disordered superconductons described by the Usadel theory, which predicts that the value of the jump depends on the interface resistance. Solving the Usadel equations together with Kupriyanov–Lukichev boundary conditions for a flat interface [61] at $T = 0$, one obtains the following implicit relation for the proximity-induced gap on the NM side [62]:

$$\frac{\Delta_n}{\Delta_s(0)} = \left[1 + \gamma_{NS}\frac{\beta}{\pi}\sqrt{1 - \frac{\Delta_n^2}{\Delta_s^2(0)}}\right]^{-1}, \tag{14}$$

where $\beta = \Delta_s(0)/kT_c = 1.76$ is the BCS ratio for a conventional superconductor [63] (T_c is the critical temperature, $\Delta_s(0)$ is the gap at $T = 0$). The parameter $\gamma_{NS} \equiv \sigma_n/(G_I\xi_n)$ describes transparency of the interface (its resistance). Here σ_n and ξ_n denote, respectively, the normal-metal conductivity and coherence length, while G_I is the interface conductance. Equation 14 shows that increasing γ_{NS} reduces the proximity-induced gap Δ_n, so the mismatch $\delta\Delta = \Delta_s(0) - \Delta_n$ between the gap values on the two sides of the interface grows when $\eta_{NS} \propto 1/G_I$ increases.

The numerical results for the pair amplitude F in Figure 3c are consistent with this prediction if one takes into account that G_I is proportional to the transmission probability T across the interface. This quantity depends on both the transmission probability of the individual conduction channels near the Fermi surface and on the total number of such channels. Both contributions are expected to decrease as the curvature η grows. At large η, the local width of the normal region near the interface decreases, reducing the number of available transmission modes in the NM due to transverse confinement [64-67] and, thereby, decreasing the number of available transmission channels. At the same time, the coupling between these confined modes on the NM side and the continuum modes on the SC side weakens because of increasing momentum mismatch, which suppresses the transmission probability of the channels through the interface. Together, the reduction in channel number and the suppressed coupling decrease the interface conductance G_I [68,69]. A lower G_I corresponds to a larger effective interface transparency parameter γ_{NS}, and, according to Equation 14, this results in a smaller proximity gap Δ_n and a larger jump $\delta\Delta$ at the interface. This provides a qualitative explanation for the numerical observation that the proximity-induced gap on the NM side diminishes as the curvature η increases.

Conclusion

In this work, we have systematically investigated the impact of the geometry of a superconductor–normal metal heterojunction

on key features of the proximity effect, namely the power-law decay of the Cooper pair amplitude, the effective transparency of the junction, and the induced proximity gap in the normal region. Employing a fully numerical self-consistent solution of the Bogoliubov–de Gennes equations, we analyzed a variety of boundary geometries without relying on simplifying assumptions such as quasiclassical approximations or linearized gap equations. Our approach thus captures both the microscopic structure of the pairing correlations and the influence of boundary-induced inhomogeneities in a unified framework.

We find that the power-law decay of the induced pair amplitude in the normal region is highly sensitive to the shape of the NS interface, as quantified by the exponent α, which varies systematically with the boundary curvature. Likewise, the effective transparency of the interface and the amplitude of the induced proximity gap are strongly modulated by geometric factors. These results demonstrate that the NS boundary geometry appears not merely to be a passive feature of the device but an active design parameter that can significantly alter the strength and spatial extent of superconducting correlations in hybrid structures.

Our findings have important implications for the engineering of superconducting heterostructures, particularly in nanoscale and mesoscopic systems where interface properties can be tailored with high precision. For example, geometric control of the proximity effect may provide an additional degree of freedom for optimizing device performance in superconducting quantum circuits, Josephson junctions, or topological superconducting platforms, where the strength and range of the induced pairing correlations are critical.

Future work could extend our analysis to incorporate the effects of disorder, finite temperature, spin–orbit coupling, and magnetic fields, which are known to interact with geometry in nontrivial ways. Furthermore, comparison with experimental data from hybrid nanostructures with engineered NS boundaries, such as those reported in [40], shows good quantitative agreement with our predictions.

In summary, we have shown that boundary geometry is a key factor in shaping the superconducting proximity effect in NS heterostructures. Our results provide both qualitative insights and quantitative predictions that can guide the design and interpretation of experiments in superconducting hybrid systems.

Funding

This work was supported by the HSE University Basic Research Program and HPC facilities of HSE University [70], which enabled the numerical calculations. V.D.N., A.V.K. also acknowledge support from the Ministry of Science and Higher Education of the Russian Federation (Grant No. 075-15-2025-010). M.D.C. acknowledges also support from the UFPE Propesq program (grant: Edital Professor Visitante – Edital Propesq No. 05.2018), Recife-PE, Brazil. V.D.N. and A.V.K. were additionally supported by the Ministry of Science and Higher Education of the Russian Federation under state task project no. FSWU-2023-0031.

Author Contributions

Munisa A. Tomayeva: formal analysis; investigation; visualization. Vyacheslav D. Neverov: investigation; writing – original draft; writing – review & editing. Andrey V. Krasavin: supervision; writing – original draft; writing – review & editing. Alexei Vagov: writing – original draft; writing – review & editing. Mihail D. Croitoru: conceptualization; formal analysis; writing – original draft; writing – review & editing.

ORCID® iDs

Munisa A. Tomayeva - https://orcid.org/0009-0005-1135-1820
Vyacheslav D. Neverov - https://orcid.org/0000-0002-8999-8297
Andrey V. Krasavin - https://orcid.org/0000-0002-9457-5360
Alexei Vagov - https://orcid.org/0000-0001-7446-7728
Mihail D. Croitoru - https://orcid.org/0000-0002-3014-8634

Data Availability Statement

Data generated and analyzed during this study is available from the corresponding author upon reasonable request.

References

1. Holm, R.; Meissner, W. *Z. Phys.* **1932,** *74,* 715–735. doi:10.1007/bf01340420
2. Parks, R. *Superconductivity;* Routledge: New York, NY, USA, 2018. doi:10.1201/9780203737958
3. Wolf, E. L. *Principles of Electron Tunneling Spectroscopy,* 2nd ed.; Oxford University Press: Oxford, UK, 2011. doi:10.1093/acprof:oso/9780199589494.001.0001
4. Klapwijk, T. M. *J. Supercond.* **2004,** *17,* 593–611. doi:10.1007/s10948-004-0773-0
5. De Gennes, P. G. *Superconductivity Of Metals And Alloys;* CRC Press: Boca Raton, FL, USA, 2018.
6. Golubov, A. A.; Kupriyanov, M. Y.; Il'ichev, E. *Rev. Mod. Phys.* **2004,** *76,* 411–469. doi:10.1103/revmodphys.76.411
7. Buzdin, A. I. *Rev. Mod. Phys.* **2005,** *77,* 935–976. doi:10.1103/revmodphys.77.935
8. Usadel, K. D. *Phys. Rev. Lett.* **1970,** *25,* 507–509. doi:10.1103/physrevlett.25.507
9. Hekking, F. W. J.; Nazarov, Y. V. *Phys. Rev. B* **1994,** *49,* 6847–6852. doi:10.1103/physrevb.49.6847
10. Bergeret, F. S.; Volkov, A. F.; Efetov, K. B. *Rev. Mod. Phys.* **2005,** *77,* 1321–1373. doi:10.1103/revmodphys.77.1321
11. Ryazanov, V. V.; Oboznov, V. A.; Rusanov, A. Y.; Veretennikov, A. V.; Golubov, A. A.; Aarts, J. *Phys. Rev. Lett.* **2001,** *86,* 2427–2430. doi:10.1103/physrevlett.86.2427

12. Zdravkov, V.; Sidorenko, A.; Obermeier, G.; Gsell, S.; Schreck, M.; Müller, C.; Horn, S.; Tidecks, R.; Tagirov, L. R. *Phys. Rev. Lett.* **2006,** *97,* 057004. doi:10.1103/physrevlett.97.057004
13. Vasenko, A. S.; Kawabata, S.; Golubov, A. A.; Kupriyanov, M. Y.; Lacroix, C.; Bergeret, F. S.; Hekking, F. W. J. *Phys. Rev. B* **2011,** *84,* 024524. doi:10.1103/physrevb.84.024524
14. Bedard, F.; Meissner, H. *Phys. Rev.* **1956,** *101,* 26–30. doi:10.1103/physrev.101.26
15. Meissner, H. *Phys. Rev.* **1958,** *109,* 686–694. doi:10.1103/physrev.109.686
16. Smith, P. H.; Shapiro, S.; Miles, J. L.; Nicol, J. *Phys. Rev. Lett.* **1961,** *6,* 686–688. doi:10.1103/physrevlett.6.686
17. McMillan, W. L. *Phys. Rev.* **1968,** *175,* 559–568. doi:10.1103/physrev.175.559
18. De Gennes, P. G.; Guyon, E. *Phys. Lett.* **1963,** *3,* 168–169. doi:10.1016/0031-9163(63)90401-3
19. Bozovic, I.; Logvenov, G.; Verhoeven, M. A. J.; Caputo, P.; Goldobin, E.; Beasley, M. R. *Phys. Rev. Lett.* **2004,** *93,* 157002. doi:10.1103/physrevlett.93.157002
20. Dai, W.; Richardella, A.; Du, R.; Zhao, W.; Liu, X.; Liu, C. X.; Huang, S.-H.; Sankar, R.; Chou, F.; Samarth, N.; Li, Q. *Sci. Rep.* **2017,** *7,* 7631. doi:10.1038/s41598-017-07990-3
21. Mani, A.; Geetha Kumary, T.; Lin, J. G. *Sci. Rep.* **2015,** *5,* 12780. doi:10.1038/srep12780
22. Galaktionov, A. V.; Zaikin, A. D. *Phys. Rev. B* **2003,** *67,* 184518. doi:10.1103/physrevb.67.184518
23. Naufal Indriatmoko, M.; Anwar, F.; Purwanto, H. *J. Phys.: Conf. Ser.* **2017,** *909,* 012017. doi:10.1088/1742-6596/909/1/012017
24. Raj, A.; Lee, P. A.; Fiete, G. A. *Phys. Rev. B* **2024,** *110,* 184504. doi:10.1103/physrevb.110.184504
25. Kupriyanov, M. Yu.; Likharev, K. K.; Lukichev, V. F. *Physica B+C (Amsterdam)* **1981,** *108,* 1001–1002. doi:10.1016/0378-4363(81)90804-4
26. Dubos, P.; Courtois, H.; Pannetier, B.; Wilhelm, F. K.; Zaikin, A. D.; Schön, G. *Phys. Rev. B* **2001,** *63,* 064502. doi:10.1103/physrevb.63.064502
27. Likharev, K. K. *Rev. Mod. Phys.* **1979,** *51,* 101–159. doi:10.1103/revmodphys.51.101
28. de Gennes, P. G. *Rev. Mod. Phys.* **1964,** *36,* 225–237. doi:10.1103/revmodphys.36.225
29. Falk, D. S. *Phys. Rev.* **1963,** *132,* 1576–1590. doi:10.1103/physrev.132.1576
30. Halterman, K.; Valls, O. T. *Phys. Rev. B* **2001,** *65,* 014509. doi:10.1103/physrevb.65.014509
31. Halterman, K.; Valls, O. T. *Phys. Rev. B* **2002,** *66,* 224516. doi:10.1103/physrevb.66.224516
32. Alexandrov, A. S.; Kabanov, V. V. *Phys. Rev. B* **2008,** *78,* 132510. doi:10.1103/physrevb.78.132510
33. Silveira, R. d. L.; Croitoru, M. D.; Pugach, N. G.; Romaguera, A. R. d. C.; Albino Aguiar, J. *New J. Phys.* **2023,** *25,* 093009. doi:10.1088/1367-2630/acf14f
34. Konschelle, F.; Cayssol, J.; Buzdin, A. I. *Phys. Rev. B* **2008,** *78,* 134505. doi:10.1103/physrevb.78.134505
35. Cayssol, J.; Montambaux, G. *Phys. Rev. B* **2004,** *70,* 224520. doi:10.1103/physrevb.70.224520
36. Konschelle, F.; Cayssol, J.; Buzdin, A. *Phys. Rev. B* **2010,** *82,* 180509. doi:10.1103/physrevb.82.180509
37. Bulaevskii, L. N.; Buzdin, A. I.; Panjukov, S. V. *Solid State Commun.* **1982,** *44,* 539–542. doi:10.1016/0038-1098(82)90141-7
38. Bergeret, F. S.; Volkov, A. F.; Efetov, K. B. *Phys. Rev. B* **2001,** *64,* 134506. doi:10.1103/physrevb.64.134506
39. Linder, J.; Zareyan, M.; Sudbø, A. *Phys. Rev. B* **2009,** *79,* 064514. doi:10.1103/physrevb.79.064514
40. Kim, J.; Chua, V.; Fiete, G. A.; Nam, H.; MacDonald, A. H.; Shih, C.-K. *Nat. Phys.* **2012,** *8,* 464–469. doi:10.1038/nphys2287
41. Blonder, G. E.; Tinkham, M.; Klapwijk, T. M. *Phys. Rev. B* **1982,** *25,* 4515–4532. doi:10.1103/physrevb.25.4515
42. Beenakker, C. W. J. *Phys. Rev. B* **1992,** *46,* 12841–12844. doi:10.1103/physrevb.46.12841
43. Boogaard, G. R.; Verbruggen, A. H.; Belzig, W.; Klapwijk, T. M. *Phys. Rev. B* **2004,** *69,* 220503. doi:10.1103/physrevb.69.220503
44. Neverov, V. D.; Lukyanov, A. E.; Krasavin, A. V.; Vagov, A.; Croitoru, M. D. *Commun. Phys.* **2022,** *5,* 177. doi:10.1038/s42005-022-00933-z
45. Croitoru, M. D.; Shanenko, A. A.; Chen, Y.; Vagov, A.; Aguiar, J. A. *Phys. Rev. B* **2020,** *102,* 054513. doi:10.1103/physrevb.102.054513
46. Croitoru, M. D.; Shanenko, A. A.; Vagov, A.; Milošević, M. V.; Axt, V. M.; Peeters, F. M. *Sci. Rep.* **2015,** *5,* 16515. doi:10.1038/srep16515
47. Zhu, J.-X. *Bogoliubov-de Gennes Method and Its Applications;* Springer International Publishing: Cham, Switzerland, 2016. doi:10.1007/978-3-319-31314-6
48. Zachmann, M.; Croitoru, M. D.; Vagov, A.; Axt, V. M.; Papenkort, T.; Kuhn, T. *New J. Phys.* **2013,** *15,* 055016. doi:10.1088/1367-2630/15/5/055016
49. Neverov, V. D.; Lukyanov, A. E.; Krasavin, A. V.; Vagov, A.; Croitoru, M. D. *Condens. Matter* **2024,** *9,* 6. doi:10.3390/condmat9010006
50. de Bragança, R. H.; de Moraes, L. M. T.; Romaguera, A. R. d. C.; Aguiar, J. A.; Croitoru, M. D. *J. Phys. Chem. Lett.* **2024,** *15,* 2573–2579. doi:10.1021/acs.jpclett.3c03448
51. Croitoru, M. D.; Shanenko, A. A.; Kaun, C. C.; Peeters, F. M. *Phys. Rev. B* **2011,** *83,* 214509. doi:10.1103/physrevb.83.214509
52. Croitoru, M. D.; Shanenko, A. A.; Peeters, F. M.; Axt, V. M. *Phys. Rev. B* **2011,** *84,* 214518. doi:10.1103/physrevb.84.214518
53. Croitoru, M. D.; Shanenko, A. A.; Vagov, A.; Vasenko, A. S.; Milošević, M. V.; Axt, V. M.; Peeters, F. M. *J. Supercond. Novel Magn.* **2016,** *29,* 605–609. doi:10.1007/s10948-015-3319-8
54. Courtois, H.; Gandit, P.; Mailly, D.; Pannetier, B. *Phys. Rev. Lett.* **1996,** *76,* 130–133. doi:10.1103/physrevlett.76.130
55. Rogachev, A.; Bezryadin, A. *Appl. Phys. Lett.* **2003,** *83,* 512–514. doi:10.1063/1.1592313
56. Mooij, J. E.; Nazarov, Y. V. *Nat. Phys.* **2006,** *2,* 169–172. doi:10.1038/nphys234
57. Neverov, V. D.; Lukyanov, A. E.; Krasavin, A. V.; Vagov, A.; Lvov, B. G.; Croitoru, M. D. *Beilstein J. Nanotechnol.* **2024,** *15,* 199–206. doi:10.3762/bjnano.15.19
58. Shanenko, A. A.; Croitoru, M. D.; Vagov, A.; Peeters, F. M. *Phys. Rev. B* **2010,** *82,* 104524. doi:10.1103/physrevb.82.104524
59. Tinkham, M. *Introduction to Superconductivity,* 2nd ed.; Dover Publications: Mineola, NY, USA, 2004.
60. Larkin, A. I.; Ovchinnikov, Y. N. *Sov. Phys. - JETP* **1968,** *55,* 1200.
61. Kurpianov, M. Y.; Lukichev, V. F. *Sov. Phys. - JETP* **1988,** *67,* 1163.
62. Aminov, B. A.; Golubov, A. A.; Kupriyanov, M. Y. *Phys. Rev. B* **1996,** *53,* 365–373. doi:10.1103/physrevb.53.365
63. Carbotte, J. P. *Rev. Mod. Phys.* **1990,** *62,* 1027–1157. doi:10.1103/revmodphys.62.1027

64. Krogstrup, P.; Ziino, N. L. B.; Chang, W.; Albrecht, S. M.; Madsen, M. H.; Johnson, E.; Nygård, J.; Marcus, C. M.; Jespersen, T. S. *Nat. Mater.* **2015,** *14,* 400–406. doi:10.1038/nmat4176
65. Croitoru, M. D.; Shanenko, A. A.; Kaun, C. C.; Peeters, F. M. *Phys. Rev. B* **2009,** *80,* 024513. doi:10.1103/physrevb.80.024513
66. Chang, W.; Albrecht, S. M.; Jespersen, T. S.; Kuemmeth, F.; Krogstrup, P.; Nygård, J.; Marcus, C. M. *Nat. Nanotechnol.* **2015,** *10,* 232–236. doi:10.1038/nnano.2014.306
67. Gill, S. T.; Damasco, J.; Car, D.; Bakkers, E. P. A. M.; Mason, N. *Appl. Phys. Lett.* **2016,** *109,* 233502. doi:10.1063/1.4971394
68. de Jong, M. J. M. *Phys. Rev. B* **1994,** *49,* 7778–7781. doi:10.1103/physrevb.49.7778
69. Maslov, D. L.; Stone, M. *Phys. Rev. B* **1995,** *52,* R5539–R5542. doi:10.1103/physrevb.52.r5539
70. Kostenetskiy, P. S.; Chulkevich, R. A.; Kozyrev, V. I. *J. Phys.: Conf. Ser.* **2021,** *1740,* 012050. doi:10.1088/1742-6596/1740/1/012050

License and Terms

This is an open access article licensed under the terms of the Beilstein-Institut Open Access License Agreement (https://www.beilstein-journals.org/bjnano/terms), which is identical to the Creative Commons Attribution 4.0 International License (https://creativecommons.org/licenses/by/4.0). The reuse of material under this license requires that the author(s), source and license are credited. Third-party material in this article could be subject to other licenses (typically indicated in the credit line), and in this case, users are required to obtain permission from the license holder to reuse the material.

The definitive version of this article is the electronic one which can be found at:
https://doi.org/10.3762/bjnano.16.155

BEILSTEIN JOURNAL OF NANOTECHNOLOGY

Terahertz-range on-chip local oscillator based on Josephson junction arrays for superconducting quantum-limited receivers

Fedor V. Khan[*1,2], Lyudmila V. Filippenko[1], Andrey B. Ermakov[1], Mikhail Yu. Fominsky[1] and Valery P. Koshelets[1]

Full Research Paper

Open Access

Address:
[1]Kotel'nikov Institute of Radio Engineering and Electronics of RAS, 11/7 Mokhovaya st., Moscow, 125009, Russian Federation and [2]Moscow Institute of Physics and Technology, 9 Institutskiy per., Dolgoprudny, Moscow Region, 141701, Russian Federation

Email:
Fedor V. Khan[*] - khanfv@hitech.cplire.ru

* Corresponding author

Keywords:
Josephson junction arrays; phase-locking; superconducting local oscillator; superconductor integrated receiver; terahertz-range oscillators

Beilstein J. Nanotechnol. **2025,** *16,* 2296–2305.
https://doi.org/10.3762/bjnano.16.158

Received: 16 September 2025
Accepted: 27 November 2025
Published: 22 December 2025

This article is part of the thematic issue "Superconducting artificial neural networks and quantum circuits".

Guest Editor: A. S. Sidorenko



© 2025 Khan et al.; licensee Beilstein-Institut.
License and terms: see end of document.

Abstract

In this paper we present the results of the development, fabrication, measurements, and analysis of terahertz-range oscillators based on Josephson junction arrays embedded into the central electrode of a coplanar line. The influence of array geometry, the presence of a matched load at the nonradiating edge, and the magnitude of the tunneling current density of Josephson junctions on such oscillator characteristics as radiation power, linewidth, and operating range are discussed. Various options are suggested for further improvement of the oscillator performance.

Introduction

Superconducting heterodyne receivers based on superconductor–insulator–superconductor (SIS) tunnel junctions have ultimate characteristics unreachable to devices based on other principles [1-3]. The unique nonlinearity of the current–voltage characteristic (IVC) near the gap voltage of the junction enables the gain of the intermediate frequency (IF) signal after mixing with the radiation from the local oscillator (LO) [4]. This effect together with the operation at cryogenic temperatures and the quantum nature of the mixer itself allow for the development of receivers with the noise temperature T_n only a few times higher than the quantum limit $\approx hf/k_B$, where h and k_B are the Planck and Boltzmann constants, respectively, and f is the frequency of the incoming radiofrequency (RF) signal [4,5]. Such receivers are used as a sensitive element of the state-of-the-art terahertz (THz) range ground-based (ALMA [6], APEX [7]) and space-based (Hershel [8], Millimetron [9]) telescopes. The ground and space-based telescopes are combined in a large net called "Event Horizon Telescope" [10] which was used for direct observation of the black hole shadow in the M87 Galaxy [11].

The LOs for the conventional SIS receivers are mostly generated by Schottky diode multipliers, which have a radiation power in the terahertz range up to 2 mW and efficiency of approx. 5% [12]. However, these devices can be fabricated only in few laboratories around the world (e.g., JPL NASA) and may not be accessible in some countries.

The other approach was suggested in previous works [13,14] where the LO based on the FFO is fabricated on the same chip and in the same technological process as that of the SIS mixer. This approach allowed for superconductor integrated receivers (SIRs) with some of the characteristics even superior to those of SIS receivers with conventional LO based on Schottky diodes. The concept of the SIR has proven itself for many times both in laboratory and in real-life conditions. The terahertz SIS-mixer integrated on the same chip with the LO based on a flux-flow oscillator (FFO) and a receiving antenna [13] was used to study the irradiation of the human body [15], gas spectroscopy [16], and the atmosphere gas components at the TELIS mission on board of the stratospheric balloon [17].

However, the LO based on FFO has some problems yet to be solved. The operation frequency of the FFO is limited by the gap frequency of the superconducting niobium that forms one or both of its electrodes [18]. Currently, Josephson junctions (JJ) are mostly fabricated using Nb–Al/AlO_x–Nb or Nb–Al/AlN–NbN technologies [19,20]. A number of attempts were made to establish the technology for the fabrication of Nb-based technologies, such as NbTiN–Al/AlN–NbTiN [21], NbN–AlN–NbN [22], NbN–TaN–NbN [23], NbN–MgO–NbN [24]. Nontheless, the use of Nb alloys will only partially solve the problem of high-frequency generation due to high surface losses in NbN and NbTiN [18,25,26]. Note that the use of Nb–Al/AlN–NbN allows for the fabrication of tunnel junctions with a tunnel current density of up to 100 kA/cm^2 with a quality ratio R_j/R_n over 20, where R_j and R_n are the resistance of the SIS junction below and above the gap voltage V_g, respectively [20]. A high tunnel current density is crucial for the RF and IF bandwidth of the mixer; however, to the best of our knowledge, the FFO based on Nb alloys has not been developed yet.

Another problem is related to the fact that the FFO operates in resonant (or Fiske-steps) mode [27] at voltages below $V_g/3$. At higher voltages, the presence of the self-pumping effect [28] leads to an increase of the attenuation of the waves propagating in the FFO and the smoothing of the Fiske steps. The operation in the Fiske steps mode is complicated by the need to search for operation points at a particular frequency with sufficient generation power. The computer procedure of the operating point selection performed by varying the bias current through the FFO and the magnetic field takes about 1 min, and it is done after each thermal cycling [13]. Also, the ratio of the radiated power to the consumed DC power is slightly higher than 5%.

Some of the aforementioned problems can be solved by the use of Josephson junction arrays as LO for the SIR. The junctions can be fabricated by the use of robust Nb-based technologies, whereas the electrodes of the transmission lines where the junctions are implemented can be fabricated using Nb compounds. In a work by Uzawa et al. the generation of up to 800 GHz was observed [29]. When a JJ array is properly matched to the load, its radiation power linearly increases with the number of synchronized junctions N, while the emission linewidth linearly decreases [30,31]. Moreover, if reflections from the ends of the array are suppressed (e.g., by using a matched load), standing waves and resonances should no longer occur. It should be noted that if the characteristic synchronization radius of the junctions in the array is smaller than the length of the array, there is a saturation of the maximum power that can be achieved [32].

Currently, there are several implementations for the arrangement of the JJs in the array. The junctions can be connected either in series and or in parallel and can be arranged in several ways: spaced by λ/2 from each other, at a distance much smaller than λ, or arranged in groups, where junctions within each group are closely packed while the groups themselves are separated by λ/2 [31,33]. Here, λ is the wavelength at the frequency of operation. When the junctions are grouped or spaced by λ/2, mutual synchronization becomes easier to achieve. However, in such cases, the generation spectrum is limited to only a few frequencies determined by the condition that the spacing between the groups or individual junctions contains an integer number of half-wavelengths. One-dimensional and two-dimensional array circuits have also been implemented. In the work [34], with 1986 JJs arranged in a two-dimensional array at λ/2, a power of 160 μW was achieved at a frequency of 240 GHz. In the paper [35], a one-dimensional array consisting of 9996 Nb/Si/Nb junctions was presented, capable of frequency tuning from 139 to 343 GHz, with a linewidth in the best points of less than 100 kHz. In the works by Uzawa et al. [29,36,37], generators and receivers based on one-dimensional arrays, where the JJs are spaced at λ/2, were investigated, demonstrating the possibility of generating frequencies from 150 to 800 GHz with power ranging from 0.2 to 10 μW.

In recent papers [38,39], we have suggested a new type of JJ arrays where the junctions are embedded into the central electrode of the coplanar transmission line (CPW). For a local oscillator in a heterodyne receiver, continuous frequency tuning is crucial. For this reason, the junctions are spaced at distances much smaller than the wavelength. We suppose that the choice

of such topology where the array is in the central electrode of the CPW enabled the synchronization between the junctions by high frequency currents. This allowed to achieve the power of up to 0.4 μW for the array consisting of 200 junctions with an area of 2.8 μm^2 and a tunnel current density of approx. 5 kA/cm^2. This power is already sufficient for on-chip applications: both for the mixer pump in the receiver and the operation of the harmonic mixer (HM) for frequency and phase locking. For the first time the possibility of phase locking of the JJ array to the local source unit was demonstrated with a spectral ratio higher than 90% at the best points [39]. We have also studied and compared the free-running linewidth of the array to theoretical estimates [32,40,41] and investigated how the array performance is affected by the matched load in the form of Klopfenstein tapering, which ends with the section of the microstrip line with the normal top electrode.

In this paper we concentrated on the high-frequency properties of JJ arrays and on the discussion about the feasibility of the LO in SIR based on them. In our previous works we observed that the radiation power at frequencies higher than 500 GHz was lower than expected. However, for the samples with higher tunnel current density, the operation frequency was observed to be higher. Here, we will give the explanation and suggest the methods for further increase of the maximum operating frequency of the JJ arrays. In addition, we fabricated a new set of samples that incorporate a matched load on the non-radiating end, improved array–SIS detector matching circuits, and varied tunnel-current densities.

The LO for SIR should satisfy the following criteria based on the previous study of a heterodyne receiver with a local oscillator based on long Josephson junctions (LJJ) [42]. First, the power of the RF signal incoming to the SIS mixer should induce the quasiparticle current step more than 0.25 of the current at the gap voltage of the mixer junction. Second, the oscillator frequency should be tunable in a wide range. Third, the ability to phase-lock to the external stable synthesizer should be implemented. Fourth, the spectral ratio (ratio of the signal power at the peak to the total radiated power, including noise and parasitic modes) in the PLL mode should exceed 90%. In this paper we will show that newly fabricated samples meet these criteria.

The paper is divided into four sections. In the first section we briefly review the topology and the fabrication technology of the samples. In the second we describe the measurement setup and methodology. After that we present the results of the measurements with the calculations and simulation. Finally, we discuss the feasibility of the LO based on JJ arrays of the proposed topology.

Experimental

Samples

The block diagram of the SIR is shown in Figure 1. The incoming RF signal is fed into the antenna and then goes into the mixer, where it is mixed with the signal from the LO. Due to the extreme nonlinearity of the SIS mixer, the signal is down-converted to the IF with moderate loss [43]. In order to stabilize the generation line of the LO, the system with the HM is used. HM is a single Josephson tunnel junction that not only helps to estimate the array radiation power while operating as a direct detector, but also mixes the radiation from the array with the high-order (up to 40) harmonics of the external commercial synthesizer (operation frequency range: 16–19 GHz). The IF signal resulting from the HM goes to the LO stabilization system, where its frequency is compared with the reference and the bias current through the array is adjusted in order to minimize the difference between the IF signal and the reference. The details on the operation principles of this system can be found in [13]. All the elements within the magenta rectangle in Figure 1 are integrated in a single chip of the SIR.

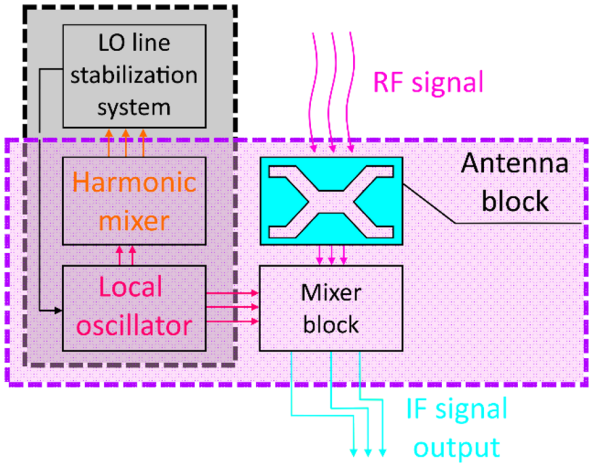


Figure 1: Principal scheme of the superconductor integrated receiver (SIR).

Here we study the local oscillator based on the JJ array together with the harmonic mixer (elements within the black dashed rectangle in Figure 1). The purpose of the samples under study is to develop the wideband matching circuits between the LO and HM and implement the phase locking loop (PLL) for a new type of LO [42].

The image of one of the experimental samples captured by an optical microscope is shown in Figure 2. The radiation from the array of the Josephson junctions is detected by a small SIS tunnel junction with an area of approx. 1 μm^2. This junction also functions as the harmonic mixer in spectral measurements.

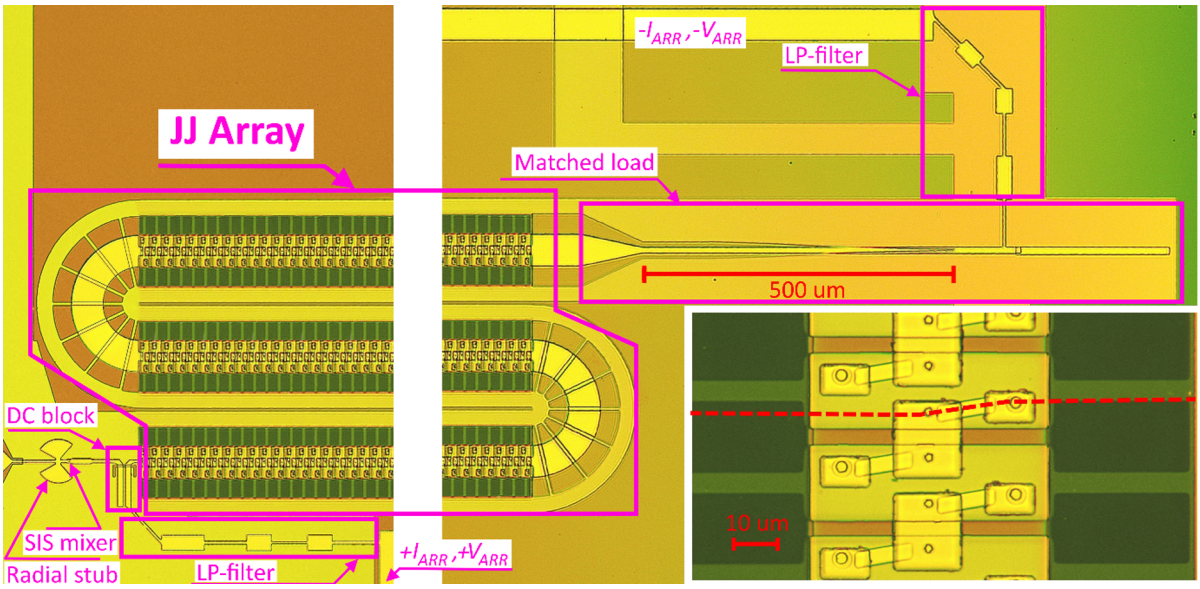


Figure 2: Capture of the experimental sample by an optical microscope; inset – enlarged image of the junctions in the array. The length of each of the three sections of the array is 2 mm (the major part is not shown for visibility). The dashed red line shows the cross-section of the layers illustrated in Figure 3.

A DC block in the form of a slot antenna allows to separate the DC connection of the array and the detector. The SIS tunnel junction has a parasitic capacitance of approx. 100 fF that becomes significant at terahertz frequencies. The microstrip line of a certain length shorted at high frequencies by a radial stub serves as the effective inductance in order to compensate the parasitic capacitance in the band of operation. The connection of the JJ array to the DC bias supply is implemented using Chebyshev low-pass filters (LP filter in Figure 2) in order to prevent the array radiation from leaking into these lines.

In order to suppress the standing waves in the array, the matched load in the form of Klopfenstein tapering [44] is used. It is made up by a 5λ/4-long transition from CPW to the microstrip line with a normal top electrode that serves for attenuation of the reflected wave.

Each JJ in the array is shunted by a thin-film resistor made of normal metal. In our technological cycle, the molybdenum film with a thickness of 100 nm (surface resistance of approx. 1 Ω/square) is used. A shunt is crucial for reducing the McCumber parameter to the value of ≈0.3 in order to provide a hysteresis-free current–voltage characteristic (IVC) [3]. The parameters of the single junctions in this work are as follows: I_c = 110 μA, C = 300 fF, L_{shunt} = 1.5 pH, and R_{shunt} = 1.9 Ω. For this set of parameters there is a bump on the single junction IVC at a voltage of approx. 0.5 mV caused by an LC resonance between the shunt inductance and the junction capacitance. Since the corresponding resonance frequency is below the operating range of the samples, we will not discuss these effects here. At certain parameter values, the IVC of the single JJ exhibits a number of features that can be quantitatively described by the RLCSJ model, as shown in [38,45,46].

The image of the technological layers near the JJ and the shunt in the cross-section shown by the dashed line in Figure 2 is shown in Figure 3. The details of the fabrication processes can be found in our previous works [19,20].

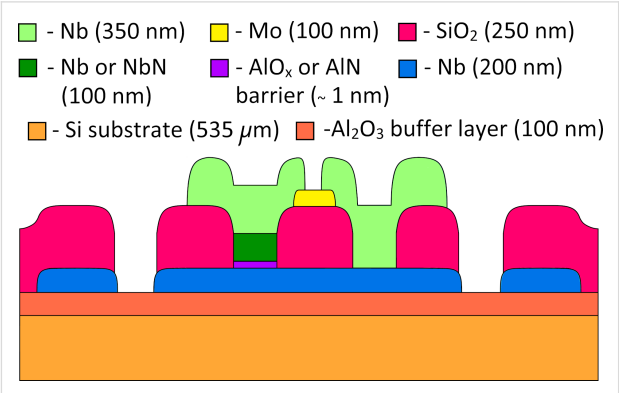


Figure 3: Cross-section of the technological layers near the JJ and the shunt (see the red dashed lines in Figure 2 and the inset).

Measurement technique

When the JJ array irradiates the SIS mixer, the probability of quasiparticle tunneling through the tunnel barrier increases. This leads to a rise in current at voltages below the gap and the

emergence of the so-called quasiparticle steps. This process is known as photon-assisted tunneling. The magnitude of the current on a quasiparticle step within the investigated range is linearly proportional to the incident power. The precise shape of the pumped IVC can be derived from the known autonomous IVC using the expressions from the Tucker–Feldman model [47]. The model is applicable for all frequencies and powers in the study, provided that a sufficient number of harmonics p are taken into account when calculating the pumped IVCs from an autonomous IVC. We selected p = 5, since beginning from p = 3 the change in the form of the calculated IVCs was comparable to the approximation error. However, one should take into account that a high incident power would likely cause junction overheating and give rise to nonequilibrium effects, thus restricting the model applicability [48].

A set of IVCs for the SIS mixer at various pump power levels is shown in Figure 4. Experimental IVCs are indicated by colored markers, while the dashed curves represent approximations obtained using the Tucker–Feldman expressions. Due to the incompletely suppressed critical current, Shapiro steps also appear on the IVC of the SIS mixer at voltages of $hf/2e$ [49]. The corresponding jumps in the theoretical IVCs arise from replicas generated when shifting the autonomous IVC by nhf/e, where n is an integer.

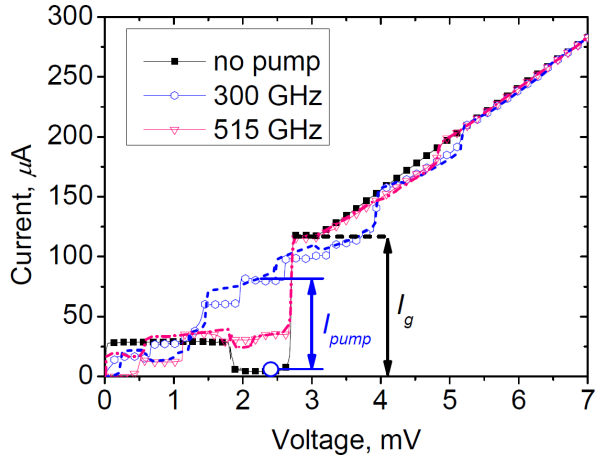


Figure 4: The set of the IVCs of the SIS mixer irradiated by the JJ array with 600 JJs at frequencies of 300 GHz and 515 GHz. The dashed curves are calculated using theoretical expressions from Tucker–Feldman model [47]. Circle at 2.4 mV denotes the operating point of the SIS mixer during DC measurements. I_{pump} is the current through the mixer that arises from photon assisted tunneling and serves for the incoming power estimate. The power level is about 0.18 μW at 300 GHz and 0.07 μW at 515 GHz. I_g is the current at the gap voltage V_g.

Figure 5 shows the IVC of the JJ array for one of the samples with 600 JJs. The color indicates the value of the I_{pump} normalized to I_g for the SIS mixer at the corresponding voltage. The steps present on the IVC (see the inset in Figure 5) arise from longitudinal resonances along the entire length of the array, which are much smaller than in previous samples with no matched load (see [38] to compare). The relation between the voltage across the array and the radiation frequency can be estimated using the expression $f = 2eV/hN$, where N is the number of synchronized junctions in the array. This formula holds with good accuracy, but is only suitable for qualitative estimates. Moreover, previous measurements have demonstrated that the actual generation frequency may deviate from the value calculated by the above formula since the generation frequency locks on the modes of the coplanar waveguide, and due to the fact that not all of the junctions in the array are synchronized [50].

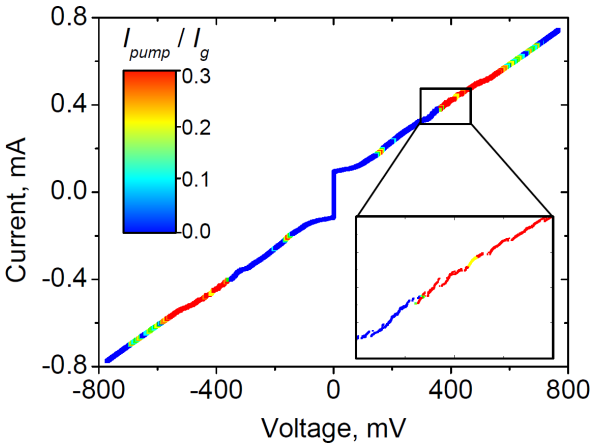


Figure 5: IVC of the 600 JJ array with 300–550 GHz matching circuit and matched load on the nonradiating end. The color indicates the I_{pump} of the SIS mixer in the corresponding operating point. The inset shows the enlarged part of the IVC, where the steps related to the resonances along the entire array length are observed.

Results and Discussion

Operation frequency band of the samples

We performed numerical calculations in order to design the coupling circuits between the JJ array and the SIS mixer. The calculation methods for the superconductor planar structures are described in works [51,52] and will not be duplicated here. In total, two designs were calculated and tested, covering the 300–550 GHz and 500–700 GHz range. The first matching circuit has a bandwidth of more than 50% relative to the central frequency (250 GHz with a central frequency of 450 GHz); the second, ≈30% (bandwidth 200 GHz with a central frequency of 600 GHz). The low-frequency matching circuit was easier to design due to the dispersion in the superconductor microstrip lines made of niobium at frequencies over 500 GHz, rising from the frequency dependence of the London penetration depth [18,53]. The experimental results for the S_{21} coefficient of the

300–550 GHz and 500–700 GHz matching circuits and the calculations are shown in Figure 6a and Figure 6b, respectively. The experimental values of I_{pump} are normalized to I_g. However, the experiment shows a discrepancy with the calculations at frequencies over 500 GHz (see Figure 6a).

We studied the possible reasons for this and found that the performance deterioration at high frequencies is likely caused by the attenuation in the CPW. We performed calculations of the CPW with the same material parameters as the those in the sample arrays. The S_{21} parameter for the coplanar line is shown by the cyan dotted line in Figure 6a and Figure 6b. The values are indicated on the right axis. The decrease is caused by the leak of the JJ array radiation into the substrate. Moreover, the parameters of the films that form the electrodes for this technological run turned out to be slightly different from those used in the calculations (in particular, the gap frequency, denoted by the vertical dash-dotted red line was found to be 650 GHz instead of 700 GHz). The estimate of the gap frequency was done from the value of V_{gap} of the tunnel junctions (see Figure 4, where $V_{gap} \approx 2.7$ mV, which corresponds to the gap frequency of niobium films ≈650 GHz).

A possible solution to address this problem is the CPW with a smaller gap width W_{gap} (see the inset in Figure 7). As can be seen from Figure 7, with a decreasing W_{gap} the attenuation in the CPW becomes smaller. This approach will be used in the topology of new designs. The width of the central electrode W_c is also changed in order to keep the characteristic impedance close to 50 Ω and the effective dielectric constant close to the ones in this study. However, the width of the central electrode of the CPW W_c = 38 μm is limited in the present design by the geometrical size of the junctions shunted by a thin-film resistor. As discussed in [54], for the CPW lines with a high W_c and small W_{gap}, the difference between the frequencies of the odd and even modes becomes smaller. The coexistence of these modes is likely to degrade the oscillator performance because two modes with different wavelengths, and therefore different propagation constants, will be present in the CPW line, which may hinder phase-locking to the external stable synthesizer. In addition, a significant change in the characteristic impedance or propagation constant will likely affect the synchronization radius [32]. This topic will be addressed in future research.

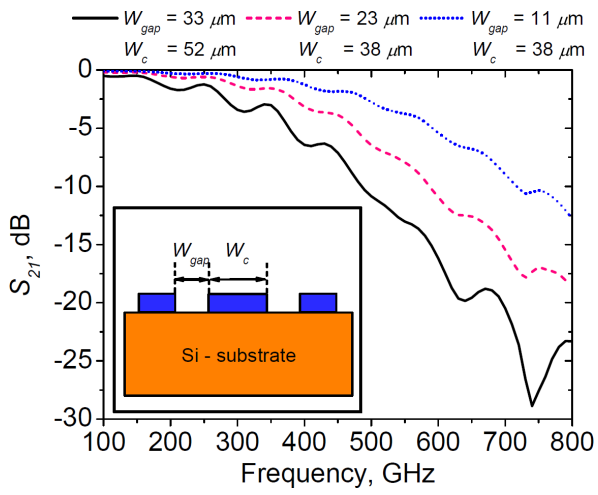


Figure 7: Transmissivity of the CPW lines with different gap widths. The inset shows the profile of the CPW.

We also compared the new results for the tunnel current density of 5 kA/cm^2 to the previous series with a 13 kA/cm^2 tunnel current density; the results are shown in Figure 8. It should be noted that the radiation power is higher for samples with a higher tunnel current density. Although synchronization and

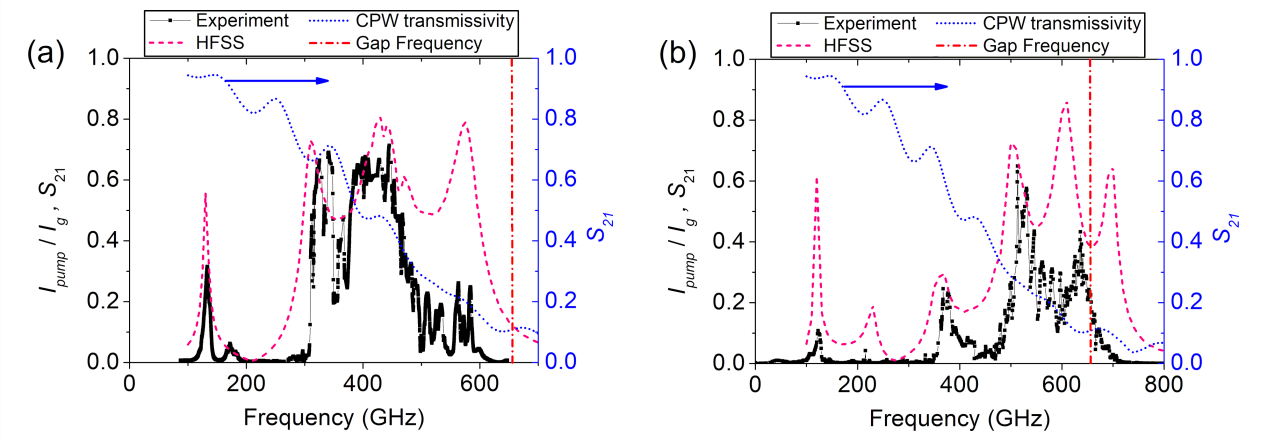


Figure 6: Pump current (black squares) and the calculated S_{21} parameter (dashed pink curve). (a) Design for the 300–550 GHz range and (b) 500–700 GHz range. The blue curve (right axis) denotes the transmissivity of the CPW line. The red vertical line depicts the gap frequency for the samples.

stable generation were not achieved across the entire bandwidth supported by the matching circuit, due to the absence of a matched load at the nonradiating end, the maximum operating frequency still was as high as 700 GHz. The possible reason for the better performance of the samples with a high tunnel current density at high frequencies is that with an increased tunnel current density, a bigger part of the RF current is flowing through the junction and less through the capacitance and the shunt (which also has finite inductance that deters high-frequency properties of the arrays). The new series of the experimental samples with higher tunnel current density is currently being fabricated.

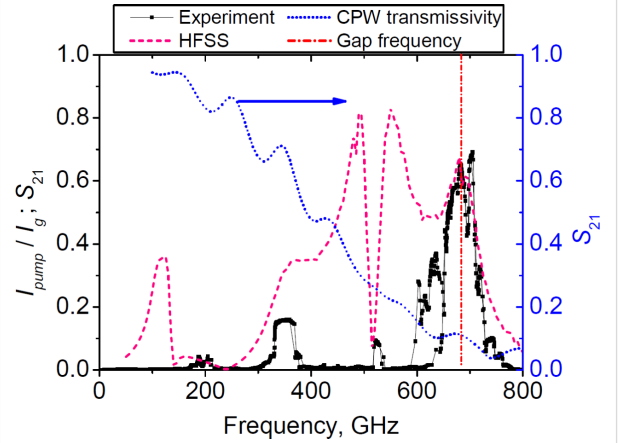


Figure 8: Pump current and calculated S_{21} parameter for the scheme with a higher critical current density. The discrepancy between the experiment and modeling is likely to be caused by the absence of the matched load at the nonradiating end.

Spectral properties of the Josephson junctions array

In this section we will discuss the results of the spectral measurements and the feasibility of the LO in SIR based on a JJ array of the proposed topology. First, for the SIR to operate, the power of the LO coupled to the SIS junction induces the current on the quasiparticle step greater than 25% of the I_g [13]. The measurements from the previous section show that this requirement is confidently met. Second, the LO radiation must be sufficiently monochromatic (spectral ratio ≥90%) in order to prevent signal spectra change while down-conversion to IF. Furthermore, for applications in spectroscopy, phase-locking to the external stable synthesizer is crucial [16]. Figure 9 shows the radiation IF spectrum of the JJ array at a frequency of 522 GHz. The linewidth of the free-running array is less than 0.5 MHz, while the signal-to-noise ratio is approx. 30 dB. The calculation using the Rogovin–Scalapino [40,41] formula with the differential resistance normalized to a single junction yields the value of approx. 0.1 MHz. This is somewhat lower than the experimental value, probably due to the presence of the thermal noise arising from the current flowing through the shunts and other low-frequency fluctuations. In our earlier works we demonstrated the feasibility of phase-locking the array to an external stable synthesizer. The spectrum in the PLL mode is shown by the dashed pink line in Figure 9. The spectral ratio reaches 92%, which is sufficient for the integrated receiver operation. In the PLL mode, the linewidth becomes very small due to the elimination of the influence of both low-frequency and high-frequency noises; its measured value is determined by the resolution bandwidth of the spectrum analyzer. The detailed study of the phase noise in the PLL mode is subject for further research.

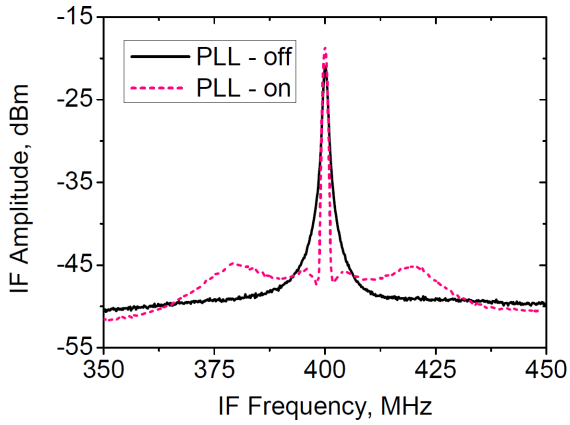


Figure 9: IF spectra of the 600 JJ arrays at 522 GHz. The free-running radiation linewidth is ≈0.5 MHz with a signal-to-noise ratio of ≈30 dB; the spectral ratio is 92% in case if the array operates in PLL mode.

The IVC of the JJ array when the PLL mode is active is shown in Figure 10. The current step induced by the PLL system is approx. 0.5 mA, which is three orders of magnitude higher than the characteristic noise level in the current bias system (≈0.5 μA) and thermal noise. This shows the robust nature of the PLL. The additional steps of smaller size are likely to be caused by the locking at different harmonics and other sidebands. It should be noted that the form of the IVC in spectral measurements in the cryostat is different from that measured in the LHe probe because the PLL system and the JJ array have comparable impedances.

Conclusion

Summing up, we state that the described oscillator based on a series-connected JJ array embedded into the central electrode of a coplanar line has sufficient output power and spectral ratio in the PLL mode to operate as LO in SIR. Based on the results presented in this work, we conclude the feasibility of tunable LO covering an entire range from 100 to 700 GHz with the only

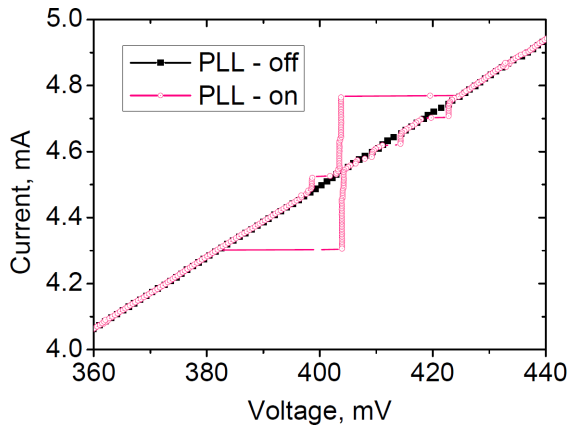


Figure 10: JJ array IVCs with (pink hollow circles) and without PLL (black squares). The PLL-induced step is much higher than the characteristic noise level (0.5 mA ≫ 0.5 μA).

limitation caused by the transmission coefficient of the matching circuit. We also demonstrated that an increase in tunnel current density through the JJs enables frequency generation at higher frequencies. Furthermore, minor corrections to the CPW topology will help to extend the maximum operation frequency further to the high-frequency region.

Acknowledgements

The authors would like to thank Prof. S.E. Bankov for helpful discussions in problems of modelling and simulations.

Funding

This study was supported by the Ministry of Science and Higher Education of the Russian Federation (agreement no. 075-15-2024-538).

ORCID® iDs

Fedor V. Khan - https://orcid.org/0000-0002-0496-2106
Mikhail Yu. Fominsky - https://orcid.org/0000-0001-6529-0465

Data Availability Statement

Data generated and analyzed during this study is available from the corresponding author upon reasonable request.

References

1. Tinkham, M. *Introduction to Superconductivity;* McGraw-Hill: New York, NY, USA, 1975.
2. Barone, A.; Paterno, G. *Physics and Applications of the Josephson Effect;* John Wiley & Sons: New York, NY, USA, 1982. doi:10.1002/352760278x
3. Likharev, K. K. *Dynamics of Josephson Junctions and Circuits;* Gordon & Breach Science Publishers: New York, NY, USA, 1996.
4. Tucker, J. R. *Appl. Phys. Lett.* **1980,** *36,* 477–479. doi:10.1063/1.91513
5. Kerr, A. R.; Feldman, M. J.; Pan, S. K. Receiver Noise Temperature, the Quantum Noise Limit, and the Role of the Zero-Point Fluctuations. In *Proceedings of the Eighth International Symposium on Space Terahertz Technology,* 1997; pp 101–109.
6. ALMA Observatory Website. https://www.almaobservatory.org/en/about-alma/ (accessed Sept 8, 2025).
7. APEX Space telescope website. http://www.apex-telescope.org/ns/ (accessed Sept 8, 2025).
8. Hershel Space Observatory website. https://herscheltelescope.org.uk/mission/ (accessed Sept 8, 2025).
9. Millimetron Space Observatory website. https://millimetron.ru/en/ (accessed Sept 8, 2025).
10. Event Horizon Telescope website. https://eventhorizontelescope.org/ (accessed Sept 8, 2025).
11. The Event Horizon Telescope Collaboration; Akiyama, K.; Alberdi, A.; Alef, W.; Asada, K.; Azulay, R.; Baczko, A.-K.; Ball, D.; Baloković, M.; Barrett, J.; Bintley, D.; Blackburn, L.; Boland, W.; Bouman, K. L.; Bower, G. C.; Bremer, M.; Brinkerink, C. D.; Brissenden, R.; Britzen, S.; Broderick, A. E.; Broguiere, D.; Bronzwaer, T.; Byun, D.-Y.; Carlstrom, J. E.; Chael, A.; Chan, C.-k.; Chatterjee, S.; Chatterjee, K.; Chen, M.-T.; Chen, Y.; Cho, I.; Christian, P.; Conway, J. E.; Cordes, J. M.; Crew, G. B.; Cui, Y.; Davelaar, J.; De Laurentis, M.; Deane, R.; Dempsey, J.; Desvignes, G.; Dexter, J.; Doeleman, S. S.; Eatough, R. P.; Falcke, H.; Fish, V. L.; Fomalont, E.; Fraga-Encinas, R.; Freeman, W. T.; Friberg, P.; Fromm, C. M.; Gómez, J. L.; Galison, P.; Gammie, C. F.; García, R.; Gentaz, O.; Georgiev, B.; Goddi, C.; Gold, R.; Gu, M.; Gurwell, M.; Hada, K.; Hecht, M. H.; Hesper, R.; Ho, L. C.; Ho, P.; Honma, M.; Huang, C.-W. L.; Huang, L.; Hughes, D. H.; Ikeda, S.; Inoue, M.; Issaoun, S.; James, D. J.; Jannuzi, B. T.; Janssen, M.; Jeter, B.; Jiang, W.; Johnson, M. D.; Jorstad, S.; Jung, T.; Karami, M.; Karuppusamy, R.; Kawashima, T.; Keating, G. K.; Kettenis, M.; Kim, J.-Y.; Kim, J.; Kim, J.; Kino, M.; Koay, J. Y.; Koch, P. M.; Koyama, S.; Kramer, M.; Kramer, C.; Krichbaum, T. P.; Kuo, C.-Y.; Lauer, T. R.; Lee, S.-S.; Li, Y.-R.; Li, Z.; Lindqvist, M.; Liu, K.; Liuzzo, E.; Lo, W.-P.; Lobanov, A. P.; Loinard, L.; Lonsdale, C.; Lu, R.-S.; MacDonald, N. R.; Mao, J.; Markoff, S.; Marrone, D. P.; Marscher, A. P.; Martí-Vidal, I.; Matsushita, S.; Matthews, L. D.; Medeiros, L.; Menten, K. M.; Mizuno, Y.; Mizuno, I.; Moran, J. M.; Moriyama, K.; Moscibrodzka, M.; Müller, C.; Nagai, H.; Nagar, N. M.; Nakamura, M.; Narayan, R.; Narayanan, G.; Natarajan, I.; Neri, R.; Ni, C.; Noutsos, A.; Okino, H.; Olivares, H.; Oyama, T.; Özel, F.; Palumbo, D. C. M.; Patel, N.; Pen, U.-L.; Pesce, D. W.; Piétu, V.; Plambeck, R.; PopStefanija, A.; Porth, O.; Prather, B.; Preciado-López, J. A.; Psaltis, D.; Pu, H.-Y.; Ramakrishnan, V.; Rao, R.; Rawlings, M. G.; Raymond, A. W.; Rezzolla, L.; Ripperda, B.; Roelofs, F.; Rogers, A.; Ros, E.; Rose, M.; Roshanineshat, A.; Rottmann, H.; Roy, A. L.; Ruszczyk, C.; Ryan, B. R.; Rygl, K. L. J.; Sánchez, S.; Sánchez-Arguelles, D.; Sasada, M.; Savolainen, T.; Schloerb, F. P.; Schuster, K.-F.; Shao, L.; Shen, Z.; Shmall, D.; Sohn, B. W.; SooHoo, J.; Tazaki, F.; Tiede, P.; Tilanus, R. P. J.; Titus, M.; Toma, K.; Torne, P.; Trent, T.; Trippe, S.; Tsuda, S.; van Bemmel, I.; van Langevelde, H. J.; van Rossum, D. R.; Wagner, J.; Wardle, J.; Weintroub, J.; Wex, N.; Wharton, R.; Wielgus, M.; Wong, G. N.; Wu, Q.; Young, A.; Young, K.; Younsi, Z.; Yuan, F.; Yuan, Y.-F.; Zensus, J. A.; Zhao, G.; Zhao, S.-S.; Zhu, Z.; Farah, J. R.; Meyer-Zhao, Z.; Michalik, D.; Nadolski, A.; Nishioka, H.; Pradel, N.; Primiani, R. A.; Souccar, K.; Vertatschitsch, L.; Yamaguchi, P. *Astrophys. J., Lett.* **2019,** *875,* L4. doi:10.3847/2041-8213/ab0e85

12. Siles, J. V.; Maestrini, A. E.; Lee, C.; Lin, R.; Mehdi, I. *IEEE Trans. Terahertz Sci. Technol.* **2024,** *14,* 607–612. doi:10.1109/tthz.2024.3430013
13. Koshelets, V. P.; Shitov, S. V. *Supercond. Sci. Technol.* **2000,** *13,* R53–R69. doi:10.1088/0953-2048/13/5/201
14. Koshelets, V. P.; Shitov, S. V.; Filippenko, L. V.; Baryshev, A. M.; Golstein, H.; de Graauw, T.; Luinge, W.; Schaeffer, H.; van de Stadt, H. *Appl. Phys. Lett.* **1996,** *68,* 1273–1275. doi:10.1063/1.115950
15. Baksheeva, K. A.; Ozhegov, R. V.; Goltsman, G. N.; Kinev, N. V.; Koshelets, V. P.; Kochnev, A.; Betzalel, N.; Puzenko, A.; Ben Ishai, P.; Feldman, Y. *IEEE Trans. Terahertz Sci. Technol.* **2021,** *11,* 381–388. doi:10.1109/tthz.2021.3066099
16. Koshelets, V. P.; Ermakov, A. B.; Filippenko, L. V.; Kinev, N. V.; Kiselev, O. S.; Torgashin, M. Y.; de Lange, A.; de Lange, G.; Pripolzin, S. I.; Vaks, V. L. *Proc. SPIE* **2010,** *7854,* 78540J. doi:10.1117/12.868916
17. Koshelets, V. P.; Shitov, S. V.; Ermakov, A. B.; Filippenko, L. V.; Koryukin, O. V.; Khudchenko, A. V.; Torgashin, M. Y.; Yagoubov, P. A.; Hoogeveen, R. W. M.; Pylypenko, O. M. *IEEE Trans. Appl. Supercond.* **2005,** *15,* 960–963. doi:10.1109/tasc.2005.850138
18. Mattis, D. C.; Bardeen, J. *Phys. Rev.* **1958,** *111,* 412–417. doi:10.1103/physrev.111.412
19. Koshelets, V. P.; Kovtonyuk, S. A.; Serpuchenko, I. L.; Filippenko, L. V.; Shchukin, A. V. *IEEE Trans. Magn.* **1991,** *27,* 3141–3144. doi:10.1109/20.133877
20. Torgashin, M. Y.; Koshelets, V. P.; Dmitriev, P. N.; Ermakov, A. B.; Filippenko, L. V.; Yagoubov, P. A. *IEEE Trans. Appl. Supercond.* **2007,** *17,* 379–382. doi:10.1109/tasc.2007.898624
21. Cyberey, M.; Farrahi, T.; Lu, J.; Kerr, A.; Weikle, R. M.; Lichtenberger, A. W. *IEEE Trans. Appl. Supercond.* **2019,** *29,* 1–6. doi:10.1109/tasc.2018.2884967
22. Wang, Z.; Terai, H.; Qiu, W.; Makise, K.; Uzawa, Y.; Kimoto, K.; Nakamura, Y. *Appl. Phys. Lett.* **2013,** *102,* 142604. doi:10.1063/1.4801972
23. Xie, J. J.; Zhang, L.; Zhong, Y. L.; Jin, H.; Wu, L.; Wang, H. W.; Peng, W.; Chen, L.; Wang, Z. *Supercond. Sci. Technol.* **2025,** *38,* 055024. doi:10.1088/1361-6668/add425
24. Kawakami, A.; Wang, Z.; Miki, S. *J. Appl. Phys.* **2001,** *90,* 4796–4799. doi:10.1063/1.1409583
25. Makise, K.; Terai, H.; Takeda, M.; Uzawa, Y.; Wang, Z. *IEEE Trans. Appl. Supercond.* **2011,** *21,* 139–142. doi:10.1109/tasc.2010.2088350
26. Lap, B. N. R.; Khudchenko, A.; Hesper, R.; Rudakov, K. I.; Dmitriev, P.; Khan, F.; Koshelets, V. P.; Baryshev, A. M. *Appl. Phys. Lett.* **2021,** *119,* 152601. doi:10.1063/5.0066371
27. Coon, D. D.; Fiske, M. D. *Phys. Rev.* **1965,** *138,* A744–A746. doi:10.1103/physrev.138.a744
28. Koshelets, V. P.; Shitov, S. V.; Shchukin, A. V.; Filippenko, L. V.; Mygind, J.; Ustinov, A. V. *Phys. Rev. B* **1997,** *56,* 5572–5577. doi:10.1103/physrevb.56.5572
29. Kawakami, A.; Uzawa, Y.; Wang, Z. *IEEE Trans. Appl. Supercond.* **1999,** *9,* 4554–4557. doi:10.1109/77.784039
30. Jain, A. K.; Likharev, K. K.; Lukens, J. E.; Sauvageau, J. E. *Phys. Rep.* **1984,** *109,* 309–426. doi:10.1016/0370-1573(84)90002-4
31. Darula, M.; Doderer, T.; Beuven, S. *Supercond. Sci. Technol.* **1999,** *12,* R1–R25. doi:10.1088/0953-2048/12/1/001
32. Shamporov, V. A.; Myasnikov, A. S.; Pankratova, E. V.; Pankratov, A. L. *Phys. Rev. B* **2017,** *96,* 064522. doi:10.1103/physrevb.96.064522
33. Pankratov, A. L.; Revin, L. S.; Pankratova, E. V.; Shitov, S. V. *Chaos, Solitons Fractals* **2024,** *182,* 114819. doi:10.1016/j.chaos.2024.114819
34. Booi, P. A. A.; Benz, S. P. *Appl. Phys. Lett.* **1996,** *68,* 3799–3801. doi:10.1063/1.116621
35. Galin, M. A.; Shereshevsky, I. A.; Vdovicheva, N. K.; Kurin, V. V. *Supercond. Sci. Technol.* **2021,** *34,* 075005. doi:10.1088/1361-6668/abfd0b
36. Kawakami, A.; Uzawa, Y.; Wang, Z. *IEEE Trans. Appl. Supercond.* **1997,** *7,* 3126–3129. doi:10.1109/77.621994
37. Murayama, Y.; Kawakami, A.; Shan, W.; Ezaki, S.; Miyachi, A.; Masui, S.; Kojima, T.; Uzawa, Y. *IEEE Trans. Appl. Supercond.* **2025,** *35,* 2400306. doi:10.1109/tasc.2024.3515971
38. Khan, F. V.; Filippenko, L. V.; Ermakov, A. B.; Paramonov, M. E.; Fominsky, M. Y.; Kinev, N. V.; Koshelets, V. P.; Nikitov, S. A. *Phys.-Usp.* **2025,** *68,* 584–596. doi:10.3367/ufne.2024.12.039864
39. Khan, F. V.; Filippenko, L. V.; Fominsky, M. Y.; Ermakov, A. B.; Orlov, A. P.; Koshelets, V. P. Z. *Tekh. Fiz.* **2025,** *95,* 1665–1672.
40. Rogovin, D.; Scalapino, D. J. *Ann. Phys. (Amsterdam, Neth.)* **1974,** *86,* 1–90. doi:10.1016/0003-4916(74)90430-8
41. Koshelets, V. P.; Dmitriev, P. N.; Sobolev, A. S.; Pankratov, A. L.; Khodos, V. V.; Vaks, V. L.; Baryshev, A. M.; Wesselius, P. R.; Mygind, J. *Phys. C (Amsterdam, Neth.)* **2002,** *372–376,* 316–321. doi:10.1016/s0921-4534(02)00659-7
42. Koshelets, V. P.; Dmitriev, P. N.; Ermakov, A. B.; Sobolev, A. S.; Torgashin, M. Y.; Kurin, V. V.; Pankratov, A. L.; Mygind, J. *IEEE Trans. Appl. Supercond.* **2005,** *15,* 964–967. doi:10.1109/tasc.2005.850140
43. Taur, Y.; Claassen, J. H.; Richards, P. L. *Rev. Phys. Appl.* **1974,** *9,* 263–268. doi:10.1051/rphysap:0197400901026300
44. Klopfenstein, R. W. *Proc. IRE* **1956,** *44,* 31–35. doi:10.1109/jrproc.1956.274847
45. Han, S.; Worsham, A. H.; Lukens, J. E. *IEEE Trans. Appl. Supercond.* **1993,** *3,* 2489–2492. doi:10.1109/77.233961
46. Kawakami, A.; Wang, Z. *IEICE Trans. Electron.* **1996,** *79,* 1242–1246.
47. Tucker, J. R.; Feldman, M. J. *Rev. Mod. Phys.* **1985,** *57,* 1055–1113. doi:10.1103/revmodphys.57.1055
48. Kinev, N. V. Heating of the SIS Detector Caused by External Terahertz Emission. In *2024 IEEE 9th All-Russian Microwave Conference (RMC),* IEEE, 2024; pp 184–187. doi:10.1109/rmc62880.2024.10845902
49. Shapiro, S. *Phys. Rev. Lett.* **1963,** *11,* 80–82. doi:10.1103/physrevlett.11.80
50. Galin, M.; Kurin, V.; Shereshevsky, I.; Vdovicheva, N.; Antonov, A.; Andreev, B.; Klushin, A. *IEEE Trans. Appl. Supercond.* **2021,** *31,* 1–5. doi:10.1109/tasc.2021.3064533
51. Belitsky, V.; Risacher, C.; Pantaleev, M.; Vassilev, V. *Int. J. Infrared Millimeter Waves* **2006,** *27,* 809–834. doi:10.1007/s10762-006-9116-5
52. Khan, F. V.; Atepalikhin, A. A.; Filippenko, L. V.; Koshelets, V. P. *J. Commun. Technol. Electron.* **2023,** *68,* 983–988. doi:10.1134/s1064226923090115
53. Kautz, R. L. *J. Appl. Phys.* **1978,** *49,* 308–314. doi:10.1063/1.324387
54. Garg, R.; Bahl, I.; Bozzi, M. *Microstrip Lines and Slotlines;* Artech House: Norwood, MA, USA, 2013.

License and Terms

This is an open access article licensed under the terms of the Beilstein-Institut Open Access License Agreement (https://www.beilstein-journals.org/bjnano/terms), which is identical to the Creative Commons Attribution 4.0 International License (https://creativecommons.org/licenses/by/4.0). The reuse of material under this license requires that the author(s), source and license are credited. Third-party material in this article could be subject to other licenses (typically indicated in the credit line), and in this case, users are required to obtain permission from the license holder to reuse the material.

The definitive version of this article is the electronic one which can be found at:
https://doi.org/10.3762/bjnano.16.158

BEILSTEIN JOURNAL OF NANOTECHNOLOGY

Competitive helical bands and highly efficient diode effect in F/S/TI/S/F hybrid structures

Tairzhan Karabassov[*1], Irina V. Bobkova[1,2], Pavel M. Marychev[1], Vasiliy S. Stolyarov[2,3], Vyacheslav M. Silkin[4,5,6] and Andrey S. Vasenko[*1,7]

Full Research Paper

Open Access

Address:
[1]HSE University, 101000 Moscow, Russia, [2]Moscow Institute of Physics and Technology, Dolgoprudny, Moscow 141700, Russia, [3]Dukhov Research Institute of Automatics (VNIIA), 127055 Moscow, Russia, [4]Donostia International Physics Center (DIPC), San Sebastián/Donostia, 20018 Basque Country, Spain, [5]Departamento de Física de Materiales, Facultad de Ciencias Químicas, UPV/EHU, 20080 San Sebastián, Basque Country, Spain, [6]IKERBASQUE, Basque Foundation for Science, 48011 Bilbao, Spain and [7]Department of Physics, Moscow State University, Moscow 119992, Russia

Email:
Tairzhan Karabassov[*] - iminovichtair@gmail.com;
Andrey S. Vasenko[*] - avasenko@hse.ru

* Corresponding author

Keywords:
hybrid structures; proximity effect; superconducting diode effect; superconductivity; topological insulators

Beilstein J. Nanotechnol. **2026,** *17,* 15–23.
https://doi.org/10.3762/bjnano.17.2

Received: 01 October 2025
Accepted: 09 December 2025
Published: 05 January 2026

This article is part of the thematic issue "Superconducting artificial neural networks and quantum circuits".

Guest Editor: A. S. Sidorenko

© 2026 Karabassov et al.; licensee Beilstein-Institut.
License and terms: see end of document.

Abstract

The diode effect in superconducting materials has been actively investigated in recent years. Plenty of different devices have been proposed as a platform to observe the superconducting diode effect. In this work, we discuss the possibility of a highly efficient superconducting diode design with controllable polarity. We propose a mesoscopic device that consists of two separated superconducting islands with proximity-induced ferromagnetism deposited on top of a three-dimensional topological insulator. Using the quasiclassical formalism of the Usadel equations, we demonstrate that the sign of the diode efficiency can be controlled by magnetization tuning of a single superconducting island. Moreover, we show that the diode efficiency can be substantially increased in such a device. We argue that the dramatic increase of the diode efficiency is due to competing contributions of the two superconducting islands to the supercurrent with single helical bands linked through the topological insulator surface.

Introduction

Superconducting nonreciprocal phenomena have been attracting a lot of attention over the last several years [1]. Particularly, the diode effect in superconducting systems has been widely discussed due to its interesting underlying physics and potential application in nondissipative superconducting electronics [2-4]. So far, the superconducting diode effect has been reported in

many different systems, including Josephson junctions [5-11], junction-free devices [12-17], superconducting microbridges [18,19], and other systems [20,21]. There have been numerous theoretical propositions demonstrating the possibility of the superconducting diode effect such as bulk superconducting materials [22-34], proximity-effect hybrid structures [35-45], Josephson structures [46-65], nanotubes [66], confined systems [67], asymmetric SQUIDs [68-70], and superconducting systems with nonuniform magnetization [71]. The diode effect might be useful not only from an application point of view, but it may be also employed as a way to detect the spin–orbital coupling (SOC) type of the material [72].

Typically, such devices require three ingredients for achieving the nonreciprocity of the critical current, including lack of inversion and time-reversal symmetries and the presence of the superconducting order parameter [1]. However, it should be emphasized that the lack of inversion symmetry is the implication of the gyrotropy in the structure of the material that supports nonreciprocal transport [39]. On the microscopic level, the lack of inversion symmetry is expressed by the SOC term. In this regard, systems based on topological insulators (TIs) are interesting since they offer strongest SOC rendering linear spin-polarized dispersion for the surface states [73].

The diode effect in TI-based structures has been reported in Josephson junctions, as well as in hybrid structures. In practice, when producing mesoscopic diode devices, it is reasonable to expect some presence of nonmagnetic impurities in the structures. However, it has been shown previously that the diode efficiency is expected to be low in diffusive TI-based systems [37,50]. Another disadvantage of the TI diffusive diodes is their limited tunability. In these devices, the polarity of the diode cannot be changed without reversing the Zeeman field, although in long ballistic S/TI/S (S denotes a superconductor) Josephson junctions such a situation is possible [52].

In the present work, we propose a superconducting diode based on two superconducting regions with a proximity-induced in-plane exchange field on top of the TI. The Fermi contour of the TI surface states is usually represented by the Dirac spectrum, that is, a single helical band, which is characterized by the strongest spin-momentum locking effect. Here, we consider the F/S/TI/S/F (F denotes ferromagnetic layer) hybrid structure depicted in Figure 1. We argue that such a hybrid structure can behave as a system with two helical bands as, for example, noncentrosymmetric superconductors [26,74]. However, the two helical bands in the structure under consideration are coupled not in the momentum space but in the real space by the TI surface. The coupling between the two islands can be controlled, for example, by the width of the non-superconducting TI part. When considering the diode effect, the proposed layout can substantially increase the diode efficiency, provided the ferromagnetic exchange fields of the two F/S regions are oriented in opposite directions. Misalignment of the exchange fields leads to the competition of the two separate helical bands in the superconducting regions in their contribution to the critical current nonreciprocity (Figure 1).

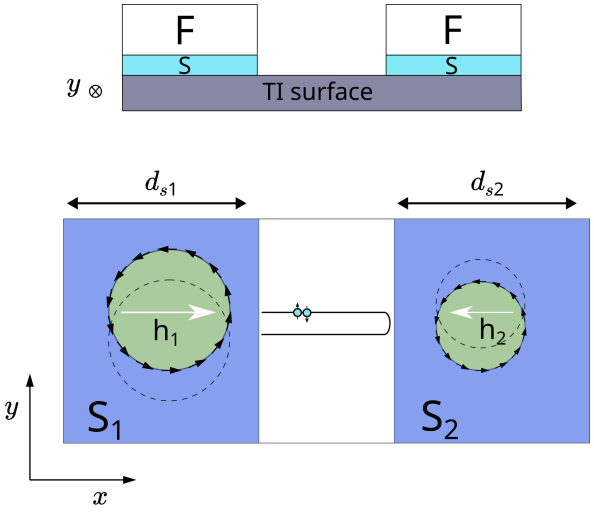


Figure 1: Geometry of the controllable diode under consideration, which consists of two superconducting islands with the proximity-induced in-plane exchange field deposited on top of the topological insulator. Schematic representation of the Fermi contours of the two superconducting regions with the exchange fields oriented in the opposite directions. S_1 and S_2 are linked through the TI surface.

Quasiclassical Theory

The F/S/TI/S/F hybrid structure can be described by the following effective low-energy Hamiltonian in the particle–hole and spin space:

$$H(\mathbf{k})=\alpha\left(k_y\sigma_x-k_x\sigma_y\right)\tau_z-\left(\mu+V\left(\mathbf{k}\right)\right)\tau_z+\mathbf{h}\cdot\boldsymbol{\sigma}\tau_0-\hat{\Delta}\left(\mathbf{k}\right), \quad (1)$$

where α is the Fermi velocity, μ is the chemical potential, and V is the impurity potential of a Gaussian form, which is used for further quasiclassical approximation in the dirty limit. $\mathbf{h}$ = (h_x, 0, 0) is the exchange field due to the adjacent ferromagnetic material. The matrices τ and $\boldsymbol{\sigma}$ are 2 × 2 Pauli matrices in the particle–hole and spin spaces, respectively. The superconducting pair potential matrix $\hat{\Delta}$ is defined as $\hat{\Delta}=i\sigma_y\hat{\Delta}_s=i\sigma_y\hat{U}i\tau_x\Delta(x)\hat{U}^\dagger$, where the transformation matrix is $\hat{U}=\exp(iqy\tau_z/2)$. The finite center of mass momentum q takes into account the helical state. The pair potential $\Delta(x)$ is a real function defined as follows:

$$\Delta(x)=\begin{cases}\Delta_1(x), & -d_{s1}-L/2<x<-L/2\\ 0, & -L/2<x<L/2\\ \Delta_2(x), & L/2<x<d_{s2}+L/2.\end{cases} \quad (2)$$

Here, Δ_1 and Δ_2 are calculated self-consistently and correspond to the superconducting regions S_1 and S_2, respectively (Figure 1). Finally, L is the width of the bare TI surface (normal N part) and $d_{s1}(d_{s2})$ is the width of S_1 (S_2) region. It is important to emphasize that, although the geometry of the considered device corresponds to a Josephson junction, in this work we consider zero macroscopic phase difference between regions S_1 and S_2, so that the Josephson supercurrent due to the phase shift is absent. The anomalous ground state phase shift ϕ_0 is also absent since we assume the exchange field component $h_y = 0$. In contrast, the h_x component is considered to be finite in the system and defined as follows:

$$h_x=\begin{cases}h_1, & -d_{s1}-L/2<x<-L/2\\ 0, & -L/2<x<L/2\\ h_2, & L/2<x<d_{s2}+L/2.\end{cases} \quad (3)$$

As we stated above, we assume the phase gradient q to be the same in the whole system. Obviously, this is not the case if $L \gg \xi$ because, in this case, the Josephson coupling between the S_1 and S_2 leads is absent, and they do not "feel" each other. In each lead, a distinct phase gradient $q_{1,2} = -2h_i/\alpha$ is established to satisfy the zero spontaneous current condition required for the helical ground state [37,75,76]. If the superconducting leads get closer to each other, Josephson coupling between them develops gradually, and Josephson currents between the leads appear. Consequently, the distribution of the superconducting phase becomes a complex two-dimensional function of spatial coordinates. Thus, a general solution of the problem requires a consideration of the two-dimensional distribution of the order parameter phase; but here we restrict ourselves to the case $d_{s1}, d_{s2} \lesssim \xi$ and the regime of relatively strong Josephson coupling between the leads S_1 and S_2. The second condition means that $L \lesssim \xi$, and the transparency of the interfaces between the superconducting leads and the TI layer is rather high. In this case, it is energetically favorable to have the same phase gradient along the whole S_1/TI/S_2 Josephson junction and the key results are obtained within this regime.

In practice, one possible implementation of the hybrid structure includes a thin layer of Nb on the surface of Bi_2Se_3 with FeMn- or CuNi-based ferromagnets deposited on top of the superconductors. Despite the challenges, it is still possible to implement heterostructures with opposite magnetization directions as in, for example, F/S/F spin valves [77]. Another possibility is more modern and is based on van der Waals structures comprised of transition-metal dichalcogenide materials such as superconducting $NbSe_2$ and magnetic VSe_2 on top of Bi_2Se_3 [78].

We solve the stated problem for the Hamiltonian in Equation 1 within the microscopic approach based on the quasiclassical Green's functions in the diffusive limit, that is, when the coherence length ξ is much larger than the electron mean free path l. Such model can be described by the Usadel equations [79-81]

$$D\hat{\nabla}\left(\hat{g}\hat{\nabla}\hat{g}\right)=\left[\omega_n\tau_z+i\hat{\Delta}_s,\hat{g}\right]. \quad (4)$$

Here D is the diffusion constant, and τ_z is the Pauli matrix in the particle–hole space. In the general case, the operator $\hat{\nabla}X=\nabla X+i(h_x\hat{e}_y-h_y\hat{e}_x)[\tau_z,\hat{g}]/\alpha$. The Green's function matrix is also transformed as $\hat{g}=\hat{U}\hat{g}_q\hat{U}^{\dagger}$.

To facilitate the solution procedures of the nonlinear Usadel equations, we employ θ parametrization of the Green's functions [82]:

$$\hat{g}_q=\begin{pmatrix}\cos\theta & \sin\theta\\ \sin\theta & -\cos\theta\end{pmatrix}. \quad (5)$$

Substituting the above matrix into the Usadel equation (Equation 4), we obtain in the superconducting S parts $|x| > L/2$:

$$\xi_s^2\pi T_{cs}\left[\partial_x^2\theta_i^s-\frac{q_i^2}{2}\sin 2\theta_i^s\right]= =\omega_n\sin\theta_i^s-\Delta_i(x)\cos\theta_i^s, \quad (6)$$

where the indices $i = 1, 2$ refer to the superconducting parts S_1 and S_2, respectively, $q_i = q + 2h_i/\alpha$, and in the normal N part $-L/2 < x < L/2$:

$$\xi_N^2\pi T_{cs}\left[\partial_x^2\theta_N-\frac{q^2}{2}\sin 2\theta_N\right]=\omega_n\sin\theta_N, \quad (7)$$

where $\theta_{s(N)}$ means the value of θ is the S(N) of the TI surface, respectively. We introduced the characteristic length $\xi_{s(N)}=\sqrt{D_{s(N)}/2\pi T_{cs}}$, where $D_{s(N)}$ is the diffusion constant in S(N) part and T_{cs} is the transition temperature of the bare S region. The self-consistency equations for the pair potentials read

$$\Delta_i(x)\ln\frac{T_{cs}}{T}=2\pi T\sum_{\omega_n>0}\left(\frac{\Delta_i(x)}{\omega_n}-\sin\theta_i^s\right), \tag{8}$$

where the summation is performed up to the Debye frequency ω_D. Finally, we supplement the above equations with two pairs of the boundary conditions (two for each S/N interface) of the following type:

$$\gamma\xi_l\hat{g}_l\nabla\hat{g}_l=\xi_r\hat{g}_r\nabla\hat{g}_r, \tag{9}$$

$$\gamma_B\xi_l\hat{g}_l\nabla\hat{g}_l=\left[\hat{g}_l,\hat{g}_r\right]. \tag{10}$$

Here, $\gamma_B = R_B\sigma_l/\xi_l$, $\gamma = \xi_r\sigma_l/\xi_l\sigma_r$ where $\sigma_{l(r)}$ is the conductivity of the material on the left (right) side of the interface. The parameter γ controls the slope of the Green's functions at the interface, whereas γ_B controls the mismatch between the functions at the interface. While for identical materials $\gamma = 1$, in general, this parameter may have arbitrary values. γ_B is the parameter that determines the transparency of the S/F interface [83-85].

The final problem comprises several equations, namely, the Usadel equations in the superconducting (S) and normal (N) parts (Equation 6 and Equation 7), two self-consistency equations (Equation 8) in each superconducting region S_1 and S_2, and the boundary conditions at the S_1/N, N/S_2 interfaces and at the free edges of the superconductors. These equations are solved simultaneously for a given phase gradient q. Using the finite difference method, the equations are discretized on a one-dimensional grid, resulting in a system of nonlinear equations that is solved by the Newton–Raphson method. We then compute the total supercurrent through the hybrid structure as a function of q, from which the supercurrent and critical current of the system are determined.

The supercurrent in the diffusive limit can be found from the expression

$$\mathbf{J}_{s(N)}=\frac{-i\pi\sigma_{s(N)}}{4e}T\sum_{\omega_n}\mathrm{Tr}\left[\tau_z\hat{g}_{s(N)}\hat{\nabla}\hat{g}_{s(N)}\right]. \tag{11}$$

Performing the unitary transformation U, the current density transforms as follows:

$$j_y^{s1(2)}(x)=-\frac{\pi\sigma_{s1(2)}}{2e}\left[q+\frac{2h_{1(2)}}{\alpha}\right]T\sum_{\omega_n}\sin^2\theta_{s1(2)}, \tag{12}$$

$$j_y^n(x)=-\frac{\pi\sigma_n q}{2e}T\sum_{\omega_n}\sin^2\theta_n. \tag{13}$$

The total supercurrent flowing through the system along the y-direction can be calculated by integrating the current density of the total width of the F/S/TI/S/F structure:

$$I=I_{s1}+I_{s2}+I_N, \tag{14}$$

where I_{s1}, I_{s2}, and I_N are the total supercurrents integrated along the x-direction in S_1, S_2 and N regions, respectively.

Results and Discussion

We fix the following system parameters throughout the discussion of the results: $d_{s1} = d_{s2} = 1.2\xi$, $\gamma_1 = \gamma_2 = 0.5$, $T = 0.1T_{cs}$. We start with the analysis of the $I(q)$ relations when the exchange fields H_1 and H_2 are the same in both superconducting regions. In Figure 2a, we observe a characteristic behavior of the supercurrent with $I(q_0) = 0$, where $q_0 \neq 0$ is the ground-state Cooper pair momentum, which reflects the helical nature of the superconducting ground state. We can also notice some nonreciprocity of the supercurrent, that is, $I_c^+ \neq I_c^-$, which is a consequence of the helical state. As we will see below, the diode efficiency is quite low and, in this case, does not exceed several percent. In the absence of any exchange field, the supercurrent is $I(q = 0) = 0$, which means that the ground state is a conventional state with zero Cooper pair momentum. To get more insight, we plot the supercurrent density J_y in Figure 2b. Hence, in the situation when H_1 and H_2 are perfectly aligned, we expect well-known behavior of the total supercurrent.

Now, we discuss the case when the exchange fields H_1 and H_2 are oriented in opposite directions (Figure 2b). When the distance between S_1 and S_2 is large ($L = 4\xi$), the superconducting regions are well separated and act almost independently with distinct critical supercurrents $I_{c1}^{\pm}$ and $I_{c2}^{\pm}$ corresponding to S_1 and S_2, respectively. This circumstance can be clearly seen from $I(q)$ dependence for $L = 4\xi$; in this sense, the distance L can be imagined as a coupling strength between S_1 and S_2. The behavior of $I(q)$ dramatically changes when L becomes smaller. The regions of the $I(q)$ curve that previously could be easily assigned to each superconducting island start to "overlap", reflecting stronger coupling between S_1 and S_2. As a result, we can achieve a situation in which the critical current of the hybrid structure in one direction is substantially renormalized. For instance, we can observe that I_c^+ is defined rather by the left maximum of $I(q)$ at $L = \xi$, while I_c^- remains approximately at the same value. Stronger coupling between the superconducting regions leads to a more complicated supercurrent density distribution across the hybrid structure (see Figure 2d). Ob-

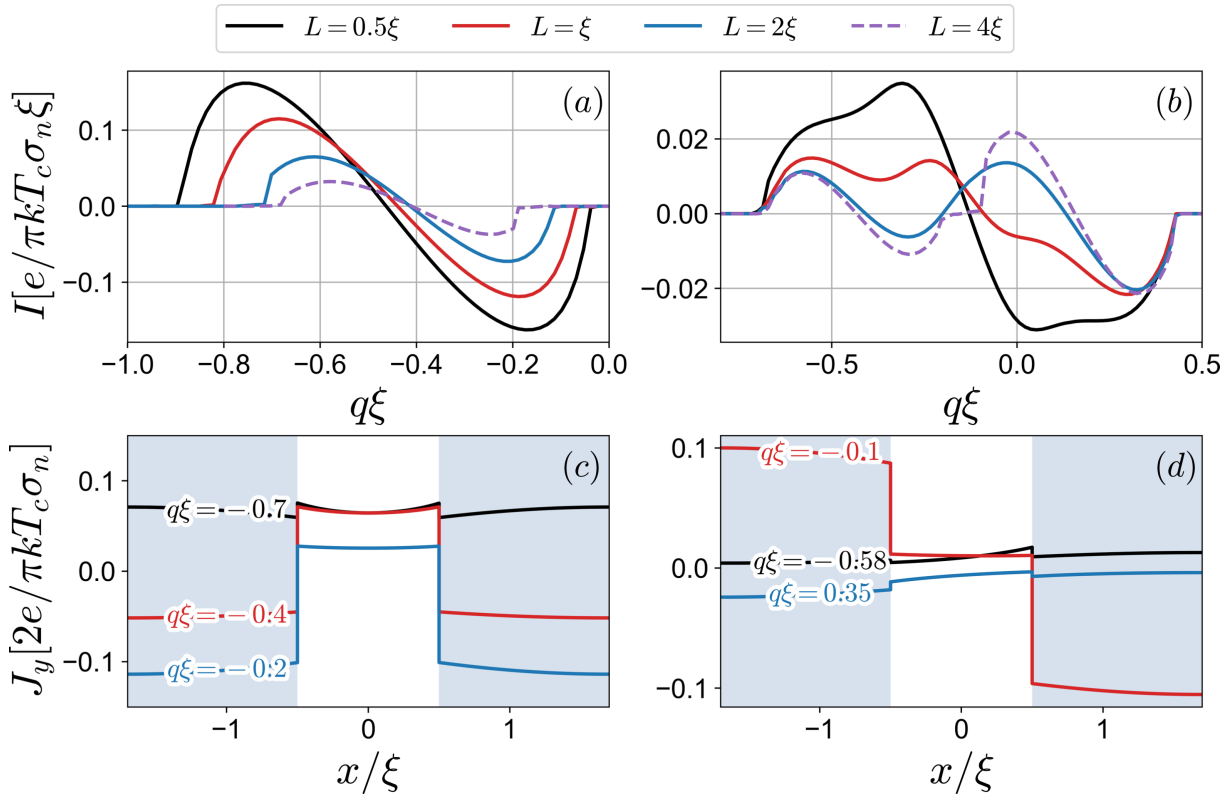


Figure 2: Supercurrent I as a function of q at $h_1 = h_2 = 0.25$ (a) and at $h_1 = -0.1$, $h_2 = 0.25$ (b). The lower panels illustrate the current density distributions at different q corresponding to the upper panels for $L = \xi$.

taining such nontrivial behavior of $I(q)$ is the key idea behind achieving a larger diode efficiency η. It should be emphasized that a similar behavior is expected in Rashba superconductors, where the Fermi surface is represented by the two helical bands with the opposite helicities [24-26]. Here, we clearly consider a single-helical-band Fermi surface. However, we can have S_1 and S_2 with the opposite h_1 and h_2 in our system as illustrated in Figure 1, which may be thought of as an effective two-helical-bands system.

The diode efficiency can be defined in a standard way, as

$$\eta = \frac{I_c^+ - \left|I_c^-\right|}{I_c^+ + \left|I_c^-\right|}. \tag{15}$$

In Figure 3, the diode efficiency along with the critical currents is demonstrated as a function of H_1, while H_2 is fixed at $H_2 = 0.25$. We observe several characteristic features of η behavior. First, the diode efficiency is quite low at large positive values of H_1, remaining under 5% at $H_1 = 0.1$. This is anticipated behavior of the diodes with single helical band in the diffusive limit [37,50,86]. As H_1 decreases, the diode efficiency rises to a certain value, and then η changes its sign rapidly reaching the maximum value. At the point when the diode changes its polarity, there is a transition from S_1 to S_2 in their contribution to the critical currents. We assume that in the vicinity of $\eta = 0$, the superconducting regions S_1 and S_2 strongly compete with each other since, individually, they have opposite efficiencies because H_1 and H_2 are of the opposite signs. We might say that, at a certain value of H_1, the critical currents I_c^+ and I_c^- of the total system are predominantly determined by S_1 and S_2, that is, the supercurrent mostly passes through one of the superconducting regions in the opposite directions. To better demonstrate this point, we plot the supercurrent density distribution (Figure 4) for values of q that correspond to the critical current momenta at $H_1 = -0.1$, $H_2 = 0.25$, and $L = \xi$. It can be seen that a larger proportion of the current density is concentrated at the corresponding superconducting region; at $q\xi = 0.35$, J_y is significantly larger at S_1, while at $q\xi = -0.58$, it is mainly at S_2. Another important observation from Figure 3 is that the sign change of the diode efficiency occurs at lower values of the critical currents. This means that higher diode efficiencies due to

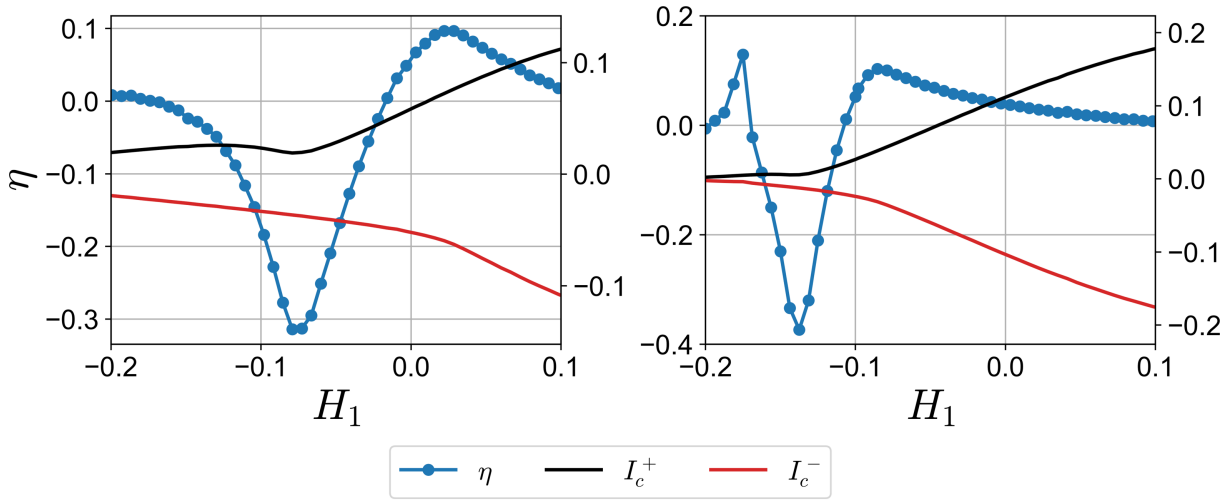


Figure 3: Critical supercurrents I_c^+ and I_c^- (right vertical scale) and diode efficiency η (left vertical scale) as functions of H_1 for $L = \xi$. Left and right plots correspond to $\gamma_{B1} = \gamma_{B2} = 0.4$ and $\gamma_{B1} = \gamma_{B2} = 0.2$, respectively. The critical currents' scale is in units of $2e/\pi k T_c \sigma_n \xi$.

the competition of S_1 and S_2 take place in a substantially suppressed superconducting state. Finally, we can see how the interface transparency affects η. Higher transparency can increase the efficiency up to 40%, however at smaller critical currents.

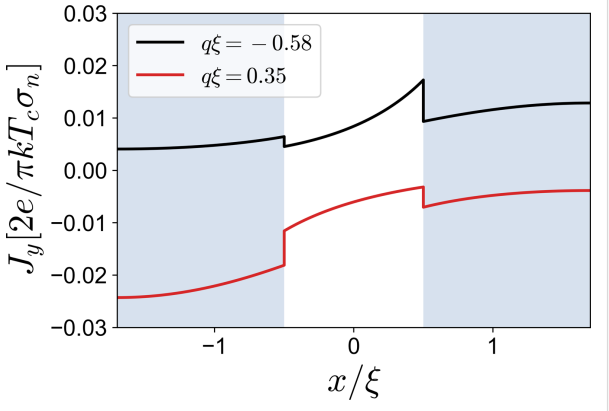


Figure 4: Supercurrent density J_y at $q\xi = -0.58$ (black line) and $q\xi = 0.35$ (red line) calculated at $L = \xi$. All other parameters are the same as in Figure 3.

The interface transparency γ_B is an important parameter of the system, which, in principle, can be used as a tuning parameter in the experiment. Control of this parameter may be achieved by applying the gating voltage at the interface. We provide more detailed analysis of the interface transparency impact on the diode effect in Figure 5. We notice that the highest efficiency is achieved at smaller $\gamma_B = 0.2$ for $L = \xi$. However, this is not the general trend as we see from the plots. For instance, the highest η is realized at $\gamma_B = 0.5$ for $L = 4\xi$. Hence, there exists an optimal value of the interface transparency for the highest efficiency. It is also important to emphasize that the exchange field H_1 at which the "major" sign change of η occurs shifts towards larger values as γ_B decreases. This means that the polarity of the diode can be altered via the control of the interface transparency, which cannot be achieved in a diffusive single-helical-band superconducting diode [37]. Finally, we observe repeated sign-changing behavior of the quality factor in Figure 5. This may reflect the competitive nature of the S_1 and S_2 behavior in the nonreciprocal supercurrent.

Conclusion

We have examined the superconducting diode effect in a F/S/TI/S/F hybrid structure. It has been shown that, under the condition that the exchange fields of the ferromagnetic regions are opposite, the diode efficiency can be dramatically increased. Such improvement can be explained in terms of the competitive behavior of the superconducting regions with single helical bands. The obtained results can be useful for achieving highly efficient superconducting diodes in the absence of an external magnetic field. Moreover, the sign of the diode efficiency can be changed as a function of the interface transparency.

As a direction for further studies, one could investigate the Josephson diode effect in the hybrid structure considered in this paper. In this case, the nonreciprocity is achieved in the Josephson critical current.

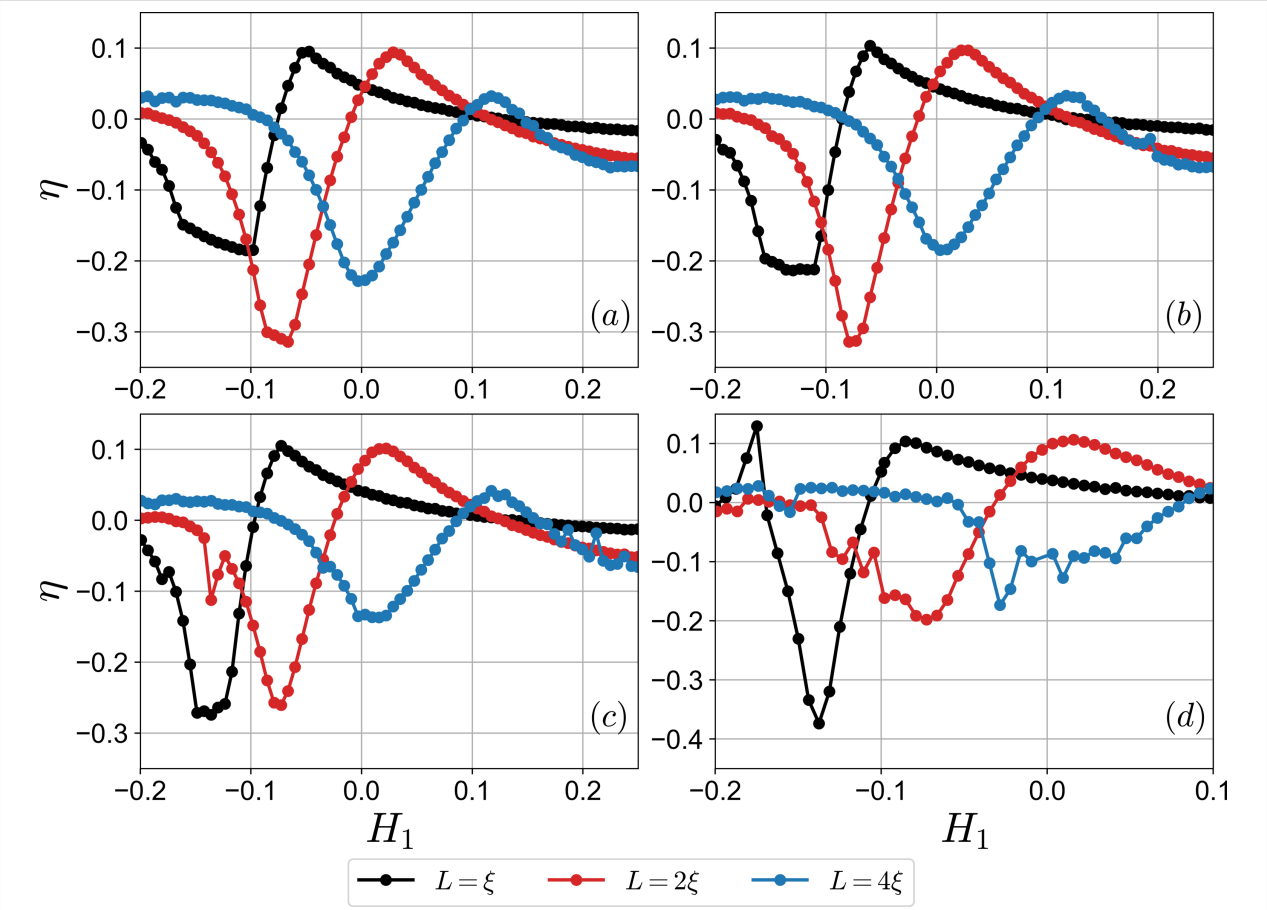


Figure 5: Superconducting diode efficiency η calculated at different interface transparencies γ_B. Plot (a) corresponds to $\gamma_{B1} = \gamma_{B2} = 0.5$, (b) $\gamma_{B1} = \gamma_{B2} = 0.4$, (c) $\gamma_{B1} = \gamma_{B2} = 0.3$, and (d) $\gamma_{B1} = \gamma_{B2} = 0.2$.

Funding

The analytical calculations were supported by MIPT via the project FSMG-2023-0014. The numerical calculations were supported by the megagrant of the Ministry of Science and Higher Education of Russian Federation No. 075-15-2024-632. T. K acknowledge the support from the Foundation for the Advancement of Theoretical Physics and Mathematics "BASIS" via the project number 25-1-4-21-1. T. K. and P. M. acknowledge the support of the HSE University Basic Research Program that was used to develop the model.

ORCID® iDs

Tairzhan Karabassov - https://orcid.org/0000-0001-7966-5221
Irina V. Bobkova - https://orcid.org/0000-0003-1469-1861
Pavel M. Marychev - https://orcid.org/0000-0002-9779-7807
Vasiliy S. Stolyarov - https://orcid.org/0000-0002-5317-0818
Andrey S. Vasenko - https://orcid.org/0000-0002-2978-8650

Data Availability Statement

Data generated and analyzed during this study is available from the corresponding author upon reasonable request.

Preprint

A non-peer-reviewed version of this article has been previously published as a preprint: https://doi.org/10.48550/arXiv.2407.14852

References

1. Nadeem, M.; Fuhrer, M. S.; Wang, X. *Nat. Rev. Phys.* **2023,** *5,* 558–577. doi:10.1038/s42254-023-00632-w
2. Soloviev, I. I.; Klenov, N. V.; Bakurskiy, S. V.; Kupriyanov, M. Y.; Gudkov, A. L.; Sidorenko, A. S. *Beilstein J. Nanotechnol.* **2017,** *8,* 2689–2710. doi:10.3762/bjnano.8.269
3. Linder, J.; Robinson, J. W. A. *Nat. Phys.* **2015,** *11,* 307–315. doi:10.1038/nphys3242
4. Eschrig, M. *Rep. Prog. Phys.* **2015,** *78,* 104501. doi:10.1088/0034-4885/78/10/104501
5. Golod, T.; Krasnov, V. M. *Nat. Commun.* **2022,** *13,* 3658. doi:10.1038/s41467-022-31256-w
6. Wu, H.; Wang, Y.; Xu, Y.; Sivakumar, P. K.; Pasco, C.; Filippozzi, U.; Parkin, S. S. P.; Zeng, Y.-J.; McQueen, T.; Ali, M. N. *Nature* **2022,** *604,* 653–656. doi:10.1038/s41586-022-04504-8
7. Baumgartner, C.; Fuchs, L.; Costa, A.; Reinhardt, S.; Gronin, S.; Gardner, G. C.; Lindemann, T.; Manfra, M. J.; Faria Junior, P. E.; Kochan, D.; Fabian, J.; Paradiso, N.; Strunk, C. *Nat. Nanotechnol.* **2022,** *17,* 39–44. doi:10.1038/s41565-021-01009-9

8. Pal, B.; Chakraborty, A.; Sivakumar, P. K.; Davydova, M.; Gopi, A. K.; Pandeya, A. K.; Krieger, J. A.; Zhang, Y.; Date, M.; Ju, S.; Yuan, N.; Schröter, N. B. M.; Fu, L.; Parkin, S. S. P. *Nat. Phys.* **2022,** *18,* 1228–1233. doi:10.1038/s41567-022-01699-5
9. Chen, C.-Z.; He, J. J.; Ali, M. N.; Lee, G.-H.; Fong, K. C.; Law, K. T. *Phys. Rev. B* **2018,** *98,* 075430. doi:10.1103/physrevb.98.075430
10. Trahms, M.; Melischek, L.; Steiner, J. F.; Mahendru, B.; Tamir, I.; Bogdanoff, N.; Peters, O.; Reecht, G.; Winkelmann, C. B.; von Oppen, F.; Franke, K. J. *Nature* **2023,** *615,* 628–633. doi:10.1038/s41586-023-05743-z
11. Yu, W.; Cuozzo, J. J.; Sapkota, K.; Rossi, E.; Rademacher, D. X.; Nenoff, T. M.; Pan, W. *Phys. Rev. B* **2024,** *110,* 104510. doi:10.1103/physrevb.110.104510
12. Ando, F.; Miyasaka, Y.; Li, T.; Ishizuka, J.; Arakawa, T.; Shiota, Y.; Moriyama, T.; Yanase, Y.; Ono, T. *Nature* **2020,** *584,* 373–376. doi:10.1038/s41586-020-2590-4
13. Narita, H.; Ishizuka, J.; Kawarazaki, R.; Kan, D.; Shiota, Y.; Moriyama, T.; Shimakawa, Y.; Ognev, A. V.; Samardak, A. S.; Yanase, Y.; Ono, T. *Nat. Nanotechnol.* **2022,** *17,* 823–828. doi:10.1038/s41565-022-01159-4
14. Itahashi, Y.; Ideue, T.; Saito, Y.; Shimizu, S.; Ouchi, T.; Nojima, T.; Iwasa, Y. *Sci. Adv.* **2020,** *6,* eaay9120. doi:10.1126/sciadv.aay9120
15. Lin, J.-X.; Siriviboon, P.; Scammell, H. D.; Liu, S.; Rhodes, D.; Watanabe, K.; Taniguchi, T.; Hone, J.; Scheurer, M. S.; Li, J. I. A. *Nat. Phys.* **2022,** *18,* 1221–1227. doi:10.1038/s41567-022-01700-1
16. Yasuda, K.; Yasuda, H.; Liang, T.; Yoshimi, R.; Tsukazaki, A.; Takahashi, K. S.; Nagaosa, N.; Kawasaki, M.; Tokura, Y. *Nat. Commun.* **2019,** *10,* 2734. doi:10.1038/s41467-019-10658-3
17. Teknowijoyo, S.; Chahid, S.; Gulian, A. *Phys. Rev. Appl.* **2023,** *20,* 014055. doi:10.1103/physrevapplied.20.014055
18. Suri, D.; Kamra, A.; Meier, T. N. G.; Kronseder, M.; Belzig, W.; Back, C. H.; Strunk, C. *Appl. Phys. Lett.* **2022,** *121,* 102601. doi:10.1063/5.0109753
19. Chahid, S.; Teknowijoyo, S.; Mowgood, I.; Gulian, A. *Phys. Rev. B* **2023,** *107,* 054506. doi:10.1103/physrevb.107.054506
20. Lyu, Y.-Y.; Jiang, J.; Wang, Y.-L.; Xiao, Z.-L.; Dong, S.; Chen, Q.-H.; Milošević, M. V.; Wang, H.; Divan, R.; Pearson, J. E.; Wu, P.; Peeters, F. M.; Kwok, W.-K. *Nat. Commun.* **2021,** *12,* 2703. doi:10.1038/s41467-021-23077-0
21. Satchell, N.; Shepley, P. M.; Rosamond, M. C.; Burnell, G. *J. Appl. Phys.* **2023,** *133,* 203901. doi:10.1063/5.0141576
22. Scammell, H. D.; Li, J. I. A.; Scheurer, M. S. *2D Mater.* **2022,** *9,* 025027. doi:10.1088/2053-1583/ac5b16
23. Yuan, N. F. Q.; Fu, L. *Proc. Natl. Acad. Sci. U. S. A.* **2022,** *119,* e2119548119. doi:10.1073/pnas.2119548119
24. He, J. J.; Tanaka, Y.; Nagaosa, N. *New J. Phys.* **2022,** *24,* 053014. doi:10.1088/1367-2630/ac6766
25. Daido, A.; Ikeda, Y.; Yanase, Y. *Phys. Rev. Lett.* **2022,** *128,* 037001. doi:10.1103/physrevlett.128.037001
26. Ilić, S.; Bergeret, F. S. *Phys. Rev. Lett.* **2022,** *128,* 177001. doi:10.1103/physrevlett.128.177001
27. Legg, H. F.; Loss, D.; Klinovaja, J. *Phys. Rev. B* **2022,** *106,* 104501. doi:10.1103/physrevb.106.104501
28. Banerjee, S.; Scheurer, M. S. *Phys. Rev. Lett.* **2024,** *132,* 046003. doi:10.1103/physrevlett.132.046003
29. Chen, K.; Karki, B.; Hosur, P. *Phys. Rev. B* **2024,** *109,* 064511. doi:10.1103/physrevb.109.064511
30. Nakamura, K.; Daido, A.; Yanase, Y. *Phys. Rev. B* **2024,** *109,* 094501. doi:10.1103/physrevb.109.094501
31. Hasan, J.; Shaffer, D.; Khodas, M.; Levchenko, A. *Phys. Rev. B* **2024,** *110,* 024508. doi:10.1103/physrevb.110.024508
32. Kubo, T. *Phys. Rev. Appl.* **2023,** *20,* 034033. doi:10.1103/physrevapplied.20.034033
33. Mironov, S. V.; Mel'nikov, A. S.; Buzdin, A. I. *Phys. Rev. B* **2024,** *109,* L220503. doi:10.1103/physrevb.109.l220503
34. Cadorim, L. R.; Sardella, E.; Silva, C. C. d. S. *Phys. Rev. Appl.* **2024,** *21,* 054040. doi:10.1103/physrevapplied.21.054040
35. Devizorova, Z.; Putilov, A. V.; Chaykin, I.; Mironov, S.; Buzdin, A. I. *Phys. Rev. B* **2021,** *103,* 064504. doi:10.1103/physrevb.103.064504
36. Karabassov, T.; Golubov, A. A.; Silkin, V. M.; Stolyarov, V. S.; Vasenko, A. S. *Phys. Rev. B* **2021,** *103,* 224508. doi:10.1103/physrevb.103.224508
37. Karabassov, T.; Bobkova, I. V.; Golubov, A. A.; Vasenko, A. S. *Phys. Rev. B* **2022,** *106,* 224509. doi:10.1103/physrevb.106.224509
38. Karabassov, T.; Amirov, E. S.; Bobkova, I. V.; Golubov, A. A.; Kazakova, E. A.; Vasenko, A. S. *Condens. Matter* **2023,** *8,* 36. doi:10.3390/condmat8020036
39. Kokkeler, T.; Tokatly, I.; Bergeret, F. S. *SciPost Phys.* **2024,** *16,* 055. doi:10.21468/scipostphys.16.2.055
40. Banerjee, S.; Scheurer, M. S. *Phys. Rev. B* **2024,** *110,* 024503. doi:10.1103/physrevb.110.024503
41. Hosur, P.; Palacios, D. *Phys. Rev. B* **2023,** *108,* 094513. doi:10.1103/physrevb.108.094513
42. Wang, J.-N.; Xiong, Y.-C.; Zhou, W.-H.; Peng, T.; Wang, Z. *Phys. Rev. B* **2024,** *109,* 064518. doi:10.1103/physrevb.109.064518
43. Kopasov, A. A.; Mel'nikov, A. S. *Phys. Rev. B* **2022,** *105,* 214508. doi:10.1103/physrevb.105.214508
44. Seleznyov, D. V.; Yagovtsev, V. O.; Pugach, N. G.; Tao, L. *J. Magn. Magn. Mater.* **2024,** *595,* 171645. doi:10.1016/j.jmmm.2023.171645
45. Neilo, A.; Bakurskiy, S.; Klenov, N.; Soloviev, I.; Kupriyanov, M. *Nanomaterials* **2024,** *14,* 245. doi:10.3390/nano14030245
46. Grein, R.; Eschrig, M.; Metalidis, G.; Schön, G. *Phys. Rev. Lett.* **2009,** *102,* 227005. doi:10.1103/physrevlett.102.227005
47. Yokoyama, T.; Eto, M.; Nazarov, Y. V. *Phys. Rev. B* **2014,** *89,* 195407. doi:10.1103/physrevb.89.195407
48. Kopasov, A. A.; Kutlin, A. G.; Mel'nikov, A. S. *Phys. Rev. B* **2021,** *103,* 144520. doi:10.1103/physrevb.103.144520
49. Davydova, M.; Prembabu, S.; Fu, L. *Sci. Adv.* **2022,** *8,* eabo0309. doi:10.1126/sciadv.abo0309
50. Kokkeler, T. H.; Golubov, A. A.; Bergeret, F. S. *Phys. Rev. B* **2022,** *106,* 214504. doi:10.1103/physrevb.106.214504
51. Zazunov, A.; Rech, J.; Jonckheere, T.; Grémaud, B.; Martin, T.; Egger, R. *arXiv* **2023,** 2307.14698. doi:10.48550/arxiv.2307.14698
52. Lu, B.; Ikegaya, S.; Burset, P.; Tanaka, Y.; Nagaosa, N. *Phys. Rev. Lett.* **2023,** *131,* 096001. doi:10.1103/physrevlett.131.096001
53. Cayao, J.; Nagaosa, N.; Tanaka, Y. *Phys. Rev. B* **2024,** *109,* L081405. doi:10.1103/physrevb.109.l081405
54. Seoane Souto, R.; Leijnse, M.; Schrade, C.; Valentini, M.; Katsaros, G.; Danon, J. *Phys. Rev. Res.* **2024,** *6,* L022002. doi:10.1103/physrevresearch.6.l022002
55. Wang, J.; Jiang, Y.; Wang, J. J.; Liu, J.-F. *Phys. Rev. B* **2024,** *109,* 075412. doi:10.1103/physrevb.109.075412
56. Wei, Y.-J.; Wang, J.-J.; Wang, J. *Phys. Rev. B* **2023,** *108,* 054521. doi:10.1103/physrevb.108.054521
57. Mao, Y.; Yan, Q.; Zhuang, Y.-C.; Sun, Q.-F. *Phys. Rev. Lett.* **2024,** *132,* 216001. doi:10.1103/physrevlett.132.216001

58. Debnath, D.; Dutta, P. *Phys. Rev. B* **2024,** *109,* 174511. doi:10.1103/physrevb.109.174511
59. Chatterjee, P.; Dutta, P. *New J. Phys.* **2024,** *26,* 073035. doi:10.1088/1367-2630/ad617a
60. Huang, H.; de Picoli, T.; Väyrynen, J. I. *Appl. Phys. Lett.* **2024,** *125,* 032602. doi:10.1063/5.0213137
61. Karabassov, T. *JETP Lett.* **2024,** *119,* 316–323. doi:10.1134/s0021364023603792
62. Samokhvalov, A. *JETP Lett.* **2024,** *119,* 511–517. doi:10.1134/s0021364024600411
63. Vakili, H.; Ali, M.; Kovalev, A. A. *arXiv* **2024,** 2406.11127. doi:10.48550/arxiv.2406.11127
64. Fu, P.-H.; Xu, Y.; Yang, S. A.; Lee, C. H.; Ang, Y. S.; Liu, J.-F. *Phys. Rev. Appl.* **2024,** *21,* 054057. doi:10.1103/physrevapplied.21.054057
65. Guarcello, C.; Pagano, S.; Filatrella, G. *Appl. Phys. Lett.* **2024,** *124,* 162601. doi:10.1063/5.0211230
66. He, J. J.; Tanaka, Y.; Nagaosa, N. *Nat. Commun.* **2023,** *14,* 3330. doi:10.1038/s41467-023-39083-3
67. de Picoli, T.; Blood, Z.; Lyanda-Geller, Y.; Väyrynen, J. I. *Phys. Rev. B* **2023,** *107,* 224518. doi:10.1103/physrevb.107.224518
68. Fominov, Y. V.; Mikhailov, D. S. *Phys. Rev. B* **2022,** *106,* 134514. doi:10.1103/physrevb.106.134514
69. Cuozzo, J. J.; Pan, W.; Shabani, J.; Rossi, E. *Phys. Rev. Res.* **2024,** *6,* 023011. doi:10.1103/physrevresearch.6.023011
70. Seleznev, G. S.; Fominov, Y. V. *Phys. Rev. B* **2024,** *110,* 104508. doi:10.1103/physrevb.110.104508
71. Roig, M.; Kotetes, P.; Andersen, B. M. *Phys. Rev. B* **2024,** *109,* 144503. doi:10.1103/physrevb.109.144503
72. Amundsen, M.; Linder, J.; Robinson, J. W. A.; Žutić, I.; Banerjee, N. *Rev. Mod. Phys.* **2024,** *96,* 021003. doi:10.1103/revmodphys.96.021003
73. Hasan, M. Z.; Kane, C. L. *Rev. Mod. Phys.* **2010,** *82,* 3045–3067. doi:10.1103/revmodphys.82.3045
74. Houzet, M.; Meyer, J. S. *Phys. Rev. B* **2015,** *92,* 014509. doi:10.1103/physrevb.92.014509
75. Kaur, R. P.; Agterberg, D. F.; Sigrist, M. *Phys. Rev. Lett.* **2005,** *94,* 137002. doi:10.1103/physrevlett.94.137002
76. Dimitrova, O.; Feigel'man, M. V. *Phys. Rev. B* **2007,** *76,* 014522. doi:10.1103/physrevb.76.014522
77. Kushnir, V. N.; Sidorenko, A.; Tagirov, L. R.; Kupriyanov, M. Y. Basic superconducting spin valves. In *Functional Nanostructures and Metamaterials for Superconducting Spintronics: From Superconducting Qubits to Self-Organized Nanostructures;* Sidorenko, A., Ed.; NanoScience and Technology; Springer: Cham, Switzerland, 2018; pp 1–29. doi:10.1007/978-3-319-90481-8_1
78. Yi, H.; Hu, L.-H.; Wang, Y.; Xiao, R.; Cai, J.; Hickey, D. R.; Dong, C.; Zhao, Y.-F.; Zhou, L.-J.; Zhang, R.; Richardella, A. R.; Alem, N.; Robinson, J. A.; Chan, M. H. W.; Xu, X.; Samarth, N.; Liu, C.-X.; Chang, C.-Z. *Nat. Mater.* **2022,** *21,* 1366–1372. doi:10.1038/s41563-022-01386-z
79. Zyuzin, A.; Alidoust, M.; Loss, D. *Phys. Rev. B* **2016,** *93,* 214502. doi:10.1103/physrevb.93.214502
80. Bobkova, I. V.; Bobkov, A. M. *Phys. Rev. B* **2017,** *96,* 224505. doi:10.1103/physrevb.96.224505
81. Ozaeta, A.; Vasenko, A. S.; Hekking, F. W. J.; Bergeret, F. S. *Phys. Rev. B* **2012,** *86,* 060509. doi:10.1103/physrevb.86.060509
82. Belzig, W.; Wilhelm, F. K.; Bruder, C.; Schön, G.; Zaikin, A. D. *Superlattices Microstruct.* **1999,** *25,* 1251–1288. doi:10.1006/spmi.1999.0710
83. Kuprianov, M. Y.; Lukichev, V. F. *JETP Lett.* **1988,** *67,* 1163.
84. Bezuglyi, E. V.; Vasenko, A. S.; Shumeiko, V. S.; Wendin, G. *Phys. Rev. B* **2005,** *72,* 014501. doi:10.1103/physrevb.72.014501
85. Bezuglyi, E. V.; Vasenko, A. S.; Bratus, E. N.; Shumeiko, V. S.; Wendin, G. *Phys. Rev. B* **2006,** *73,* 220506. doi:10.1103/physrevb.73.220506
86. Karabassov, T.; Bobkova, I. V.; Silkin, V. M.; Lvov, B. G.; Golubov, A. A.; Vasenko, A. S. *Phys. Scr.* **2024,** *99,* 015010. doi:10.1088/1402-4896/ad1376

License and Terms

This is an open access article licensed under the terms of the Beilstein-Institut Open Access License Agreement (https://www.beilstein-journals.org/bjnano/terms), which is identical to the Creative Commons Attribution 4.0 International License (https://creativecommons.org/licenses/by/4.0). The reuse of material under this license requires that the author(s), source and license are credited. Third-party material in this article could be subject to other licenses (typically indicated in the credit line), and in this case, users are required to obtain permission from the license holder to reuse the material.

The definitive version of this article is the electronic one which can be found at:
https://doi.org/10.3762/bjnano.17.2

BEILSTEIN JOURNAL OF NANOTECHNOLOGY

Microscopic study of the intermediate mixed state in intertype superconductors

Vyacheslav D. Neverov[1,2], Alexander V. Kalashnikov[3], Andrey V. Krasavin[*2,3] and Alexei Vagov[2]

Full Research Paper

Open Access

Address:
[1]Moscow Institute of Physics and Technology, 141700 Dolgoprudny, Russian Federation, [2]HSE University, Moscow 101000, Russian Federation and [3]National Research Nuclear University MEPhI, Moscow 115409, Russian Federation

Email:
Andrey V. Krasavin[*] - avkrasavin@gmail.com

* Corresponding author

Keywords:
Bogoliubov–de Gennes equations; intertype regime; microscopic calculations; superconductivity; vortices in superconductors

Beilstein J. Nanotechnol. **2026,** *17,* 57–62.
https://doi.org/10.3762/bjnano.17.5

Received: 30 October 2025
Accepted: 15 December 2025
Published: 07 January 2026

This article is part of the thematic issue "Superconducting artificial neural networks and quantum circuits".

Guest Editor: A. S. Sidorenko



© 2026 Neverov et al.; licensee Beilstein-Institut.
License and terms: see end of document.

Abstract

We present a comprehensive microscopic study of the intermediate mixed state in superconductors of the intertype (IT) regime separating types I and II. Using fully self-consistent Bogoliubov–de Gennes calculations for a lattice model, we analyze few-vortex configurations across the entire temperature range $0 < T < T_c$. Our results demonstrate the key features of IT superconductivity, namely, nonmonotonic vortex interactions and formation of vortex clusters. Using results of the calculations, we construct a "temperature–coupling" phase diagram that delineates distinct superconducting regimes and shows their convergence at a single Bogomolnyi point, consistent with earlier predictions of extended Ginzburg–Landau theory. Additionally, we identify a deep IT region of irregular vortex configurations apparently dominated by many-body vortex effects. The results establish a fully microscopic foundation for the IT superconductivity and extend its description beyond the vicinity of the critical temperature.

Introduction

The magnetic response of superconductors has long served as a fundamental criterion for their classification into distinct types. Traditionally, two types are recognized, namely, type I, in which magnetic fields are completely expelled from the material (the Meissner state), and type II, with magnetic flux penetration in the form of quantized vortices forming a mixed state [1-3]. Within the Ginzburg–Landau (GL) framework, the boundary between these regimes is determined by the GL parameter $\kappa = \lambda_L/\xi_{GL}$, where λ_L is the magnetic London penetration depth and ξ_{GL} is Ginsburg–Landau coherence length, with the critical value $\kappa_0 = 1/\sqrt{2}$ separating type-I ($\kappa < \kappa_0$) and type-II ($\kappa > \kappa_0$) behavior [4].

However, experimental studies have shown that this traditional dichotomy is incomplete even for superconductors with a single gap function (single-band superconductors). In materials with κ_{GL} close to κ_0, the magnetic flux penetrates the sample in complex, irregular patterns that cannot be attributed to type-I or type-II behavior [5-16]. These patterns are referred to as intermediate mixed state (IMS) and are characterized by the coexis-

tence of Meissner domains and vortex clusters, chains, or fragmented lattices.

Initially referred to as type II/1 superconductivity [14], this regime has since been understood as a manifestation of a more general intertype (IT) superconductivity [17-20], which fundamentally extends the conventional classification. The physics of IT superconductivity is closely related to the infinite degeneracy of the superconducting state at the so-called Bogomolnyi ($\mathscr{B}$) point (κ_0, T_c) with T_c being the critical temperature [21,22]. At this point, the surface energy between the superconducting and normal phases vanishes, allowing for a continuum of flux–condensate configurations with equal energy. Deviations from the $\mathscr{B}$ point lift this degeneracy, creating a finite IT domain in the (κ, T) phase diagram [17,23,24]. Within this domain, the system supports a variety of states with close energies that feature nonuniform flux distributions and complex vortex arrangements.

Based on the perturbation expansion of the BCS theory, also referred to as the extended Ginzburg-Landau (EGL) formalism [23-25], it has been demonstrated that the emergence of IT behavior is a universal phenomenon and occurs in both single- and multiband superconductors [17]. One of its key features is nonmonotonic vortex–vortex interactions, which are attractive at long and repulsive at short ranges [14]. The long-range attraction destabilizes the regular Abrikosov lattice, promoting the formation of vortex clusters. Subsequent studies have also highlighted the important role of many-vortex effects, which extend beyond simple pairwise interactions and decisively shape IMS vortex configurations [26,27].

Despite the long-standing experimental evidence and theoretical efforts, IT superconductivity remains insufficiently explored. This gap arises from the limitations of perturbative approaches, which are strictly valid only in the vicinity of $\mathscr{B}$ close to T_c. Although higher-order expansions of the BCS theory beyond the GL level successfully describe certain features of the IMS, a fully microscopic description applicable across the entire temperature range has been lacking until now. Recent zero-temperature calculations within the Bogoliubov–de Gennes (BdG) framework [1] have demonstrated IT behavior by studying few-vortex configurations, revealing the coexistence of repulsion and attraction that leads to vortex clustering [28].

In this work, we extend these microscopic BdG calculations to the entire temperature range $0 < T < T_c$ and investigate the evolution of few-vortex states as the system changes between type-I and type-II regimes. Our results show that the key qualitative features of the IT superconductivity persist throughout this range; however, the IT domain gradually narrows as the temperature increases, shrinking to a single point at T_c. Based on these findings, we construct a phase diagram of the IT regime, which appears qualitatively consistent with that obtained earlier from perturbation theory for the conventional BCS model with a spherical Fermi surface.

Results and Discussion

Model and method

The vortex configurations are analyzed within a microscopic lattice model of a superconductor described by the attractive Hubbard Hamiltonian:

$$\widehat{\mathcal{H}} = \sum_{\langle ij\rangle,\sigma} t_{ij}\hat{c}^{\dagger}_{i\sigma}\hat{c}_{j\sigma} - g\sum_{i}\hat{n}_{i\uparrow}\hat{n}_{i\downarrow}, \tag{1}$$

where $\hat{c}_{i\sigma}$ ($\hat{c}^{\dagger}_{i\sigma}$) are the annihilation (creation) operator for an electron with spin σ at site i, $\hat{n}_{i\sigma} = \hat{c}^{\dagger}_{i\sigma}\hat{c}_{i\sigma}$ is the electron number operator, $t_{ij} = -t$ is the nearest-neighbor hopping amplitude, and $g > 0$ denotes the onsite attraction strength. An external magnetic field is incorporated via the Peierls substitution in the hopping matrix elements as

$$\tilde{t}_{ij} = t_{ij}\exp\left[-i\frac{e}{\hbar c}\int_{\mathbf{r}_i}^{\mathbf{r}_j}\mathbf{A}(\mathbf{r})\,\mathrm{d}\mathbf{r}\right], \tag{2}$$

where $\mathbf{A}(\mathbf{r})$ is the vector potential associated with the magnetic field $\mathbf{B} = \nabla \times \mathbf{A}$.

Within the mean-field approximation, the superconducting state is determined by solving the BdG equations [1,29]:

$$\begin{aligned}\sum_j\left[t_{ij} + (U_i - \mu)\delta_{ij}\right]u_j + \Delta_i v_i &= Eu_i,\\ \sum_j\left[-t^{*}_{ij} - (U_i - \mu)\delta_{ij}\right]v_j + \Delta^{*}_i u_i &= Ev_i,\end{aligned} \tag{3}$$

where u_i and v_i are the particle and hole components of the quasiparticle wave function, and μ is the chemical potential. The superconducting gap Δ_i and Hartree–Fock potential U_i are obtained self-consistently from

$$\begin{aligned}\Delta_i &= g\sum_n u^{(n)}_i v^{(n)*}_i \tanh\left(\frac{E_n}{k_B T}\right),\\ U_i &= g\sum_n\left[\left|u^{(n)}_i\right|^2 f(E_n) + \left|v^{(n)}_i\right|^2 f(-E_n)\right],\end{aligned} \tag{4}$$

where n labels the BdG eigenstates, and $f(E)$ is the Fermi–Dirac distribution function. The electron density

$$n_e = 2\sum_n \left[\left| u_i^{(n)} \right|^2 f\left(E_n\right) + \left| v_i^{(n)} \right|^2 f\left(-E_n\right) \right]$$

is kept constant at $n_e = 0.25$ throughout all calculations by adjusting the chemical potential μ. Notice that the system is well away from the resonance at $n_e = 1$ and, at the chosen value, the electronic dispersion is well approximated by a quadratic dependence.

The BdG equations are coupled self-consistently to the magnetic field through the Ampère–Maxwell law, expressed in the Biot–Savart form for the induced vector potential $\mathbf{A}_{\text{ind}}$:

$$\mathbf{A}_{\text{ind}}\left(\mathbf{r}\right) = \int_V \frac{\mathbf{j}(\mathbf{r}', \mathbf{A})}{||\mathbf{r} - \mathbf{r}'||} \mathrm{d}^3\mathbf{r}'. \tag{5}$$

The total vector potential is $\mathbf{A} = \mathbf{A}_0 + \mathbf{A}_{\text{ind}}$, where $\mathbf{A}_0$ corresponds to the uniform external field. The current density $\mathbf{j}$, defined on the links between neighboring sites i and j, is given by

$$j_{ij} = \mathrm{Re}\left(\frac{2et_{ij}}{i\hbar} \sum_n \left\{ u_i^{(n)*} u_j^{(n)} f\left(E_n\right) + v_i^{(n)} v_j^{(n)*} \left[1 - f\left(E_n\right)\right] \right\} \right), \tag{6}$$

where the Peierls phase in t_{ij} ensures coupling to the magnetic field. The coupled system of Equation 3–Equation 6 is solved self-consistently using an iterative algorithm developed in [28,30].

The calculations are performed for a 3D slab geometry, finite in the xy-plane with size $N \times N$ and infinite along the z-axis. The magnetic field $\mathbf{B} = (0,0,B)$ is applied along the z-axis, rendering the problem effectively 2D, except for the Biot–Savart equation (Equation 5), where the integral remains 3D.

In the calculations we set $u,v = 0$ at the boundaries of the system often referred to as "open boundary conditions". We consider a sample with the relatively small linear size of $N = 31$ due to the high computational cost of achieving convergence with respect to both the superconducting gap and the magnetic field. However, this length exceeds the characteristic superconducting coherence length, which limits the influence of the finite-size effects. The electron density along z is absorbed into the parameters of the BdG and Biot–Savart equations. All energies are expressed in units of the hopping amplitude t, and lengths are measured in units of the lattice constant a.

To identify the superconductivity type, we analyze vortex configurations obtained from self-consistent microscopic calculations. We focus on configurations containing three vortices, which is sufficient to capture both vortex clustering and multivortex (many-body) interaction effects while remaining computationally feasible.

Vortex configurations

The results of these calculations are presented in Figure 1 and Figure 2, which display the minimal-energy three-vortex configurations for representative values of the pairing constant g and temperature T. The variation of g and T modifies both the coherence length ξ and the magnetic penetration depth λ, and hence their ratio κ = λ/ξ, which determines the superconductivity type. Within the GL theory, ξ and λ share the same temperature dependence, $\xi,\lambda \propto (1 - T/T_c)^{-1/2}$, making the superconductivity type temperature-independent. In contrast, microscopic theory allows for distinct temperature dependencies of these characteristic lengths, so the type of superconductivity may vary with T. This effect is clearly visible in both Figure 1 and Figure 2.

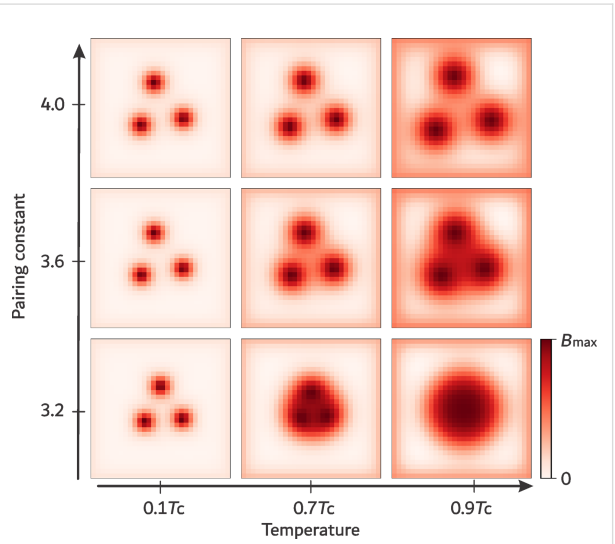


Figure 1: Spatial profile of the magnetic field inside the sample for the IT/2 regime, showing three-vortex configurations computed for pairing constants g = 3.2, 3.6, and 4.0 at temperatures T/T_c = 0.1, 0.7, and 0.9, respectively. The external magnetic field is defined as $H = 3\Phi_0/N^2$ where Φ_0 denotes the superconducting flux quantum.

At strong coupling ($g = 4.0$) and high temperature ($T = 0.9T_c$), vortices form an equilateral triangle with maximal inter-vortex separation, which is typical for type-II superconductivity. As the temperature decreases to $T = 0.1T_c$, the triangular arrangement persists, but the inter-vortex distance shrinks, indicating the appearance of a minimum in the vortex–vortex interaction potential. This behavior indicates the coexistence of long-range

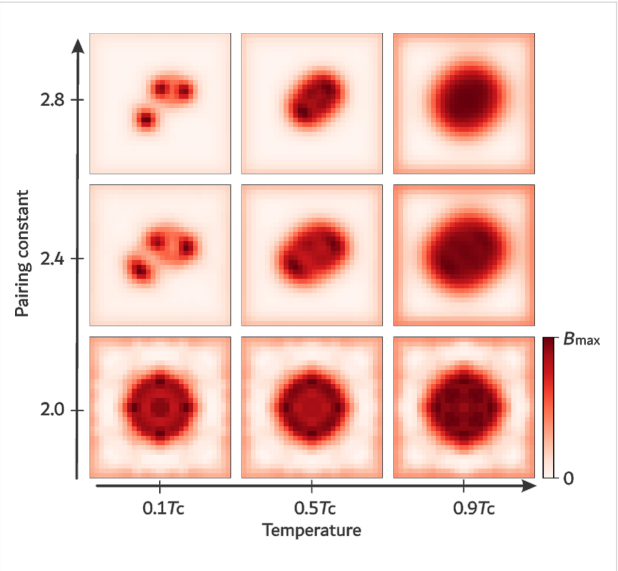


Figure 2: Spatial profile of the magnetic field inside the sample for the IT/1 regime, showing three-vortex configurations computed for pairing constants g = 2.0, 2.4, and 2.8 at temperatures T/T_c = 0.1, 0.5, and 0.9, respectively. The external magnetic field is defined as $H = 3\Phi_0/N^2$, where Φ_0 denotes the superconducting flux quantum.

attraction with short-range repulsion, which is characteristic of the IT superconductivity regime.

At weaker coupling (g = 3.2), the system exhibits type-I behavior at high temperature: The three vortices merge into a single giant vortex at $T = 0.9T_c$. As T decreases, this giant vortex splits, eventually forming a compact cluster of three vortices at $T = 0.1T_c$, signaling a crossover from type-I to IT superconductivity. Notably, at $T = 0.1T_c$, the vortices again arrange into an equilateral triangle.

The case g = 3.6, shown in the middle row of Figure 1, corresponds to the boundary between the two different IT regimes. In this case, vortices form an equilateral triangle, revealing the IT character of the vortex state at all the temperatures considered. However, the inter-vortex separation is smaller than that for the type-II regime (g = 4.0, $T = 0.9T_c$), which is consistent with the crossover behavior. Therefore, the high-temperature results ($T = 0.9T_c$) clearly demonstrate how decreasing g drives the system from type-II to type-I superconductivity: Isolated Abrikosov vortices gradually merge into a giant vortex also referred to as lamella.

Figure 2 shows results for lower coupling values (g = 2.0–2.8), where the system approaches the type-I superconductivity regime. At high temperature ($T = 0.9T_c$), vortices coalesce into a giant vortex for all g in this interval. For the weakest coupling (g = 2.0), the system remains in the type-I regime at all temperatures. Increasing g induces a transition from type-I to IT behavior upon cooling, manifested by the splitting of the giant vortex into single Abrikosov vortices. In this case, however, the vortex configuration becomes asymmetric: Two vortices are closer together than the third. Similar asymmetric arrangements have been previously reported in zero-temperature calculations [30] and have been attributed to enhanced effects of many-body interaction.

Phase diagram

The complete set of calculations for all values of g and T is summarized in the phase diagram shown in Figure 3. The diagram reveals three distinct regimes, namely, conventional type-I and type-II superconductivity and the IT regime, where Abrikosov vortices form nonstandard configurations.

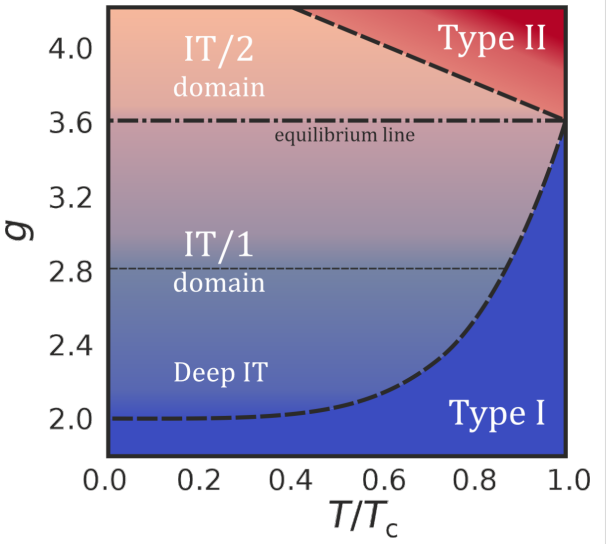


Figure 3: Temperature–coupling (T–g) phase diagram of vortex matter showing the transition from type I to type II via the IT superconducting regime. The IT type is subdivided into the IT/2 regime with the pairwise vortex interaction and the IT/1 regime with the many-body contribution to the vortex interaction. The thin dashed line separates the "Deep IT" region characterized by significant many-body interaction of vortices.

The phase diagram shows that the IT regime occupies a larger interval of coupling values g at smaller temperatures so that, at T = 0, this interval is widest. It narrows as temperature increases, disappearing in the limit $T \to T_c$, where all three superconductivity types, type I, type II, and IT, meet at a single point. This critical point has previously been discussed within the EGL expansion of BCS theory and is called the $\mathscr{B}$ point, at which the GL parameter takes the value $\kappa = \kappa_0$. In this work, the $\mathscr{B}$ point corresponds to g = 3.6, which is indicated as the "equilibrium" line in Figure 3. For $g > 3.6$, the system exhibits a crossover between the type-II and IT regimes, while, for $g < 3.6$, the crossover is between the type-I and IT regimes.

The phase diagram in Figure 3 closely resembles that obtained within the EGL formalism in the κ–T-plane, where the GL parameter κ is related to the coupling strength g. The sequence of regimes, type I→IT→type II, persists at all temperatures. Thus, microscopic calculations reproduce the known topology of superconductivity-type transitions and also extend it beyond the near-T_c regime to the entire temperature interval $0 < T < T_c$.

We note that, at lower temperatures ($T \lesssim 0.9T_c$), the microscopic results reveal a subdivision within the IT regime: Around $g \simeq 2.8$, the vortex structure changes from equilateral triangular arrangements (IT/2 domain) to irregular, asymmetric configurations (IT/1 domain) indicating the increasing role of many-body interactions. Similar structural changes were also observed in perturbative analysis, though they become especially apparent in the microscopic study of three-vortex configurations presented here.

Conclusion

This work presents a fully microscopic analysis of the intermediate mixed state in IT superconductors between the type-I and type-II regimes. Using self-consistent Bogoliubov–de Gennes simulations, we traced the evolution of vortex configurations throughout the temperature range from zero temperature to critical temperature T_c.

Our results demonstrate that the characteristic features of the IT regime, such as nonmonotonic vortex–-vortex interactions and the emergence of vortex clusters, are not limited to the vicinity of T_c but persist throughout the entire range of possible temperatures. However, the width of the IT interval in terms of the superconducting coupling strength decreases with increasing temperature, eventually collapsing to a single point (Bogomolnyi point), where type-I and type-II superconductivity merge.

The phase diagram constructed from the microscopic calculations provides a unified view of the superconductivity types and their transitions for any superconducting system, conforming and extending earlier predictions of the perturbation theory. In particular, the results confirm the presence of a deep IT region characterized by complex, non-pairwise vortex interactions that lead to irregular vortex patterns. This finding emphasizes the many-body nature of vortex matter in this regime and highlights the limitations of simplified models based on pairwise interaction.

In general, this study establishes a microscopic foundation for the IT regime in single-band superconductors and clarifies its persistence and transformation with temperature. These insights open a path for future investigations of materials tuned near the Bogomolnyi point, where unconventional vortex structures and collective effects may play a decisive role in superconducting behavior and functionality.

Funding

This work was supported by the HSE University project “International academic cooperation”.

Author Contributions

Vyacheslav D. Neverov: investigation; software; visualization. Alexander V. Kalashnikov: investigation; methodology. Andrey V. Krasavin: visualization; writing – original draft; writing – review & editing. Alexei Vagov: conceptualization; validation; writing – original draft; writing – review & editing.

ORCID® iDs

Vyacheslav D. Neverov - https://orcid.org/0000-0002-8999-8297
Andrey V. Krasavin - https://orcid.org/0000-0002-9457-5360
Alexei Vagov - https://orcid.org/0000-0001-7446-7728

Data Availability Statement

Data generated and analyzed during this study is available from the corresponding author upon reasonable request.

References

1. De Gennes, P. G. *Superconductivity of Metals and Alloys;* Benjamin: New York, NY, USA, 1966.
2. Landau, L. D.; Lifshitz, E. M. *Statistical Physics, Part 2;* Pergamon Press: Oxford, UK, 1980.
3. Ketterson, J. B.; Song, S. N. *Superconductivity;* Cambridge University Press: Cambridge, UK, 1999. doi:10.1017/cbo9781139171090
4. Landau, L. D. *Collected Papers of L. D. Landau;* Pergamon Press: Oxford, UK, 1965.
5. Träuble, H.; Essmann, U. *Phys. Status Solidi* **1967,** *20,* 95–111. doi:10.1002/pssb.19670200108
6. Krägeloh, U. *Phys. Lett. A* **1969,** *28,* 657–658. doi:10.1016/0375-9601(69)90493-9
7. Essmann, U. *Physica (Amsterdam)* **1971,** *55,* 83–93. doi:10.1016/0031-8914(71)90244-8
8. Aston, D. R.; Dubeck, L. W.; Rothwarf, F. *Phys. Rev. B* **1971,** *3,* 2231–2236. doi:10.1103/physrevb.3.2231
9. Auer, J.; Ullmaier, H. *Phys. Rev. B* **1973,** *7,* 136–145. doi:10.1103/physrevb.7.136
10. Kerchner, H. R.; Christen, D. K.; Sekula, S. T. *Phys. Rev. B* **1980,** *21,* 86–101. doi:10.1103/physrevb.21.86
11. Weber, H. W.; Seidl, E.; Botlo, M.; Laa, C.; Mayerhofer, E.; Sauerzopf, F. M.; Schalk, R. M.; Wiesinger, H. P.; Rammer, J. *Phys. C (Amsterdam, Neth.)* **1989,** *161,* 272–286. doi:10.1016/0921-4534(89)90337-7
12. Laver, M.; Forgan, E. M.; Brown, S. P.; Charalambous, D.; Fort, D.; Bowell, C.; Ramos, S.; Lycett, R. J.; Christen, D. K.; Kohlbrecher, J.; Dewhurst, C. D.; Cubitt, R. *Phys. Rev. Lett.* **2006,** *96,* 167002. doi:10.1103/physrevlett.96.167002

13. Mühlbauer, S.; Pfleiderer, C.; Böni, P.; Laver, M.; Forgan, E. M.; Fort, D.; Keiderling, U.; Behr, G. *Phys. Rev. Lett.* **2009,** *102,* 136408. doi:10.1103/physrevlett.102.136408
14. Brandt, E. H.; Das, M. P. *J. Supercond. Novel Magn.* **2011,** *24,* 57–67. doi:10.1007/s10948-010-1046-8
15. Ge, J.-Y.; Gladilin, V. N.; Sluchanko, N. E.; Lyashenko, A.; Filipov, V. B.; Indekeu, J. O.; Moshchalkov, V. V. *New J. Phys.* **2017,** *19,* 093020. doi:10.1088/1367-2630/aa8246
16. Biswas, P. K.; Rybakov, F. N.; Singh, R. P.; Mukherjee, S.; Parzyk, N.; Balakrishnan, G.; Lees, M. R.; Dewhurst, C. D.; Babaev, E.; Hillier, A. D.; Paul, D. M. K. *Phys. Rev. B* **2020,** *102,* 144523. doi:10.1103/physrevb.102.144523
17. Vagov, A.; Shanenko, A. A.; Milošević, M. V.; Axt, V. M.; Vinokur, V. M.; Aguiar, J. A.; Peeters, F. M. *Phys. Rev. B* **2016,** *93,* 174503. doi:10.1103/physrevb.93.174503
18. Vagov, A.; Wolf, S.; Croitoru, M. D.; Shanenko, A. A. *Commun. Phys.* **2020,** *3,* 58. doi:10.1038/s42005-020-0322-6
19. Vagov, A.; Saraiva, T. T.; Shanenko, A. A.; Vasenko, A. S.; Aguiar, J. A.; Stolyarov, V. S.; Roditchev, D. *Commun. Phys.* **2023,** *6,* 284. doi:10.1038/s42005-023-01395-7
20. Marychev, P. M.; Shanenko, A. A.; Vagov, A. V. *Front. Phys.* **2024,** *19,* 43205. doi:10.1007/s11467-023-1379-y
21. Bogomolnyi, E.; Vainstein, A. *Sov. J. Nucl. Phys.* **1976,** *23,* 588.
22. Bogomolnyi, E. *Sov. J. Nucl. Phys.* **1976,** *24,* 449.
23. Kramer, L. *Z. Phys.* **1973,** *258,* 367–380. doi:10.1007/bf01391501
24. Luk'yanchuk, I. *Phys. Rev. B* **2001,** *63,* 174504. doi:10.1103/physrevb.63.174504
25. Vagov, A. V.; Shanenko, A. A.; Milošević, M. V.; Axt, V. M.; Peeters, F. M. *Phys. Rev. B* **2012,** *85,* 014502. doi:10.1103/physrevb.85.014502
26. Wolf, S.; Vagov, A.; Shanenko, A. A.; Axt, V. M.; Aguiar, J. A. *Phys. Rev. B* **2017,** *96,* 144515. doi:10.1103/physrevb.96.144515
27. Córdoba-Camacho, W. Y.; Vagov, A.; Shanenko, A. A.; Aguiar, J. A.; Vasenko, A. S.; Stolyarov, V. S. *J. Phys. Chem. Lett.* **2021,** *12,* 4172–4179. doi:10.1021/acs.jpclett.1c00764
28. Neverov, V. D.; Lukyanov, A. E.; Krasavin, A. V.; Shanenko, A. A.; Croitoru, M. D.; Vagov, A. *Phys. Rev. B* **2024,** *110,* 054502. doi:10.1103/physrevb.110.054502
29. Zhu, J.-X. *Bogoliubov-de Gennes Method and Its Applications;* Lecture Notes in Physics; Springer International Publishing: Cham, Switzerland, 2016. doi:10.1007/978-3-319-31314-6
30. Neverov, V. D.; Kalashnikov, A.; Lukyanov, A. E.; Krasavin, A. V.; Croitoru, M. D.; Vagov, A. *Condens. Matter* **2024,** *9,* 8. doi:10.3390/condmat9010008

License and Terms

This is an open access article licensed under the terms of the Beilstein-Institut Open Access License Agreement (https://www.beilstein-journals.org/bjnano/terms), which is identical to the Creative Commons Attribution 4.0 International License (https://creativecommons.org/licenses/by/4.0). The reuse of material under this license requires that the author(s), source and license are credited. Third-party material in this article could be subject to other licenses (typically indicated in the credit line), and in this case, users are required to obtain permission from the license holder to reuse the material.

The definitive version of this article is the electronic one which can be found at:
https://doi.org/10.3762/bjnano.17.5

BEILSTEIN JOURNAL OF NANOTECHNOLOGY

Capabilities of the 3D-MLSI software tool in superconducting neuron design

Irina E. Tarasova[*1,2,3], Nikita S. Shuravin[1], Liubov N. Karelina[1], Fedor A. Razorenov[1,2], Evgeny N. Zhardetsky[1,4], Aleksandr S. Ionin[1,2,3], Mikhail M. Khapaev[1,5] and Vitaly V. Bol'ginov[1]

Full Research Paper

Open Access

Address:
[1]Osipyan Institute of Solid State Physics RAS, 2 Academician Osipyan str., Chernogolovka, Moscow Region, 142432, Russia, [2]Moscow Institute of Physics and Technology, 9 Institutskiy per., Dolgoprudny, Moscow Region, 141701, Russia, [3]Russian Quantum Center, 30 Bolshoy Boulevard, bld. 1, Moscow, 121205, Russia, [4]HSE University, 20 Myasnitskaya str., Moscow, 101000, Russia and [5]Faculty of Computational Mathematics and Cybernetics, Moscow State University, 1-52 Leninskiye gory, Moscow, 119991, Russia

Email:
Irina E. Tarasova[*] - tarasova.ie@phystech.edu

* Corresponding author

Keywords:
adiabatic superconductor cells; inductance extraction; Josephson interferometers; multilayer niobium technology; superconductivity

Beilstein J. Nanotechnol. **2026,** *17,* 122–138.
https://doi.org/10.3762/bjnano.17.8

Received: 30 September 2025
Accepted: 12 December 2025
Published: 13 January 2026

This article is part of the thematic issue "Superconducting artificial neural networks and quantum circuits".

Guest Editor: A. S. Sidorenko



© 2026 Tarasova et al.; licensee Beilstein-Institut.
License and terms: see end of document.

Abstract

3D-MLSI is a software tool made for inductance extraction of superconducting multilayer structures. Despite long history, its capabilities had not been explored sufficiently deep for Josephson circuits based on niobium technology. Here, we present a thorough study and verification of this program in relation to adiabatic neurons, which are extremely sensitive to variations of inductive parameters. Good agreement of experimental and extracted inductances confirms the high potential of the 3D-MLSI software package for the design of superconducting electronics components.

Introduction

This article is devoted to one of the issues related to the design of adiabatic superconducting neurons, in particular, of sigma and Gauss neuron types [1]. They are, in fact, a single-junction and a two-junction interferometer, respectively, shunted by an additional inductance, which is also used to generate the output signal. The designation of such a neuron originates from the type of transfer (or activation) function (TF) that can be realized for a given neuron type. More specifically, the single-junction interferometer may possess a sigmoidal TF (useful for implementation of a superconducting perceptron [2]), while the

two-junction interferometer may realize a Gaussian TF suitable for implementation of radial basis function (RBF) neural networks [3]. However, the desired shape of the TF is realized only for specific values of inductive parameters. This makes inductance estimation highly important for superconducting neuron design.

In fact, inductance is a crucial parameter for almost all types of superconducting electronics (SCE) circuits. Indeed, taking advantage of the high performance of SCE devices implies their operation in the gigahertz frequency range, in which incorrect circuit operation may be caused by small fluctuations in inductance. Digital and quantum SCE circuits are based on Josephson interferometers, the energy potential of which strongly depends on the inductance of the loop. For that reason, the extraction of inductances of superconducting structures has been attracting a lot of attention for many decades. Simple estimates can be made for a long line over continuous ground plane [4,5] and other primitive geometries [6]. A variety of two-dimensional (2D) programs for inductance extraction were proposed in the period of 1990–2000 (see, for example, [7,8]), which allow one to estimate self- and mutual inductances per unit length of a system of infinitely long superconducting strip lines. However, inductors of most practical devices have more complicated shapes. So, three-dimensional (3D) numerical methods are required to extract inductances needed for the design of dense and large-scale superconducting circuits.

Currently, a number of software tools have been developed that are able to simulate 3D superconducting circuits [9-13]. One of the most popular tools [14] is InductEx [9], which is based on the FastHenry engine [10] originally developed for conventional CMOS circuits [15]. In 2001, the 3D-MLSI software tool was presented [11], which is capable of extracting a three-dimensional magnetic field distribution and a planar current distribution by solving a system of integro-differential equations on a 2D grid. Recently, VoxHenry [12] and SuperVoxHenry [13] simulators were developed, which use voxel-based discretization as well as advanced numerical methods to reduce memory overhead and speed up inductance extraction. The high-frequency structure simulator by Ansys (HFSS) [16] and the Sonnet EM software [17] allow one to extract the frequency dependence of a device's impedance. Several other methods can be mentioned that are not widely used as a tool (see, for example, [18-21]) due to the limitations on geometries and materials.

The use of a given program as a tool within computer-aided design systems (see [14,22] for reviews) requires a comparison with experimental data for validation. For InductEx, an accuracy of about 2% relative to the experimental data was reached for certain types of structures suitable for superconducting rapid single flux quantum (RSFQ) circuits [23,24]. In [13], a very good agreement was demonstrated for the newly proposed SuperVoxHenry simulator. In this article, we study the potential of the 3D-MLSI software tool [11,25], which is also a powerful inductance extractor for complex multilayer structures [22]. It seems that abilities of 3D-MLSI software package have never been checked up to now despite its well-known advantages [14,22]. Here, we present its experimental verification using two types of structures designed on the basis of low-T_c Nb–Al multilayer technology similar to that used for RSFQ-circuit fabrication. First, we compare results of experiment and simulation for simple C-shaped two-junction SQUIDs placed over a thick superconducting screen. Then more complicated objects, namely, sigma and Gauss neurons [1,26,27], are studied in experiment and simulation. Good agreement between measured and extracted values of inductances followed by the TF analysis confirms the high potential of the 3D-MLSI software package for the design of SCE devices.

Results

C-shaped SQUIDs

For in-depth testing regarding the capability of 3D-MLSI for inductance extraction, several series of simple C-shaped two-junction SQUIDs were fabricated and studied. The fabricated samples contained three superconducting niobium layers separated by insulating layers (see Figure 1). The first superconducting layer (M1) served both as a superconducting ground plane and the bottom electrode of the Josephson junctions. The second (M2) and third (M3) layers formed interferometers loops, control lines, and wiring. Overlap areas between layers M2 and M3 provided inductive coupling between elements. The thicknesses of the superconducting layers were 200, 250, and 350 nm for M1, M2, and M3, respectively. The SiO_2 insulating layers had thicknesses of 200 nm (I1) and 300 nm (I2). Deposition of metallic layers was performed via magnetron sputtering in argon atmosphere, while insulating layers were thermally deposited (see parameters in [28]). The Josephson junctions (JJs) had a circular shape with 4 μm diameter (see [28] for details) and represented Nb–Al–AlO_x–Nb tunnel junctions at about 100 A/cm^2 critical current density. JJs incorporated into SQUID loops were shunted with 1 Ω molybdenum resistors to suppress capacitive hysteresis in I–V curves. Overall, this fabrication process is a type of one previously used for RSFQ logic circuits [29].

In Figure 2, four types of C-shaped SQUIDs are shown schematically. Each type corresponds to one of the methods of implementation and coupling of inductive elements that can be used in neurons' designs. In particular, inductive elements can be formed either in layer M2 (see Figure 2b,c), or in layer M3 (either fully or partially, as shown in Figure 2a,d); the control

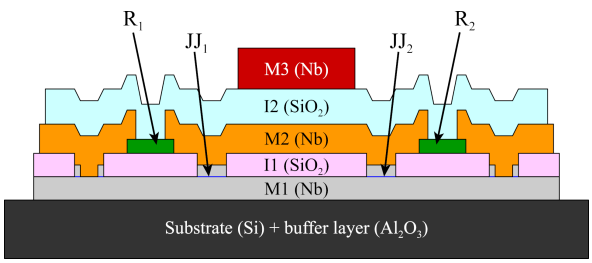


Figure 1: Cross-sectional diagram of a two-junction SQUID containing three superconducting layers (M1, M2, and M3) separated by insulating layers (I1 and I2). Josephson junctions are labeled as $JJ_{1,2}$, and their shunt resistors are $R_{1,2}$. Layer heights are to scale.

line can be wider or narrower than the SQUID loop in the coupling zone (realized by overlapping strip lines fabricated in layers M2 and M3). The designed samples included segments of variable length $\Delta_{x,y}$ (also indicated in Figure 2), which enabled more detailed comparison with the simulation results (see below). For each design type, two series were studied, manufactured in different fabrication runs. This further expanded the possibilities for testing the 3D-MLSI software and provided insight into the reproducibility of fabrication parameters.

All experiments were performed at $T = 4.2$ K with the use of a ^{4}He cryostat. The main type of experiments is related to measurements of inductances of the two-junction SQUIDs. Experimental details can be found in Appendix A. Figure 3 shows a comparison of simulated and experimental self-inductance values for the simplest case, where the variable-length segment is aligned across the control line (denoted by Δ_x in Figure 2a,b). In this case (see also insets in Figure 3), the variable segment has the simplest (two-layer) cross section. The simulation was performed with mesh steps of 0.125…1 μm, using a reduced-size superconducting screen truncated at a distance of 10 μm from the structure edges (see next section for details). For clarity, the data is presented as points on the (x,y)-plane, where x corresponds to experimental values and y to simulated ones. This format provides better visualization for comparing results obtained for different sample designs. Clearly, for perfect agreement, all points should lie on the line $y = x$ (solid line in Figure 3). This cannot be the case in experiment; but, in fact, all points in Figure 3 lie within the 6% divergence angle (indicated by dashed lines) between simulated and experimental values. Such agreement should be considered good as a parameter spread of around 5% is typical even for leading RSFQ device manufacturers [30].

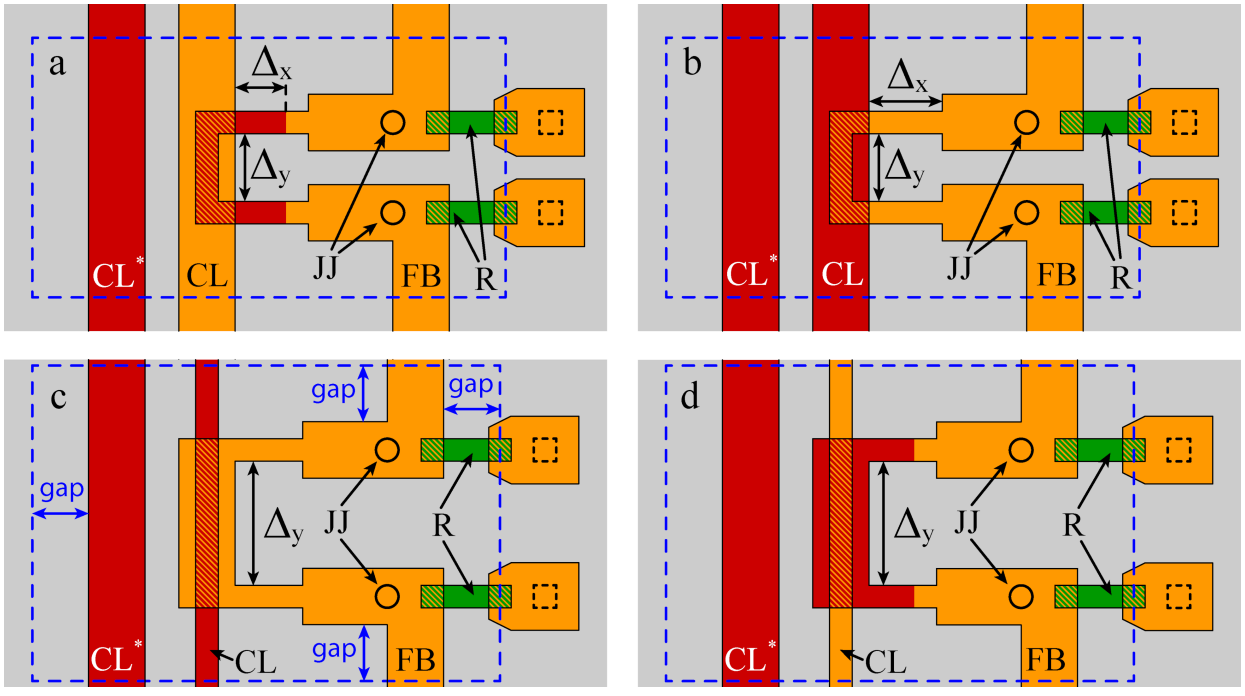


Figure 2: Schematics of test C-shaped SQUIDs. Gray color indicates the superconducting ground plane (layer M1), orange corresponds to the middle superconducting layer M2, and red represents the top superconducting layer M3. Inductive coupling zones (regions where M2 and M3 overlay) are shown with red hatching. Circles denote Josephson junctions. Green marks indicate shunt resistors of Josephson junctions, with hatching showing the connection of resistors to layer M2. Dashed squares indicate superconducting connections to the ground plane. Segments of variable length $\Delta_{x,y}$ are also shown, as well as control lines CL and FB. CL* denotes an additional control line which was not used in the present experiment. Blue dashed lines demonstrate the screen size in the simulations (see next section for details). The real boundaries of the ground plane are located at a large distances from the panel edges.

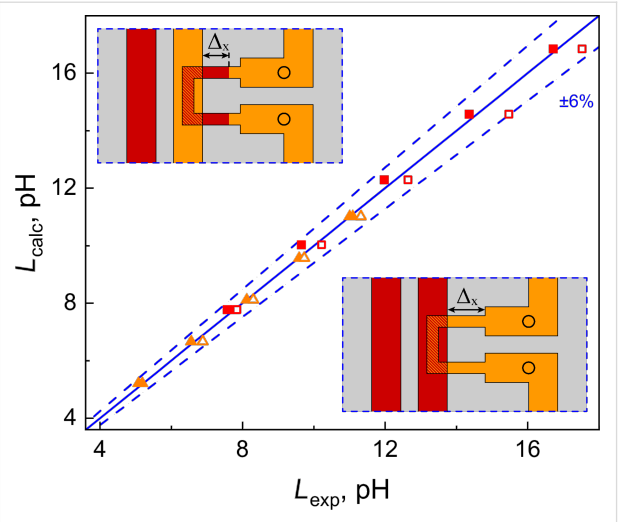


Figure 3: Comparison of calculated L_{calc} and experimental L_{exp} self-inductances for two-junction SQUIDs shown in Figure 2a (red squares) and Figure 2b (orange triangles). Filled and empty symbols correspond to samples obtained in the first and the second fabrication run, respectively. Identical symbols correspond to samples that differ only in Δ_x. The blue solid lines represent $L_{calc} = L_{exp}$, while dashed lines represent ±6% divergence angle.

Figure 4 shows the comparison of experimental and simulated values of self- and mutual inductances for C-shaped SQUIDs with different lengths of the coupling region. In fact, it is the design of this region that demonstrates the most significant difference among the C-shaped SQUIDs shown in Figure 2. Figure 4a,c presents data for designs where the SQUID loop has a smaller width than the control line in the overlap area (see Figure 2a,b). For brevity, one can refer to this design type as a "narrow loop". Figure 4b,d corresponds to the "wide loop" design, where the loop is wider than the control line in the overlapping region (see Figure 2c,d). Regarding the self-inductance values (Figure 4a,b), all points fall well within the 6% divergence angle. Regarding the mutual inductances (see Figure 4c,d), the accuracy is slightly worse. Several groups of points lie on the angle boundary, and one of them falls well outside. However, even for this case, the divergence is not too large; the relative error is as small as 10% of the experimental values.

The reasons for discrepancies require additional analysis, including those related to the sample fabrication process. Note that symbols in Figure 3 and Figure 4 differ in color, shape, and filling. The color denotes the layer in which the SQUID loop is made (M2 or M3), the shape indicates the relative width of the SQUID loop and the control line, and the filling represent two series of identical samples produced in different fabrication runs. One can see that filled and empty symbols do not coincide with each other. The difference is small and does not exceed 6% of the inductances values, but it is clearly visible in the experiments. Obviously, this is due to inevitable deviations from the goal parameters during sample fabrication and, therefore, provides a criterion for good agreement between experiment and simulation. A noticeable deviation of one group of symbols from the target line (see, for example, triangles in Figure 4a) may indicate an inaccuracy in layer thickness or superconducting line width. Incomplete correspondence between the modeling and the experiment is also possible. This may be the case for red diamonds in Figure 4d since a noticeable deviation is observed for both filled and empty symbols. Fortunately, this type of coupling area design was not used in layouts of neurons studied below.

Superconducting neurons

Next, let us consider the applicability of the 3D-MLSI program for the design of adiabatic superconducting neurons. The challenges are the more complicated shapes of inductive elements and the greater importance of inductance values for realizing the desired TF. We mainly focus on the design of a superconducting sigma neuron since its theoretical models are more developed and allow for approximation of the TF of the experimental device (see Section "Discussion"). The purpose of the sigma neuron is a sigmoidal transformation of the input signal, and the desired shape of the TF is achieved at certain values of the inductances of its loop parts (arms). The schematic of the sigma neuron was first presented in [31] (see also Appendix B). It represents a single-junction interferometer (a superconducting quantron according to [32]), the loop of which is split by an additional (output) inductance. In the simplest form, the design criterion can be stated as follows: the output inductance should divide the quantron loop into two parts with equal inductance, taking into account the effective inductance of the Josephson junction. The experimental device (see description in [26] and Appendix A) must be supplemented with elements that supply and read out the input and output magnetic fluxes, respectively. Possible interactions between parts of the experimental device complicate the analysis of its TF; however, the necessary design criteria can still be expressed through the components of a 5 × 5 inductance matrix [33].

The Gauss neuron represents a two-junction interferometer that is also shunted symmetrically to generate the output signal. This type of circuit was considered for the first time in [34-37] and named the quantum flux parametron (QFP). In [38], it was demonstrated that the energy consumption of digital SCE circuits based on QFPs can be reduced down to the fundamental limit ($kT\ln(2)$ per switching event). In [31], a QFP was proposed as a basic cell for RBF neural networks. Due to the more complicated form of the TF equation for the Gauss neuron, an analytical constraint for its inductances has not yet been obtained, and the optimal parameter values are selected

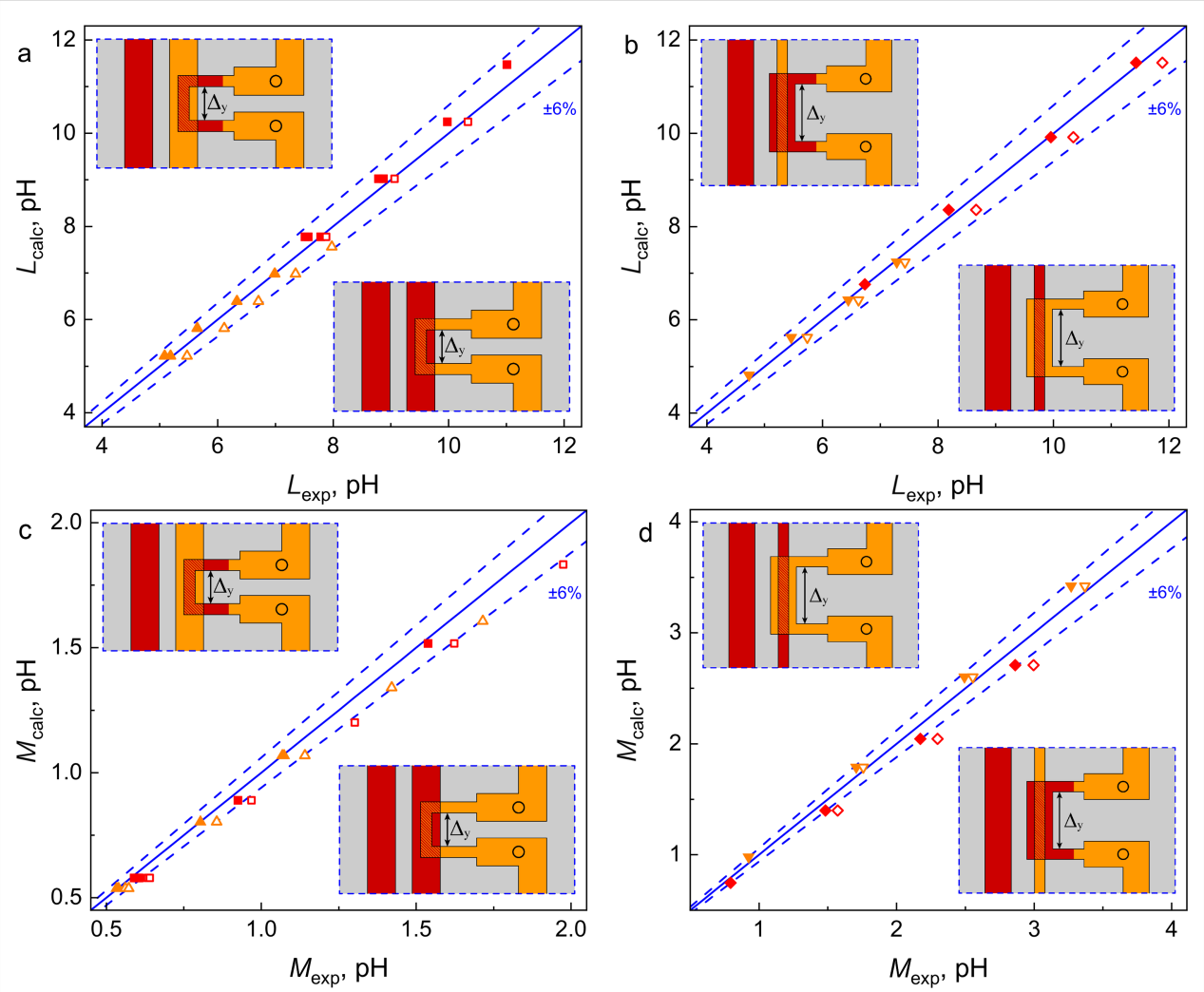


Figure 4: Comparison of calculated L_{calc} vs experimental L_{exp} self-inductances (a, b) and calculated M_{calc} vs experimental M_{exp} mutual inductances (c, d) for two-junction SQUIDs presented in Figure 2 and here in the insets. Identical symbols correspond to samples that differ only in Δ_y. Orange triangles in panels (a) and (c) correspond to Figure 2b, while red squares in these panels correspond to Figure 2a. Orange inverted triangles and red diamonds on panels (b) and (d) correspond to Figure 2c and Figure 2d, respectively. Filled and empty symbols correspond to samples obtained in the first and second fabrication runs, respectively. Blue solid lines represent $L_{calc} = L_{exp}$ (a, b) and $M_{calc} = M_{exp}$ (c, d), while dashed lines represent a ±6% divergence angle.

numerically [1,31,39-42]. A generalized theory of the Gauss neuron, accounting for the interaction of all five elements of the experimental device, is currently under development by our group.

The necessity of accounting for interaction between neuron elements was revealed during the first experimental measurements of TFs presented in [26,27]. The samples were fabricated as multilayer structures above a thick superconducting screen. Experimental curves generally agreed with theoretical expectations, but included an additional linear component. One of the reasons is that the input (control line) and the readout (two-junction SQUID) elements can exchange magnetic flux via circulating currents in the superconducting ground plane [33]. It was shown in [43] that such interaction effectively results in asymmetry of the neuron's receiving parts with respect to receiving the input signal. The corresponding component of the inductance matrix is quite small; however, it significantly affects the shape of the TF. Therefore, the designs proposed in [26,27] require further refinement.

In this work, we study sigma and Gauss neurons whose layouts (see Figure 5) were obtained mainly by scaling down previously studied prototypes [26,27]. Some design adjustments were made also to explore the scalability of neurons layouts and to suppress screen-mediated interactions. In particular, the minimum linewidth of the strip was reduced from 10 to 4 μm thanks to a more advanced fabrication process implemented at

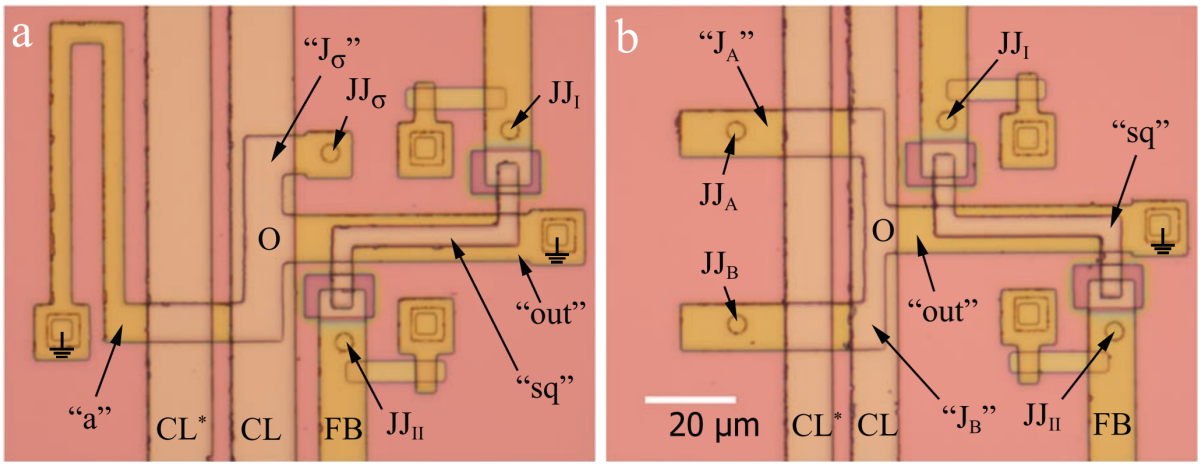


Figure 5: Microphotographs of investigated (a) sigma and (b) Gauss neurons. Figures show neuron's Josephson junctions $JJ_{A,B,\sigma}$; the read-out SQUID consisting of the loop "sq" and Josephson junctions $JJ_{I,II}$; control lines CL and FB; parts (arms) of neurons "$J_{A,B,\sigma}$", "a", "out"; and the central zone "O". Grounding symbols mark galvanic connections of the neuron to the superconducting ground plane. Boundaries of ground planes are located at large distances from the edges of the figures. CL* denotes an additional control line that was not used in the present experiment.

IREE RAS [44-46]. As a result, the area occupied by the sigma neuron was reduced by a factor of 4.4 (to 10,500 μm^2). Conversely, the area of the superconducting ground plane was increased by a factor of 5.3 (to 400,000 μm^2). Similar modifications were applied to the layout of the Gauss neuron sample described in [27]. Its size was reduced by a factor of 4.7 (to 8,050 μm^2), and its ground plane area was increased by a factor of 6.3 (to 400,000 μm^2). The neurons were placed in the center of the screen with their output arm, which has the same shape for sigma and Gauss neurons, aligned along the symmetry axis of the screen. Suppression of screen-mediated interaction was expected due to the inverse proportionality of the coupling to the transverse (relative to the control line) size of the screen [26].

Experimental TF and their analysis will be discussed in the Section Discussion. Here, we consider extraction of inductances necessary for TF analysis. To do this, a series of specific samples were made and studied, which are two-junction SQUIDS based on partial loops of the sigma neuron. Note that the loop of either neuron in Figure 5 consists of three arms ("J_σ", $L_{"a"}$, $L_{"out"}$ in Figure 5a and "J_A", "J_B", $L_{"out"}$ in Figure 5b) and has three connection points to the ground plane. To transform the neuron into a two-junction SQUID, one of the connections must be opened, while the other two should be closed via Josephson junctions. This can be done in three ways, while the fourth interferometer type is a readout SQUID coupled to a neuron in which all three arms are opened. Experimental and numerical studies of partial loops inductances provide values necessary for further substitution into theoretical formulas. Details of neurons decomposition and inductance calculations are given in Appendix B.

The fabrication process was the same as described above. All inductive arms of the neurons were formed in the M2 layer, while the control line and the loop of the readout SQUID lied mostly in the M3 layer. Thus, when studying the interaction of neuron arms with the control line, the inductive coupling was implemented like in the "narrow M2" test SQUIDs (Figure 2b). When measuring the mutual inductances of neuron arms to the readout SQUID, an inductive coupling type "wide M2 loop" was realized (Figure 2c). Experimental investigations were performed as described in Appendix A. Numerical simulations were carried out assuming a truncated superconducting screen with a gap between the structure and the screen edge of 50 μm. Thus, the screen size (225…170 μm × 243…177 μm) was larger compared to test C-shaped SQUIDs, which led to an increase in the main mesh step to ah = 2 μm and the edge step to ahb = 0.25 μm in order to meet the limitations on the amount of allocated RAM and execution time (see Section "Extraction Details"). Results are presented in Figure 6 as a dependence of calculated vs measured values, similar to Figure 3 and Figure 4. One can see that almost all experimental points fall within the 6% divergence angle for self- and mutual inductances for partial loops of both types of neurons.

A couple of points in Figure 6b can be found that are noticeably out of the 6% divergence angle (see "truncated" points in the lower inset on Figure 6b). However, there are several objective reasons for this. First, these experimental points are located in the vicinity of the origin, where the area determined by ±6% divergence angle is very small in absolute units. Second, these points correspond to the smallest inductances M_{sq} that describe the parasitic screen-mediated interaction between the control line and readout SQUID of experimental neurons. These points

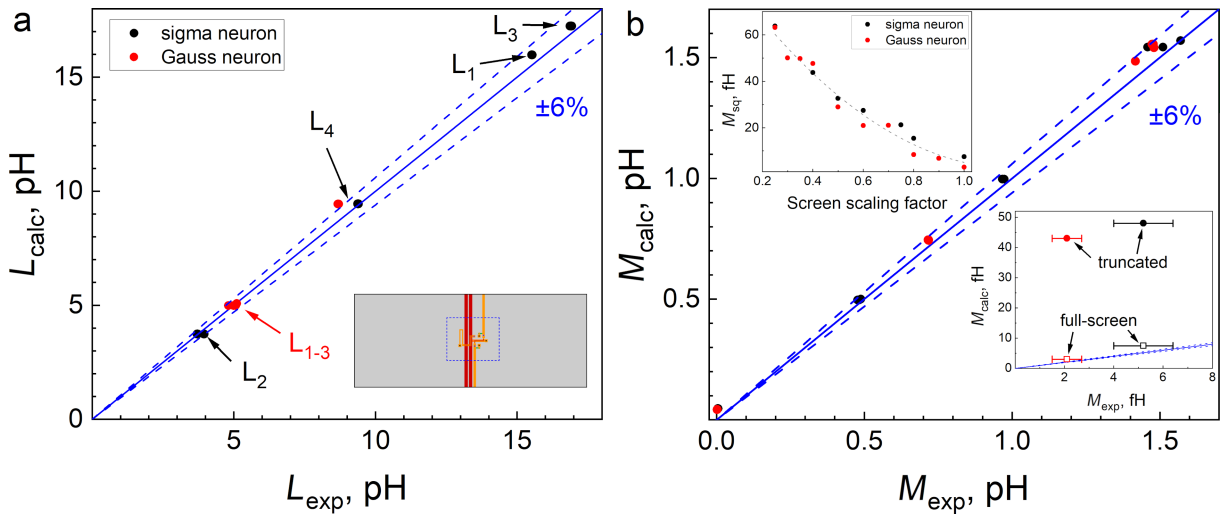


Figure 6: Comparison of calculated (L_{calc} and M_{calc}) and experimental (L_{exp} and M_{exp}) values of self- (a) and mutual (b) inductances of partial loops of sigma (black dots) and Gauss (red dots) neurons (see definitions in Appendix B). Solid blue lines represent $L_{calc} = L_{exp}$ and $M_{calc} = M_{exp}$, while dashed lines represent the ±6% divergence angle. The inset in panel (a) shows a sigma neuron placed on the full-size ground plane with blue dashed lines designating the boundary of the truncated ground plane used in simulation. The upper inset in panel (b) shows the dependence of M_{sq} on the truncated screen size (see details in the text). The lower inset shows the section of the diagram located near the origin. Filled and empty symbols corresponds to simulation on the truncated and full screen, respectively.

lie above the 6% divergence angle, indicating that actual M_{sq} values are substantially smaller than the calculated ones. This is explained by the high sensitivity of M_{sq} to the size of superconducting ground plane. In fact, the screen-mediated interaction is determined by the ring currents circulating in the screen to close the return current caused by the magnetic field of the control line. Obviously, the forced truncation of the ground plane in simulations (see lower inset in Figure 6a) can greatly affect the distribution of the ring currents. This is demonstrated in the upper inset on Figure 6b, which shows the dependence of the calculated parasitic inductance on the screen scaling factor (the ratio of the size in simulation to the real size, same for both lateral dimensions) at ah = 4 μm and ahb = 0.5 μm. As the scale factor increases, the result tends to values of about 3–7 fH, which agrees with the measured values by an order of magnitude. That is why "full-screen" points in the lower inset in Figure 6b lie much closer to the divergence angle.

The measured M_{sq} values, in turn, are 10–20 times less than estimated in [26,47]. This is probably due to the increase in the size of the superconducting screen, which was intended just to suppress screen-mediated interaction. Thus, at least one way to dump screen-mediated interaction exists, and this type of coupling is not an impassable barrier on the way to implementation of superconducting neurons. Increasing the neuron integration density in practical devices can be achieved by expanding the screen to cover the entire substrate area. In this case, the actual size of each neuron will be determined by the outer boundaries of its elements (arms). Potential challenges of this approach will be addressed in our future publications.

As was proposed in [47], another possible way to dump the screen-mediated interaction is the use of an additional control line CL* (see Figure 2 and Figure 5), which is located near the main control line CL and carries the same control current in the opposite direction. This allows for localization of the circulating currents between CL and CL*, diminishing their effect on other elements. However, this method could not be tested in the present work due to the high efficiency of the previous one. Indeed, the actual values of these inductances are extremely small (about 2–5 fH) and correspond to the limit of sensitivity of our experimental technique. Therefore, the relative error of such measurements is too high and any conclusion would not be reliable enough.

Extraction Details

The primary subject of this article is the detailed verification of 3D-MLSI software tool. The main task of this inductance extractor is an evaluation of two-terminal partial inductances [48] associated with equivalent scheme ones. The general mathematical model for all superconductor inductance calculations are Maxwell and London equations with proper excitation. Based on them, the inductance can be evaluated using the free energy functional. Therefore, the basic equations for 3D-MLSI are static London and Biot–Savart expressions for magnetic field $\vec{H} = \nabla \times \vec{A}$, vector potential $\vec{A}$, and full energy E. The only

free parameter here is the London penetration depth [5], which was taken as 85 nm according to manufacturer data.

Details of 3D-MLSI numerical technique can be found in [49,50]. An input data file, specified in text format, must contain the geometry of the device in the plane of the substrate, the parameters of the superconducting layers (thicknesses, relative positions, and London lengths) as well as commands related to the numerical process. This internal format is different from the conventional representation of design in the form of GDSII and DXF data. However, this data can be easily converted into 3D-MLSI format using, for example, the KLayout editor [51]. The input file should also specify current paths through terminals to enable calculation of the partial inductances. The supercurrent can be transmitted between layers using internal current sources as described in [49]. 3D-MLSI contains native support for currents around holes (moats) as well as evaluation of the related inductances. Several improvements have been made compared to the previous [49] version of the program. First, OpenMP multithreading was implemented for computationally heavy procedures. Second, easy support for non-planarized processes was developed ("nonplanar" option), where the height of a wire can vary in-plane (see Figure 1). Third, input data preparation was simplified, which allows to present conductors as polylines.

The distinctive feature of 3D-MLSI is an advanced finite element method (FEM), a numerical technique based on averaging the 3D current over the thin thickness of a superconductor film [49,50]. In contrast to InductEx and SuperVoxHenry, it leads to a set of 2D integro-differential equations instead of three-dimensional ones. As a result, 3D-MLSI can work without the large matrix procession techniques implemented, for example, in the SuperVoxHenry tool (e.g., fast-Fourier tensor acceleration, Tucker decompositions, fast multipoles method, and the AGMG-based sparse preconditioner for fast convergence). Instead of that, 3D-MLSI FEM brings the solution to the direct filling of two dense matrices of large size, that is, a matrix for interactions between mesh cells and a Galerkin matrix for solution of integro-differential equations. Filling the matrices needs $O(N^2)$ operations, and the solution procedure needs $O(N^3)$ operations, where N is the number of mesh nodes. These two operations basically define the total time and memory needed for calculations. In practice, the $O(N^2)$ part can be comparable with the $O(N^3)$ solution time for moderate N values. Advanced matrix compression methods can be implemented in future versions to be used for dense multilayered schemes of large sizes.

A good agreement with the experiment for all investigated structures was mainly achieved by the consideration of the in-plane coordinate dependence of the metal layer heights, which is implemented in the current version of the program as a "nonplanar" option. Figure 7 presents a comparison of experimental data with simulation results obtained with and without the "nonplanar" option enabled. The comparison was performed using the "narrow M2 loop" structure fabricated in the first run (see Figure 2b). One can see that the simulation results without the "nonplanar" option overestimate the experimental values by approximately 20%. In contrast, when the curvature of the M3 layer is taken into account, the experimental and calculated points show excellent agreement. Thus, accounting for the curvature of the metallic layers is an important condition for improving the extraction accuracy. This factor can only be neglected when the dielectric layers are planarized, as is done, for example, in the process described in [6].

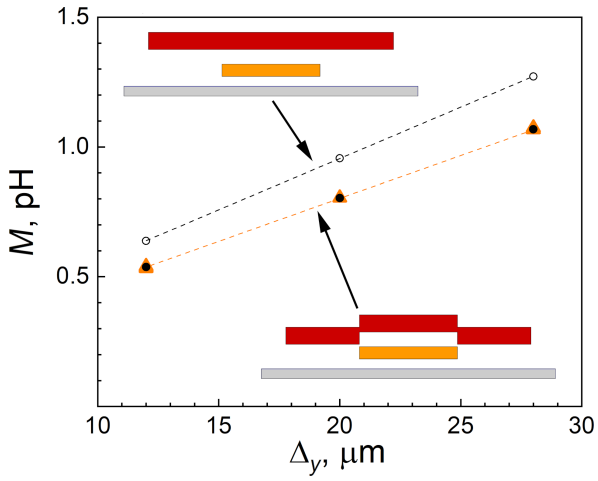


Figure 7: Mutual inductance dependence on the Δ_y variable part length for the test SQUID sample presented in Figure 2b. Orange triangles show experimental data, filled black dots correspond to calculations with non-planar cross section (lower inset), and empty black dots were calculated with planar cross section (upper inset).

One more important feature of the program is non-uniform meshing related to the Triangle meshing engine [52]. It allows for a reduction of allocated memory and solution time, and provides better accuracy as well. Calculations are performed on a highly graded mesh of triangular cells (see inset on Figure 8a) based on two mesh step parameters. The first parameter, *ah*, defines the size of triangular cells inside the superconducting film far enough from the nearest boundary. The other parameter, *ahb*, is related to the cell size in the vicinity of the boundary. This allows for more accurate modeling of regions of strong current density changes located just in the vicinity of strip line edges (see inset on Figure 8b). The choice of the upper grid scale value *ah* is defined mainly by the minimal strip line

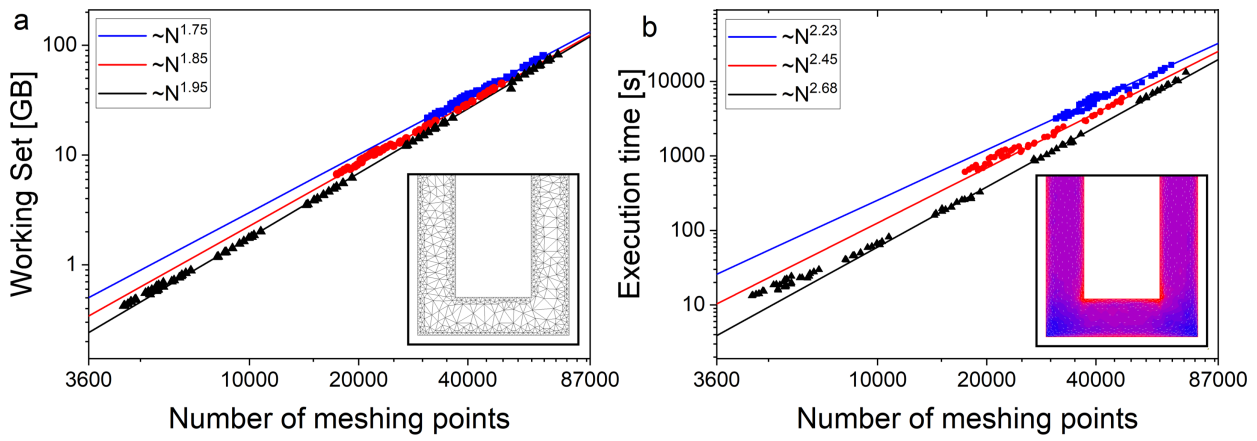


Figure 8: Dependence of (a) the allocated memory and (b) the execution time on the number of meshing points for a set of simulated structures (14 two-junction interferometers obtained by the decomposition of neurons as described in Appendix B). The change in the number of grid points is achieved by changing the step *ahb* at constant *ah*. Blue, red, and black dots correspond to *ah* values of *ah* = 1.5, 2.0, and 4.0 μm, respectively. Straight lines represent a power-law fit with exponent given in the legend. The inset in panel (b) shows an example of meshing produced by Triangle meshing engine. The inset in panel (a) shows the current distribution in the sigma neuron arm pivot area obtained in 3D-MLSI simulation. Red areas correspond to higher current density.

width according to manufacturer's design rules. So *ah* can hardly be chosen larger then 2 μm since the minimal width was 4 μm for all samples studied here.

In principle, the lower grid scale *ahb* < *ah* should be related to the London penetration depth λ = 85 nm for all superconducting layers. However, *ahb*, and *ah* as well, must not be too small since they define the amount of required memory via the number of mesh nodes. The working set of RAM used by the numerical core of 3D-MLSI depends on the number of meshing nodes in a power-law manner (see Figure 8a). The power of the dependence is slightly below two and depends on the grid step *ah*, which is related to the complexity of assembling the matrix $O(N^2)$. Thus, for the most accurate calculations performed on structures of the smallest size (C-shaped two-junction SQUIDs, Figure 2), the smallest steps *ah* = 1 μm and *ahb* = 0.125 μm (default parameters) were chosen. For certain interferometer designs, this allows for the extraction of self- and mutual inductances to be achieved with an accuracy of 1–2%, as shown in Figure 9. When modeling large SQUIDs based on partial loops of neurons, the values *ah* = 2 μm and *ahb* = 0.25 μm were mostly used. One can see that a relative accuracy within 5% can be achieved at *ahb* = *ah*/8 for *ah* ≤ 2 μm. A reasonable estimate can be obtained even for *ah* as large as 4 μm if *ahb* is substan-

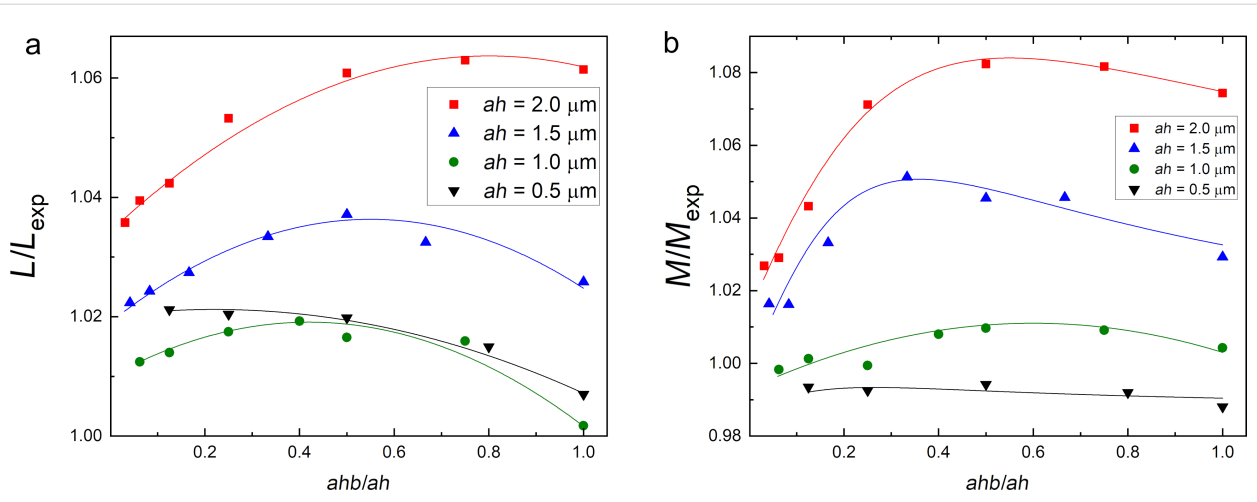


Figure 9: Dependence of calculated self- (a) and mutual (b) inductances of the test two-junction interferometer (see Figure 2b) on the edge discretization step *ahb* for several values of the general spatial discretization step *ah* (indicated in the Figure). Calculated values are normalized to the experimental ones.

tially small. In particular, for *ahb* = 125 nm the error did not exceed 15% of the experimental value.

An increase in the number of mesh nodes affects not only the required RAM volume but also the total computation time. Figure 8b shows that in single-threaded mode, the calculation time follows a power-law dependence on the number of mesh nodes with the power ranging from two to three, depending on the main discretizations step *ah*. The maximum number of mesh nodes reached approximately 65,000 at *ah* = 1.5 μm and *ahb* = 0.25 μm when simulating the third partial loop of the sigma neuron (see Appendix B for definition). The computation time in this case was about 7.5 h on an AMD Ryzen 9 5900X 12-core Processor with 128 GB RAM. In the current version of 3D-MLSI, the calculation time can be reduced using OpenMP multithreading. Figure 10 shows the results of calculations performed with different numbers of threads for the design of the second partial loop of the sigma neuron. To test multithreading on meshes with varying numbers of meshing points, the design was simulated with varying *ahb* at a fixed *ah* = 2 μm. Simulations were performed on an Intel Core(TM) i9-13900KF with 128 GB RAM and 24 cores (16 efficiency cores and 8 performance cores). When OpenMP multithreading is used, the computation time depends on the number of threads n_{thr} approximately with inverse square root law (see Figure 10a). The deviation from the expected n_{thr}^{-1} scaling indicates incomplete parallelization related seemingly to the use of the Cholesky decomposition method. With an increasing number of threads, the computed value slightly increases, within 1% for self-inductances and 2% for mutual inductances (see Figure 10b). Nevertheless, in this work, the multithreading option was not used in order to achieve maximum calculation accuracy.

The increase in the ground plane size, motivated by physical considerations, made it impossible to simulate the actual structures with optimal mesh steps (*ah* = 1 μm, *ahb* = 0.125 μm). Indeed, according to the data in Figure 8, the simulation of, for example, the sigma neuron would require a mesh consisting of more than 650,000 nodes, more than 53 days of computation time, and definitely more than 3.6 TB of RAM. Therefore, it was necessary to "trim" the screen for the purpose of simulation. The relevant parameter here is the gap (see Figure 2c) between the structure and the screen edge. Figure 11 shows the dependence of the simulated inductance of the test SQUID (see Figure 2b) on the gap parameter. The structure size was 64 μm × 26 μm; so the screen size varied from 74 μm × 36 μm to 264 μm × 226 μm. The obtained values of the self- and mutual inductance were normalized to the experimentally measured ones. It can be seen that for *gap* ≤ 50 μm, the deviation of the simulation results from the experimental values is only about 1–2% for *ah* = 1 μm and *ahb* = 0.125 μm. These parameters were used in Section "Results – C-shaped SQUIDs" for simulating test SQUIDs with a gap parameter of 10 μm. The maximum allowable gap (50 μm for the given *ah* and *ahb*) was determined by the available RAM (128 GB). Increasing *ah* to 2 μm and *ahb* to 0.25 μm makes it possible to increase the gap to 100 μm, though this results in a deviation of 4–6% from the experimental values. Full-screen calculations were performed only to evaluate screen-mediated coupling, which is very sensitive to the superconducting screen size. For this type of calcula-

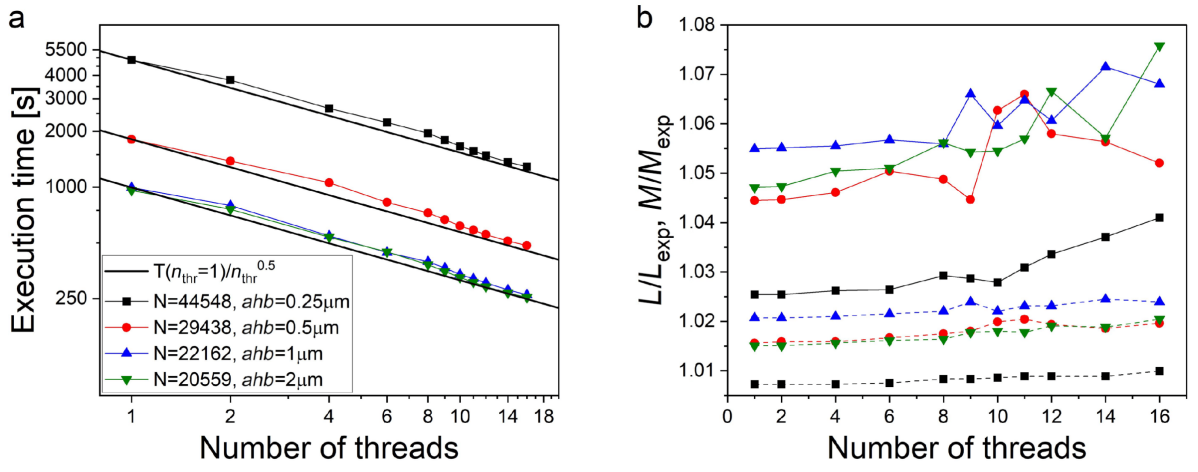


Figure 10: Results of OpenMP multithreading testing as applied to the simulation of the second partial loop of the sigma neuron (see Appendix B for definition). Step *ah* = 2 μm is fixed, while *ahb* varies, causing a change in the number of meshing points *N*. (a) Execution time-dependence on the number of threads at different edge discretization steps *ahb*. Solid lines represent the ratio of the program execution time in the single-threaded mode $T(n_{\text{thr}} = 1)$ to the square root of the number of threads $\sqrt{n_{\text{thr}}}$. Different symbols denote simulations with various mesh steps *ahb*. (b) Dependence of estimated mutual (solid connecting lines) and self- (dotted connecting lines) inductances on the number of threads used. Simulation results are normalized to the experimental value.

tions, a set of parameters *ah* = 4 μm and *ahb* = 0.5 μm was used, which provides a reasonable estimate, as was stated above.

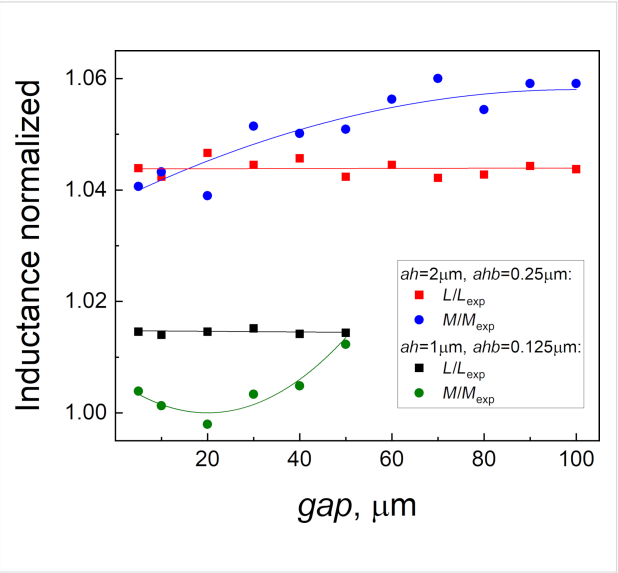


Figure 11: Dependence of self- and mutual inductances of the test SQUID (see Figure 2b) on the size of the superconducting screen in simulation. The horizontal axis corresponds to the distance from the outer boundaries of the structure to the truncated screen boundaries in simulation (see Figure 2c for definition).

Summarizing, 3D-MLSI evaluates two-terminal partial inductances of thin multilayer structures, with the only free parameter being the London penetration depth. A fairly good performance rate is achieved due to the use of a set of 2D integro-differential equations instead of three-dimensional ones and non-uniform meshing based on the "Triangle" meshing engine. A good accuracy of simulation was reached for the mesh with the cell size varying between 0.125 and 1 μm, as was set by parameters in the input file. We have shown that accounting for the layers' height in-plane coordinate dependence is an important condition for a good agreement with experiment. This was done using newly the added "nonplanar" option. One more helpful new feature is "nmthreads" option, which reduces calculations time using OpenMP multithreading. The limitation on the minimum mesh cell size is defined by the amount of memory ready to be allocated. To meet this limitation, a truncation of the superconducting screen can be made, which slightly affects simulated values of self- and mutual inductances, although it strongly modifies the screen-mediated coupling, as was described in Section "Results – Superconducting neurons".

Discussion

At present time, we continue the investigation of 3D-MLSI abilities, and new data (if any) will be published elsewhere. However, a good agreement between experiment and simulation can already be seen now. Therefore, it is interesting to consider the possibility of predicting the TF of a sigma neuron, the implementation of which is one final purpose of our studies. In [1], a simple parametric expression for the sigma neuron TF was obtained theoretically, which was further elaborated in [26] to account for the method of output signal measurement and for the interaction between input and readout elements. Taking all modifications into account, the theoretical formula takes the form:

$$I_{\mathrm{cl}} = k_1 I_{\mathrm{c}} \left(\varphi + k_2 \sin\varphi - \varepsilon\right), \tag{1}$$

$$I_{\mathrm{fb}} = k_3 \left(\left(k_4 + \Delta k_4\right) I_{\mathrm{cl}} - I_{\mathrm{c}} \sin\varphi + I_{\mathrm{c}}\zeta\right), \tag{2}$$

where I_{cl} is the control current (input signal), I_{fb} is the compensating ("feedback") current (i.e., output signal), I_{c} is the critical current, φ is the phase difference across the Josephson junction, and the coefficients k_i (as well as Δk_4) are expressed in terms of the self- and mutual inductances of the neuron arms. The "offset terms" ε and ζ depend on the initial flux in the readout element and do not affect the shape of the TF. That is why we used them as free parameters for fitting the experimental curve.

The experimental TF of the sigma neuron (and the Gauss neuron as well) was measured at T = 4.2 K using flux compensation technique described in [26] (see also Appendix A). This curve was fitted by the dependence in Equation 1 and Equation 2 with values k_i evaluated from the arms inductances. The necessary quantities were calculated using self- and mutual inductance values of the neurons' partial loops, both measured experimentally and extracted with the 3D-MLSI program (see Figure 6 for comparison and Appendix B for details on partial loops). We had to use Δk_4 as a free parameter since it depends on the indirect coupling value M_{sq}, which could not be reliably measured or calculated. Then, M_{sq} was calculated on the basis of the Δk_4 fit value with further comparison with the above results. One can see that experimental and numerical curves coincide rather well in Figure 12. The extracted value of M_{sq} was 10.5 fH, which is consistent with both experimental and numerical estimates obtained above. One more fitting parameter could be the critical current I_{c}, whose value cannot be measured directly and may, in principle, vary slightly from one junction to another. Nevertheless, a good agreement between calculated and experimental results was obtained using a value of 12 μA, which agrees with the experimentally measured one on a test SIS junction (see the upper inset in Figure 12). Thus, the high potential of the 3D-MLSI software for designing artificial superconducting neurons is clearly confirmed.

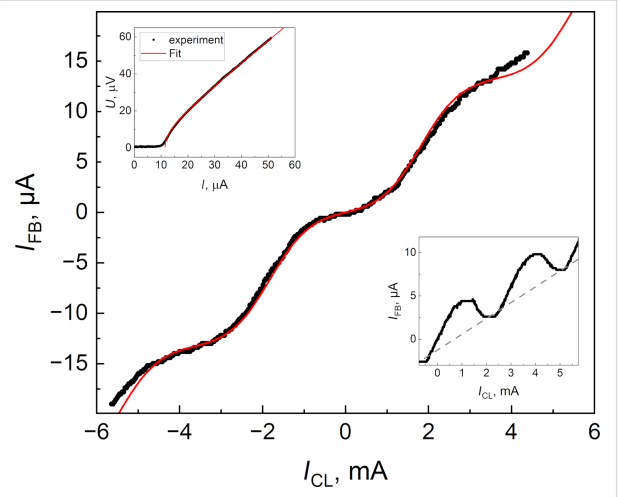


Figure 12: Comparison of the experimental (black dots) and the approximated (solid red curve) TFs of the sigma neuron (see Figure 5a). The upper left inset presents the measured voltage–current characteristic for a test SIS junction and RSJ fit with I_c = 12 μA critical current. In the bottom right inset, the measured TF (black dots) of the Gauss neuron (see Figure 5b) is given. The dotted line corresponds to the linear slope caused by the screen-mediated interaction between control and readout parts of the device.

The TF of the Gauss neuron was measured as well (see the lower inset in Figure 12); however, it cannot be fitted at the moment due to lack of theory accounting for interaction of all of the Gauss neuron parts. Some analysis can be made based on recently presented results [43]. Similarly to earlier experiments [27], the TF represents a bell-shaped curve based on a tilted line. The slope of the line is defined by a real or effective asymmetry of the input arms couplings $M_{\text{in}}^{\text{A,B}}$ to the incoming signal. The asymmetry can be characterized by the parameter $t = \left(M_{\text{in}}^{\text{A}} - M_{\text{in}}^{\text{B}}\right) \Big/ \left(M_{\text{in}}^{\text{A}} + M_{\text{in}}^{\text{B}}\right)$ and results in an unequal supply of the input flux in proportions $(1 \pm t)\Phi_{\text{in}}/2$ to the receiving arms $J_{\text{A,B}}$. As a consequence, a part of the input signal $t\Phi_{\text{in}}/2$ is mixed to the output one Φ_{out}, resulting in the undesired linear component of the TF. This type of asymmetry was noted in [47] when simulating the older sigma neuron design [26], despite identical shape of its receiving parts. Here, both experiment and simulation have shown the absence of coupling asymmetry ($M_{\text{in}}^{\text{A}} = M_{\text{in}}^{\text{B}}$, t = 0 within several percent uncertainty), seemingly, due to the increase in the screen size. Nevertheless, screen-mediated interaction between the input ("CL") and readout ("sq") elements can give the same effect, with an effective asymmetry parameter [43]

$$t_{\text{eff}} = \frac{2L_{\text{out}}M_{\text{sq}}}{M_{\text{out}}M_{\text{in}}}.$$

Based on experimental measurements ($L_{\text{out}} \approx 2.40$ pH, $M_{\text{sq}} \approx 2$ fH, $M_{\text{out}} \approx 1.47$ pH, $M_{\text{in}} \approx 1.43$ pH), we estimate $t_{\text{eff}} \approx 0.005$. Using calculated values ($L_{\text{out}} \approx 2.45$ pH, $M_{\text{sq}} \approx 3$ fH, $M_{\text{out}} \approx 1.55$ pH, $M_{\text{in}} \approx 1.48$ pH), the estimate gives $t_{\text{eff}} \approx 0.006$. Despite the small value of t, the effective asymmetry significantly distorts the TF, likely because of the really small amplitude of the output signal. Therefore, the presented design of the Gauss neuron require further improvement. By now, an increase in sensitivity to the input signal and in efficiency of the output flux transfer, as well as a suppression of parasitic coupling, seems to be the most promising strategy. The potential of 3D-MLSI software demonstrated in this work will be useful in this process.

Conclusion

Capabilities of the 3D-MLSI software tool were thoroughly tested for several designs of practical multilayer superconducting structures. Advantages of the numerical methods, non-uniform triangular meshing, non-planarized superconducting layers support, and OpenMP multithreading were demonstrated aimed at the enhancement of accuracy and performance. An agreement as good as ±6% of the experimental values was demonstrated for the set of two-junction Josephson interferometers, including partial loops of superconducting sigma and Gauss neurons. The experimental TF of a sigma neuron was successfully fitted on the basis of calculated inductances, which reveals the high potential of the 3D-MLSI software tool for the design of superconducting neurons as well as superconducting electronics devices in general.

Appendix A

To measure inductance and coupling of a two-junction SQUID loop, we connect the latter to a current source "B" for biasing and a voltmeter "V" for voltage measurement in a four-point scheme (see Figure 13a). The source "B" supplies a current slightly above the critical one, causing the SQUID to operate in the resistive state. To vary the magnetic flux through the SQUID loop, current sources "C" or "F" are used. When the control current is applied using these sources, the SQUID voltage changes periodically with a period corresponding to one flux quantum. The value of self- or mutual inductance is determined as the ratio of the magnetic flux quantum Φ_0 to the period of the experimental curve. The type of obtained value depends on the circuit configuration used for the control current source (either "C" or "F"). When using the "C" source, the control current passes through the control line "CL", which is inductively coupled to the SQUID loop. This way, the mutual inductance M between the SQUID loop and the control line "CL" is determined. When using the source "F", the control current flows via the feedback line connected to the SQUID loop. In this case, the period is determined by the loop inductance L. This method is widely used for measuring of self- and mutual inductance of superconducting strip lines [53,54].

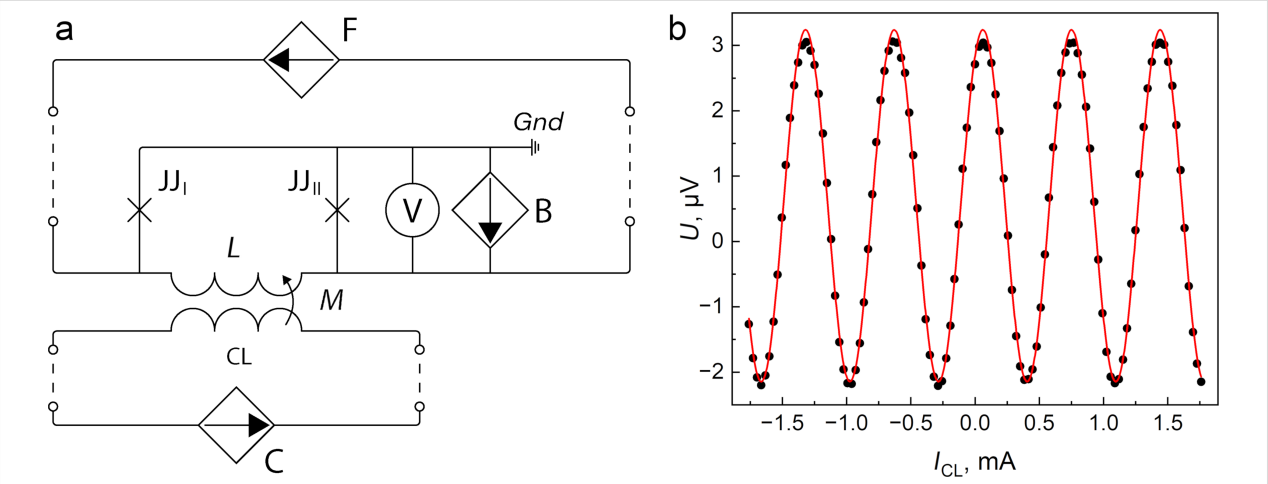


Figure 13: a) A principal scheme of inductance measurements. “B”, “C”, and “F” are current sources. Crosses indicate Josephson junctions JJ_I and JJ_{II}, which are included in the loop of the two-junction SQUID. *L* stands for the SQUID loop inductance, and *M* is its mutual inductance with the control line CL. b) Typical voltage–flux curve of the investigated SQUIDs. The red curve shows the approximation by a sinusoidal dependence carried out to determine the period.

It can be noted that the connection of the “B” source to the SQUID is asymmetric in Figure 13a, which can lead to asymmetry in the voltage–flux curve. This does not affect inductance measurements since the period of the voltage–flux curve corresponds to one quantum of applied magnetic flux as determined by a sinusoidal current–phase relationship assumed for tunnel-type junctions. Moreover, the experimental curves were quite symmetrical (see Figure 13b), which allowed for sinusoidal approximation and period determination with an accuracy of the order of 1%. Difficulties could only arise when measuring mutual inductances less than 10 fH, for which it was not possible to record even a single period of the voltage–flux curve due to some limitations related to the large control current (e.g., sample overheating, null voltage drift, and vortex motion). Such weak coupling occurs for distant conductors interacting via the superconducting screen (in particular, the “CL” and “sq” elements in Figure 5). In the case of ultrasmall inductances, measurements were performed using a magnetic flux compensation method with a feedback algorithm [26]. In this method, both sources from the circuit in Figure 13a are used: The “C” source sweeps the control signal, while the “F” current is varied to maintain a constant voltage across the SQUID with an accuracy of 0.1–0.3 μV. A similar method was used for the measurements of TFs of neuron samples [26,27].

Appendix B

To measure an inductance of the arms of, to be specific, a sigma neuron, the latter should be transformed into a two-junction SQUID coupled to some kind of a control line. Note that the loop of the sigma neuron (consisting of "J_σ", $L_{\text{"a"}}$, and $L_{\text{"out"}}$ arms in Figure 5a and Figure 14a) is, in fact, connected to the ground plane in three points. To transform the neuron into a two-junction SQUID, one of the connections must be opened, while the other two should be closed via Josephson junctions. This can be done in three ways (see Figure 14b–Figure 14d), resulting in the following partial loops of the sigma neuron: (1) the input loop consisting of elements “J_σ” and “a” (Figure 14b), (2) the Josephson loop consisting of elements “J_σ” and “out” (Figure 14c), and (3) the inductive loop consisting of elements “out” and “a” (Figure 14d). The fourth interferometer type is a readout SQUID coupled to a neuron in which all three arms are opened (Figure 14e).

A series of specific samples were made, which are two-junction SQUIDS based on partial loops of the sigma neuron. Then, self- and mutual inductances were measured as described in Appendix A. Additionally, the same structures were simulated using the 3D-MLSI software. While measuring the coupling $M_i^{(\text{sq})}$ to the readout SQUID loop, the element “sq” (see Figure 5) was used as a control line with its Josephson junctions removed (see Figure 14f for example). As a result, a set of values, L_k, $M_k^{(\text{CL})}$, and $M_k^{(\text{sq})}$ (k = 1…4), was obtained. These values are shown in Figure 6. Next, one can express the inductances of the arms as:

$$L = \frac{1}{2}\left(L_1 + L_2 - L_3\right), \tag{3}$$

$$L_{\text{a}} = \frac{1}{2}\left(L_1 + L_3 - L_2\right), \tag{4}$$

$$L_{\text{out}} = \frac{1}{2}\left(L_2 + L_3 - L_1\right). \tag{5}$$

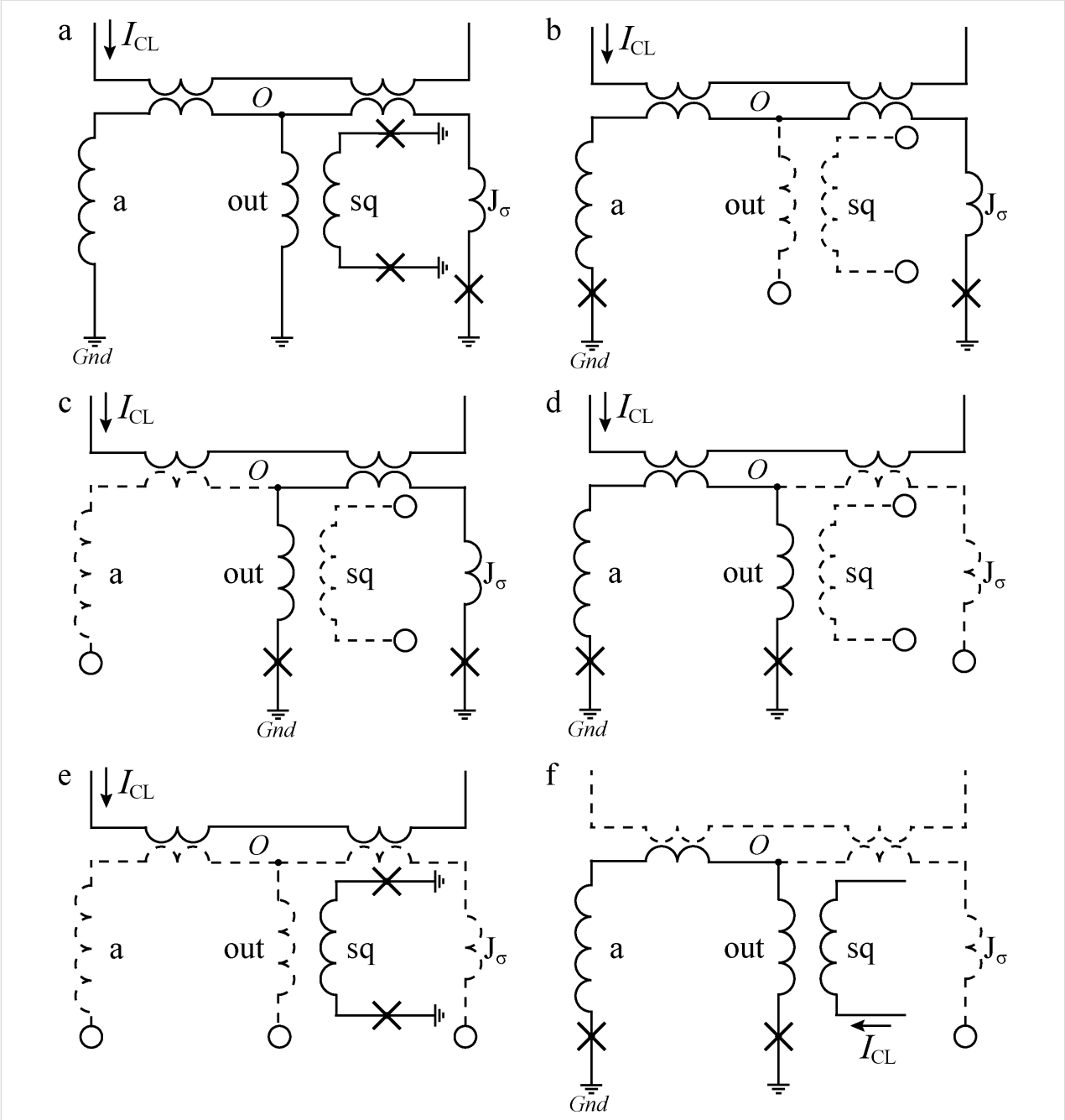


Figure 14: Schematic representation of a sigma neuron and examples of its partial loops (see details in text). JJs are marked with crosses, and the wavy lines stand for inductances. Circles indicate the nodes where the circuit is open, and the corresponding arms are drawn with dashed lines, as well as the elements “CL” and “sq” in case they are not used.

The designations in Equations 3–5 and further correspond to those introduced in [26] to fit the experimental TF. The input mutual inductance,

$$M_{\text{in}} = M_1^{(\text{CL})} = M_2^{(\text{CL})} + M_3^{(\text{CL})}, \tag{6}$$

and the output one,

$$M_{\text{out}} = M_2^{(\text{sq})} = M_3^{(\text{sq})}, \tag{7}$$

were measured directly. Additionally, couplings of each receiving arm (i.e., J_σ and a) to the control line were determined as:

$$M_{\mathrm{J}} = M_2^{(\mathrm{CL})},\ M_{\mathrm{a}} = M_3^{(\mathrm{CL})}. \tag{8}$$

The screen-mediated coupling of the "CL" and "sq" elements can be defined as $M_{\mathrm{sq}} = M_4^{(\mathrm{CL})}$. The values defined above allow for a thorough comparison with simulation as well as approximation of the experimental TF shape with a single fit parameter instead of four.

Decomposition of a Gauss neuron (see microphotograph in Figure 5b and the schematic in Figure 15a) yields the same loops upon a change in the designations of elements "J_σ" and "a" to "J_A" and "J_B", respectively (see Figure 14b and Figure 15b for comparison). For the purposes of Section "Discussion", the definitions $M_{\mathrm{in}}^{\mathrm{A}} = M_1^{(\mathrm{CL})}$ and $M_{\mathrm{in}}^{\mathrm{B}} = M_2^{(\mathrm{CL})}$ are to be introduced in accordance with [43], which denote coupling of receiving arms to the control line. The total coupling of the Gauss neuron to the control line is $M_{\mathrm{in}} = M_{\mathrm{in}}^{\mathrm{B}} + M_{\mathrm{in}}^{\mathrm{B}}$, which was valid within 1% accuracy (also for the sigma neuron).

Funding

Experimental research and numerical simulations were performed at ISSP RAS within Russian Science Foundation grant no. 23-72-00053. The samples were fabricated using the large-scale research facilities "Cryointegral" (no. 352529) at V. A. Kotelnikov Institute of Radio Engineering and Electronics of the Russian Academy of Sciences.

OpenMP multithreading performance tests (see Figure 10) were carried out by M. M. Khapaev under his research program at the Computational Mathematics and Cybernetics Faculty of Lomonosov Moscow State University. The effect of meshing parameters on simulation results (see Figure 9) was investigated by the Moscow Institute of Physics and Technology (MIPT) students within their research practice. The dependence of simulated inductances on ground plane size (see Figure 11) was studied by E. N. Zhardetsky (HSE University) as a part of a student internship. The dependencies presented in Figure 8 were obtained within the collaboration of I. E. Tarasova and A. S. Ionin with Russian Quantum Center.

ORCID® iDs

Irina E. Tarasova - https://orcid.org/0009-0000-8380-2233
Nikita S. Shuravin - https://orcid.org/0009-0004-2612-0366
Liubov N. Karelina - https://orcid.org/0000-0003-4981-6599
Fedor A. Razorenov - https://orcid.org/0009-0008-2681-5722
Evgeny N. Zhardetsky - https://orcid.org/0009-0006-9538-0625
Aleksandr S. Ionin - https://orcid.org/0009-0004-0249-1234
Mikhail M. Khapaev - https://orcid.org/0000-0003-0701-7043
Vitaly V. Bol'ginov - https://orcid.org/0000-0002-6948-7975

Data Availability Statement

Data generated and analyzed during this study is available from the corresponding author upon reasonable request.

References

1. Soloviev, I. I.; Schegolev, A. E.; Klenov, N. V.; Bakurskiy, S. V.; Kupriyanov, M. Y.; Tereshonok, M. V.; Shadrin, A. V.; Stolyarov, V. S.; Golubov, A. A. *J. Appl. Phys.* **2018,** *124,* 152113. doi:10.1063/1.5042147
2. Popescu, M.-C.; Balas, V. E.; Perescu-Popescu, L.; Mastorakis, N. *WSEAS Trans. Circuits Syst.* **2009,** *8,* 579–588.
3. Orr, M. J. L. Introduction to radial basis function networks. Centre for Cognitive Science, University of Edinburgh: Edinburgh, Scotland, 1996; https://faculty.cc.gatech.edu/~isbell/tutorials/rbf-intro.pdf (accessed Feb 7, 2025).
4. Chang, W. H. *J. Appl. Phys.* **1979,** *50,* 8129–8134. doi:10.1063/1.325953
5. Schmidt, V. *The Physics of Superconductors: Introduction to Fundamentals and Applications;* Springer-Verlag: Berlin and Heidelberg, 1997.

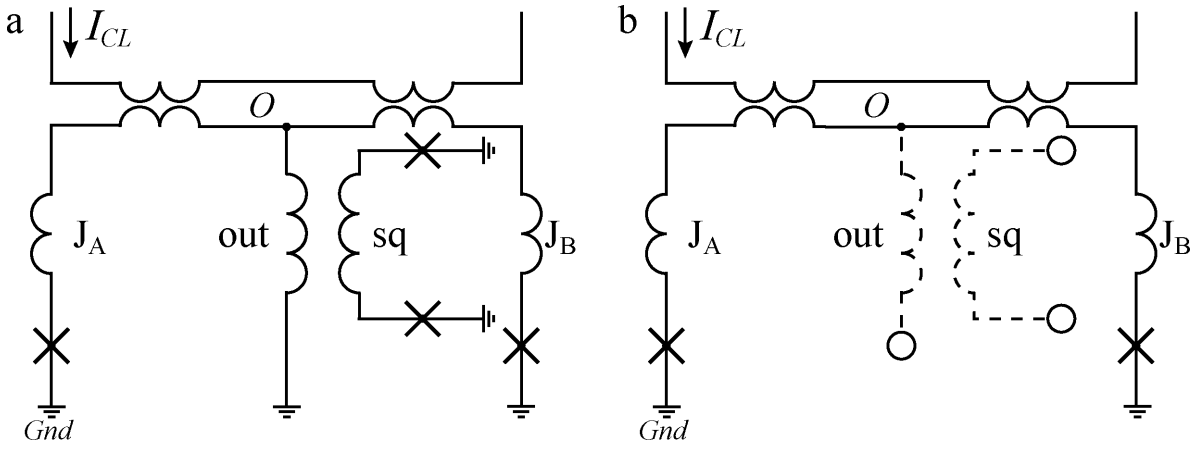


Figure 15: Schematic representation of a Gauss neuron (a) and one of its partial loops (b) (see details in text).

6. Tolpygo, S. K.; Golden, E. B.; Weir, T. J.; Bolkhovsky, V. *IEEE Trans. Appl. Supercond.* **2022,** *32,* 1–31. doi:10.1109/tasc.2022.3162758
7. Bunyk, P. I.; Rylov, S. V. Automated calculation of mutual inductance matrices of multilayer superconductor integrated circuits. Proc. Ext. Abstracts 4th Int. Supercond. Electron. Conf. (ISEC'93); 1993; p 62.
8. Khapaev, M. M., Jr. *Supercond. Sci. Technol.* **1996,** *9,* 729–733. doi:10.1088/0953-2048/9/9/002
9. Fourie, C. J.; Perold, W. J. *IEEE Trans. Appl. Supercond.* **2005,** *15,* 300–303. doi:10.1109/tasc.2005.849806
10. Kamon, M.; Tsuk, M. J.; White, J. K. *IEEE Trans. Microwave Theory Tech.* **1994,** *42,* 1750–1758. doi:10.1109/22.310584
11. Khapaev, M. M.; Kidiyarova-Shevchenko, A. Yu.; Magnelind, P.; Kupriyanov, M. Yu. *IEEE Trans. Appl. Supercond.* **2001,** *11,* 1090–1093. doi:10.1109/77.919537
12. Yucel, A. C.; Georgakis, I. P.; Polimeridis, A. G.; Bağcı, H.; White, J. K. *IEEE Trans. Microwave Theory Tech.* **2018,** *66,* 1723–1735. doi:10.1109/tmtt.2017.2785842
13. Wang, M.; Qian, C.; Di Lorenzo, E.; Gomez, L. J.; Okhmatovski, V.; Yucel, A. C. *IEEE Trans. Appl. Supercond.* **2021,** *31,* 1–11. doi:10.1109/tasc.2021.3105715
14. Krylov, G.; Kawa, J.; Friedman, E. G. *IEEE Nanotechnol. Mag.* **2021,** *15,* 54–67. doi:10.1109/mnano.2021.3113218
15. Vaisband, I. P.; Jakushokas, R.; Popovich, M.; Mezhiba, A. V.; Köse, S.; Friedman, E. G. *On-Chip Power Delivery and Management;* Springer International Publishing: Cham, Switzerland, 2016. doi:10.1007/978-3-319-29395-0
16. Ansys HFSS. 3D Electromagnetic Field Simulator for RF and Wireless Design. https://www.ansys.com/products/electronics/ansys-hfss (accessed Sept 25, 2025).
17. Rautio, J. C.; Harrington, R. F. *IEEE Trans. Microwave Theory Tech.* **1987,** *35,* 726–730. doi:10.1109/tmtt.1987.1133738
18. Toepfer, H.; Uhlmann, H. F. *Phys. C (Amsterdam, Neth.)* **1999,** *326-327,* 53–62. doi:10.1016/s0921-4534(99)00409-8
19. Xiao, P. M.; Charbon, E.; Sangiovanni-Vincentelli, A.; Van Duzer, T.; Whiteley, S. R. *IEEE Trans. Appl. Supercond.* **1993,** *3,* 2629–2632. doi:10.1109/77.233517
20. Teh, C. K.; Kitagawa, M.; Okabe, Y. *Supercond. Sci. Technol.* **1999,** *12,* 921–924. doi:10.1088/0953-2048/12/11/368
21. Du, Z.; Whiteley, S. R.; Van Duzer, T. *Appl. Supercond.* **1999,** *6,* 519–523. doi:10.1016/s0964-1807(99)00006-x
22. Fourie, C. J. *IEEE Trans. Appl. Supercond.* **2018,** *28,* 1300412. doi:10.1109/tasc.2018.2797253
23. Fourie, C. J.; Wetzstein, O.; Kunert, J.; Toepfer, H.; Meyer, H.-G. *Supercond. Sci. Technol.* **2013,** *26,* 015016. doi:10.1088/0953-2048/26/1/015016
24. Fourie, C. J.; Wetzstein, O.; Ortlepp, T.; Kunert, J. *Supercond. Sci. Technol.* **2011,** *24,* 125015. doi:10.1088/0953-2048/24/12/125015
25. Khapaev, M. M.; Kupriyanov, M. Y.; Goldobin, E.; Siegel, M. *Supercond. Sci. Technol.* **2003,** *16,* 24–27. doi:10.1088/0953-2048/16/1/305
26. Ionin, A. S.; Shuravin, N. S.; Karelina, L. N.; Rossolenko, A. N.; Sidel'nikov, M. S.; Egorov, S. V.; Chichkov, V. I.; Chichkov, M. V.; Zhdanova, M. V.; Shchegolev, A. E.; Bol'ginov, V. V. *J. Exp. Theor. Phys.* **2023,** *137,* 888–898. doi:10.1134/s1063776123120191
27. Ionin, A. S.; Karelina, L. N.; Shuravin, N. S.; Sidel'nikov, M. S.; Razorenov, F. A.; Egorov, S. V.; Bol'ginov, V. V. *JETP Lett.* **2023,** *118,* 766–772. doi:10.1134/s002136402360324x
28. Dmitiriev, P. N.; Ermakov, A. B.; Kovalenko, A. G.; Koshelets, V. P.; Iosad, N. N.; Golubov, A. A.; Kupriyanov, M. Y. *IEEE Trans. Appl. Supercond.* **1999,** *9,* 3970–3973. doi:10.1109/77.783897
29. Kaplunenko, V. K.; Khabipov, M. I.; Koshelets, V. P.; Likharev, K. K.; Mukhanov, O. A.; Semenov, V. K.; Serpuchenko, I. L.; Vystavkin, A. N. *IEEE Trans. Magn.* **1989,** *25,* 861–864. doi:10.1109/20.92422
30. Rapid Single Flux Quantum (RSFQ) – Design Rules for Nb/Al2O3-Al/Nb-Process at Leibniz IPHT. https://www.fluxonics.org/foundry/#process (accessed Feb 7, 2025).
31. Schegolev, A. E.; Klenov, N. V.; Soloviev, I. I.; Tereshonok, M. V. *Beilstein J. Nanotechnol.* **2016,** *7,* 1397–1403. doi:10.3762/bjnano.7.130
32. Likharev, K. *IEEE Trans. Magn.* **1977,** *13,* 242–244. doi:10.1109/tmag.1977.1059351
33. Shuravin, N. S.; Karelina, L. N.; Ionin, A. S.; Razorenov, F. A.; Sidel'nikov, M. S.; Egorov, S. V.; Bol'ginov, V. V. *JETP Lett.* **2024,** *120,* 829–836. doi:10.1134/s0021364024603427
34. Goto, E. Josephson pair elements. In *Proc. 1st RIKEN Symp. Josephson Electronics,* 1984; pp 48–51.
35. Goto, E.; Loe, K. F. *Dc Flux Parametron: A New Approach To Josephson Junction Logic;* World Scientific, 1986; Vol. 6.
36. Hosoya, M.; Hioe, W.; Casas, J.; Kamikawai, R.; Harada, Y.; Wada, Y.; Nakane, H.; Suda, R.; Goto, E. *IEEE Trans. Appl. Supercond.* **1991,** *1,* 77–89. doi:10.1109/77.84613
37. Likharev, K.; Rylov, S.; Semenov, V. *IEEE Trans. Magn.* **1985,** *21,* 947–950. doi:10.1109/tmag.1985.1063673
38. Takeuchi, N.; Ozawa, D.; Yamanashi, Y.; Yoshikawa, N. *Supercond. Sci. Technol.* **2013,** *26,* 035010. doi:10.1088/0953-2048/26/3/035010
39. Klenov, N. V.; Schegolev, A. E.; Soloviev, I. I.; Bakurskiy, S. V.; Tereshonok, M. V. *IEEE Trans. Appl. Supercond.* **2018,** *28,* 1301006. doi:10.1109/tasc.2018.2836903
40. Schegolev, A.; Klenov, N.; Soloviev, I.; Tereshonok, M. *Supercond. Sci. Technol.* **2021,** *34,* 015006. doi:10.1088/1361-6668/abc569
41. Schegolev, A. E.; Klenov, N. V.; Soloviev, I. I.; Gudkov, A. L.; Tereshonok, M. V. *Nanobiotechnol. Rep.* **2021,** *16,* 811–820. doi:10.1134/s2635167621060227
42. Schegolev, A. E.; Klenov, N. V.; Bakurskiy, S. V.; Soloviev, I. I.; Kupriyanov, M. Y.; Tereshonok, M. V.; Sidorenko, A. S. *Beilstein J. Nanotechnol.* **2022,** *13,* 444–454. doi:10.3762/bjnano.13.37
43. Razorenov, F. A.; Ionin, A. S.; Shuravin, N. S.; Karelina, L. N.; Sidel'nikov, M. S.; Egorov, S. V.; Bol'ginov, V. V. *Beilstein J. Nanotechnol.* **2025,** *16,* 1160–1170. doi:10.3762/bjnano.16.85
44. V. A. Kotelnikov Institute of Radioengineering and Electronics Russian Academy of Sciences, Laboratory of Superconducting Devices for Signal Detection and Processing. Technological and measuring research facilities for the creating of superconducting nanosystems based on new materials. https://nanolith.ru/unu.html (accessed Sept 16, 2025).
45. V. A. Kotelnikov Institute of Radioengineering and Electronics Russian Academy of Sciences, Laboratory of Superconducting Devices for Signal Detection and Processing. Methodology of manufacturing multilayer integrated superconducting microcircuits. 2007; https://nanolith.ru/methods.html (accessed Sept 16, 2025).

46. V. A. Kotelnikov Institute of Radioengineering and Electronics Russian Academy of Sciences, Laboratory of Superconducting Devices for Signal Detection and Processing. Methodology of manufacturing single-barrier tunnel junctions Superconductor-Isolator-Superconductor. 2007; https://nanolith.ru/methods.html (accessed Sept 16, 2025).
47. Ionin, A. S.; Egorov, S. V.; Sidelnikov, M. S.; Karelina, L. N.; Shuravin, N. S.; Khapaev, M. M.; Bol'ginov, V. V. *Phys. Solid State* **2024,** *66,* 987–993.
48. Paul, C. R. *Inductance: Loop and Partial;* John Wiley & Sons, Inc., 2010. doi:10.1002/9780470561232
49. Khapaev, M. M.; Kupriyanov, M. Y. *Supercond. Sci. Technol.* **2015,** *28,* 055013. doi:10.1088/0953-2048/28/5/055013
50. Bakurskiy, S. V.; Klenov, N. V.; Kupriyanov, M. Y.; Soloviev, I. I.; Khapaev, M. M. *Comput. Math. Math. Phys.* **2021,** *61,* 854–863. doi:10.1134/s096554252105002x
51. Koerner, M. KLayout Layout Viewer and Editor. https://www.klayout.de/ (accessed July 29, 2025).
52. Shewchuk, J. R. Triangle: Engineering a 2D Quality Mesh Generator and Delaunay Triangulator. In *Applied Computational Geometry: Towards Geometric Engineering;* Lin, M. C.; Manocha, D., Eds.; Lecture Notes in Computer Science, Vol. 1148; Springer-Verlag: Berlin, Heidelberg, 1996; pp 203–222. doi:10.1007/bfb0014497 From the First ACM Workshop on Applied Computational Geometry.
53. Fulton, T. A.; Dunkleberger, L. N.; Dynes, R. C. *Phys. Rev. B* **1972,** *6,* 855–875. doi:10.1103/physrevb.6.855
54. Henkels, W. H. *Appl. Phys. Lett.* **1978,** *32,* 829–831. doi:10.1063/1.89940

License and Terms

This is an open access article licensed under the terms of the Beilstein-Institut Open Access License Agreement (https://www.beilstein-journals.org/bjnano/terms), which is identical to the Creative Commons Attribution 4.0 International License (https://creativecommons.org/licenses/by/4.0). The reuse of material under this license requires that the author(s), source and license are credited. Third-party material in this article could be subject to other licenses (typically indicated in the credit line), and in this case, users are required to obtain permission from the license holder to reuse the material.

The definitive version of this article is the electronic one which can be found at:
https://doi.org/10.3762/bjnano.17.8

BEILSTEIN JOURNAL OF NANOTECHNOLOGY

Fast vortex dynamics and relaxation times in NbRe-based heterostructures

Francesco De Chiara[1], Zahra Makhdoumi Kakhaki[1,2], Francesco Avitabile[1], Francesco Colangelo[1,3], Abhishek Kumar[1,3], Carmine Attanasio[1,3,4] and Carla Cirillo[*3]

Full Research Paper

Open Access

Address:
[1]Dipartimento di Fisica “E. R. Caianiello”, Università degli Studi di Salerno, I-84084 Fisciano (Sa), Italy, [2]Institute for Electrical Measurement Science and Fundamental Electrical Engineering, Technische Universität Braunschweig, D-38106 Braunschweig, Germany, [3]CNR-SPIN, c/o Università degli Studi di Salerno, I-84084 Fisciano (Sa), Italy and [4]Centro NANO_MATES, c/o Università degli Studi di Salerno, I-84084 Fisciano, Salerno, Italy

Email:
Carla Cirillo[*] - carla.cirillo@spin.cnr.it

* Corresponding author

Keywords:
flux-flow instability; quasiparticle relaxation time; superconducting heterostructures; superconductivity; vortex dynamics

Beilstein J. Nanotechnol. **2026,** *17,* 292–302.
https://doi.org/10.3762/bjnano.17.20

Received: 25 November 2025
Accepted: 09 January 2026
Published: 12 February 2026

This article is part of the thematic issue "Superconducting artificial neural networks and quantum circuits".

Guest Editor: A. S. Sidorenko

© 2026 De Chiara et al.; licensee Beilstein-Institut.
License and terms: see end of document.

Abstract

An in-depth analysis of Abrikosov vortex dynamics and flux-flow instabilities was performed in NbRe/Au and NbRe/Py bilayers to compare superconducting/normal metal (S/N) and superconducting/ferromagnetic (S/F) heterostructures based on the same superconducting layer. The heterostructures, fabricated by sputtering, were characterized through electrical transport measurements. The *I*–*V* characteristics show that, in the NbRe/Py bilayer, vortices reach higher critical velocities than those observed in the NbRe/Au structure. The analysis of the flux-flow instability within the Larkin–Ovchinnikov framework allows one to extract the quasiparticle energy relaxation time. For external magnetic field values for which edge barrier pinning is dominant and thermal effects are negligible, the relaxation times are about 150 ps and 24 ps for NbRe/Au and NbRe/Py bilayers, respectively. These results indicate that NbRe/Py bilayers, having a relaxation time one order of magnitude smaller than values reported in NbRe microbridges, have great potential for the realization of devices where fast relaxation processes are required.

Introduction

Vortex dynamics plays a central role in the electrical transport under magnetic fields in type-II superconductors and is an essential subject of research in superconductivity [1]. In inhomogeneous type-II superconductors, structural defects create pinning centers that trap vortices. As a result, a finite current density is required to initiate vortex motion. When the value of the external current density, j_{ex}, applied to the superconductor exceeds the value of the critical current density, j_c, vortices

begin to move, giving rise to a viscous flow regime known as flux flow, which is associated with energy dissipation [2]. As the current increases further, $j_{ex} \gg j_c$, and as the vortex velocity approaches a maximum critical value, this regime may become unstable. A sudden voltage jump is observed in the *I*–*V* characteristic, attributed to the collapse of superconducting coherence. This phenomenon, known as flux-flow instability (FFI), depends on several factors such as structural disorder and defects [3], pinning mechanisms [4,5], thermal effects [6], and sample geometry [7]. FFI is effectively described by the Larkin–Ovchinnikov (LO) model [8], which relates the onset of the instability to the maximum value of vortex velocity, v^*, and the quasiparticle relaxation time, τ_E. The latter characterizes how efficiently quasiparticles (unpaired electrons) return to their equilibrium state from a non-equilibrium one [9]. τ_E represents a key parameter for the optimization of superconducting quantum technologies, including superconducting detectors [10-12], superconducting qubits [13,14], and superconducting nano- and microstrips used in high-speed electronics [15], as well as for the development of hybrid architectures enabling magnon–fluxon interactions [16]. The enhancement of vortex dynamics and the reduction of τ_E are strongly linked to the optimization of quasiparticle relaxation mechanisms. Excited quasiparticles can relax primarily through two processes, namely thermal electron–phonon (e–ph) interaction and electron–electron (e–e) recombination [1]. In classical, low-T_c superconductors, the dominant relaxation channel is provided by e–ph scattering events [17], while in high-T_c superconductors the situation is reversed, with e–e recombination playing a major role in energy relaxation [18]. The efficiency of these processes and the value of τ_E strongly depend on the microscopic properties of the superconductor and on the degree of electronic disorder [1]. In this context, NbRe has emerged as a promising material that exhibits exceptionally fast vortex dynamics [19]. Extensive structural characterizations performed by X-ray diffraction have shown that NbRe thin films are polycrystalline with oriented grains of nanometric size, of the order of a few nanometers [20,21]. Furthermore, earlier investigations have demonstrated that the superconducting and transport properties of NbRe are robust against moderate thickness variations [19]. These characteristics, together with disorder-dominated transport, favor very short temperature-independent quasiparticle relaxation times of the order of hundreds of picoseconds [22] making NbRe-based films particularly attractive for studying non-equilibrium effects and for the realization of fast superconducting devices [23-25].

To modify quasiparticles relaxation mechanism, one of the most promising strategies involves engineering hybrid heterostructures in which the superconducting layer (S) is brought into contact with a normal metal (N) or a ferromagnetic layer (F). Several studies have shown that, in S/N [26-30] or S/F [31-34] systems, different mechanisms can influence the vortex dynamics depending on the thickness and conductivity of the capping layer. In particular, a sufficiently thick metallic overlayer may lead to a damping of vortex motion due to eddy currents induced by the time-dependent magnetic flux, resulting in a magnetic breaking effect [29,30]. In the opposite limit of thin capping layers, the proximity effect plays a dominant role leading to an enhancement of the critical vortex velocity and promoting faster relaxation processes [26-28].

In this work, we systematically investigate vortex dynamics and flux-flow instability phenomena in micrometer-wide bilayers in which NbRe is brought into contact with either thin N or F materials. In particular, we measure transport properties in the presence of a magnetic field in NbRe/Au and NbRe/Py microstrips. Experimental data show that the two materials modify the vortex dynamics of NbRe differently, with Py allowing for larger v^* as a function of the magnetic field. Furthermore, the calculation of the quasiparticle energy relaxation times reveals faster relaxation times in NbRe/Py than in NbRe/Au. This result demonstrates the larger effectiveness of ferromagnetic materials in further promoting the energy relaxation process.

Larkin and Ovchinnikov Theory

As pointed out by Larkin and Ovchinnikov [8], FFI originates from the finite energy relaxation time of quasiparticles, which causes significant variations in the quasiparticle distribution function, $f(E)$. During vortex motion, quasiparticles inside the vortex core are accelerated by the electric field associated with flux flow and undergo successive Andreev reflections at the core boundaries [35]. As their energy approaches the temperature-dependent superconducting gap, $\Delta(T)$, quasiparticles diffuse into the surrounding superconducting region, reducing the number of excitations within the core. This process results in a shrinkage of the vortex followed by a decrease of the viscous drag force, f_{vd}, and an increase in the vortex velocity v [9]. When v exceeds the critical value v^*, the Lorentz force dominates the viscous drag force, leading to instabilities in vortex motion. The dependence of v^* on T is given by:

$$v^* = \frac{D^{1/2}\left[14\zeta(3)\right]^{1/4}}{\left(\pi\tau_E\right)^{1/2}}\left(1-\frac{T}{T_c}\right)^{1/4}, \qquad (1)$$

where T_c is the superconducting critical temperature, D is the quasiparticles diffusion coefficient, and $\zeta(x)$ is the Riemann zeta function. The critical velocity is inversely proportional to the square root of the inelastic scattering time τ_E, and it is indepen-

dent on the external magnetic field. This result follows from the core assumption of the LO theory, namely that $f(E)$ is spatially uniform within the superconductor. Consequently, while the vortex core contracts, its shape preserves axial symmetry. Furthermore, the flux-flow instability nucleates simultaneously throughout the superconductor, leading to a field-independent critical velocity v^* at which the instability is established [1]. It is worth emphasizing that, since the nucleation of the flux-flow instability is strongly influenced by the quality of the sample edges, the estimation of an intrinsic quasiparticle relaxation time from Equation 1 is justified only when the field dependence of the critical current evidences a dominant edge-barrier pinning mechanism. In this regime, the assumptions underlying the LO model remain valid and the deduced relaxation time can be regarded as an intrinsic property of the superconducting system [1].

Experimentally, biasing a superconducting strip with a current I, leads, in the flux flow regime, to the appearance of a jump to normal state at an instability current I^*, which corresponds to the instability voltage V^*. I^* is usually smaller than the depairing current, I_d, and, therefore, sets the actual limit for the use of superconductors in applications [1]. When the Larkin–Ovchinnikov instability develops from a well-established flux-flow regime, characterized by a homogeneous vortex motion, the instability voltage allows one to quantify the critical vortex velocity using the relation $v^* = V^*/(\mu_0 HL)$ [5,9] and then, using Equation 1, to calculate the relaxation time τ_E and estimate the lifetimes of electronic excitations in superconductors.

S/N and S/F bilayer

One way to enhance the critical vortex velocity and reduce the relaxation time is to use multilayer superconducting heterostructures [28,33]. It was experimentally observed that thin superconducting strips coated by a lowly resistive normal metal present stronger non-linear properties and higher vortex velocity than a single superconducting strip [27]. This result may be attributed to proximity-induced superconductivity in the normal layer. At the interface, superconductivity is induced into the normal metal over the coherence length

$$\xi_N = \sqrt{\hbar D_N / 2\pi k_B T}, \tag{2}$$

where $D_N = v_F l/3$ [36] is the electron diffusion coefficient in the normal layer with v_F the Fermi velocity and l the electron mean free path. For typical Fermi velocities [36] and low-temperature mean free paths measured in normal metals, ξ_N lies in the range of tens to hundreds of nanometers. According to Belzig et al. [37], the superconducting correlation in N produces a minigap at the Fermi energy, smaller than the superconducting gap of S and related to the thickness of the N layer, d_N, by the relation

$$\Delta^N_{mini} \sim \Delta_S \left(\xi_N / d_N\right)^2, \tag{3}$$

where Δ_S is the superconducting gap of the S layer. Since in the S/N bilayers $\xi_N \leq d_N$, quasiparticles will be more easily removed from the vortex core, and due to their lower energy, they will relax faster. This implies smaller τ_E and higher critical velocity.

Based on these considerations, it is expected that coupling the superconductor with a ferromagnetic material should lead to a further increase in critical velocity, as experimentally observed [31-34]. In S/F bilayers, although no minigap is formed in the ferromagnetic layer, superconducting correlations can penetrate into F, but over much shorter distances compared to a normal metal. In the dirty limit, the characteristic coherence length ξ_F can be written as [38]

$$\xi_F = \sqrt{\hbar D_F / E_{ex}}, \tag{4}$$

where D_F and E_{ex} are the electron diffusion coefficient and the ferromagnet exchange energy, respectively. Since, at low temperatures, E_{ex} (≈0.01–1 eV) largely exceeds the thermal energy, $k_B T$, ξ_F is typically of the order of 1–5 nm [33]. As a result, in contrast to the much longer decay observed in S/N systems, superconducting properties in S/F bilayers are confined to just a few nanometers in the ferromagnetic layer where the overall superconducting properties are very much suppressed. Consequently, S/F hybrids are expected to exhibit reduced quasiparticle relaxation times and enhanced critical velocities compared to S/N bilayers.

Finally, in addition to the spectral argument, general considerations related to increased scattering rates should also be considered. In S/N and S/F systems, additional scattering channels become available for quasiparticles both in the proximized superconducting layer and in the adjacent region where superconducting correlations are induced. In particular, Ryan and Chandrasekhar [26] have shown that a thin disordered normal layer enhances the inelastic scattering rate, leading to a significant reduction of the effective relaxation time without degrading superconductivity. This finding supports the idea that both spectral and kinetic proximity effects cooperate in promoting faster quasiparticle relaxation in hybrid systems.

Experimental

Bilayers were deposited by DC magnetron sputtering in an ultrahigh vacuum system at room temperature from $Nb_{0.18}Re_{0.82}$ (NbRe), Au, and $Ni_{0.80}Fe_{0.20}$ (permalloy, Py) targets on SiO_2 substrates. The base pressure was $P = 2.2 \times 10^{-8}$ mbar, and the Ar pressure during the deposition was $P_{Ar}^{NbRe} = 6.6$ μbar, $P_{Ar}^{Au} = 12$ μbar and $P_{Ar}^{Py} = 6.3$ μbar. During the deposition, the film thickness was monitored in situ by a thickness monitor, which provides a real-time measurement of the growth rate. The deposition rates were later calibrated ex situ using a Bruker Dektak XT stylus profilometer by measuring step heights in samples. In the NbRe/Au sample, the NbRe layer has a thickness $d_{NbRe}^{NbRe/Au} = 20$ nm, while $d_{NbRe}^{NbRe/Py} = 15$ nm in the NbRe/Py sample. The corresponding Au and Py layers are $d_{Au} = 5$ nm and $d_{Py} = 4$ nm. Given the ultrathin thickness of the metallic overlayers, electromagnetic damping effects due to eddy currents are expected to be strongly reduced, placing the present samples in the thin-layer regime where proximity-induced effects are dominant [29,30]. The samples were patterned into a four-probe geometry by optical lithography using a direct laser writer exposure followed by an ion-etching procedure. This technique results in microstrips with straight edges, ensuring a uniform width, w, of the device [39]. The geometrical values of the microstrips are reported in Table 1. Electrical contacts were realized using an ultrasonic wire bonder, ensuring a highly reproducible and comparable contact quality for both NbRe/Au and NbRe/Py microbridges. The electrical transport measurements were performed using a cryogen-free measurement system from Cryogenic Ltd. The samples were mounted in the measurement system with the surface perpendicular to the applied field. Resistive transition measurements were performed using a DC bias current $I_b = 10$ μA. For all samples, the critical temperature was defined as the temperature at which the resistance drops to 50% of the normal-state value measured at $T = 10$ K (R^{10K}). Finally, I–V characteristics were measured as a function of the applied magnetic field at the reduced temperature $t = T/T_c \approx 0.5$ for both samples. The curves were obtained by applying rectangular current pulses with a pulse width of 20 μs and a waiting time of 2 s.

Results and Discussion

Superconducting characterization

The normalized resistive transitions, R/R^{10K}, of the two microbridges are reported in Figure 1a. The critical temperatures are $T_c^{NbRe/Au} = 6.8$ K and $T_c^{NbRe/Py} = 5.6$ K. The obtained values are smaller than those reported for NbRe thin films of similar thickness [19,22], with a stronger reduction observed in the NbRe/Py bilayer, where the superconductivity is more suppressed by the proximity to the F layer. Notably, the magnitude of the T_c suppression observed in the NbRe/Py bilayer is comparable to that reported for NbRe/CuNi hybrid structures ($T_c^{NbRe/CuNi} = 5.86$ K) reported in [22], supporting the conclusion that proximity to a ferromagnetic layer leads to a stronger suppression of superconductivity than in S/N bilayers. From R^{10K}, the low-temperature resistivities of the two strips have been calculated, yielding $\rho_{10K}^{NbRe/Au} = 52$ μΩ·cm and $\rho_{10K}^{NbRe/Py} = 124$ μΩ·cm. The significant difference in resistivity observed between the two bilayers cannot be ascribed to the different thicknesses of the NbRe layers since NbRe films of the same thickness exhibit nearly identical superconducting critical temperatures (around 7 K, $\Delta T_c \approx 0.1$ K) and low-temperature resistivities, of the order of $\rho = 140$ μΩ·cm [19]. In contrast, the capping layers are characterized by significantly different electrical resistivities, with Au being an excellent electrical conductor even at small thicknesses and Py films showing high resistivity in the ultrathin film regime [40,41]. To calculate the London penetration depth at $T = 0$ K, the formula $\lambda(0) = 1.05 \times 10^{-3}\sqrt{\rho_{10K}/T_c}$ [42] was used, resulting in $\lambda^{NbRe/Au}(0) = 288$ nm and $\lambda^{NbRe/Py}(0) = 494$ nm. The upper critical field, $\mu_0 H_{c2}$, as a function of temperature was obtained from $R(H)$ measurements, and the corresponding experimental data are presented in Figure 1b. Assuming for $\mu_0 H_{c2}(T)$ a linear dependence, it follows that the upper critical fields at $T = 0$ K of the two microbridges are $\mu_0 H_{c2}^{NbRe/Au}(0) = 8.30$ T and

Table 1: Values of some characteristic parameters of the NbRe/Au, NbRe/Py, and NbRe [19,22] microstrips. The thickness (in nm) of each layer is specified in parentheses. L is the distance between the voltage contacts, and w is the width of the microstrips. T_c is the critical temperature at 50% of the transition, ρ_{10K} is the resistivity in the normal state at $T = 10$ K, $\lambda(0)$ and $\xi(0)$ are, respectively, the London penetration length and the coherence length at zero temperature, and D is the quasiparticles diffusion coefficient.

Parameters	NbRe(20)/Au(5)	NbRe(15)/Py(4)	NbRe(60) [19]	NbRe(15) [22]
L (μm)	80.0 ± 0.1	80.0 ± 0.1	1000	100
w (μm)	10.0 ± 0.1	6.3 ± 0.1	100	10
T_c (K)	6.8 ± 0.1	5.6 ± 0.1	7.3	6.7
ρ_{10K} (μΩ·cm)	52 ± 5	124 ± 12	148	143
$\lambda(0)$ (nm)	288 ± 14	494 ± 24	472	483
$\xi(0)$ (nm)	6.3 ± 0.3	6.2 ± 0.3	4.80	—
D (×10^{-4} m^2/s)	0.90 ± 0.06	0.70 ± 0.06	0.56	0.5

$\mu_0 H_{c2}^{NbRe/Py}(0)$ = 8.70 T. From these values, the coherence length, ξ, at T = 0 K can be determined using the formula $\xi(0) = [\Phi_0/2\pi\mu_0 H_{c2}(0)]^{1/2}$ yielding $\xi^{NbRe/Au}(0)$ = 6.3 nm and $\xi^{NbRe/Py}(0)$ = 6.2 nm. The quasiparticle diffusion coefficient D is evaluated from the slope of the $\mu_0 H_{c2}(T)$ curve, since $D = (4k_B/\pi e)(\mu_0 dH_{c2}/dT|_{T=T_c})$. The quasiparticle diffusion coefficients are $D^{NbRe/Au} = 0.9 \times 10^{-4}$ m^2/s and $D^{NbRe/Py} = 0.7 \times 10^{-4}$ m^2/s. Table 1 summarizes the superconducting characteristics of the two microstrips. It is worth noting that the formulas employed were derived for single-layer superconducting films, whereas, in the present study, the microbridges are bilayer structures. As a result, the calculated parameters do not fully account for proximity-induced modifications of the electronic properties.

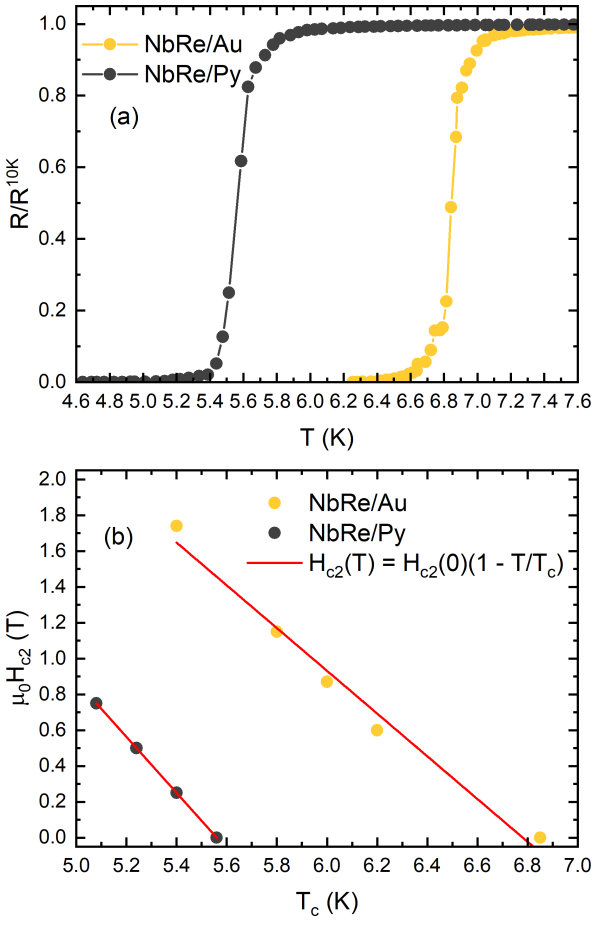


Figure 1: (a) Normalized resistive transitions and (b) $\mu_0 H_{c2}(T)$ for the NbRe/Au and NbRe/Py bilayers. The red lines represent the linear fit to the data.

Current–voltage characteristics and critical currents

Figure 2 shows the I–V characteristics measured for the NbRe/Au and NbRe/Py microbridges at the reduced temperature $t = T/T_c \approx 0.5$ as a function of the external magnetic field. The curves exhibit a zero-voltage regime at small bias currents where vortices remain pinned. It is clearly shown in the insets of Figure 2 that, as the current further increases, a nonlinear conductivity regime appears until I^* is reached. When the magnetic field increases, the critical voltage at which the jump occurs also increases, while the values of I^* decrease. The I–V curves allow one to determine the so-called saturation magnetic field, H_{SAT}, that is, the field beyond which the jumps disappear and the transition to the normal state occurs smoothly. The values are $H_{SAT}^{NbRe/Au}$ = 0.9 T and $H_{SAT}^{NbRe/Py}$ = 1.2 T.

To gain insight into the pinning mechanism at play, the behavior of the critical current density $J_c = I_c/wd$ as a function of the external magnetic field was analyzed as reported in [39,43]. The critical current values were measured based on a voltage criterion V_c = 20 μV, corresponding to $E_c = V_c/L$ = 0.25 V/m. Figure 3a and Figure 3b show the $J_c(H)$ curves on a double-logarithmic scale for NbRe/Au and NbRe/Py bilayers at $t \approx 0.5$, respectively. For sufficiently low values of the magnetic field, the experimental data follow the linear dependence $J_c^{lin}(B) = J_c(B = 0)(1 - B/B_s)$ (see red lines). The magnetic field B_s determines the point at which vortices overcome the edge barrier and enter the material, and it is expressed by the equation $B_s = \Phi_0\sqrt{1 + w/(\pi\Lambda)}/\sqrt{3}\pi\xi w$ [43], where $\Lambda = 2\lambda^2/d$ is the Pearl penetration length. The theoretical values of B_s are $B_{s_{th}}^{NbRe/Au}$ = 5.3 mT and $B_{s_{th}}^{NbRe/Py}$ = 7.4 mT. The linear fits to the data were carried out fixing the value of J_c at $\mu_0 H = 0$ T to the experimental values $J_c^{NbRe/Au}(0) = 2.64 \times 10^9$ A/m^2 and $J_c^{NbRe/Py}(0) = 8.7 \times 10^9$ A/m^2. The fits yield B_s equal to $B_{s_{exp}}^{NbRe/Au} \approx 60$ mT and $B_{s_{exp}}^{NbRe/Py} \approx 11$ mT for the two microbridges, respectively. Given the physical meaning of B_s, the discrepancy between the experimental and theoretical values indicates that vortices overcome the edge barrier and penetrate the material only at magnetic fields larger than theoretically predicted. This enhancement of B_s can be understood by considering that the theoretical expression accounts for the suppression of the edge barrier, whereas the experimental B_s extracted from $J_c(B)$ reflects the onset of vortex penetration into the bulk, which, in the presence of bulk pinning, may require magnetic fields larger than the barrier-suppression one [44,45]. Moreover, the theoretical estimate of B_s relies on parameters such as Λ and ξ, evaluated using expressions derived for single-layer superconducting films. Since our samples are bilayer heterostructures, proximity-induced modifications of the superconducting properties are not fully taken into account, introducing an additional uncertainty in the theoretical value of B_s. Considering edge quality, according to Plourde et al. [46], imperfections or geometric irregularities along the edges of the strip lower the effective entry field for vortices. The larger experimental B_s measured for the NbRe/Au microbridge thus points to a more efficient edge

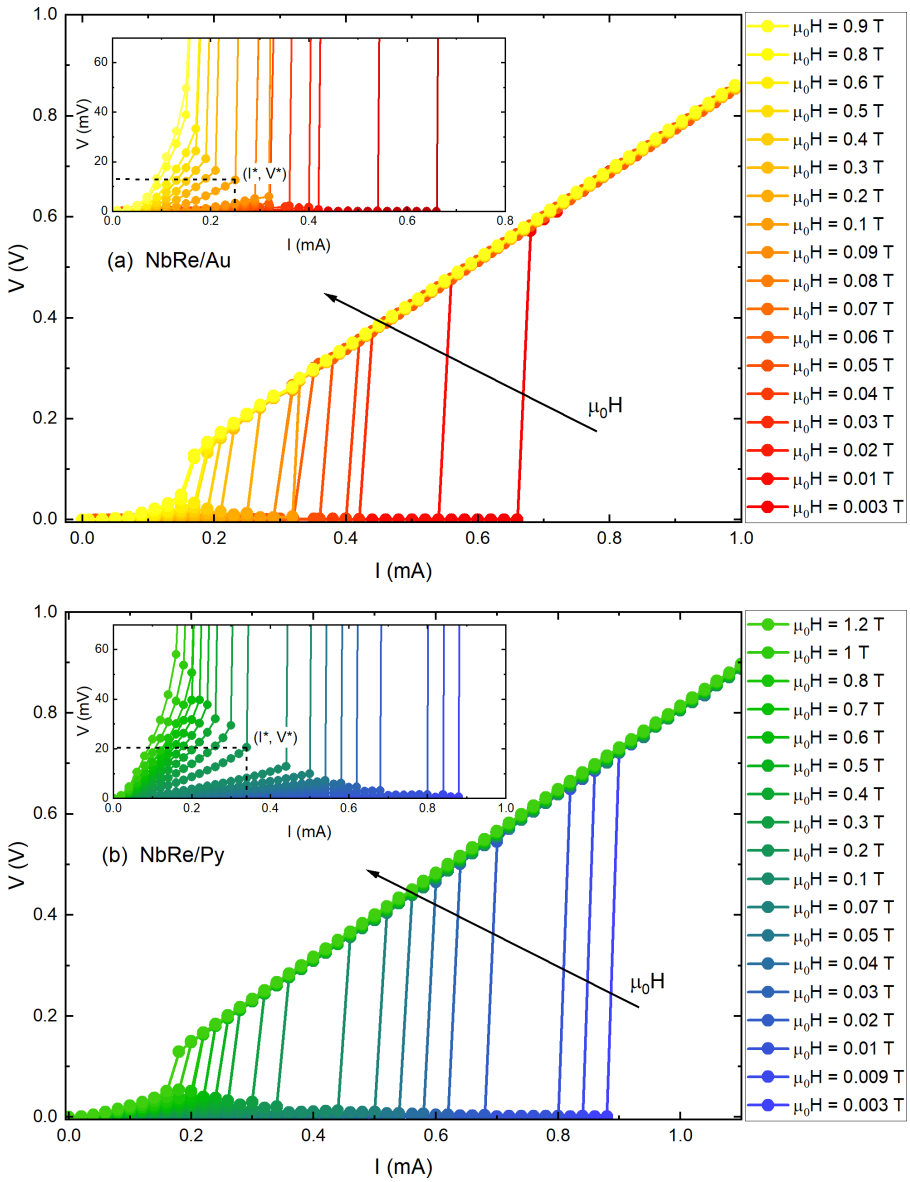


Figure 2: *I*–*V* curves of (a) NbRe/Au and (b) NbRe/Py bilayers at $t \approx 0.5$ in different magnetic fields from 3 mT to the respective magnetic saturation field, H_{SAT}. Insets: enlarged plot in the low-voltage region to show the nonlinear conductivity regime. The coordinates I^* and V^* denote the values of the instability current and voltage, respectively.

barrier with respect to the case of NbRe/Py bilayer where the value of B_s is smaller. The latter also exhibits a higher J_c compared to NbRe/Au, indicating a stronger vortex pinning force in this range. Furthermore, the results of NbRe/Py show a steeper slope than NbRe/Au. This could be related to a larger suppression and spatial inhomogeneity of the superconducting order parameter induced by the Py layer, which further decreases the value of the critical current density at low fields [34]. For magnetic fields between the experimentally obtained values of B_s and 0.1 T, $J_c(B)$ is well described by the dependence $J_c^{edge}(B) \propto B_s/(4B)$, indicating the dominant role of the edge barrier pinning for vortex entry into the samples in this regime [43] (see cyan lines). Last, at higher magnetic fields, a gradual transition toward the dependence $J_c(B) \sim B^{-0.5}$ is expected due to the onset of intrinsic volume pinning. For this reason, the experimental data were fitted to the equation $J_c^{vol}(B) = A_0 B^{-m}$ leaving m as a free parameter (see magenta lines). For the two samples, the fit yields $m_{NbRe/Au} = 1.12$ and $m_{NbRe/Py} = 0.75$, indicating a stronger attenuation of the critical current density at high fields than expected. This suggests a weaker volume pinning effect compared to the theoretical result for both microbridges. These results demonstrate that edge-barrier pinning dominates over volume pinning in both samples, despite their large strip widths.

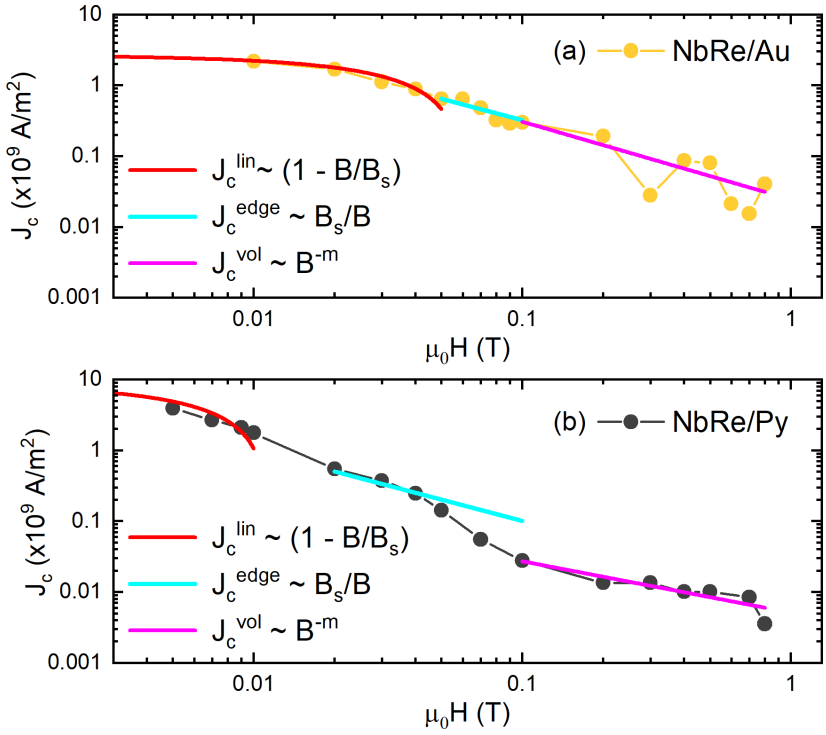


Figure 3: Magnetic field dependence for the critical current density at $t \approx 0.5$ of NbRe/Au (a) and NbRe/Py (b). The red curves represent the dependence $J_c^{lin} \sim (1 - B/B_s)$, the cyan curves the dependence $J_c^{edge}(B) \sim B_s/B$, and the magenta curves the dependence $J_c^{vol} \sim B^{-m}$.

Thermal effects

Before starting the analysis of flux-flow instability at the critical velocity, it is crucial to rule out the possibility that the sudden transition to the normal state is due to Joule heating. To do this, according to Bezuglyj and Shklovskij (BS) theory [6], we analyzed the behavior of the critical power $P^* = I^*V^*$ as a function of the external magnetic field via the equation $P^* = P_0(1 - a)$, where $a = (1 + b + \sqrt{b^2 + 8b + 4}) / (3(1 + 2b))$ with $b = H/H_T$. In the BS theory, $B_T = \mu_0 H_T$ is a thermal field and represents the magnetic field value beyond which thermal effects become dominant in the vortex instability dynamics. Figure 4 shows the behavior of the critical power as a function of $\mu_0 H$ for the two microbridges. In both cases, the fits (red solid lines) provide a good approximation of the experimental data. For NbRe/Au, the fit yields a thermal field $\mu_0 H_T^{NbRe/Au} = 1$ T, which is larger than the corresponding saturation magnetic field values $\mu_0 H_{SAT} = 0.9$ T. This ensures that, for the NbRe/Au bilayer, thermal effects do not play a significant role in the flux-flow instability phenomenon. In contrast, for the NbRe/Py bilayer, the thermal field is $\mu_0 H_T^{NbRe/Py} = 0.1$ T, which is much smaller than its saturation field $\mu_0 H_{SAT} = 1.2$ T. This indicates that, for magnetic fields larger than 0.1 T, the NbRe/Py microbridge is affected by thermal effects and that the vortex instability dynamics is influenced by thermal dissipation mechanisms. The different impact of thermal effects observed in the two microbridges can be traced back to material-dependent and intrinsic geometrical factors. The thermal dissipation affecting the flux-flow instability is dominated by processes occurring within the superconducting microstrip itself, namely vortex motion and flux-flow dissipation, which are strongly influenced by the nature of the capping layer. In addition, the

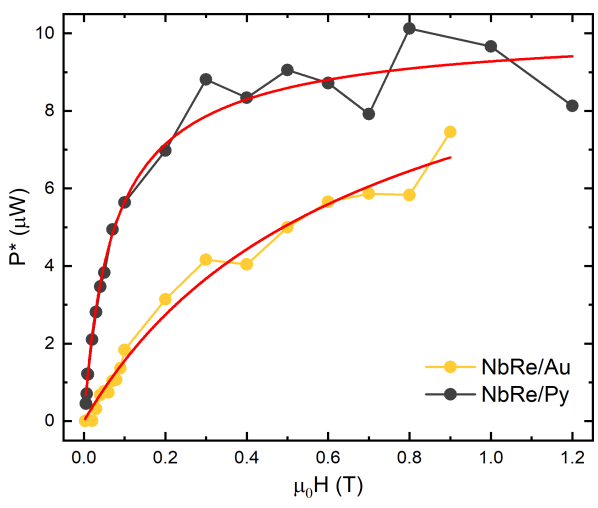


Figure 4: Dissipated power at the instability point as a function of the magnetic field at $t \approx 0.5$ for NbRe/Au and NbRe/Py bilayers. The red solid lines are the fit to the data according to the BS theory [6].

reduced strip width of the NbRe/Py microbridge leads to a less efficient heat evacuation toward the substrate, thereby enhancing the role of Joule heating and amplifying the impact of thermal dissipation on vortex dynamics. For this reason, and since, according to the LO theory, τ_E can be reliably estimated only when $J_c(H)$ reflects a dominant edge-barrier pinning mechanism (i.e., in this case, in the interval [Bs; 0.1 T] for both bridges), the critical vortex velocity and the corresponding quasiparticle relaxation time will be reported and compared at $\mu_0 H = 0.1$ T.

Vortex critical velocity and quasiparticles relaxation time

The dependence of v^* as a function of the magnetic field is reported for both the NbRe/Au and the NbRe/Py bridges at $t \approx 0.5$ in Figure 5. The figure clearly shows that the critical velocity values measured for the NbRe/Py are larger than those obtained for the NbRe/Au microstrip. The critical velocity increases with H up to approximately 0.1 T for the NbRe/Au sample and up to 0.01 T for NbRe/Py. This behavior can be linked to the fact that, in this regime, fluxons do not penetrate the film with a uniform front but advance with an irregular front characterized by protrusions. Thus, the magnetic field is non-uniformly distributed in the film, and preferential stationary movement channels for the vortices are generated [5,47]. At larger fields, the NbRe/Au sample displays a nearly field-independent v^*, as predicted by Larkin–Ovchinnikov theory. In contrast, the NbRe/Py sample shows a decreasing v^* with increasing H, consistent with previous experimental observations [48-50]. Furthermore, at larger fields, because of the small H_T, the critical velocity in the NbRe/Py sample is limited by Joule dissipation. The latter facilitates the breakdown of superconductivity and reduces the vortex velocity in the bridge. Despite that, the S/F bilayer exhibits a significantly higher v^* than the S/N bilayer. This enhancement may be attributed to the enhanced quasiparticle scattering and increased disorder introduced by the Py layer. At the field of 0.1 T, the microbridges reach critical vortex velocities values of $v^{*\mathrm{NbRe/Au}} \approx 740$ m/s and $v^{*\mathrm{NbRe/Py}} \approx 1600$ m/s, corresponding to a relaxation time of $\tau_E^{\mathrm{NbRe/Au}} \approx 150$ ps and $\tau_E^{\mathrm{NbRe/Py}} \approx 24$ ps.

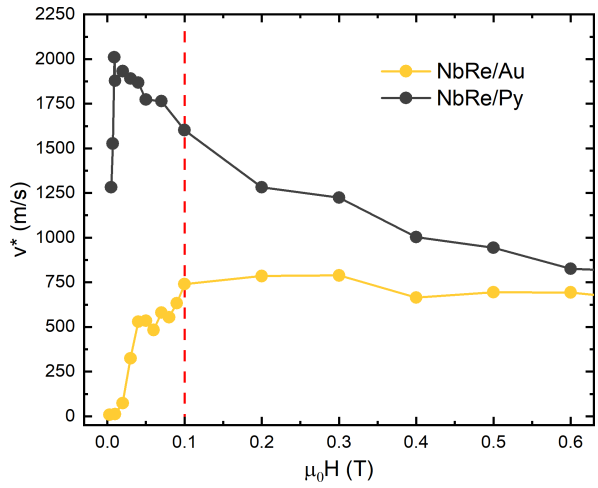


Figure 5: Vortex critical velocity as a function of the magnetic field for NbRe/Au and NbRe/Py at $t \approx 0.5$. The red dashed line indicates the thermal field of NbRe/Py.

The values of τ_E obtained for the heterostructures can be compared to those reported in the literature for single NbRe microstrips of similar geometric dimensions ($d^{\mathrm{NbRe}} = 15$ nm, $L^{\mathrm{NbRe}} = 100$ μm, and $w^{\mathrm{NbRe}} = 10$ μm) [22]. In this case, a relaxation time equal to $\tau_E^{\mathrm{NbRe}} \approx 200$ ps at $t \approx 0.5$ was reported. As a result, while the presence of the Au overlayer does not produce a significant reduction in the relaxation time, the ferromagnetic Py layer leads to a much more pronounced decrease of τ_E, by almost one order of magnitude. The result observed in the NbRe/Au hybrid can be understood by estimating $\Delta_{\mathrm{mini}}^{\mathrm{Au}}$ from Equation 3. Being $v_F^{\mathrm{Au}} = 1.4 \times 10^6$ m/s [36], and assuming that the mean free path is limited by the thickness d_{Au}, the electron diffusion coefficient is $D_{\mathrm{Au}} = 2.3 \times 10^{-3}$ m^2/s. This value yields a coherence length of $\xi_{\mathrm{Au}} \approx 30$ nm at the measurement temperature ($T = 3.5$ K). Because $\xi_{\mathrm{Au}} \gg d_{\mathrm{Au}}$, the layer is completely proximized ($\xi_N = d_{\mathrm{Au}}$), and $\Delta_{\mathrm{mini}}^{\mathrm{Au}} \approx \Delta^{\mathrm{NbRe}}$. Therefore, the escape of quasiparticles from the vortex core is not effectively facilitated by the Au layer. As a consequence, the relaxation time does not exhibit any significant reduction and remains mainly governed by the underlying NbRe layer. The small improvement in the energy relaxation time could be related to the presence of the interface that moderately influences the quasiparticle relaxation mechanisms of the system [26]. In contrast, in an S/F system with a strong ferromagnet such as Py, the superconducting order parameter is strongly depressed over a very short distance ($\xi_{\mathrm{Py}} = 2$ nm [33]) due to the large exchange field. Moreover, since Py is a disordered alloy, quasiparticles experience an enhanced scattering rate, further reducing the coherence of the induced correlations and promoting faster relaxation rates.

Finally, it is important to consider the possible role of thermal dissipation in the relaxation process. While a quantitative evaluation of the thermal effects is not straightforward, some considerations can be done. First, in both samples, the NbRe layer is in contact with the substrate. Therefore, the dominant heat dissipation channel into the thermal bath is common to both systems and does not affect the relative comparison between Au- and Py-capped samples. Consequently, substrate-related thermal effects can be considered equivalent, and the observed differences can be attributed to the specific properties of the capping layers and their interaction with the superconducting film. In

this respect, Au and Py are expected to affect the vortex dynamics in qualitatively different ways when considering thermal dissipation and phonon-mediated quasiparticle recombination. In fact, Au is a non-magnetic metal with high electronic and thermal conductivity, providing a more effective heat removal. This is confirmed from the analysis performed in the framework of Bezuglyj and Shklovskij theory [6], from which it emerged that the NbRe/Au bilayer is less affected by thermal effects at the instability current. In contrast, Py is a ferromagnetic and more disordered metal, characterized by enhanced scattering processes. The latter can, in principle, provide an efficient energy relaxation channel, promoting faster quasiparticle recombination. However, this effect competes with additional spin-related relaxation channels due to the splitting of the electronic band, which can lead to a slower recovery of the superconducting condensate. Therefore, in general, the net effect of a disordered ferromagnetic capping layer on the critical velocity is not trivial and depends on the balance between different mechanisms. Our experiment suggests that, for these specific systems, disorder-related mechanisms play a dominant role in setting the value of v^* with respect to the thermal effects.

Conclusion

NbRe-based heterostructures with different capping materials have been fabricated and electrically characterized by measuring their *I*–*V* characteristics under external magnetic fields. From the current and voltage values at the instability points, the behavior of the critical vortex velocity as a function of the magnetic field was investigated to understand how normal metals and ferromagnetic materials affect vortex motion. The experimental data show that the NbRe/Py bilayer exhibits larger critical vortex velocities than those of the NbRe/Au structure. Furthermore, the estimation of the energy relaxation time at 0.1 T yields $\tau_E^{NbRe/Py} \ll \tau_E^{NbRe/Au}$. The comparison with the relaxation time reported for single NbRe microbridges indicates that, while the Au overlayer does not substantially modify the intrinsic relaxation dynamics of the superconducting layer, the presence of Py leads to a pronounced decrease in τ_E by almost one order of magnitude. This behaviour can be understood both in terms of proximity-induced modifications of the superconducting energy gap and the additional quasiparticle scattering present in the proximity coupled layers. In the NbRe/Au bilayer, the induced minigap in Au is comparable to that of NbRe, and therefore Au does not enhance the quasiparticle escape from the vortex cores. In contrast, in the NbRe/Py system, the more efficient quasiparticle energy dissipation is due to both the strong depression of the superconductivity and an increased scattering rate in the disordered Py layer. These findings confirm that spectral proximity effects play a key role in determining the vortex dynamics in hybrid systems.

Acknowledgements

The authors thank L. Parlato and M. Peluso for performing the lithographic process.

Author Contributions

Francesco De Chiara: data curation; formal analysis; investigation; writing – original draft; writing – review & editing. Zahra Makhdoumi Kakhaki: data curation; formal analysis; investigation; writing – review & editing. Francesco Avitabile: data curation; investigation; software; writing – review & editing. Francesco Colangelo: investigation; writing – review & editing. Abhishek Kumar: investigation; writing – review & editing. Carmine Attanasio: conceptualization; supervision; writing – review & editing. Carla Cirillo: conceptualization; supervision; writing – review & editing.

ORCID® iDs

Francesco De Chiara - https://orcid.org/0009-0003-6934-2543
Zahra Makhdoumi Kakhaki - https://orcid.org/0000-0003-0330-8943
Francesco Avitabile - https://orcid.org/0009-0009-3926-9609
Abhishek Kumar - https://orcid.org/0000-0002-7462-7442
Carmine Attanasio - https://orcid.org/0000-0002-3848-9169
Carla Cirillo - https://orcid.org/0000-0001-8755-4484

Data Availability Statement

Data generated and analyzed during this study is available from the corresponding author upon reasonable request.

References

1. Dobrovolskiy, O. V. Fast dynamics of vortices in superconductors. In *Encyclopedia of Condensed Matter Physics,* 2nd ed.; Chakraborty, T., Ed.; Academic Press: Oxford, 2024; Vol. 2, pp 735–754. doi:10.1016/b978-0-323-90800-9.00015-9
2. Schmidt, V. V. In *The Physics of Superconductors: Introduction to Fundamentals and Applications;* Müller, P.; Ustinov, A. V., Eds.; Springer: Berlin, Heidelberg, 1997. doi:10.1007/978-3-662-03501-6
3. Peroz, C.; Villard, C. *Phys. Rev. B* **2005,** *72,* 014515. doi:10.1103/physrevb.72.014515
4. Shklovskij, V. A.; Nazipova, A. P.; Dobrovolskiy, O. V. *Phys. Rev. B* **2017,** *95,* 184517. doi:10.1103/physrevb.95.184517
5. Silhanek, A. V.; Leo, A.; Grimaldi, G.; Berdiyorov, G. R.; Milošević, M. V.; Nigro, A.; Pace, S.; Verellen, N.; Gillijns, W.; Metlushko, V.; Ilić, B.; Zhu, X.; Moshchalkov, V. V. *New J. Phys.* **2012,** *14,* 053006. doi:10.1088/1367-2630/14/5/053006
6. Bezuglyj, A. I.; Shklovskij, V. A. *Phys. C (Amsterdam, Neth.)* **1992,** *202,* 234–242. doi:10.1016/0921-4534(92)90165-9
7. Grimaldi, G.; Leo, A.; Nigro, A.; Pace, S.; Cirillo, C.; Attanasio, C. *Phys. C (Amsterdam, Neth.)* **2008,** *468,* 765–768. doi:10.1016/j.physc.2007.11.043
8. Larkin, A. I.; Ovchinnikov, Y. N. *Sov. Phys. - JETP* **1975,** *41,* 960–965.
9. Klein, W.; Huebener, R. P.; Gauss, S.; Parisi, J. *J. Low Temp. Phys.* **1985,** *61,* 413–432. doi:10.1007/bf00683694

10. Esmaeil Zadeh, I.; Chang, J.; Los, J. W. N.; Gyger, S.; Elshaari, A. W.; Steinhauer, S.; Dorenbos, S. N.; Zwiller, V. *Appl. Phys. Lett.* **2021,** *118,* 190502. doi:10.1063/5.0045990
11. Berggren, K. K.; Dauler, E. A.; Kerman, A. J.; Nam, S.-W.; Rosenberg, D. Chapter 6 - Detectors Based on Superconductors. In *Single-Photon Generation and Detection;* Migdall, A.; Polyakov, S. V.; Fan, J.; Bienfang, J. C., Eds.; Experimental Methods in the Physical Sciences, Vol. 45; Academic Press, 2013; pp 185–216. doi:10.1016/b978-0-12-387695-9.00006-8
12. Salvoni, D.; Ejrnaes, M.; Parlato, L.; Sannino, A.; Boselli, A.; Pepe, G. P.; Cristiano, R.; Wang, X. *J. Phys.: Conf. Ser.* **2019,** *1182,* 012014. doi:10.1088/1742-6596/1182/1/012014
13. Carroll, M.; Rosenblatt, S.; Jurcevic, P.; Lauer, I.; Kandala, A. *npj Quantum Inf.* **2022,** *8,* 132. doi:10.1038/s41534-022-00643-y
14. Patel, U.; Pechenezhskiy, I. V.; Plourde, B. L. T.; Vavilov, M. G.; McDermott, R. *Phys. Rev. B* **2017,** *96,* 220501. doi:10.1103/physrevb.96.220501
15. Bulaevskii, L. N.; Graf, M. J.; Batista, C. D.; Kogan, V. G. *Phys. Rev. B* **2011,** *83,* 144526. doi:10.1103/physrevb.83.144526
16. Dobrovolskiy, O. V.; Sachser, R.; Brächer, T.; Böttcher, T.; Kruglyak, V. V.; Vovk, R. V.; Shklovskij, V. A.; Huth, M.; Hillebrands, B.; Chumak, A. V. *Nat. Phys.* **2019,** *15,* 477–482. doi:10.1038/s41567-019-0428-5
17. Aronov, A. G.; Spivak, B. Z. *Sov. Phys. - JETP* **1979,** *50,* 328–329.
18. Doettinger, S. G.; Kittelberger, S.; Huebener, R. P.; Tsuei, C. C. *Phys. Rev. B* **1997,** *56,* 14157–14162. doi:10.1103/physrevb.56.14157
19. Cirillo, C.; Carapella, G.; Salvato, M.; Arpaia, R.; Caputo, M.; Attanasio, C. *Phys. Rev. B* **2016,** *94,* 104512. doi:10.1103/physrevb.94.104512
20. Cirillo, C.; Caputo, M.; Divitini, G.; Robinson, J. W. A.; Attanasio, C. *Thin Solid Films* **2022,** *758,* 139450. doi:10.1016/j.tsf.2022.139450
21. Makhdoumi Kakhaki, Z.; Martinelli, A.; Avitabile, F.; Di Bernardo, A.; Attanasio, C.; Cirillo, C. *Supercond. Sci. Technol.* **2024,** *37,* 125002. doi:10.1088/1361-6668/ad8122
22. Caputo, M.; Cirillo, C.; Attanasio, C. *Appl. Phys. Lett.* **2017,** *111,* 192601. doi:10.1063/1.4997675
23. Cirillo, C.; Chang, J.; Caputo, M.; Los, J. W. N.; Dorenbos, S.; Esmaeil Zadeh, I.; Attanasio, C. *Appl. Phys. Lett.* **2020,** *117,* 172602. doi:10.1063/5.0021487
24. Cirillo, C.; Ejrnaes, M.; Ercolano, P.; Bruscino, C.; Cassinese, A.; Salvoni, D.; Attanasio, C.; Pepe, G. P.; Parlato, L. *Sci. Rep.* **2024,** *14,* 20345. doi:10.1038/s41598-024-66991-1
25. Avitabile, F.; Colangelo, F.; Mikhailov, M. Yu.; Makhdoumi Kakhaki, Z.; Kumar, A.; Esmaeil Zadeh, I.; Attanasio, C.; Cirillo, C. *Appl. Phys. Lett.* **2025,** *127,* 172601. doi:10.1063/5.0282478
26. Ryan, K. M.; Chandrasekhar, V. *Appl. Phys. Lett.* **2025,** *127,* 072603. doi:10.1063/5.0268707
27. Ustavschikov, S. S.; Levichev, M. Y.; Pashenkin, I. Y.; Klushin, A. M.; Vodolazov, D. Y. *Supercond. Sci. Technol.* **2021,** *34,* 015004. doi:10.1088/1361-6668/abc2ad
28. Blatter, G.; Sirena, M.; Haberkorn, N. *Mater. Sci. Eng., B* **2024,** *299,* 116943. doi:10.1016/j.mseb.2023.116943
29. Peroz, C.; Villard, C.; Sulpice, A.; Butaud, P. *Phys. C (Amsterdam, Neth.)* **2002,** *369,* 222–226. doi:10.1016/s0921-4534(01)01246-1
30. Adami, O.-A.; Jelić, Ž. L.; Xue, C.; Abdel-Hafiez, M.; Hackens, B.; Moshchalkov, V. V.; Milošević, M. V.; Van de Vondel, J.; Silhanek, A. V. *Phys. Rev. B* **2015,** *92,* 134506. doi:10.1103/physrevb.92.134506
31. Blatter, G.; Sirena, M.; Lee, Y.; Yun, J.; Kim, J.; De Biasi, E.; Haberkorn, N. *Supercond. Sci. Technol.* **2024,** *37,* 035007. doi:10.1088/1361-6668/ad221f
32. Cirillo, C.; Pagliarulo, V.; Myoren, H.; Bonavolontà, C.; Parlato, L.; Pepe, G. P.; Attanasio, C. *Phys. Rev. B* **2011,** *84,* 054536. doi:10.1103/physrevb.84.054536
33. Attanasio, C.; Cirillo, C. *J. Phys.: Condens. Matter* **2012,** *24,* 083201. doi:10.1088/0953-8984/24/8/083201
34. Armenio, A. A.; Bell, C.; Aarts, J.; Attanasio, C. *Phys. Rev. B* **2007,** *76,* 054502. doi:10.1103/physrevb.76.054502
35. Andreev, A. F. *Sov. Phys. - JETP* **1964,** *19,* 1228.
36. Ashcroft, N. W.; Mermin, N. D. *Solid State Physics;* Holt, Rinehart and Winston: New York, 1976.
37. Belzig, W.; Bruder, C.; Schön, G. *Phys. Rev. B* **1996,** *54,* 9443–9448. doi:10.1103/physrevb.54.9443
38. Buzdin, A. I. *Rev. Mod. Phys.* **2005,** *77,* 935–976. doi:10.1103/revmodphys.77.935
39. Makhdoumi Kakhaki, Z.; Leo, A.; Spuri, A.; Ejrnaes, M.; Parlato, L.; Pepe, G. P.; Avitabile, F.; Di Bernardo, A.; Nigro, A.; Attanasio, C.; Cirillo, C. *Mater. Sci. Eng., B* **2024,** *304,* 117376. doi:10.1016/j.mseb.2024.117376
40. Gilani, T. H.; Rabchuk, D. *Can. J. Phys.* **2018,** *96,* 272–274. doi:10.1139/cjp-2017-0484
41. Guittoum, A.; Bourzami, A.; Layadi, A.; Schmerber, G. *Eur. Phys. J.: Appl. Phys.* **2012,** *58,* 20301. doi:10.1051/epjap/2012110343
42. Kes, P. H.; Tsuei, C. C. *Phys. Rev. B* **1983,** *28,* 5126–5139. doi:10.1103/physrevb.28.5126
43. Budinská, B.; Aichner, B.; Vodolazov, D. Y.; Mikhailov, M. Y.; Porrati, F.; Huth, M.; Chumak, A. V.; Lang, W.; Dobrovolskiy, O. V. *Phys. Rev. Appl.* **2022,** *17,* 034072. doi:10.1103/physrevapplied.17.034072
44. Silhanek, A. V.; Jiang, L.; Xue, C.; Vanderheyden, B. *Appl. Phys. Rev.* **2025,** *12,* 041324. doi:10.1063/5.0282694
45. Elistratov, A. A.; Maksimov, I. L. *Phys. Solid State* **2000,** *42,* 201–206. doi:10.1134/1.1131147
46. Plourde, B. L. T.; Van Harlingen, D. J.; Vodolazov, D. Y.; Besseling, R.; Hesselberth, M. B. S.; Kes, P. H. *Phys. Rev. B* **2001,** *64,* 014503. doi:10.1103/physrevb.64.014503
47. Grimaldi, G.; Leo, A.; Zola, D.; Nigro, A.; Pace, S.; Laviano, F.; Mezzetti, E. *Phys. Rev. B* **2010,** *82,* 024512. doi:10.1103/physrevb.82.024512
48. Doettinger, S. G.; Huebener, R. P.; Gerdemann, R.; Kühle, A.; Anders, S.; Träuble, T. G.; Villégier, J. C. *Phys. Rev. Lett.* **1994,** *73,* 1691–1694. doi:10.1103/physrevlett.73.1691
49. Lefloch, F.; Hoffmann, C.; Demolliens, O. *Phys. C (Amsterdam, Neth.)* **1999,** *319,* 258–266. doi:10.1016/s0921-4534(99)00297-x
50. Doettinger, S. G.; Huebener, R. P.; Kühle, A. *Phys. C (Amsterdam, Neth.)* **1995,** *251,* 285–289. doi:10.1016/0921-4534(95)00411-4

License and Terms

This is an open access article licensed under the terms of the Beilstein-Institut Open Access License Agreement (https://www.beilstein-journals.org/bjnano/terms), which is identical to the Creative Commons Attribution 4.0 International License (https://creativecommons.org/licenses/by/4.0). The reuse of material under this license requires that the author(s), source and license are credited. Third-party material in this article could be subject to other licenses (typically indicated in the credit line), and in this case, users are required to obtain permission from the license holder to reuse the material.

The definitive version of this article is the electronic one which can be found at:
https://doi.org/10.3762/bjnano.17.20

BEILSTEIN JOURNAL OF NANOTECHNOLOGY

Ferroelectric nanodot reservoir for neuromorphic computing

Anna Razumnaya*[1], Yuri Tikhonov[2], Dmitrii Naidenko[3], Léo Boron[2], Valerii Vinokur[4,§] and Igor Lukyanchuk[2,5]

Full Research Paper

Open Access

Address:
[1]Condensed Matter Physics Department, Jožef Stefan Institute, Ljubljana, Slovenia, [2]Laboratoire de Physique de la Matière Condensée, Université de Picardie Jules Verne, Amiens, France, [3]International Research Institute for Intelligent Materials, Southern Federal University, Rostov-on-Don, Russia, [4]Terra Quantum AG, St. Gallen, Switzerland and [5]L. D. Landau Institute for Theoretical Physics, Moscow, Russia

Email:
Anna Razumnaya* - anna.razumnaya@ijs.si

* Corresponding author
§ deceased

Keywords:
ferroelectric nanodots; multilevel logic; neuromorphic circuits; polarization; topological states

Beilstein J. Nanotechnol. **2026,** *17,* 352–364.
https://doi.org/10.3762/bjnano.17.24

Received: 12 August 2025
Accepted: 22 December 2025
Published: 20 February 2026

Associate Editor: J. M. van Ruitenbeek



© 2026 Razumnaya et al.; licensee Beilstein-Institut.
License and terms: see end of document.

Abstract

We present a ferroelectric-based data reservoir designed for neuromorphic computing applications. The reservoir consists of an ensemble of nonlinear ferroelectric nanodots capable of storing information through their stable polarization states. These nanodots are confined between electrodes and form a network of parallel connected capacitive elements, which can either be addressed individually or integrated between common conducting plates. By leveraging the intrinsic nonlinearity and memory of ferroelectric polarization switching, the device maps incoming signals into a high-dimensional space of polarization configurations. This physical transformation enables efficient temporal information encoding and provides a rich dynamic representation for subsequent processing in a readout layer of a neuromorphic circuit.

Introduction

Neuromorphic computing aims to emulate the architecture and processing mechanisms of the human brain to achieve energy-efficient and adaptive information processing [1-6]. Among various neuromorphic approaches, reservoir computing has emerged as a particularly promising paradigm, owing to its conceptual simplicity and hardware amenability [7-11]. In reservoir computing, a high-dimensional, nonlinear dynamical system, called the reservoir, transforms input signals into a rich temporal multiplexed feature space, from which a linear readout extracts the target output for further neuromorphic processing. In recent years, significant efforts have been devoted to realizing physical implementations of reservoirs using diverse material platforms, including photonics [12], spintronics [13], and different types of memristors [14,15].

Ferroelectric materials offer a unique combination of properties (i.e., nonlinearity, nonvolatility, analog state tunability, and compatibility with CMOS platforms) that make them particularly attractive for energy-efficient neuromorphic circuits [16-21]. They inherently possess a multitude of metastable polarization orientations, corresponding to different local minima of the free energy [22-24]. This intrinsic multistability facilitates analog and digital information encoding, retention, and logic operations within a single physical unit, and is one of the key reasons for their growing relevance in neuromorphic computing and multivalued logic architectures [17,25]. Ferroelectrics also host a wide variety of nonuniform topological soliton-like polarization states, especially at the nanoscale [26-33]. The presence of such topological states provides not only robust multistability but also new functional degrees of freedom, including topologically protected switching, enhanced memory capacity, and localized polarization textures that can act as multilevel logic or signal-processing elements [34].

Ferroelectric field-effect transistors (FeFETs), ferroelectric tunnel junctions (FTJs), and memcapacitive synapses revealing ferroelectric properties, have been proposed and demonstrated as viable candidates for synaptic and reservoir elements [25,35]. In FeFET-based reservoirs, for example, the polarization-dependent hysteresis provides both the nonlinearity and memory required for temporal signal encoding [36]. Moreover, recent advances in material engineering have enabled reliable multilevel operation and subnanosecond switching speeds, which are essential for real-time neuromorphic processing [37]. A topologically configurable multilevel logic unit based on interacting ferroelectric domains proposed in [38,39] showed how polarization states can be harnessed for logic operations within a compact physical structure.

While various approaches have demonstrated the use of ferroelectrics in neuromorphic computing at the level of individual elements, most existing implementations treat each ferroelectric component as an isolated device or a deterministic node within a predefined circuit. However, such approaches often neglect the rich collective dynamics emerging from ensembles of interacting nonlinear elements, an aspect especially compelling when analyzed through the lens of statistical physics models such as the Ising spin system with disorder. Harnessing the emergent behavior of ferroelectric interconnected nanostructures as physical reservoirs thus represents a largely underexplored yet potentially transformative direction for neuromorphic computing.

In this work, we present a ferroelectric-based data reservoir concept grounded in the collective nonlinear response of an ensemble of ferroelectric nanodots. The system consists of a network of nanodots, each carrying the bistable polarization state, arranged between electrodes in configurations that allow for parallel electrical addressing. By receiving temporal input signals, the ensemble evolves into distinct polarization states that encode input history through a combination of nonlinear switching and spatial interactions. This physical reservoir naturally maps the input signal into a high-dimensional space, making it suitable for neuromorphic inference tasks.

The objective of this work is to establish the physical principles and theoretical framework of a charge-driven ferroelectric reservoir based on nanodot ensembles. We delineate the mechanisms that endow the system with nonlinearity, and high dimensionality, linking electrostatic coupling, hysteretic switching, and the resulting frustrated-Ising energy landscape, and outline practical interface schemes for signal injection and readout. Altogether, the presented framework connects the collective polarization dynamics of ferroelectric nanodots with emergent nonlinear and memory effects, providing a solid foundation for developing and engineering compact, energy-efficient, and scalable ferroelectric platforms for neuromorphic information processing.

The objectives of this work are to introduce a physically realizable reservoir architecture based on ferroelectric nanodots, to highlight the mechanisms enabling nonlinearity, fading memory, and high dimensionality in such a system, and to position this architecture relative to existing approaches in neuromorphic hardware. Our findings suggest that ensembles of ferroelectric nanodots offer a compact, low-power, and scalable solution for implementing physical reservoirs with emergent computational capabilities.

Results and Discussion

General concept

The proposed reservoir architecture is designed to physically implement the principles of reservoir computing using the interconnected ferroelectric nanodots as nonlinear memory-storage nodes. The system enables efficient temporal information processing by exploiting polarization dynamics under external input signals. Figure 1 illustrates two conceptual configurations of the ferroelectric-based reservoir and its integration into a neuromorphic computing framework.

In Figure 1a, a single input channel delivers time-dependent electrical or optical signals into the ferroelectric reservoir. The reservoir consists of an ensemble of nanodots, each exhibiting a nonlinear bistable polarization response $\pm P_s(i)$ (where i is the nanodot index and P_s is the magnitude of the spontaneous polarization) to external excitation. The ensemble of these nanodots forms a network of parallel connected capacitors,

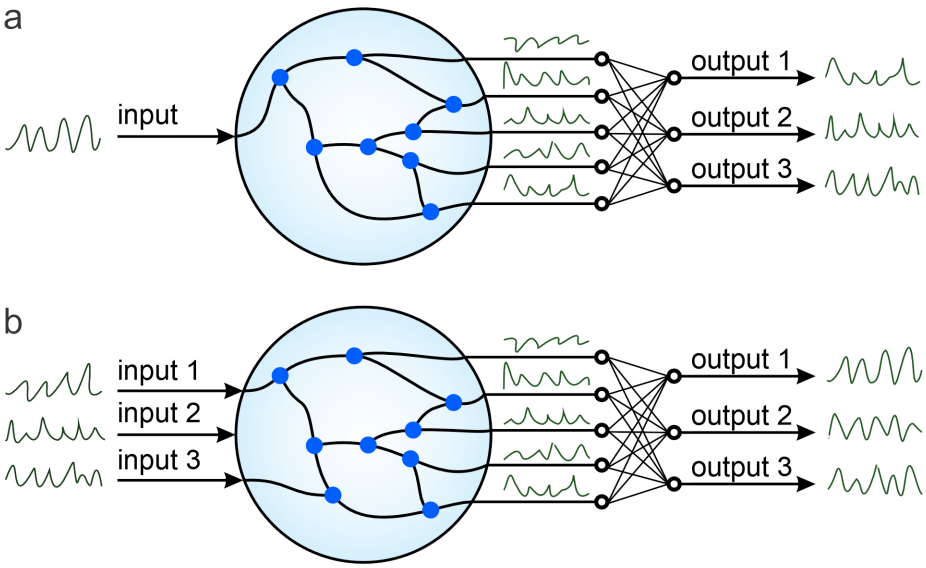


Figure 1: The reservoir computing system consists of an array of ferroelectric nanodots (blue points) forming an ensemble of capacitors that are electrically connected either through a network of wires or via common electrodes. (a) Configuration with a single input channel integrated into the neuromorphic circuit. (b) Configuration with multiple input channels integrated into the neuromorphic circuit.

either through a wired interconnection or via a shared common electrode. Upon receiving the common input signal $x(t)$, the polarization states of the nanodots evolve collectively, producing a high-dimensional internal state. This internal state is projected onto the readout layer, which samples the states of a selected subset of nanodots j and performs linear operations (e.g., weighted summation) to generate the multidimensional system output $y_j(t)$.

In Figure 1b, a more general case is presented, where multiple input electrical channels $x_j(t)$ feed the reservoir simultaneously. These can represent different signal modalities, spatially distributed sensors, or temporally multiplexed spike trains. The multichannel configuration allows the reservoir to integrate and correlate complex spatiotemporal patterns, offering an increase in expressive power and applicability for multidimensional signal processing tasks.

Conceptually, such architectures align with theoretical foundations established in traditional reservoir computing frameworks. However, unlike systems relying on sequential switching or delay-based dynamics, the proposed design enables true parallel evolution of polarization states with low energy consumption and fast switching speeds, leveraging the intrinsic properties of ferroelectrics.

Furthermore, while previous considerations of neuromorphic ferroelectric nanodot-based setups [38,39] demonstrated static logic functions in topologically structured ferroelectric domain networks, the present system shifts toward dynamic, time-dependent processing, essential for tasks such as time-series prediction, temporal pattern recognition, and classification. The reservoir's ability to encode temporal correlations through physical polarization evolution distinguishes it from traditional logic-oriented implementations and brings it closer to biologically inspired neural architectures.

The distinction between the single- and multiinput configurations shown in Figure 1 reflects the system's scalability and adaptability. In real-world neuromorphic systems, multiple input streams are often required to represent multimodal sensory information or parallel processing pipelines. The ability of ferroelectric reservoirs to naturally support such integration without increasing circuit complexity presents a significant advantage over transistor-based logic systems.

Core nanodot unit

To describe the basic operational mechanism of the ferroelectric reservoir introduced in Figure 1, we now examine its elementary building block, the ferroelectric nanodot. Figure 2 illustrates the structure and the nonlinear switching behavior of a single nanodot under external electrical excitation.

As shown in Figure 2a, the nanodot is confined between two metallic electrodes. It exhibits a spontaneous polarization P_s with at least two stable orientations: "up" and "down". These polarization states are denoted as mP_s where $m = +1$ corresponds to the "up" state and $m = -1$ to the "down" state. Termi-

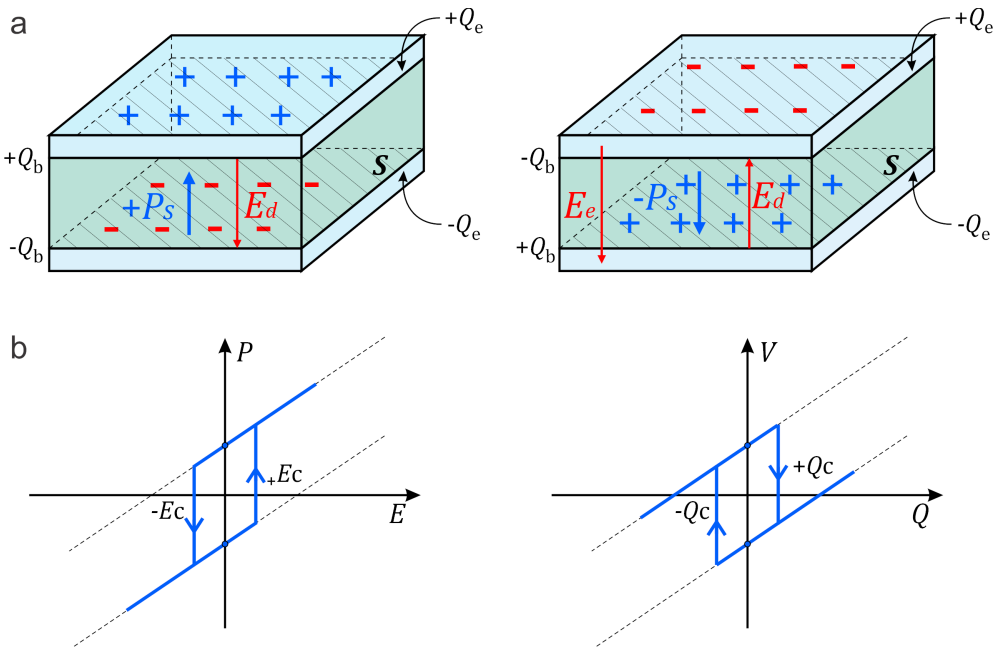


Figure 2: The basic operations of a single ferroelectric nanodot. (a) Schematic of a ferroelectric nanodot placed between two conducting plates, representing the constitutive unit of the ferroelectric reservoir. (b) Polarization–electric field $P(E)$ and voltage–charge $V(Q)$ hysteresis loops characteristic of ferroelectric switching.

nation of polarization at the top and bottom surfaces results in bound charges of magnitude $mQ_b = mSP_s$, where S is the cross-sectional area of the nanodot. These surface-bound charges produce an internal depolarization field, $E_d = -mP_s/\varepsilon_0\varepsilon_f$, where ε_0 is the vacuum dielectric permittivity and ε_f is the dielectric constant of the ferroelectric material. An external charge $\pm Q_e$ applied to the electrodes generates an additional electric field inside the nanodot, $E_e = -Q_e/\varepsilon_0\varepsilon_f S$. Therefore, the total electric field inside the nanodot is the sum of the depolarization field, E_d, and the electric field produced by the conducting plates, E_e, and can be written as $E = -(mP_sS + Q_e/S)/\varepsilon_0\varepsilon_f$.

The corresponding electrostatic energy stored in the nanodot of thickness d is:

$$U = \frac{1}{2}\varepsilon_0\varepsilon_f E^2 Sd = \frac{\left(mP_s + Q_e/S\right)^2}{2\varepsilon_0\varepsilon_f}\cdot Sd. \qquad (1)$$

This energy has two local minima corresponding to the two polarization orientations, and the system tends to settle in the one with lower energy under the given external charge. That is, for $Q_e < 0$, the "up" state ($m = +1$) is energetically favorable, for $Q_e > 0$, the "down" state ($m = -1$) is preferred. Notably, the switching between these states occurs via a nonlinear, hysteretic transition. This transition is governed by the coercive electric field E_c. The coercive charge required for switching is: $Q_c = \varepsilon_0\varepsilon_f SE_c$, where the positive value corresponds to switching from "up" to "down", and the negative value corresponds to the reverse process. This behavior is illustrated in Figure 2b, showing typical hysteresis loops for both polarization vs electric field $P(E)$ and voltage vs charge $V(Q)$.

These hysteresis curves realize the bistability and nonlinearity that are central to the function of the reservoir. Similar behaviors have been experimentally verified in a variety of ferroelectric materials, such as HfO_2-based FeFETs [36], and $Pb(Zr,Ti)O_3$ or $BiFeO_3$ nanostructures [16,17]. In addition to their bistable switching behavior, ferroelectric nanodots can exhibit negative capacitance under specific conditions, particularly during polarization reversal processes. This regime, where an increase in voltage leads to a decrease in charge, arises from the energy-lowering feedback between polarization and internal electric field. Negative capacitance not only enhances the effective electrostatic tunability of the system but also provides a potential route to voltage amplification and energy-efficient signal processing at the nanoscale [40,41]. Incorporating such effects into the reservoir architecture could further enrich its nonlinear dynamics and expand the range of neuromorphic functionalities.

Networking of ferroelectric nanodots

The total reservoir is realized by assembling a network of such nanodots between shared or interconnected conducting plates,

enabling electrical connectivity and collective dynamics among nodes. This configuration allows for the emergence of spatio-temporal polarization patterns, which can encode input histories and project them into high-dimensional internal states. This architecture goes beyond prior logic-function-based designs [38,39], enabling dynamic computation within a neuromorphic reservoir framework. Such physically grounded bistable elements correspond to the neurons in traditional recurrent neural networks or echo state networks [7,42], offering energy-efficient, scalable, and high-speed alternatives to digital implementations of reservoir computing.

Figure 3 illustrates two exemplary charge-driven network architectures in which the total external charge Q_e applied to the electrodes governs the internal electric field and polarization state of the nanodots. In Figure 3a, each ferroelectric nanodot is embedded in an individual capacitor structure, and the capacitors are electrically connected in parallel through metallic interconnects. In Figure 3b, an alternative layout is shown in which all nanodots share the same pair of extended electrodes. In this case, the nanodots are arranged between two continuous conductive plates, with a dielectric filler possibly present between adjacent units.

Both configurations presented in Figure 1 can be described as an array of capacitors connected in parallel, where each nanodot represents an individual binary unit i with a specific polarization orientation, either "up" or "down", denoted as $m_i = \pm 1$. The corresponding bound charges on the surfaces of the nanodots are equal to $Q_{bi} = m_i P_s S_i$, where S_i is the cross-sectional area of the i-th nanodot. The total free charge, $Q = \pm\Sigma_i P_s S_i m_i \pm Q_e$, redistributes over the electrodes to maintain equipotentiality, ensuring that the internal electric field across each nanodot, $E = -Q/\varepsilon_0\varepsilon_f S$, is uniform. Here $\pm Q_e$ is the externally applied charge and $S = \Sigma_i S_i$ is the total electrode area. The condition of the uniformly constant electric field throughout the array is a crucial feature for simultaneous control of polarization dynamics across nanodots.

The total electrostatic energy of the reservoir system becomes:

$$U = \frac{1}{2}\varepsilon_0\varepsilon_f E^2 Sd = \frac{1}{2}\sum_{ij} J_{ij} m_i m_j + \mu\sum_i h_i m_i + U_0. \quad (2)$$

Here, the system assumes the form of a frustrated Ising model with long-range antiferromagnetic interactions. The first term describes interactions between all pairs of sites via:

$$J_{ij} = \frac{SdP_s^2}{\varepsilon_0\varepsilon_f}\cdot\frac{S_i S_j}{S^2}. \quad (3)$$

The second term captures the interaction of local polarization with an effective dipolar field, where:

$$\mu = P_s d, \quad h_i = \frac{Q_e}{\varepsilon_0\varepsilon_f}\cdot\frac{S_i}{S}. \quad (4)$$

The final term U_0 is independent of the configuration $\{m_i\}$. Because all J_{ij} are positive, the system is highly frustrated, meaning it has many nearly degenerate states near the energy minimum, a property that enables high information storage and computational richness. Such statistical properties are closely related to neuromorphic architectures. In analogy with the brain, each nanodot (site) functions similarly to a binary neuron, being in an "active" or "inactive" state, corresponding to $m_i = +1$ and -1, respectively. The overall system thus mimics the dynamics of a large neural ensemble, offering capabilities for associative

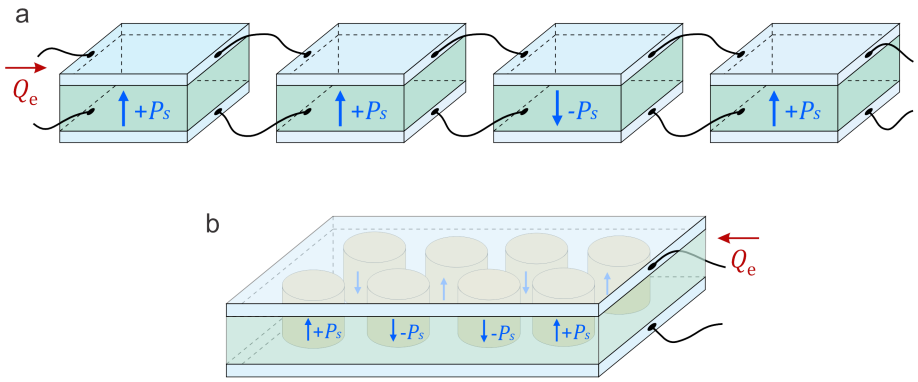


Figure 3: A schematic construction of a ferroelectric reservoir operated under charge-controlled conditions, with the injected charge Q_e represented by the arrow showing charge input at the electrode. (a) Ferroelectric reservoir realized as a network of wire-connected capacitors, each containing a single nanodot. (b) Ferroelectric reservoir in which all nanodots are confined between two common electrodes.

memory, pattern recognition, and temporal processing, consistent with the goals of physical reservoir computing.

A key feature of this reservoir is that the polarization switching at each site is hysteretic. The local coercive field at site i is expressed as:

$$h_{ci} = \frac{Q_{ci}}{\varepsilon_0 \varepsilon_f} \cdot \frac{S_i}{S}. \tag{5}$$

where Q_{ci} is the site-specific coercive charge. This introduces an additional layer of dynamic complexity into the system.

To illustrate the reservoir behavior, consider a simplified case: All nanodots have equal area $S_i = S/N$, but different coercive thresholds h_{ci}. In this case, the interactions become homogeneous:

$$J_{ij} = J = \frac{SdP_s^2}{N^2 \varepsilon_0 \varepsilon_f}, \quad h_i = h = \frac{Q_e}{N \varepsilon_0 \varepsilon_f}. \tag{6}$$

The energy simplifies to:

$$U = \frac{1}{2} J \sum_{ij} m_i m_j + \mu h \sum_i m_i + \text{const.} \tag{7}$$

Such a system has a high degree of degeneracy. At zero applied charge $Q_e = 0$, the minimum energy of the system corresponds to the state with zero total polarization, where half of the nanodots have up-directed polarization and the other half have down-directed polarization. For an even number N of nanodots, the degeneracy of this state is given by $C_N^{N/2} = (N!/\frac{N}{2}!)^2$. If a positive charge increment $q = J/h$ is applied, it flips the polarization of one nanodot from down to up, yielding a new configuration with $N/2 - 1$ nanodots oriented downward and $N/2 + 1$ upward. The degeneracy of this excited state is:

$$C_N^{N/2-1} = \frac{N!}{\left(\frac{N}{2}-1\right)!\left(\frac{N}{2}+1\right)!}. \tag{8}$$

More generally, for n units of positive charge (with integer $n < N$), the resulting degeneracy becomes:

$$C_N^{N/2-n} = \frac{N!}{\left(\frac{N}{2}-n\right)!\left(\frac{N}{2}+n\right)!}. \tag{9}$$

This exponential multiplicity of nearly degenerate states constitutes a powerful computational feature of the ferroelectric reservoir, enabling rich dynamic response to time-varying inputs, as required for real-time neuromorphic tasks. Notably, our approach leverages the electrostatic physics of nanoscale ferroelectrics to implement a scalable, low-power analog computing substrate. The described system relies solely on dielectric polarization degrees of freedom, making it especially attractive for dense and passive neuromorphic computing elements.

Collective switching dynamics

Figure 4 illustrates the possible variety of transitions within small-scale ferroelectric reservoirs comprising nanodots with different coercive fields, in response to various sequences of electrical charge pulses. These transitions exemplify the non-commutative and history-dependent behavior intrinsic to the system, stemming from the interplay of electrostatic interactions and local switching thresholds.

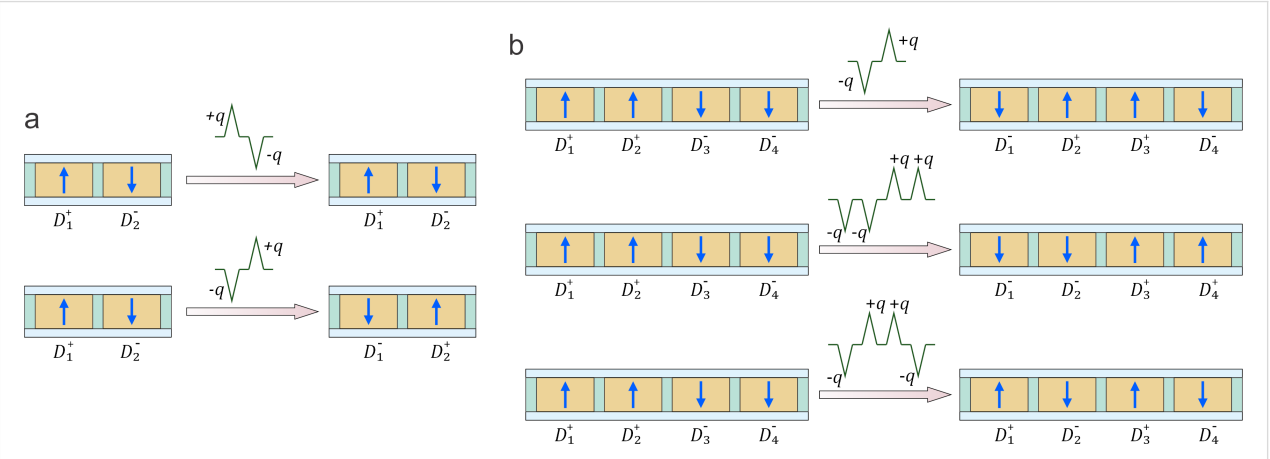


Figure 4: Switching behavior in ferroelectric reservoirs with a small number of nanodots driven by charge pulses. Evolution of the polarization states in (a) a two-nanodot reservoir under different charge pulse sequences and (b) a four-nanodot reservoir under different charge pulse sequences.

Figure 4a depicts a two-nanodot system with an initial configuration (D_1^+, D_2^-), where the superscripts "+" and "−" denote up- and down-oriented polarization, respectively, and the subscripts label the associated coercive fields $h_{c1} < h_{c2}$. Under the application of a positive charge unit $+q$, the nanodot D_1^+, having the lowest coercive field, undergoes polarization reversal, yielding the intermediate state (D_1^-, D_2^-). Upon applying a subsequent negative pulse $-q$, the same nanodot reverts to its original up-polarized state, restoring the initial configuration. Thus, the pulse sequence $(+q,-q)$ leads to a reversible switching cycle:

$$\left(D_1^+, D_2^-\right) \xrightarrow{+q} \left(D_1^-, D_2^-\right) \xrightarrow{-q} \left(D_1^+, D_2^-\right).$$

In contrast, reversing the order of pulses produces a distinct final state. Starting from (D_1^+, D_2^-), applying $-q$ flips D_2^-, resulting in (D_1^+, D_2^+). Then, $+q$ switches D_1^+ to (D_1^-, D_2^+). The final configuration thus depends on the order of the applied pulses:

$$\left(D_1^+, D_2^-\right) \xrightarrow{-q} \left(D_1^+, D_2^+\right) \xrightarrow{+q} \left(D_1^-, D_2^+\right).$$

This demonstrates the non-commutative behavior of polarization dynamics in the reservoir, arising from the hierarchy of coercive fields. Figure 4b extends this analysis to a four-nanodot system with initial configuration $(D_1^+, D_2^+, D_3^-, D_4^-)$, and coercive fields ordered as $h_{c1} < h_{c2} < h_{c3} < h_{c4}$. Here, multiple pulse sequences lead to distinct final polarization states depending on their magnitude and order.

The sequence $(-q,+q)$ results in

$$\left(D_1^+, D_2^+, D_3^-, D_4^-\right) \xrightarrow{-q} \left(D_1^+, D_2^+, D_3^+, D_4^-\right) \xrightarrow{+q} \left(D_1^-, D_2^+, D_3^+, D_4^-\right),$$

whereas the sequence $(-2q,+2q)$ results in

$$\left(D_1^+, D_2^+, D_3^-, D_4^-\right) \xrightarrow{-2q} \left(D_1^+, D_2^+, D_3^+, D_4^+\right) \xrightarrow{+2q} \left(D_1^-, D_2^-, D_3^+, D_4^+\right).$$

Finally, the sequence $(-q,+2q,-q)$ results in

$$\left(D_1^+, D_2^+, D_3^-, D_4^-\right) \xrightarrow{-q} \left(D_1^+, D_2^+, D_3^+, D_4^-\right) \xrightarrow{+2q} \left(D_1^-, D_2^-, D_3^+, D_4^-\right) \xrightarrow{-q} \left(D_1^+, D_2^-, D_3^+, D_4^-\right).$$

Here, each pulse of magnitude q denotes a unit of applied charge sufficient to flip the polarization of a nanodot with the lowest coercive field among those opposing the applied field. A double pulse of magnitude $2q$ corresponds to either a single pulse of double strength or two consecutive unit pulses, $(2q) = (+q,+q)$. The results emphasize the resetting behavior of specific sequences. For instance, a sequence $(+2q,-2q)$ can drive the reservoir first into a fully down-polarized state $(D_1^-, D_2^-, D_3^-, D_4^-)$, and then reinitialize it back to the original configuration $(D_1^+, D_2^+, D_3^-, D_4^-)$. Likewise, the inverse sequence $(-2q,+2q)$ results in full up-polarization, followed by relaxation into a new asymmetric state $(D_1^-, D_2^-, D_3^+, D_4^+)$. These examples highlight the rich state transition dynamics available in ferroelectric reservoirs due to the combination of hysteresis, coercive field inhomogeneity, and global electrostatic interactions. Such dynamics provide the essential nonlinear temporal memory required for time-dependent information processing in neuromorphic systems.

Signal processing

We now turn to large systems where the collective behavior of many interacting elements enables rich spatiotemporal dynamics. We illustrate this behavior by simulating a square $N^2 = 16 \times 16$ ferroelectric nanodot array arranged in a square lattice, as shown in Figure 5. Each nanodot in the array shares the same geometry but differs in its coercive field $E_{c,i}$, which is randomly assigned to reflect intrinsic material inhomogeneity. These coercive fields are taken from a static random distribution that remains fixed throughout the simulation, emulating quenched disorder and the inherent variability of switching thresholds in nanoscale ferroelectrics. The polarization state of each dot is binary, taking either +1 ("up") or −1 ("down"). Switching occurs when the applied electric field E exceeds the local threshold $E_{c,i}$.

After assigning the static coercive-field distribution, the simulation begins with a reset protocol: Alternating bipolar charge pulses $(+nq, -nq)$ with $n = [N^2/2] = 132$ are applied through common top and bottom electrodes, initializing the array into an initial reproducible state. Then, during signal processing, the field E is allowed to evolve in discrete steps, randomly increasing or decreasing by one unit, within a bounded range $(-n$ to $+n)$. At each step, the dot with the lowest switching threshold among the eligible ones undergoes a polarization reversal, thereby updating the system state.

This discrete event simulation captures the nonlinear hysteretic evolution of the entire reservoir. Importantly, because of the broad distribution of E_c and the collective nature of switching, the system explores a high-dimensional space of metastable configurations. The response depends not only on the current field but also on the sequence of past stimuli, a hallmark of temporal memory.

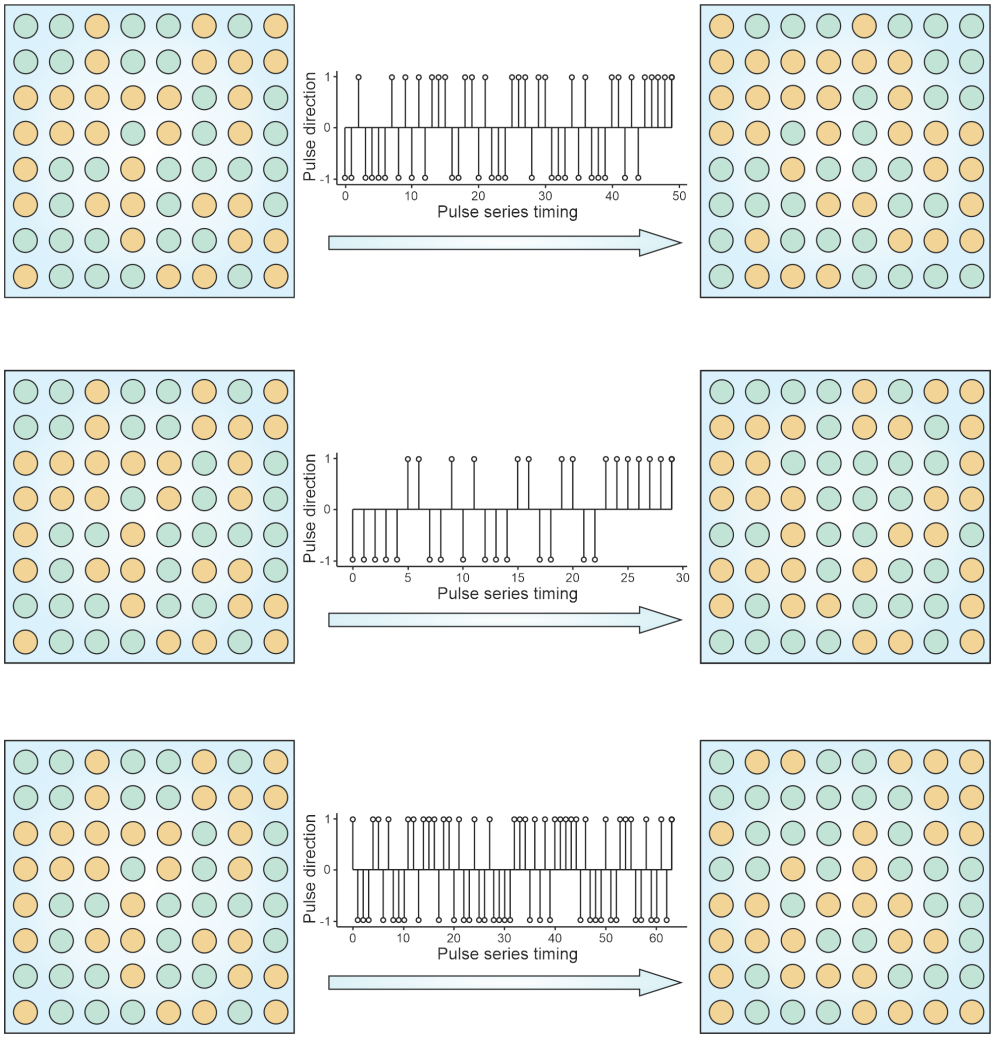


Figure 5: Dynamic evolution of polarization configurations in a square array of 256 ferroelectric nanodots with uniform cross-sectional area and randomly distributed coercive fields h_{ci}, subjected to varying sequences of charge pulses. The reservoir is initialized by a reset pulse sequence (+*nq*,–*nq*), with n = 132, and subsequent signal pulses reconfigure the polarization pattern. The complexity and exponential state space of the system illustrate its suitability for high-dimensional temporal information processing in neuromorphic circuits.

Each time the system returns to a balanced state with an equal number of +1 and −1 polarizations, the corresponding field trajectory is saved. These trajectories encode distinct input histories and illustrate how the reservoir transforms temporal sequences into spatial polarization patterns. Such behavior enables robust nonlinear signal processing and supports the implementation of neuromorphic tasks, including classification, prediction, and temporal pattern recognition.

This type of driven evolution has several profound consequences for neuromorphic reservoir operations: (i) Nonlinear input mapping. Due to the broad distribution of coercive thresholds, even small changes in the input sequence (field trajectory) can cause large and qualitatively different polarization responses. This sensitivity enables powerful separation of input classes in the reservoir state space. (ii) Short-term memory. The system retains a history of past field variations through its current polarization configuration. This memory is distributed and may decay over time due to charge leakage, mimicking the fading memory property of biological neural networks. (iii) High-dimensional projection. The number of accessible metastable states scales exponentially with the number of nanodots, ensuring that even simple temporal inputs are transformed into complex, spatially structured responses that can be linearly separated by a readout layer. (iv) History dependence and non-commutativity. Because switching paths depend on the temporal order of inputs, the same final field value may lead to different system states. This context-dependent behavior is vital for tasks such as temporal pattern recognition and sequence classification. In the present study, we focus on the intrinsic

physical dynamics of the ferroelectric reservoir, which performs the major part of nonlinear preprocessing. Consequently, the associated readout layer can remain minimal, typically linear, while the principal feature transformation occurs within the reservoir itself.

Interface architecture

The setup considered in the previous section corresponds to the case where all nanodots are confined between the same pair of conducting electrodes, creating a global capacitive structure. Also, similar input-output behavior and dynamic configurability can be realized in an alternative configuration, where each ferroelectric nanodot is embedded in an individual parallel-connected capacitor, as shown earlier, in Figure 3a. In both scenarios, the incoming data pulses are injected as electrical signals (e.g., current or voltage spikes) and dynamically reconfigure the reservoir state by switching local polarizations.

The readout layer, responsible for interpreting the reservoir's final polarization state, may be connected to synaptic circuits that transduce polarization configurations into output signals for downstream neuromorphic processing. This integration strategy supports both dense analog information storage and real-time parallel processing. Although several previous works have modeled large-scale Ising-type networks for neuromorphic purposes using abstract or spin-based physical systems [43,44], the ferroelectric platform described here uniquely combines analog configurability, scalability, and low-energy operation due to the intrinsic dielectric polarization physics. In contrast to spintronic or CMOS-based implementations, the ferroelectric reservoir utilizes no active current-driving elements, allowing for passive, high-density neuromorphic integration.

To interface the ferroelectric reservoir with external neuromorphic systems, specific schemes for signal injection and readout are required. Several architectures illustrated in Figure 6 demonstrate the versatility of input/output integration mechanisms compatible with ferroelectric reservoir operation.

In the scheme shown in Figure 6a, the input dataset is time-multiplexed into a series of current pulses or a continuous current signal $I(t)$, which is applied to the upper electrode of the ferroelectric reservoir. The time-integrated current produces a sequence of charge pulses $Q(t) = \int I(t)\mathrm{d}t$, effectively driving the reservoir with a controlled temporal charge profile. The lower electrode is grounded. This setup ensures that the data is encoded as variations in total driving charge, enabling the dynamic evolution of polarization states across the nanodot network in response to temporal input patterns.

An alternative implementation, depicted in Figure 6b, implements a voltage-driven input by connecting the reservoir capacitor C_r in series with a smaller dielectric capacitor C_d. A time-dependent voltage signal $V(t)$, composed of pulses or a continu-

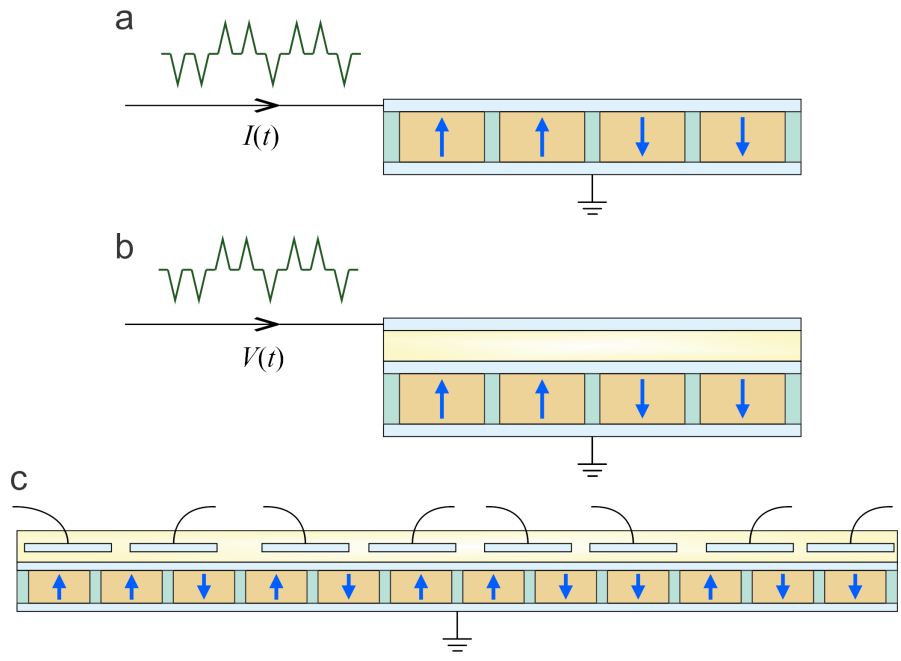


Figure 6: Signal injection and readout schemes for the ferroelectric reservoir. (a) Time-integrated current produces charge pulses for driving the reservoir. (b) Time-dependent voltage applied across a dielectric-reservoir capacitor pair enables voltage-controlled charge input and nonlinear readout. (c) Spatially multiplexed data is injected via spot electrodes and read out through similar localized outputs.

ous waveform, is applied to the entire structure. If $C_d \ll C_r$, then most of the voltage drop occurs across the dielectric capacitor, and the charge delivered to the reservoir electrode is approximated by $Q(t) = C_d V(t)$. This configuration effectively converts the voltage signal into a corresponding charge signal, allowing for reservoir driving through voltage control. Moreover, the time-dependent voltage at the reservoir electrode, resulting from internal polarization dynamics, can be monitored as a readout signal. Since the voltage response reflects complex nonlinear processes such as switching and relaxation, it serves as a rich source of output features, analogous to synaptic signals in neuromorphic circuits.

A further signal integration scheme, illustrated in Figure 6c, uses spatial multiplexing, where individual data units are injected into specific locations of the reservoir via an array of small spot electrodes placed above the common charge-driving electrode. These local input electrodes modulate the nearby charge distribution, which in turn alters the polarization states of underlying ferroelectric nanodots. For readout, a similar array of spatially resolved electrodes senses the local electric fields that reflect the polarization configuration of the reservoir. These electrodes can be directly interfaced with synaptic elements in a downstream neural layer, enabling spatially structured output. In practical implementations, the readout vector is constructed from either local voltage responses of selected nanodots or from the global polarization configuration, which can be directly sensed via electrode potentials or piezoresponse amplitude mapping. To enhance the locality and tunability of charge manipulation, the charge-driving electrode may be fabricated from a semiconducting material with partial screening, allowing for both global and locally addressable control. This configuration supports combined time- and space-multiplexed data handling, expanding the functional versatility of ferroelectric reservoirs for neuromorphic computing tasks.

In the present study, we focus on the intrinsic physical dynamics of the ferroelectric reservoir, which performs the major part of nonlinear preprocessing. Consequently, the associated readout layer can remain minimal, typically linear in subsequent computational implementations.

Contactless interfaces

Contactless input and output methods of data integration between the reservoir and external neuromorphic interfaces are of particular importance for the development of scalable, high-resolution, ultrafast, and non-invasive neuromorphic systems. They enable direct interaction with the ferroelectric reservoir without physical wiring, expanding integration possibilities with optical platforms, scanning probe tools, and flexible electronics. In the implementations illustrated in Figure 7, the ferroelectric reservoir is operated using contactless methods for data input and output, where the array of ferroelectric nanodots serves as a pixel-wise data storage matrix.

In the configuration shown in Figure 7a, optoelectronic techniques are employed. At the input stage, a pixel-resolved optical beam locally excites charges at the top electrode, inducing spatially resolved switching of individual ferroelectric nanodots. The processed information, stored in the polarization states of the nanodots, is subsequently read out optically, again in a pixel-by-pixel manner. This approach enables fully contactless operation and is compatible with scalable, high-throughput optical interfaces.

An alternative configuration is shown in Figure 7b, where atomic force microscopy or piezoresponse force microscopy are used for both input and output operations. Here, the localized tip of the microscope is used to inject or sense charges at specific positions in the ferroelectric array, allowing for direct control or readout of the nanodots' polarization states with nanoscale

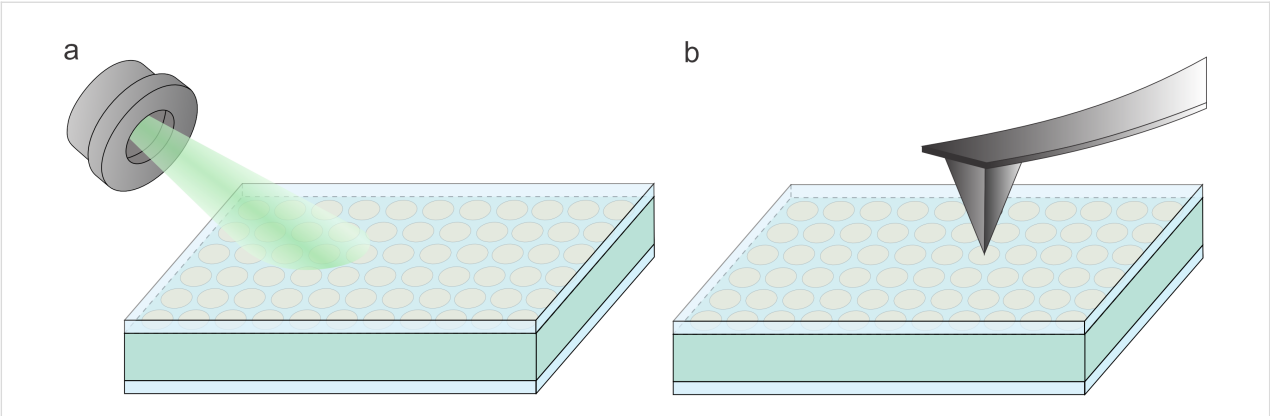


Figure 7: Contactless input and output methods for the ferroelectric reservoir. (a) Input and readout based on optoelectronic addressing and sensing. (b) Input and readout realized via atomic or piezoresponse force microscopy.

precision. Such techniques offer a high-resolution interface with the reservoir and can be particularly effective in prototyping, diagnostics, or specialized neuromorphic functions.

These contactless schemes are fully compatible with the broader architecture of ferroelectric reservoir computing and complement the time- and space-multiplexed electrical methods discussed in previous figures. Importantly, the ability to selectively write and read polarization states without electrodes enhances the potential for integrating the reservoir with optical systems, probe-based tools, or even hybrid analog-digital platforms.

Conclusion

In this work, we have proposed and analyzed a ferroelectric-based data processing reservoir composed of nonlinear, bistable nanodots arranged in capacitor-like configurations. Each nanodot supports multiple polarization states with hysteretic switching, enabling robust information storage and processing. The assembled ferroelectric reservoir exhibits behavior governed by a frustrated Ising-type energy landscape, where the polarization configuration minimizes the electrostatic energy of the coupled system. Interaction matrix and local fields arise naturally from electrostatic coupling, while the discrete polarization states map to binary Ising variables. This analogy provides a physically grounded platform for implementing neuromorphic functionality.

The system operates through charge-controlled switching of polarization states, and its dynamic behavior depends not only on external inputs but also on prior polarization history. This results in noncommutative and path-dependent evolution trajectories, as demonstrated through examples involving two-, four-, and many-dot arrays. Particularly, sequential application of charge pulses leads to rich dynamics in high-dimensional configuration spaces, with the number of accessible metastable states growing combinatorially with the number of nanodots. Such complexity enables the encoding and transformation of temporal information in a manner suitable for reservoir computing architectures.

We demonstrated several architectures for signal injection and readout, including time- and voltage-driven schemes, spatially multiplexed control using localized electrodes, and contactless access via optoelectronic or scanning probe methods. These multiple input/output schemes offer a high degree of flexibility and compatibility with different system architectures. Notably, all implementations rely solely on dielectric polarization degrees of freedom, requiring no active current-driving elements. This makes the system particularly attractive for low-energy, high-density neuromorphic circuits.

The proposed ferroelectric reservoir benefits from several advantageous physical properties intrinsic to nanoscale ferroelectrics – high capacity, with exponentially growing configuration space, fading memory, provided by the slow relaxation dynamics of polarization in individual nanodots, intrinsic nonlinearity, stemming from the hysteretic switching behavior, and flexible integration, including time- and space-multiplexing schemes for efficient data exchange with synaptic layers.

As an extension of the proposed platform, the ferroelectric nanodots can be designed to host complex topological excitations, such as domains [45,46], vortices [47-49], helices [50], skyrmion-like structures [51,52], and hopfions [53], forming multistable polarization textures with nontrivial topology. These topological polarization configurations are not only stable against perturbations but can also support multilevel logic states beyond simple binary encoding. Their internal structure provides additional degrees of freedom that can be exploited for multivalued neuromorphic processing, enabling richer spatio-temporal dynamics and increased information density. Integration of topological excitations into the reservoir computing framework may further enhance robustness, programmability, and parallelism, opening up new opportunities for topologically protected logic and neuromorphic computation in future nanoscale devices.

Funding

This research was funded by the European Union HORIZON action MSCA-SE-3D-TOPO (project number 101236483). A.R. acknowledges the Slovenian Research Agency support (P1-0125). The work of V.V. was supported by Terra Quantum AG.

Author Contributions

Anna Razumnaya: conceptualization; methodology; supervision; writing – original draft; writing – review & editing. Yuri Tikhonov: conceptualization; methodology; writing – original draft; writing – review & editing. Dmitrii Naidenko: conceptualization; methodology; writing – original draft. Léo Boron: conceptualization; methodology; writing – original draft. Valerii Vinokur: conceptualization; methodology; writing – review & editing. Igor Lukyanchuk: conceptualization; methodology; supervision; writing – original draft; writing – review & editing.

ORCID® iDs

Anna Razumnaya - https://orcid.org/0000-0001-8486-7303
Valerii Vinokur - https://orcid.org/0000-0002-0977-3515

Data Availability Statement

Data generated and analyzed during this study is available from the corresponding author upon reasonable request.

References

1. Marković, D.; Mizrahi, A.; Querlioz, D.; Grollier, J. *Nat. Rev. Phys.* **2020,** *2,* 499–510. doi:10.1038/s42254-020-0208-2
2. Zhu, J.; Zhang, T.; Yang, Y.; Huang, R. *Appl. Phys. Rev.* **2020,** *7,* 011312. doi:10.1063/1.5118217
3. Xiao, Y.; Gao, C.; Jin, J.; Sun, W.; Wang, B.; Bao, Y.; Liu, C.; Huang, W.; Zeng, H.; Yu, Y. *Adv. Devices Instrum.* **2024,** *5,* 0044. doi:10.34133/adi.0044
4. Kudithipudi, D.; Schuman, C.; Vineyard, C. M.; Pandit, T.; Merkel, C.; Kubendran, R.; Aimone, J. B.; Orchard, G.; Mayr, C.; Benosman, R.; Hays, J.; Young, C.; Bartolozzi, C.; Majumdar, A.; Cardwell, S. G.; Payvand, M.; Buckley, S.; Kulkarni, S.; Gonzalez, H. A.; Cauwenberghs, G.; Thakur, C. S.; Subramoney, A.; Furber, S. *Nature* **2025,** *637,* 801–812. doi:10.1038/s41586-024-08253-8
5. Enuganti, P. K.; Sen Bhattacharya, B.; Serrano Gotarredona, T.; Rhodes, O. *Wiley Interdiscip. Rev.: Data Min. Knowl. Discovery* **2025,** *15,* e70014. doi:10.1002/widm.70014
6. Pawlak, W. A.; Howard, N. *Front. Neurosci.* **2025,** *19,* 1570104. doi:10.3389/fnins.2025.1570104
7. Tanaka, G.; Yamane, T.; Héroux, J. B.; Nakane, R.; Kanazawa, N.; Takeda, S.; Numata, H.; Nakano, D.; Hirose, A. *Neural Networks* **2019,** *115,* 100–123. doi:10.1016/j.neunet.2019.03.005
8. Gauthier, D. J.; Bollt, E.; Griffith, A.; Barbosa, W. A. S. *Nat. Commun.* **2021,** *12,* 5564. doi:10.1038/s41467-021-25801-2
9. Cucchi, M.; Abreu, S.; Ciccone, G.; Brunner, D.; Kleemann, H. *Neuromorph. Comput. Eng.* **2022,** *2,* 032002. doi:10.1088/2634-4386/ac7db7
10. Wringe, C.; Trefzer, M.; Stepney, S. *Int. J. Parallel Emergent Distrib. Syst.* **2025,** *40,* 313–351. doi:10.1080/17445760.2025.2472211
11. Liu, J.; Feng, G.; Li, W.; Hao, S.; Han, S.; Zhu, Q.; Tian, B.; Duan, C.; Chu, J. *Innovation Mater.* **2025,** *3,* 100127. doi:10.59717/j.xinn-mater.2025.100127
12. Pierangeli, D.; Marcucci, G.; Conti, C. *Photonics Res.* **2021,** *9,* 1446–1454. doi:10.1364/prj.423531
13. Torrejon, J.; Riou, M.; Araujo, F. A.; Tsunegi, S.; Khalsa, G.; Querlioz, D.; Bortolotti, P.; Cros, V.; Yakushiji, K.; Fukushima, A.; Kubota, H.; Yuasa, S.; Stiles, M. D.; Grollier, J. *Nature* **2017,** *547,* 428–431. doi:10.1038/nature23011
14. Zhong, Y.; Tang, J.; Li, X.; Liang, X.; Liu, Z.; Li, Y.; Xi, Y.; Yao, P.; Hao, Z.; Gao, B.; Qian, H.; Wu, H. *Nat. Electron.* **2022,** *5,* 672–681. doi:10.1038/s41928-022-00838-3
15. Choi, S.; Shin, J.; Park, G.; Eo, J. S.; Jang, J.; Yang, J. J.; Wang, G. *Nat. Commun.* **2024,** *15,* 2044. doi:10.1038/s41467-024-46323-7
16. Chen, Z.; Li, W.; Fan, Z.; Dong, S.; Chen, Y.; Qin, M.; Zeng, M.; Lu, X.; Zhou, G.; Gao, X.; Liu, J.-M. *Nat. Commun.* **2023,** *14,* 3585. doi:10.1038/s41467-023-39371-y
17. Luo, Z.; Wang, Z.; Guan, Z.; Ma, C.; Zhao, L.; Liu, C.; Sun, H.; Wang, H.; Lin, Y.; Jin, X.; Yin, Y.; Li, X. *Nat. Commun.* **2022,** *13,* 699. doi:10.1038/s41467-022-28303-x
18. Mikolajick, T.; Park, M. H.; Begon-Lours, L.; Slesazeck, S. *Adv. Mater. (Weinheim, Ger.)* **2023,** *35,* 2206042. doi:10.1002/adma.202206042
19. Wang, Z. *arXiv* **2024,** 2406.13946. doi:10.48550/arxiv.2406.13946
20. Lee, D.; Sung, J.; Kim, M.; Kim, N.-H.; Lee, S.; Lee, H.-Y.; Lee, E. K.; Jeong, D.; Lee, E. *ACS Appl. Mater. Interfaces* **2024,** *16,* 58940–58951. doi:10.1021/acsami.4c11731
21. Wen, Z.; Chen, J.; Zhang, Q.; Wang, G.; Wang, X.; Yang, F.; Liu, Q.; Luo, X.; Liu, F. *Small* **2025,** *21,* 2412761. doi:10.1002/smll.202412761
22. Baudry, L.; Luk'yanchuk, I. A.; Razumnaya, A. *Phys. Rev. B* **2015,** *91,* 144110. doi:10.1103/physrevb.91.144110
23. Van Lich, L.; Shimada, T.; Sepideh, S.; Wang, J.; Kitamura, T. *Acta Mater.* **2017,** *125,* 202–209. doi:10.1016/j.actamat.2016.11.065
24. Baudry, L.; Lukyanchuk, I.; Vinokur, V. M. *Sci. Rep.* **2017,** *7,* 42196. doi:10.1038/srep42196
25. Pei, M.; Zhu, Y.; Liu, S.; Cui, H.; Li, Y.; Yan, Y.; Li, Y.; Wan, C.; Wan, Q. *Adv. Mater. (Weinheim, Ger.)* **2023,** *35,* 2305609. doi:10.1002/adma.202305609
26. Ramesh, R.; Schlom, D. G. *Nat. Rev. Mater.* **2019,** *4,* 257–268. doi:10.1038/s41578-019-0095-2
27. Tian, G.; Yang, W. D.; Gao, X. S.; Liu, J.-M. *APL Mater.* **2021,** *9,* 020907. doi:10.1063/5.0039139
28. Chen, S.; Yuan, S.; Hou, Z.; Tang, Y.; Zhang, J.; Wang, T.; Li, K.; Zhao, W.; Liu, X.; Chen, L.; Martin, L. W.; Chen, Z. *Adv. Mater. (Weinheim, Ger.)* **2021,** *33,* 2000857. doi:10.1002/adma.202000857
29. Das, S.; Hong, Z.; McCarter, M.; Shafer, P.; Shao, Y.-T.; Muller, D. A.; Martin, L. W.; Ramesh, R. *APL Mater.* **2020,** *8,* 120902. doi:10.1063/5.0034914
30. Guo, X.; Zhou, L.; Roul, B.; Wu, Y.; Huang, Y.; Das, S.; Hong, Z. *Small Methods* **2022,** *6,* 2200486. doi:10.1002/smtd.202200486
31. Junquera, J.; Nahas, Y.; Prokhorenko, S.; Bellaiche, L.; Íñiguez, J.; Schlom, D. G.; Chen, L.-Q.; Salahuddin, S.; Muller, D. A.; Martin, L. W.; Ramesh, R. *Rev. Mod. Phys.* **2023,** *95,* 025001. doi:10.1103/revmodphys.95.025001
32. Wang, Y. J.; Tang, Y. L.; Zhu, Y. L.; Ma, X. L. *Acta Mater.* **2023,** *243,* 118485. doi:10.1016/j.actamat.2022.118485
33. Luk'yanchuk, I.; Razumnaya, A.; Kondovych, S.; Tikhonov, Y.; Vinokur, V. M. *arXiv* **2024,** 2406.19728. doi:10.48550/arxiv.2406.19728
34. Lukyanchuk, I.; Zaitseva, E.; Levashenko, V.; Kvassay, M.; Kondovych, S.; Tikhonov, Y.; Baudry, L.; Razumnaya, A. *Ferroelectrics* **2019,** *543,* 213–221. doi:10.1080/00150193.2019.1592436
35. Hu, Y.; Zhu, Y.; Chen, X.; Wan, Q. *Nanomaterials* **2025,** *15,* 863. doi:10.3390/nano15110863
36. Toprasertpong, K.; Nako, E.; Wang, Z.; Nakane, R.; Takenaka, M.; Takagi, S. *Commun. Eng.* **2022,** *1,* 21. doi:10.1038/s44172-022-00021-8
37. Wang, C.; Agrawal, A.; Yu, E.; Roy, K. *Front. Neurosci.* **2021,** *15,* 661667. doi:10.3389/fnins.2021.661667
38. Razumnaya, A. G.; Tikhonov, Y. A.; Vinokur, V. M.; Lukyanchuk, I. A. *Neuromorph. Comput. Eng.* **2023,** *3,* 024003. doi:10.1088/2634-4386/acce61
39. Razumnaya, A.; Tikhonov, Y.; Lukyanchuk, I.; Vinokur, V. Ferroelectric nanoparticle capacitor for non-binary logics. EP4354477B1, Oct 11, 2022.
40. Salahuddin, S.; Datta, S. *Nano Lett.* **2008,** *8,* 405–410. doi:10.1021/nl071804g
41. Luk'yanchuk, I.; Razumnaya, A.; Sené, A.; Tikhonov, Y.; Vinokur, V. M. *npj Comput. Mater.* **2022,** *8,* 52. doi:10.1038/s41524-022-00738-2
42. Jaeger, H.; Haas, H. *Science* **2004,** *304,* 78–80. doi:10.1126/science.1091277
43. Mizushima, K.; Goto, H.; Sato, R. *Appl. Phys. Lett.* **2017,** *111,* 172406. doi:10.1063/1.5007231
44. Chen, Z.; Xiao, Z.; Akl, M.; Leugering, J.; Olajide, O.; Malik, A.; Dennler, N.; Harper, C.; Bose, S.; Gonzalez, H. A.; Samaali, M.; Liu, G.; Eshraghian, J.; Pignari, R.; Urgese, G.; Andreou, A. G.; Shankar, S.; Mayr, C.; Cauwenberghs, G.; Chakrabartty, S. *Nat. Commun.* **2025,** *16,* 3086. doi:10.1038/s41467-025-58231-5

45. Martelli, P.-W.; Mefire, S. M.; Luk'yanchuk, I. A. *EPL* **2015,** *111,* 50001. doi:10.1209/0295-5075/111/50001
46. Luk'yanchuk, I.; Tikhonov, Y.; Sené, A.; Razumnaya, A.; Vinokur, V. M. *Commun. Phys.* **2019,** *2,* 22. doi:10.1038/s42005-019-0121-0
47. Naumov, I. I.; Bellaiche, L.; Fu, H. *Nature* **2004,** *432,* 737–740. doi:10.1038/nature03107
48. Lahoche, L.; Lukyanchuk, I.; Pascoli, G. *Integr. Ferroelectr.* **2008,** *99,* 60–66. doi:10.1080/10584580802107684
49. Xiong, P. C.; Ma, W. B.; Yuan, S.; Liu, Y. L.; Wang, B. *AIP Adv.* **2022,** *12,* 015001. doi:10.1063/5.0076281
50. Olaniyan, I.; Tikhonov, I.; Hevelke, V. V.; Wiesner, S.; Zhang, L.; Razumnaya, A.; Cherkashin, N.; Schamm-Chardon, S.; Lukyanchuk, I.; Kim, D.-J.; Dubourdieu, C. *Nat. Commun.* **2024,** *15,* 10047. doi:10.1038/s41467-024-54285-z
51. Tikhonov, Y.; Kondovych, S.; Mangeri, J.; Pavlenko, M.; Baudry, L.; Sené, A.; Galda, A.; Nakhmanson, S.; Heinonen, O.; Razumnaya, A.; Luk'yanchuk, I.; Vinokur, V. M. *Sci. Rep.* **2020,** *10,* 8657. doi:10.1038/s41598-020-65291-8
52. Chen, H.; Yang, W.; Li, C.; Jiao, P.; Liu, Z.; Lin, C.; Chen, Y.; Tian, G.; Deng, Y.; Nie, Y.; Wu, Y.; Liu, J.-M.; Hong, Z.; Gao, X.; Wu, D. *Appl. Phys. Rev.* **2024,** *11,* 031420. doi:10.1063/5.0209179
53. Luk'yanchuk, I.; Tikhonov, Y.; Razumnaya, A.; Vinokur, V. M. *Nat. Commun.* **2020,** *11,* 2433. doi:10.1038/s41467-020-16258-w

License and Terms

This is an open access article licensed under the terms of the Beilstein-Institut Open Access License Agreement (https://www.beilstein-journals.org/bjnano/terms), which is identical to the Creative Commons Attribution 4.0 International License (https://creativecommons.org/licenses/by/4.0). The reuse of material under this license requires that the author(s), source and license are credited. Third-party material in this article could be subject to other licenses (typically indicated in the credit line), and in this case, users are required to obtain permission from the license holder to reuse the material.

The definitive version of this article is the electronic one which can be found at:
https://doi.org/10.3762/bjnano.17.24